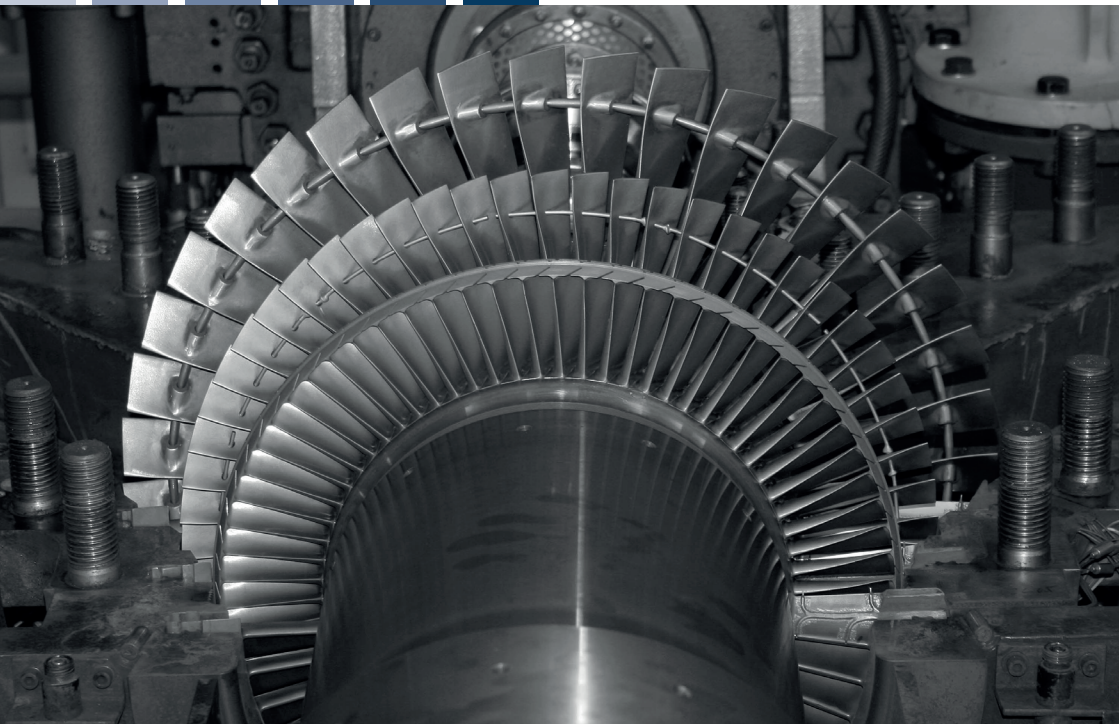


Experimental and Numerical Investigation on Aero-Thermodynamics in a Low-Pressure Industrial Steam Turbine with Part-Span Connectors

Markus Häfele



Experimental and Numerical Investigation on Aero-Thermodynamics in a Low-Pressure Industrial Steam Turbine with Part-Span Connectors

Von der Fakultät Energie-, Verfahrens- und Biotechnik
der Universität Stuttgart zur Erlangung der Würde eines Doktors
der Ingenieurwissenschaften (Dr.-Ing.) genehmigte Abhandlung

vorgelegt von
Markus Häfele
aus Lima/Peru

Hauptberichter: Prof. Tekn. Dr. Damian Vogt
Mitberichter: Univ.-Prof. Dr.-Ing. habil. Manfred Wirsum

Tag der mündlichen Prüfung: 16.07.2020

Institut für Thermische Strömungsmaschinen
und Maschinenlaboratorium der Universität Stuttgart

2020

Berichte aus der Strömungstechnik

Markus Häfele

**Experimental and Numerical Investigation on
Aero-Thermodynamics in a Low-Pressure Industrial
Steam Turbine with Part-Span Connectors**

D 93 (Diss. Universität Stuttgart)

Shaker Verlag
Düren 2020

Bibliographic information published by the Deutsche Nationalbibliothek

The Deutsche Nationalbibliothek lists this publication in the Deutsche Nationalbibliografie; detailed bibliographic data are available in the Internet at <http://dnb.d-nb.de>.

Zugl.: Stuttgart, Univ., Diss., 2020

Copyright Shaker Verlag 2020

All rights reserved. No part of this publication may be reproduced, stored in a retrieval system, or transmitted, in any form or by any means, electronic, mechanical, photocopying, recording or otherwise, without the prior permission of the publishers.

Printed in Germany.

ISBN 978-3-8440-7697-4

ISSN 0945-2230

Shaker Verlag GmbH • Am Langen Graben 15a • 52353 Düren

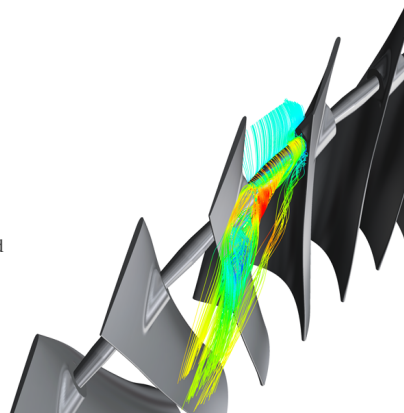
Phone: 0049/2421/99011-0 • Telefax: 0049/2421/99011-9

Internet: www.shaker.de • e-mail: info@shaker.de

In Loving Memory of my Father

Friedrich G. HÄFELE (1944–2020)

Simulated three-dimensional viscous condensing wet steam flow around part-span connectors in a low-pressure industrial steam turbine using a non-equilibrium steam model



Preface

The present doctoral thesis summarizes the outcome of my work as research assistant at the Institute of Thermal Turbomachinery and Machinery Laboratory (ITSM) of the University of Stuttgart. It is based on, but not limited to, articles no. 1–2 and conference papers no. 3–4 listed below. For these publications the underlying material was part of the work elaborated in this thesis. Particularly, fluid-dynamical aspects are addressed, utilizing experimental, numerical and analytical approaches. Besides the experimental investigation and numerical modelling of a low-pressure (LP) industrial steam turbine with part-span connectors (PSC), the impact of PSCs on aero-thermodynamics in condensing steam flow and corresponding losses are discussed.

1. HÄFELE, M.; TRAXINGER, C.; GRÜBEL, M.; SCHATZ, M.; VOGT, D. M.; AND DROZDOWSKI, R.: **Experimental and Numerical Investigation of the Flow in a Low-Pressure Industrial Steam Turbine with Part-Span Connectors**¹, Trans. ASME, J. Eng. Gas Turb. Power, Vol. 138(7), 072604. Copyright © 2016 by ASME. *Republished with permission of ASME.*
2. HÄFELE, M.; TRAXINGER, C.; GRÜBEL, M.; SCHATZ, M.; VOGT, D. M.; AND DROZDOWSKI, R.: **Numerical and Experimental Study on Aero-dynamic Optimization of Part-Span Connectors in the Last Stage of a Low-Pressure Industrial Steam Turbine**², Proc. IMechE, Part A: J. Power and Energy, Vol. 229(5), pp. 465-476. Copyright © 2015 by IMechE. *Republished with permission of SAGE Publications.*
3. HÄFELE, M.; STARZMANN, J.; GRÜBEL, M.; SCHATZ, M.; VOGT, D. M.; DROZDOWSKI, R.; AND VÖLKER, L.: **Numerical Investigation of the Impact of Part-Span Connectors on Aero-Thermodynamics in a Low Pressure Industrial Steam Turbine**, ASME Paper No. GT2014-25177, in: Proc. ASME Turbo Expo 2014: Turbine Technical Conference and Exposition, Düsseldorf, Germany, June 16–20, 2014. Copyright © 2014 by ASME. *Republished with permission of ASME.*
4. HÄFELE, M.; VOGT, D. M.; AND DROZDOWSKI, R.: **Numerical Modelling of a Three Stage Low Pressure Industrial Steam Turbine with Part-Span Connectors**, in: Proc. ANSYS Conference & 32nd CADFEM Users' Meeting, Nürnberg, Germany, June 4–6, 2014. Copyright © 2014 by CADFEM GmbH.

¹Presented at the ASME Turbo Expo 2015: Turbine Technical Conference and Exposition, Montréal, Canada, June 15–19, 2015, ASME Paper No. GT2015-42202 [49]

²Presented at the 11th European Conference on Turbomachinery, Fluid Dynamics and Thermodynamics (ETC11), Madrid, Spain, March 23–27, 2015, Paper No. ETC2015-054 [51]

Furthermore, co-authored publications are focused on mechanical aspects. In particular, the vibrational behavior of coupled LP rotor blading is analyzed by means of experimental and numerical methods. The author's main contribution to article no. 5 and conference paper no. 6 was in terms of experimental investigations at the industrial steam turbine test rig at ITSM, and parts of their contents serve as basis for this dissertation.

5. DROZDOWSKI, R.; VÖLKER, L.; HÄFELE, M.; AND VOGT, D. M.: **Numerical and Experimental Analysis of Low-Pressure Steam Turbine Blades Coupled with Lacing Wire**³, Proc. IMechE, Part A: J. Power and Energy, Vol. 230(3), pp. 332-342. Copyright © 2016 by IMechE.
6. DROZDOWSKI, R.; VÖLKER, L.; HÄFELE, M.; AND VOGT, D. M.: **Experimental and Numerical Investigation of the Nonlinear Vibrational Behavior of Steam Turbine Last Stage Blades with Friction Bolt Damping Elements**, ASME Paper No. GT2015-42244, in: Proc. ASME Turbo Expo 2015: Turbine Technical Conference and Exposition, Montréal, Canada, June 15–19, 2015. Copyright © 2015 by SIEMENS Energy, Inc.

³Presented at the 11th European Conference on Turbomachinery, Fluid Dynamics and Thermodynamics (ETC11), Madrid, Spain, March 23–27, 2015, Paper No. ETC2015-105 [28]

Abstract

Industrial steam turbines (IST) are designed for flexible, reliable and robust operation with the ability for short start-up times. Basically assigned to the power class up to 250 MW, this type of turbine is normally operated over an extremely wide range of speed, loading and backpressure. In order to ensure safe turbine operation, even in blade resonance condition, part-span connectors (PSC) are mounted between adjacent blades. These cylindrical elements provide blade damping and coupling. However, additional losses are generated, affecting the turbine performance. Since steam turbines are the workhorses of nowadays global power industry, improvements of existing and new designs in terms of turbine efficiency have a large leverage effect. Consequently, for the research on low-pressure (LP) industrial steam turbines, the question on the impact of PSCs on aero-thermodynamics has been raised in the light of still incomplete understanding of its complexity and so far missing comprehensive studies.

At the Institute of Thermal Turbomachinery and Machinery Laboratory (ITSM) of the University of Stuttgart, an industrial steam turbine test rig has been modernized and commissioned for testing of typical SIEMENS LP IST blading with respect to aero-thermodynamics and the vibrational behavior. The investigated three-stage section of a full-scale turbine features conical friction bolts (FB) & blade reinforcements (BR) in the last and a lacing wire (LW) in the penultimate rotor blade row. Measurements under real steam conditions and three-dimensional computational fluid dynamics (3D CFD) utilizing a non-equilibrium steam (NES) model reveal strongly pronounced aero-thermodynamic effects of the PSCs on the wet steam flow, whereby the presence of FB & BR in the last stage blading (LSB) results in a considerably large reduction of stage efficiency by almost 4% at the best efficiency point (BEP). The applied CFD models have been developed to investigate the impact of PSCs with engineering accuracy, suitable for an industrial design process. Based on the successful experimental validation carried out, the models prove validity to capture the 3D flow field in LP steam turbine blading with PSC.

3D CFD discloses a modification of blade design parameters caused by the presence of the PSC within the flow channel and further reveals additional non-equilibrium condensation effects, suggesting the PSC to be generally considered within a numerical model for the blade design process. On the other hand, results of a PSC parameter study show that besides the facing flow condition, the PSC blockage area is governing the loss. Based on a huge variety of PSC configurations highlighting the popular concepts of FB & BR and LW, a performance assessment by means of specific work output and the PSC vortex system is carried out. Moving a cylindrical PSC down to mid-span and further lowering its diameter provides the largest leverage. The shape of a streamlined PSC cross section can gain additional benefit.

Within the early design process, blade designers often rely on drag-based loss correlations like the one of TRAUPEL or DUNHAM AND PHILLIPSEN in order to estimate the deteriorating effect of PSCs on the stage efficiency, while usually accepting their unknown quantitative correspondence to reality. The present thesis supports this field and additionally provides insights into the loss composition. It shows that for the investigated type of LSB, both approaches perform well at mid-span but only the latter can cope with a span-wise PSC variation. The findings presented for BEP condition are promising with respect to further refinement of the correlations. Care should be taken for defining appropriate drag coefficients in LP steam turbine blading, especially for streamlined shapes. Regarding this matter, the present work delivers helpful indications.

Kurzfassung

Industriedampfturbinen sind für einen flexiblen, zuverlässigen und robusten Betrieb ausgelegt und können in kürzester Zeit auf Betriebszustand gebracht werden. Dieser der Leistungsklasse bis 250 MW zugeordnete Turbinentyp wird in der Regel über einen extrem weiten Drehzahl-, Last- und Gegendruckbereich betrieben. Zur Gewährleistung des sicheren Turbinenbetriebs, auch im Resonanzzustand der Laufschaufeln, werden Koppелеlemente (PSC) im Strömungskanal zwischen benachbarten Laufschaufeln montiert. Diese zylindrischen Bauteile sorgen für die erforderliche Dämpfung und Kopplung der Schaufeln. Es entstehen jedoch zusätzliche Strömungsverluste, die sich negativ auf die Turbinenleistung auswirken. Aufgrund der Tatsache, dass Dampfturbinen die Zugpferde der heutigen globalen Energiewirtschaft sind, haben Verbesserungen bestehender und neuer Konstruktionen hinsichtlich des Turbinenwirkungsgrads eine große Hebelwirkung. Im Bereich der Forschung an Niederdruck (ND)-Industriedampfturbinen wurde daher die Frage nach der Auswirkung von Koppелеlementen auf die Aerothermodynamik aufgeworfen, insbesondere im Hinblick auf das noch unzureichende Verständnis dieser Thematik und bislang fehlender umfassender Studien hierzu.

Am Institut für Thermische Strömungsmaschinen und Maschinenlaboratorium (ITSM) der Universität Stuttgart wurde ein Industriedampfturbinen-Versuchsstand modernisiert und in Betrieb genommen, um typische SIEMENS ND-Beschaufelungen hinsichtlich Aerothermodynamik und ihres Schwingungsverhaltens zu untersuchen. Der betrachtete dreistufige Abschnitt einer Turbine im Originalmaßstab weist konische Koppelbolzen (FB) & Schaufelverstärkungen (BR) in der letzten und einen Bindedraht (LW) in der vorletzten Laufschaufelreihe auf. Messungen unter realen Dampfbedingungen und dreidimensionale numerische Strömungssimulationen (3D CFD) unter Verwendung eines Ungleichgewichtsdampfmodells (NES) zeigen stark ausgeprägte aerothermodynamische Effekte der Koppелеlemente auf die Nassdampfströmung, wobei die Präsenz von FB & BR zu einer beträchtlichen Verminderung des Endstufenwirkungsgrads um nahezu 4 % im Optimalpunkt (BEP) führt. Die verwendeten CFD-Modelle sollen einem industriellen Entwicklungsprozess dienlich sein und wurden mit dem Ziel entwickelt, die Auswirkung von Koppелеlementen auf die Strömung mit ingenieurtechnischer Genauigkeit zu untersuchen. Basierend auf der erfolgreich durchgeführten experimentellen Validierung erweisen sich die Modelle als geeignet, um das 3D-Strömungsfeld in ND-Dampfturbinen mit gekoppelter Laufradbeschaufelung zu erfassen.

Mithilfe von 3D CFD wird in der vorliegenden Arbeit gezeigt, dass durch die Koppелеlemente im Strömungskanal grundlegende Schaufelauslegungsparameter beeinflusst werden. Darüber hinaus kommt es zu zusätzlichen Ungleichgewichtskondensationseffekten. Die Erkenntnisse legen nahe, dass ein

Koppelement generell im numerischen Modell eines Auslegungsprozesses berücksichtigt werden sollte. Die Ergebnisse einer PSC-Parameterstudie zeigen außerdem, dass neben den vorherrschenden Strömungsbedingungen im Bereich des Koppelements die Höhe der Strömungsverluste hauptsächlich durch die versperrte Fläche dominiert wird. Basierend auf einer Vielzahl von PSC-Konfigurationen, welche auf den gängigen Konzepten von FB & BR und LW beruhen, wird eine Leistungsbewertung mittels spezifischer Arbeit sowie der PSC-Wirbelsysteme durchgeführt. Hierbei bietet das Absenken der radialen Position eines zylindrischen Koppelements bis auf Höhe des Mittenschnitts den größten Effekt hinsichtlich einer Leistungssteigerung. Eine weitere Optimierung wird durch verkleinern des PSC-Durchmessers erreicht. Die Form eines stromlinienförmigen PSC-Querschnitts kann zusätzlichen Nutzen bringen.

Im frühen Stadium eines Entwurfsprozesses verlassen sich Schaufelentwickler oft auf Widerstandskraft-basierte Verlustkorrelationen wie jene von TRAUPEL oder DUNHAM UND PHILLIPSEN, um die negative Wirkung von Koppelementen auf den Stufenwirkungsgrad abzuschätzen. Hierbei wird akzeptiert, dass die quantitative Übereinstimmung der Korrelationen mit der Realität üblicherweise unbekannt ist. Die vorliegende Arbeit leistet diesbezüglich einen Beitrag und gibt darüber hinaus Einblicke in die Verlustzusammensetzung. Ein Vergleich mit CFD-Ergebnissen zeigt, dass für die untersuchte Art von ND-Beschaufelung beide analytischen Korrelationen die Höhe des Verlustes durch ein im Mittenschnitt positioniertes Koppelement erfassen können, aber nur letztere den Effekt einer radialen PSC-Variation abbilden kann. Die für den Optimalpunkt gezeigten Ergebnisse sind vielversprechend im Hinblick auf eine Erweiterung der Korrelationen. Es ist allerdings darauf zu achten, dass geeignete Widerstandsbeiwerte für die Koppelemente der Beschaufelung von ND-Dampfturbinen verwendet werden, insbesondere für stromlinienförmige PSC-Formen. In diesem Zusammenhang bietet die vorliegende Arbeit eine Hilfestellung.

Acknowledgment

Throughout the progress of my research work at ITSM, I have received a great deal of advice and assistance. This dissertation would not have been possible without the continuous support of many.

First, and foremost, I would like to express my very great appreciation to my supervisor Prof. Tekn. Dr. Damian VOGT, director of ITSM, for his valuable guidance and the trust he has placed in me. His endorsement of taking over the main report is highly appreciated. Furthermore, I would like to sincerely thank Univ.-Prof. Dr.-Ing. Manfred WIRSUM from the Institute of Power Plant Technology, Steam and Gas Turbines (IKDG) of the RWTH Aachen, who kindly took over the co-report. Also, many thanks to the chairman of the audit committee, Prof. Dr.-Ing. Stefan RIEDELBAUCH from the Institute of Fluid Mechanics and Hydraulic Machinery (IHS), for conducting the doctoral examination.

I am particularly grateful to Prof. Michael CASEY, D. Phil, former director of ITSM. He is the one who enthused me as a student for the field of turbomachinery and later provided me the opportunity to work as a research assistant at his chair. His outstanding knowledge in this field was always of great help.

Gratitude goes to the entire ITSM staff. I would like to thank especially my office colleagues, namely Dr.-Ing. Christoph HEINZ, Dr.-Ing. Timo EBERLE, Fabian MÜLLER and Christoph BRÜGGEMANN, for their helpfulness and enjoyable years in the *Endstufenzimmer*. A special mention is due to Univ.-Prof. Dr.-Ing. Markus SCHATZ, former head of Thermal Turbomachinery Group, for his continuous personal and academic encouragement. Advice given by Dr.-Ing. Jörg STARZMANN and Marius GRÜBEL has been of great help in conducting the CFD simulations. I would further like to thank these gentlemen for fruitful technical discussions.

I wish to acknowledge the invaluable help provided by the ITSM lab staff for preparing the tests and operating the turbine. Especially the time spent in the *Warte* is remembered with great pleasure. Thank you, Martin BRAUSEWETTER, Martin KRINN and Pavlos TIPSIOS. This appreciation is extended to Dr.-Ing. Gerhard EYB, former head of the Machinery Laboratory and Measurement Technique, for troubleshooting and support regarding operational concerns with the test rig. Thanks is also given to Benjamin KUSCHEL for his tremendous helpfulness.

The commitment of numerous students, whom I supervised in preparing their own student works, has contributed significantly to the success of this doctoral thesis. In particular the highly productive and very pleasant cooperation with Christoph TRAXINGER, sometimes resulting in technical discussions until late into the night, is very well remembered.

Thanks is given to SIEMENS Energy for providing the financial means to support this project and their permission to publish research findings. In this regard I would like to offer my special thanks to Dr.-Ing. Lutz VÖLKER, Rico SCHNEIDER and Dr.-Ing. Roman DROZDOWSKI for their commitment in supporting the project from industrial side. The help of Ulf MODEL for commissioning the test rig has been also greatly appreciated.

The proofreading of this dissertation was kindly conducted by Dr.-Ing. Jörg STARZMANN, Marius GRÜBEL and Christoph TRAXINGER. I am particularly thankful for their critical comments and valuable suggestions. In this context I don't want to miss thanking the technical turbomachinery community for peer-reviewing my articles and conference contributions.

I am deeply grateful to my parents, who always pushed forming my technical skills and who have provided me through moral and emotional support in my life. Finally, I would like to thank my wife Nicole (*Nicki*) from the bottom of my heart, especially for her love, support and understanding she has shown me during the preparation of this work.

Waldkirch, November 2020

Markus Häfele

Contents

Preface	v
Abstract	vii
Kurzfassung	ix
Acknowledgment	xi
Nomenclature	xvii
1 Introduction	1
1.1 Motivation	2
1.1.1 Steam Power Plant	2
1.1.2 Industrial Steam Turbine	3
1.1.3 Part-Span Connector (PSC)	6
1.1.4 Problem Definition	8
1.2 Research Objective	10
1.3 Thesis Outline	11
1.4 Literature Review and Discussion	12
1.4.1 Brief Overview	12
1.4.2 Loss Correlations for PSCs	13
1.4.3 Experimental Investigations	21
1.4.4 Numerical Investigations	27
2 Industrial Steam Turbine Test Rig	37
2.1 Basic Features	38
2.2 Measuring Equipment and Data Acquisition	39
2.2.1 Stage Pressures and Temperatures	39
2.2.2 Diffuser Pressure	41
2.2.3 Torque and Speed	41
2.2.4 Mass Flow Rate	41
2.2.5 Bearing Oil Flow Rate and Temperature	41
2.2.6 Pneumatic 5-Hole Cone-Head Probes	42
2.2.7 Probe Traversing Systems	43
2.2.8 Continuous Purging	45
2.2.9 Blade Vibration	45
2.3 Introduction to Experimental Investigations	47

2.4	Evaluation of Measurement Data	49
2.4.1	Data Averaging	49
2.4.2	Purging Correction	50
2.4.3	Measurement Uncertainties	50
2.4.4	Reproducibility	51
3	Numerical Flow Simulation	53
3.1	Introduction to Computational Fluid Dynamics (CFD)	53
3.1.1	Turbulent Flow Modelling	53
3.1.2	Flow Discretization	55
3.2	Wet Steam Effects and Modelling with ANSYS CFX	58
3.3	LP Steam Turbine CFD Models with PSCs	63
3.3.1	Three-Stage Model	64
3.3.2	One-Stage Models	65
3.4	Evaluation of CFD Results	69
3.4.1	Data Averaging	69
3.4.2	Determination of Static Enthalpy	70
3.4.3	Determination of Work Output	71
3.4.4	Determination of Kinetic Energy	71
4	Experimental Validation of LP Steam Turbine CFD Model	73
4.1	Basic Overview	73
4.2	Comparison of 1D Values	74
4.3	Pressure Field in the Diffuser	75
4.4	Total Pressure Profile Downstream of PSCs	76
4.4.1	Remarks on Vortices in Turbomachines	78
4.4.2	Vortices in R2 and Effect on Total Pressure in E30	80
4.4.3	Vortices in R3 and Effect on Total Pressure in E32	86
4.5	Static Pressure Profile Downstream of PSCs	87
4.5.1	Static Pressure in E32	87
4.5.2	Static Pressure in E30	88
4.6	Flow Angle and Velocity Profile Downstream of PSCs	90
4.6.1	Flow Angle and Velocity in E30	90
4.6.2	Flow Angle and Velocity in E32	90
4.7	Key Points on the Experimental Validation	92

5	Loss due to PSCs in LP Steam Turbine Blading	93
5.1	General Definition of Loss Coefficients	95
5.2	Basics on Fluid-Dynamic Drag	97
5.3	Drag Coefficient of a Circular Cylinder	99
5.3.1	Incompressible Flow	99
5.3.2	Compressible Flow	103
5.3.3	REYNOLDS and MACH Numbers in LP Blading with PSC	105
5.3.4	Applicability of c_D for Real Flow Applications	105
5.3.5	Consideration on Numerical Approaches of c_D	106
5.4	Introduction to Loss Correlations for PSCs	108
5.4.1	Relation of Loss to Drag	109
5.4.2	Loss Correlation of TRAUPEL	110
5.4.3	Loss Correlation of DUNHAM AND PHILLIPSEN	112
5.4.4	Evaluation of Loss Correlations	116
5.5	Non-Equilibrium Condensation Effects	118
5.5.1	Overview on Condensation in Three-Stage LP Turbine	119
5.5.2	PSC Nucleation	120
5.5.3	Thermodynamic Wetness Loss	122
5.6	Vortex System in Rotor R3 with PSC	124
5.6.1	Friction Bolt (FB) & Blade Reinforcements (BR)	125
5.6.2	Lacing Wire (LW)	125
5.7	Introduction to PSC Parameter Study	128
5.7.1	Review of Investigated PSC Variations	128
5.7.2	Review of Investigated Operating Points	130
5.8	Performance Assessment of PSC Designs	134
5.8.1	Radial PSC Position	140
5.8.2	PSC Diameter	145
5.8.3	Cross-Sectional PSC Shape	151
5.8.4	Axial PSC Position	159
5.8.5	Zigzag PSC Angle	161
5.9	Comparison of CFD Results to Analytical Loss Correlations	163
5.9.1	Overview on Loss Correlation Results	163
5.9.2	Numerical Validation of Loss Correlations	165
5.10	Key Points on Loss due to PSCs	174

6 Conclusion and Outlook	177
6.1 Conclusion	177
6.2 Outlook	178
Bibliography	181
A CFD and Wet Steam Modelling	195
A.1 NAVIER-STOKES Equations	195
A.2 Grid Independency Study	196
A.3 The Condensation Model	198
A.4 MOLLIER h, s -diagram	199
B PSC Parameter Study	201
B.1 PSC Parameters and Cross Sections	201
B.2 Supplementary CFD Results	204
B.3 Remarks on OPs and Loss Correlations	211
C Steam Cycle and Test Facility at ITSM	213
Lebenslauf	215

Nomenclature

Roman Letters

A	m^2	area / drag reference area
A_{PSC}	m^2	cross-sectional area of the PSC projected in z -direction (PSC blockage area)
A_{BP}	m^2	cross-sectional area of the blade passage projected in z -direction
A^*	m^2	area projected in relative flow direction
A^*	m^2	area projected in meridional direction
a	m/s	sound velocity (speed of sound)
$a_{t,avg}$	m/s	sound velocity at rest (E30)
a_{th}	m^2/s	thermal diffusivity
C	m	blade chord length
C	-	flow rate coefficient
c	m/s	absolute flow velocity
c_D	-	drag coefficient
c_p	$J/(kg\ K)$	specific heat at constant pressure
c_v	$J/(kg\ K)$	specific heat at constant volume
c_τ	m/s	wall friction velocity
D	m	droplet diameter / tube diameter
D_{PSC}	m	radial PSC position
d	m	PSC diameter in r -direction / minor axis of the ellipse / orifice plate diameter
d^*	m	PSC diameter in z -direction / major axis of the ellipse
d_{eqv}	m	equivalent PSC diameter in r -direction
d_{eqv}^*	m	equivalent PSC diameter in z -direction
e	J/kg	specific internal energy
F_D	N	drag force
\vec{F}_m		vector of convective fluxes
\vec{G}_m		vector of diffuse fluxes
h	J/kg	specific enthalpy

h	m	blade height / diameter or side of the conduit cross section
h_t	J/kg	specific total/stagnation enthalpy
I	J/kg	rothalpy
J	$1/(\text{m}^3 \text{ s})$	nucleation rate
j	J/kg	specific dissipation
k_B	J/K	BOLTZMANN constant
k	m^2/s^2	turbulent kinetic energy
L	m	length / blade profile length / (representative) physical length scale
L	J/kg	latent heat
l	m	length
l_{PSC}	m	PSC length
\bar{l}	-	blade span
M	J	torque
m_m	kg	mass of one water molecule
\dot{m}	kg/s	mass flow rate
N	$1/\text{m}^3$	number of droplets per volume
\dot{P}	$1/\text{s}$	expansion rate
P	J/s	power
p	Pa	static pressure
p_{dyn}	Pa	dynamic pressure
p_t	Pa	total/stagnation pressure
\dot{Q}	$\text{J}/(\text{m}^3 \text{ s})$	heat flux
q_c	-	condensation coefficient
\dot{q}_m	$\text{J}/(\text{m}^2 \text{ s})$	heat flux density
R	$\text{J}/(\text{kg K})$	specific gas constant
R_D	-	reduction divisor
R_{mean}	m	mean radius (EULER radius)
R_{PSC}	m	PSC fillet radius
r	m	droplet radius
r_k	-	enthalpy-based degree of reaction
r_p	-	pressure-based degree of reaction
r, z	m	radial and axial cylindrical coordinates

S	-	supersaturation
\dot{S}_{th}	J/(K s)	entropy production rate
s	m	blade pitch or spacing
s	J/(kg K)	specific entropy
T	K	temperature
ΔT	K	subcooling
t	s	time
\vec{U}		state or solution vector
u	m/s	blade velocity
V	m ³	volume
V_c	m ³	cell volume
w	m/s	relative flow velocity
w	J/kg	specific work
x	kg/kg	vapor mass fraction or dryness fraction
x_m	m	Cartesian coordinates (index notation)
x, y, z	m	Cartesian coordinates
Y	-	total pressure loss coefficient
y	m	wall distance
y	kg/kg	liquid mass fraction or wetness fraction
y	m	distance of the obstruction's center of mass from the conduit axis
y^+	-	dimensionless wall distance
Z_{PSC}	m	axial PSC position

Greek Letters

α	°	absolute flow angle
α	-	constant in the YOUNG growth model
α_B	-	BAUMANN factor
β	°	relative flow angle / yaw angle
β	-	diameter ratio
β_l	1/m	interfacial area density
β_{PSC}	°	PSC inflow angle
γ	°	mixing angle / pitch angle

Δ	-	difference or change
Δh_{loss}	J/kg	enthalpy loss
$\Delta p_{t,\text{loss}}$	Pa	total pressure loss
Δs	J/(kg K)	entropy change
δ	m	boundary layer thickness
δ_{ij}	-	KRONECKER delta
δ_{zigzag}	°	zigzag PSC angle
ε	m^2/s^3	turbulent eddy dissipation (dissipation rate)
ε	-	non-isothermal correction according to KANTROWITZ / expansion number
ζ	-	enthalpy loss coefficient
ζ_s	-	entropy loss coefficient
η	-	efficiency
Θ	°	circumferential cylindrical coordinate
κ	-	specific heat ratio $\kappa = c_p/c_v$
λ	-	work coefficient
λ	J/(s m K)	thermal conductivity
λ_M	m	molecular mean free path
μ	Pa s	dynamic viscosity
ν	m^2/s	kinematic viscosity
ν	-	correction factor of YOUNG
ξ	-	auxiliary variable
π	-	ARCHIMEDES' constant
ρ	kg/m^3	density
Σ	-	sum
σ	Pa	maximum equivalent VON MISES stress
σ	N/m	surface tension
τ	-	empirical coefficient
τ_{ij}	N/m^2	normal or shear stress
τ_W	N/m^2	wall shear stress
φ	-	flow coefficient
ψ	-	head or pressure coefficient
ω	1/s	angular frequency / turbulent frequency

Subscripts

0	stator inlet
1	stator outlet / rotor inlet
2	rotor outlet
30, 31, 32	evaluation plane E30, E31, E32
∞	free stream
abs	absolute
aero	aerodynamic
avg	average
BP	blade passage
BR	blade reinforcement
CC	CRAIG AND COX
Cyl	cylinder
con	condenser
crit	critical
cross	cross flow
DP	DUNHAM AND PHILLIPSEN
diff	diffusion
eqv	equivalent
FB	friction bolt
g	gaseous
H	hub
I	IDEL'ČIK
in	inlet
i, j, k, l, m	indices
KS	KOCH UND SMITH
LW	lacing wire
l	liquid
m	meridional / mixture / measurement
min	minimum
max	maximum
norm	normalized
off	offset

opt	optimum
out	outlet
PS	pressure side
PSC	part-span connector
RT	RZHEZNIKOV AND TROSHCHENKOVA
ref	reference
rel	relative
r, Θ, z	Cylindrical coordinates
S	shroud
SS	suction side
s	isentropic / saturated
T	TRAUPEL
t	total/stagnation state in absolute reference system
t,rel	total/stagnation state in relative reference system
th	thermodynamic
ts	total-static
V0	configuration with freestanding blades
vf	very fine
w/o	without
x, y, z	Cartesian coordinates

Superscripts

$\overline{(\cdot)}$	averaged value
$(\cdot)'$	fluctuating quantity
$\vec{(\cdot)}$	vector

Dimensionless Numbers

Kn	$:= \lambda_M / L$	KNUDSEN number
Ma	$:= \ \vec{c}\ / a$	absolute MACH number
Ma _{rel}	$:= \ \vec{w}\ / a$	relative MACH number
Pr	$:= \nu / a_{th}$	PRANDTL number
Re	$:= \ \vec{c}\ L / \nu$	REYNOLDS number

Abbreviations

1/2/3D	one/two/three-dimensional
ASME	American Society of Mechanical Engineers
ATM	automated topology and meshing
BEP	best efficiency point
BR	blade reinforcement
CAD	computer aided design
CEng	Chartered Engineer
CFD	computational fluid dynamics
CO ₂	Carbon dioxide
DES	detached-eddy simulation
DNS	direct numerical simulation
E30/E31/E32	evaluation planes
EO	engine order
EQS	equilibrium steam
ETH	Eidgenössische Technische Hochschule
EXP	experimental
FB	friction bolt
FDM	finite difference method
FEA	finite element analysis
FEM	finite element method
FFT	fast FOURIER transform
FIMechE	Fellow of the Institution of Mechanical Engineers
FRAP-HTH	fast response aerodynamic probe - high temperature heated
FVM	finite volume method
GE	General Electric
GUM	guide to the expression of uncertainty in measurement
HKW	Heizkraftwerk (combined heat and power plant)
IAPWS-IF97	International Association for the Properties of Water and Steam - Industrial Formulation 1997
IGTI	International Gas Turbine Institute
IEA	International Energy Agency
IEC	International Electrotechnical Commission
IMechE	Institution of Mechanical Engineers

IPCC	Intergovernmental Panel on Climate Change
ISO	International Organization for Standardization
IST	industrial steam turbine
ITSM	Institute of Thermal Turbomachinery and Machinery Laboratory
LE	leading edge
LES	large eddy simulation
LP	low-pressure
LSB	last stage blading
LW	lacing wire
MHPS	Mitsubishi Hitachi Power Systems
Mtoe	million tonnes of oil equivalent
NACA	National Advisory Committee for Aeronautics
NASA	National Aeronautics and Space Administration
ND	nodal diameter
NES	non-equilibrium steam
OP	operating point
OT	Oberteil (upper part)
PhD	Doctor of Philosophy
PIV	particle image velocimetry
PS	pressure side
PSC	part-span connector; PSC is used here as hypernym for any kind of constructive element joining adjacent rotor blades within the blade passage at part-span (compare to Fig. 1.4)
R	rotor
RANS	REYNOLDS-averaged NAVIER-STOKES equations
RMS	root mean square
S	stator
S/G	strain gauge
SS	suction side
SST	shear stress transport / SIEMENS steam turbine
TE	trailing edge
TT	tip timing
UN	United Nations
UT	Unterteil (lower part)
V	variation or configuration

Operators, Functions and Symbols

$\ \bullet\ $	norm (length) of a vector
∂	partial differential
d	ordinary derivative

Angle Convention

$$\alpha = \arctan\left(\frac{c_\Theta}{c_z}\right), \quad \beta = \arctan\left(\frac{w_\Theta}{c_z}\right), \quad \gamma = \arcsin\left(\frac{c_r}{c}\right)$$

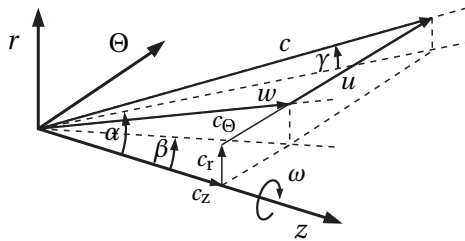


Figure 1 Velocity components, flow angles and turbine rotational direction

1 | Introduction

The latest Key World Energy Statistics [57] of the INTERNATIONAL ENERGY AGENCY (IEA) reveal that in the year 2016 over 80% of the worldwide demand for electricity was covered by fossil energy sources, see Fig. 1.1 (left). Overall, burning fuels like coal, oil or natural gas led to a global production of over 32,000 million tons of CO₂ (whereof electricity and heat generation account for roughly 42%), see Fig. 1.1 (right). This is more than twice as much as back in 1973 [57]. According to the INTERGOVERNMENTAL PANEL ON CLIMATE CHANGE (IPCC), the human influence on climate change is undeniable and nowadays, greenhouse gas emissions, of which CO₂ is the main contributor, are the highest in human history [58]. In order to limit the global warming to a maximum of +2 °C and thus decrease the probability of serious causes to the ecological system and the human kind, substantial reductions of emissions have to be accomplished over the next decades using effective counteractions. According to the IPCC [58], power generation out of fossil energy sources has to virtually cease by the end of this century, in order to meet the formulated goals. The Kyoto protocol, a resolution passed by the UNITED NATIONS (UN) in 1997, is acting as a self-commitment for the signing countries to counteract the increasing emission of greenhouse gases. Following the UN Framework Convention on Climate Change in Lima/Peru (2014), the Paris agreement (2015) is seeking "... to keep the global temperature rise within this century well below 2 degrees Celsius and to drive efforts to limit the temperature increase even further to 1.5 degrees Celsius above pre-industrial levels." [128]

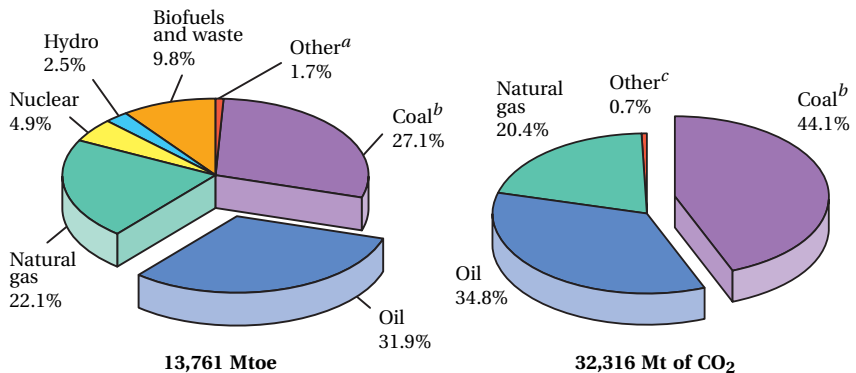


Figure 1.1 Global^d fuel shares of total primary energy supply (left) and of overall CO₂ emissions from fuel combustion (right) in the year 2016, according to Ref. [57]

^aIncludes geothermal, solar, wind, tide/wave/ocean, heat and other.

^bIn these graphs, peat and oil shale are aggregated with coal.

^cIncludes industrial waste and non-renewable municipal waste.

^dIncludes international aviation and international marine bunkers.

1.1 Motivation

Steam turbines are the workhorses of nowadays global power generation industry. Approximately 70% of the global power generation is realized with the help of this type of axial-flow turbine¹ [118]. Due to this important fact, improvements of existing and new designs in terms of turbine efficiency have a large leverage effect on the reduction of global CO₂ emissions. It is therefore indispensable to further push forward research and development in this field.

1.1.1 Steam Power Plant

Despite new local aspects in energy conversion,² lately published [57, 130] trends suggest that the worldwide rising demand for electrical power will inevitably lead to a continued expansion of new conventional installations in future. Nowadays, a large number of emergent and industrially strong growing countries are continuously extending their conventional power plant fleet. According to Refs. [57, 130], nations like the USA, Russia, and Canada are still focusing on the installation of new fossil and nuclear power plants. Despite the Japanese event in 2011, nuclear power is still popular these days and also players like China as well as several European countries are extending or at least are maintaining their count of nuclear installations, in order to keep up with the goal of reducing their CO₂ footprint. Therefore, steam power plants will further play a key role. The fact that steam turbines are generally independent of applied energy sources will additionally boost this type of technology in future. Nowadays, steam turbines are already used in solar thermal, geothermal or biomass power plants, which lets them act as bridge technology between conventional and renewable power generation.

An aspect, which became more and more important in recent years, is operational flexibility. Due to the increasing amount of green electricity on the power markets and its dependency on the availability of fluctuating sources like wind or solar energy, conventional plants can no longer solely be operated for ensuring base load but have to adjust to the current energy mix and requested power demand. According to Ref. [130], on such markets "... the primacy of efficiency is increasingly being replaced by the need for flexibility." Therefore, load conditions of turbines may vary more often between part load and overload. Concerning this matter, newly developed power plants have

¹Its modern manifestation goes back to the invention of British engineer Sir Charles PARSONS (1854–1931) in 1884. It converts thermal energy from pressurized, saturated or superheated steam into mechanical rotational energy by expansion of the steam flow in multi-stage turbine blading.

²German turnaround in energy policy and move towards an increasing capacity of renewables.

been laid out for particularly flexible operation, especially in Germany [130]. This rising demand for flexibility of base load turbines leads to the need of rethinking the aero-mechanical blade design process, since especially the low-pressure (LP) blading of steam turbines faces new challenges in terms of mechanical loading and operating conditions apart from design load. In terms of increasing operational flexibility, coupling the rotor blades at part-span is one feature widely used across all types of steam power plants. Although the present work focuses on industrial steam turbines (IST), conventional steam power plants can also benefit from the given results.

1.1.2 Industrial Steam Turbine

Industrial steam turbines, basically assigned to the power class up to 250 MW, are designed for flexible, reliable, robust and still fairly efficient operation with the ability for short start-up times. They are normally distributed as individually conceived base frame packaged units according to the customers' request, compare to Ref. [106]. This type of steam turbine is for example used as mechanical drive for compressors, fans or pumps in the process industry, for driving feedwater pumps in conventional steam power plants or as turbo set for power generation in industrial applications as well as solar thermal, geothermal or biomass power plants. Although efficiency plays an important

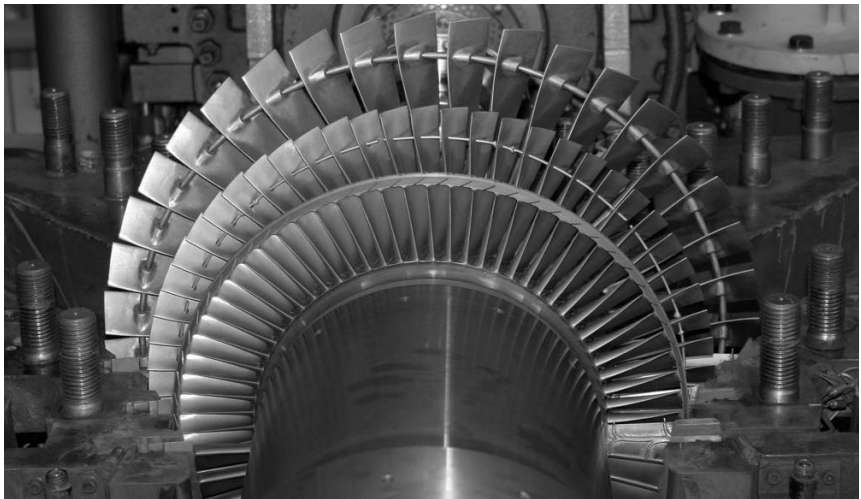


Figure 1.2 Industrial steam turbine runner in test rig at ITSM, HÄFELE ET AL. [53]

role in nowadays turbine design, for many industrial steam turbine applications robustness at all operating points (OP) is of major importance. Especially the last stage of LP blading is of major concern for fail-safe operation of steam turbine plants. According to DROZDOWSKI ET AL. [27, 29], High Cycle Fatigue induced from blade vibration is the main failure risk for the blading, especially for industrial steam turbine applications. Thus, special effort is normally spend on investigating the vibrational behavior of the blade system.³

Regarding excitations on the moving blades, it is known that these are primarily induced by non-uniformities in the steam flow – for example the wakes of upstream vanes, downstream vanes or struts in the exhaust casing or general asymmetries in vane pitch or casings, as discussed by DROZDOWSKI ET AL. [27, 29]. Whether these disturbances are rotational symmetric or asymmetric, the excitation on the moving blades will be periodic and thus can be decomposed into its harmonics. While the frequency of excitation equals to multiples of the rotational speed (speed harmonics), the magnitude of the excitation force depends on the steam loads, i.e. aero-thermodynamic operating conditions, especially the back pressure level. In addition to the harmonic excitation effects on the blade, other sources of excitation can occur, such as flutter, which is a self-excited phenomenon, or rotating stall, originated from flow separation of the blade when operating at severe off-design. As stall cells propagate around the circumference relative to the rotor, the excitation also occurs at frequencies that are non-synchronous to the rotational speed.

The best way to keep vibration amplitudes low is to avoid blade resonance. For fixed speed applications, this is done by tuning the blade frequencies apart from the speed harmonics. In contrast, in many industrial applications, turbines have to run with variable speed and blade resonance vibration will occur when a blade natural frequency coincides with one of the harmonics.

³DROZDOWSKI ET AL. [27] investigated the vibrational behaviour of steam turbine last stage blades with friction bolt damping elements by applying state-of-the-art experimental methods and FEM techniques. Based on test rig measurements, a CAMPBELL diagram as plotted in the background of Fig. 1.3 could be used to detect several resonance points in the considered speed range, whereby the highest vibrational amplitudes have been observed at approximately 60% and 70% speed. According to Ref. [27], this clearly corresponds to blade resonance of the 1st mode with the 8th and the 7th engine order (EO), marked with ⊗. An additional resonance point could be observed at 85% speed which corresponds to resonance of the 1st mode with the 6th speed harmonic, marked with ⊙. In Fig. 1.3, the calculated natural frequencies from the modal analysis of the 1st (red colored lines) and 2nd (yellow colored lines) mode families are also shown. For a better visibility, not all nodal diameter (ND) frequency lines are plotted. However, according to DROZDOWSKI ET AL. [27] the lowest line corresponds to ND0 and the highest one to the maximal ND of a family. Considering only speed harmonic excitation, resonance is only possible if ND = EO. These resonance points are marked with colored dots. Note that the type of diagram shown in Fig. 1.3 is named after English engineer Wilfried CAMPBELL (1884–1924), who introduced this concept in order to compare blade vibration modes to potential blade excitation sources [17].

Thus, LP blades for industrial purpose must have a robust design that can also withstand blade resonance vibration, DROZDOWSKI ET AL. [27, 29].

At the Institute of Thermal Turbomachinery and Machinery Laboratory (ITSM) of the University of Stuttgart, an industrial steam turbine test rig is operated for performance testing as well as for flow and vibration measurements. Currently, a full scale three-stage LP section of an industrial steam turbine is being investigated, see Fig. 1.2 and Fig. 2.1 on Page 37. Due to its field of application, this type of turbine is normally operated at variable operating conditions regarding speed, loading and backpressure, which is highly demanding for the rotor blades. In LP stages where moderate centrifugal loading is present, shrouded blading is normally used to couple adjacent blades and increase the stiffness of the bladed-disk assembly, while additional frictional damping is introduced on the shroud contact areas. However, the last and penultimate rotor blade rows often require the introduction of special structural elements connecting the LP rotor blades at part-span, since shrouded blading would exceed the mechanical load capacity of the relatively long blades at the blade root section.

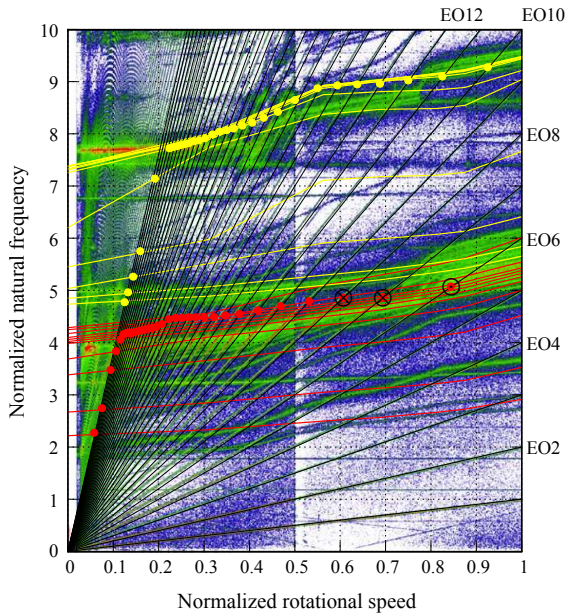


Figure 1.3 CAMPBELL diagram of last stage rotor blading (Fig. 1.5) coupled with friction bolt damping elements (see also Ftn. 3 on Page 4), DROZDOWSKI ET AL. [27]

1.1.3 Part-Span Connector (PSC)

Due to the benefits that can be gained from an enlarged exhaust area⁴, increasing the blade length has ever been the main development focus for LP steam turbine blades in the history. This development was accompanied by the development of coupling and damping element designs. An overview of possible applications is given in the work of PANNING [87], see Fig. 1.4. In the investigated three-stage section of a full-scale LP industrial steam turbine, the first rotor blade row is coupled by integral shrouds, whereas blades in the penultimate and last rotor blade rows are shroudless and coupled at part-span, see Figs. 1.2, 2.1 and 2.2.

Object of main interest for the present study is the last stage rotor blading (R3) shown in Fig. 1.5 (left), which is a current blade design used in SIEMENS Steam Turbines SST-500, SST-600, and SST-800. This rotor blade row features conical friction bolts (FB) which are loosely mounted between blade reinforcements (BR) of adjacent blades. Their purpose is to provide blade coupling and frictional damping during turbine operation. Dynamic stresses are suppressed due to micro-slips on the bolt contacts while operating in blade resonance. If the blade excitation force is lower than the threshold force on the friction bolt contacts, they impede blade excitation by providing structural coupling of adjacent blades, leading to a coupled blade system with fewer resonance points and giving additional stiffness to the blades. The coupling and damping capabilities of this kind of LP blade with part-span connector (PSC) were experimentally proven by PFEIFFER [90] and JAROSCH [61] in the 1980s (compare to Fig. 1.6), using the industrial steam turbine test rig at ITSM. The mechanical properties and the scaling concept of the blade family has been recently

⁴According to SENOO ET AL. [102], increasing the exhaust steam annulus area has three possible major benefits: 1) mass flow rate $\uparrow \Rightarrow$ power output \uparrow ; 2) mass flow rate \approx const. \Rightarrow kinetic energy at the outlet $\downarrow \Rightarrow$ efficiency \uparrow ; 3) number of LP cylinders $\downarrow \Rightarrow$ axial turbine length \downarrow (\Rightarrow costs \downarrow).

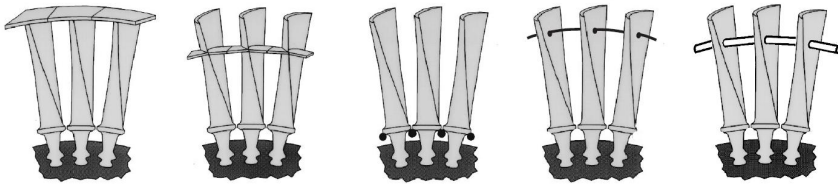


Figure 1.4 Constructive elements for blade coupling and frictional damping according to PANNING [87]; left to right: integral shroud, part-span shroud/damper or snubber or tie-boss or strut or stub, underplatform damper, damping/lacing/lashing/tie wire, friction bolt or damping/braced pin

described and numerically evaluated by SZWEDOWICZ ET AL. [116, 117]. In addition, an experimental and numerical study on the nonlinear vibrational behavior of the blades, applying state-of-the-art FEM techniques in order to investigate the frictional damping performance of the system was presented by DROZDOWSKI ET AL. [27]. The resonance situation of the coupled LP blading is exemplarily shown by means of a measured CAMPBELL diagram in Fig. 1.3.

In the penultimate rotor blade row (R2) of the investigated turbine configuration, a simple lacing wire (LW) is installed, see Fig. 1.5 (right). This type of PSC is used since the early steam turbine developments, see e.g. TRAUPEL [121] or KIRILLOV AND KUZ'MIČEV [64], and is still very common in industrial steam turbine applications nowadays, DROZDOWSKI ET AL. [29].⁵ Lacing wires are also still occasionally applied to LP blading of steam turbines running in conventional power plants at constant speed, often in combination with shrouded blade coupling. It is a relatively simple, nevertheless effective way to introduce additional damping and stiffness to the blade system. The mechanical performance and vibrational behavior of the blade shown in Fig. 1.5 (right) was recently investigated by DROZDOWSKI ET AL. [29], whereby the physical principle of operation is related to the one of FB & BR, described in Ref. [29]. Depending on the application, the holes for the lacing wire might need reinforcements, in order to ensure sufficient low-cycle fatigue life [31].

⁵According to TRAUPEL [123], the cross section of an LW might be circular or elliptical.

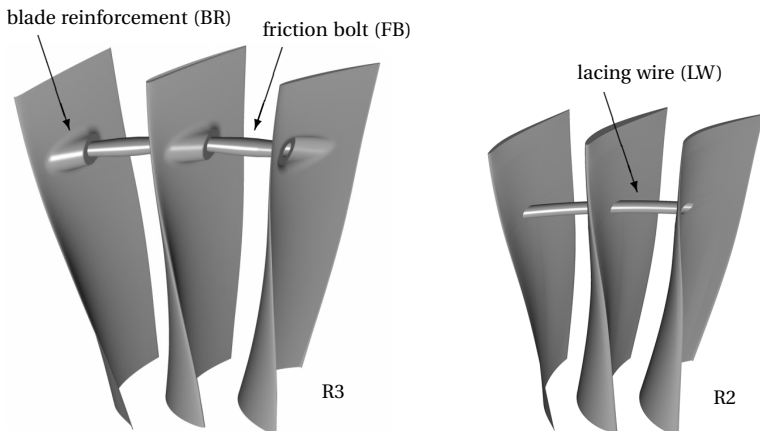


Figure 1.5 Current design of coupled last (left) and penultimate (right) stage rotor blading used in SIEMENS Steam Turbines SST-500, SST-600, and SST-800

With regard to the huge variety of publications it can be stated that nowadays, the impact of PSCs on the vibrational behavior of the rotor blades is fairly understood and documented quite well in literature.

1.1.4 Problem Definition

As already mentioned, PSCs like friction bolts or lacing wires provide blade coupling and frictional damping during turbine operation. Due to their mechanical design, they lead to a high safety margin regarding the materials fatigue of the rotor blades and therefore guarantee safe turbine operation, even in blade resonance condition. However, the presence of these cylindrical elements within the flow channel leads to additional losses, which affect the performance of the turbine. With respect to the importance of robustness, this is generally accepted to date. Although the blading depicted in Fig. 1.5 (left) is a current design, the aerodynamic features of the PSC have not received much attention in recent decades, as can be seen in Fig. 1.6. Up to the current knowledge (Sec. 1.4), the impact of PSCs on aero-thermodynamics is not considered by steam turbine designers in the conventional 3D flow path design so far,⁶ mainly due to the extra effort necessary for generating high quality grids. In contrast, state-of-the-art FEA considers the PSC by default. A shape optimization or a reduction of PSC blockage area may however offer the opportunity for a significant aerodynamic performance increase. However, the mechanical performance of the blade system must not be compromised.

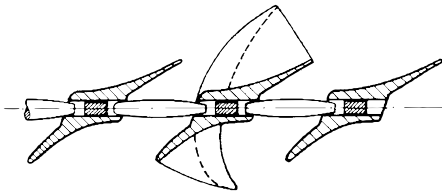


Figure 1.6 Coupled last stage blading design investigated by PFEIFFER [90] in the mid 1980s

of steam. However, as the numerical modelling of flow around cylinders is still a challenging task in engineering practice, setting high demands on the CFD model applied, an experimental validation is crucial.

The following literature review reveals that there is quite a limited availability of experimental data from flow field measurements downstream of rotors with PSCs. Accordingly, there is a lack of validated CFD models which include the PSC within the flow channel, especially not with consideration of non-equilibrium condensation

⁶This is particularly surprising since the majority of publications on this topic has been provided by industry or is at least industry-related.

In order to estimate the losses due to PSCs within the blade design process, simple loss correlations are normally used. However, it is known that these correlations are fraught with uncertainties, arising from simplifications and the fact that not all relevant effects are covered. Especially when it comes to steam turbines, published documents in this field are rare to find. Up to now, a detailed analysis of the applicability for wet steam flow in LP steam turbines cannot be found in open literature.

Research Question In consequence of the above stated problems, the research on fluid-dynamics in LP industrial steam turbines with PSCs has to be further extended. The central question can be raised as follows: *What is the impact of PSCs on aero-thermodynamics in LP steam turbine blading?* In this context, further subquestions can be formulated:

1. How well can the flow-impact be captured with 3D CFD methods and test rig measurements and how is the correspondence?
2. Which potential for efficiency improvements is available and how is the loss sensitivity on global PSC parameters?
3. On the other hand, how accurate can the loss due to PSCs be described by analytical approaches?
4. Last but not least, does the presence of the PSC affect the process of non-equilibrium condensation of steam?

By following the research objectives, the present work will give answers to these major questions and highlights further aspects and research in this field.

1.2 Research Objective

In the light of still incomplete understanding of the complexity of the three-dimensional flow field in LP stages of steam turbines with PSCs and so far missing comprehensive studies in this field, the following research objectives for the present doctoral thesis and its underlying publications [50, 52–54] were formulated. These have been accomplished by utilizing experimental and numerical methods as well as analytical approaches.

- Generally, improve the physical understanding of the flow around PSCs and the losses induced by these elements, especially in condensing steam flow of last stage blading.
- Provide a comprehensive literature review in a field that is fairly poor documented in the free accessible literature.
- Contribute rare-to-find experimental data from extensive performance and flow field measurements under real steam conditions in an LP steam turbine with PSCs to the technical community.
- Develop appropriate 3D CFD models to capture the impact of PSCs. Investigate the effects of non-equilibrium condensation of steam in LP stages with PSCs by applying state-of-the-art CFD methods.
- Validate a multi-stage, one-passage CFD model with test rig measurement data and examine its applicability for engineering practice.
- Based on 3D CFD results, gain deeper insights into the impact of PSCs on aero-thermodynamics and blade design aspects related to the presence of the PSCs. Study vortex systems in LP rotor blading with PSC.
- Based on CFD models with parameterized PSC geometry, numerically assess the aerodynamic performance of different PSC designs. Reveal their sensitivity and potential for efficiency improvements, particularly with regard to the large leverage effect of steam turbine improvements on the reduction of global CO₂ emissions.
- Study relevant, analytical loss correlations for PSCs available in the literature. Compare the loss predicted by CFD for real LP steam turbine blading to these simplified correlations. Highlight deficiencies and give recommendations for further work in this field.

1.3 Thesis Outline

In general, this doctoral thesis is built on three pillars, namely experimental data derived from measurements in an LP steam turbine, numerical methods applied to gain deeper insights into the flow field in the turbine and analytical considerations to approach the loss due to PSCs. Six chapters are constructed based on this foundation.

Chapter 1 The motivation, a comprehensive literature review and the research objectives are presented. The review focuses on fluid-dynamical aspects of PSCs and discusses numerical, experimental and analytical approaches for capturing the flow field and related losses induced by PSCs.

Chapter 2 First, basic features of the experimental test facility at ITSM and its measurement equipment are described. Next, details about the performed experimental investigations and the measurement data evaluation are given.

Chapter 3 Numerical modelling aspects are addressed here. This includes a short introduction to the relevant principles of CFD. Thereafter, detailed information about the developed three- and one-stage CFD models of the investigated steam turbine, together with details about the parameterization of PSC geometries are given. Relevant evaluation aspects of CFD results are also briefly addressed.

Chapter 4 Major part of this chapter is an in-depth discussion about the validation of CFD results with experimental data. This includes a thorough introduction to the vortex systems in rotors with PSCs, derived from 3D CFD results and also detectable in the presented measurement data.

Chapter 5 The loss due to PSCs is major topic of this chapter. In the first part, general loss coefficients are discussed and defined. This is followed by an introduction to fluid-dynamic drag, which is further detailed in a comprehensive section about drag coefficients. Relevant loss correlations out of literature, indicated in the literature review, are derived and closely examined in this chapter. As a result of the PSC parameter study performed with CFD, a performance assessment of different PSC designs is presented and finally a comparison of CFD results to analytical loss correlations is carried out.

Chapter 6 The final chapter concludes most relevant findings and proposes further steps to be taken in successive studies and measurement campaigns.

1.4 Literature Review and Discussion

While nowadays the impact of PSCs on the vibrational behavior of the rotor blades is fairly understood and documented quite well in literature, the impact on aero-thermodynamics has been given far less attention in recent decades. This is reflected by the relatively small amount of available publications concentrating on that issue and can be basically drawn back to the fact that PSCs in the first place are applied in order to ensure safe turbomachinery operation without accepting compromises regarding the mechanical robustness and integrity of the rotor blades. In this context, fluid-dynamical aspects of PSCs will always play a minor role and a certain efficiency decrease is to be accepted.

In order to put the topic described in Sec. 1.1 into the current state of science and technology, a chronologically review and discussion of available and relevant open literature, being published by the end of the year 2016 and covering fluid-dynamical aspects of PSCs, is carried out in this section.

1.4.1 Brief Overview

Loss Correlations A detailed overview on research work related to loss correlations for PSCs is given in Subsec. 1.4.2. TRAUPEL [121–123] provided an analytical loss correlation which has found wide usage in industry. KIRILLOV AND KUZ'MIČEV [63, 64] performed measurements in a hot-air model turbine with LWs, draw conclusions regarding the impact of the wires on the flow field and compare their experimental findings to a total pressure loss correlation provided by IDEL'ČIK [56] for flow around cylinders within a straight pipe. RZHEZNIKOV AND TROSHCHENKOVA [98] carried out cascade measurements with LP steam turbine blading and present a correlation for the total pressure loss due to a lacing wire⁷. In their paper about performance estimation of axial-flow turbines, CRAIG AND COX [21] briefly address the issue of loss due to PSCs and present a simple correlation for estimating the efficiency drop. Extensive research activity has been shown by NASA [35, 66, 71, 72, 93, 94] in the field of transonic axial-flow compressor and fan blades connected with part-span dampers or shrouds (snubbers) and LWs. Subsequently, ROBERTS [93, 94] presented total pressure loss correlations for design and off-design conditions

⁷In the literature, several variants of wires connecting the rotor blades can be found, often referred to as damping/lacing/lashing/tie wire. Depending on their assembly mode – loosely mounted through blade holes or additionally fixed (brazed) to the blades, see e.g. Ref. [124] – they provide a certain amount of additional damping and stiffness to the blade system. However, in this work the focus is on the aerodynamic performance of this type of PSC and thus, the term lacing wire (LW) or generally PSC is used for all types of wires in the further context of this thesis, neglecting differences in the mechanical working principle.

and later [95] design guidelines. KOCH AND SMITH, JR. [65] discuss a loss correlation for part-span shrouds in axial-flow compressors, which they based on the concept of drag turned into an entropy rise. DENTON [25] examines various loss mechanisms in turbomachines and introduces a loss correlation in terms of drag coefficient. DUNHAM AND PHILLIPSEN [31] investigated the flow in turbocharger turbines with LW by using 3D CFD and experiments and provide a correlation for the application in a streamline curvature code.

Experimental Work An overview on relevant experimental work is given in Subsec. 1.4.3. ACCORNERO AND MARETTO [1] and ACCORNERO ET AL. [2] provided measurement data from an LP steam turbine with PSCs during power plant operation. MAIER [77] identified the efficiency drop due to cylindrical damping pins in an LP model steam turbine. VÖLKER [132] carried out measurements in an LP model steam turbine with snubbers by using multi-hole probes and detected a small impact of the PSC on the flow field. BOSDAS ET AL. [12] presented time-resolved data from measurements in the LP stages of a model steam turbine with snubbers and make conclusions regarding the secondary flow structures downstream of the rotor blading.

CFD Studies Publications focusing on numerical flow simulation of turbomachinery stages with PSCs are introduced in Subsec. 1.4.3. RUBECHINI ET AL. [96] presented a simple model to consider PSCs in 3D CFD calculations and performed a comparison with experimental data. WADIA AND SZUCS [133] compared 3D CFD results of two similar fans with and without part-span shrouds. SIGG ET AL. [107] numerically and experimentally investigated an LP model steam turbine with snubber during windage condition. MISTRY ET AL. [82] carried out 3D CFD calculations and indicate the efficiency drop due to the presence of the snubber in the last stage blading (LSB) of an LP steam turbine. WU ET AL. [137] performed a multidisciplinary numerical parameter study on the design optimization of snubbers in a gas turbine. SHIBUKAWA ET AL. [105] reflect on the mechanical and fluid-dynamical aspects of a newly developed titanium 48-inch last stage blade with streamlined PSC, optimized by utilizing a simplified CFD model of the snubber. LI AND LI [74] present 3D CFD results of a three-stage LP steam turbine with snubber and compare two span-wise PSC positions.

1.4.2 Loss Correlations for PSCs

In the following, publications with the focus on loss correlations for PSCs are reviewed and discussed. Please note that the given loss correlations have been rewritten, in order to meet the nomenclature used in the present thesis.

TRAUPEL [121–123] Up to the current knowledge, TRAUPEL [121] was the first who published a loss correlation for PSCs within his standard reference work on thermal turbomachinery in the late 1950s. The author [121] based his first approach on the total pressure loss due to a lacing wire. This attempt is revised in the subsequent editions [122, 123] of his fundamental work and TRAUPEL [123] finally considers an enthalpy loss coefficient⁸. Furthermore, he enhances his first attempt [121] by introducing a correction factor of two in Refs. [122, 123], which apparently gives better agreement with experimental data.⁹ The loss correlation of TRAUPEL [123] has found wide usage in industry and is for example implemented in the streamline curvature code SC90T [88]. Recently, DUNHAM AND PHILLIPSEN [31] as well as HÄFELE ET AL. [50] compared the loss due to PSCs predicted by TRAUPEL'S correlation [123] to experimental data from turbocharger turbines and to CFD results from LP steam turbine blading, respectively. Both research groups state that the loss derived by this correlation [123] is generally too low. Nevertheless, TRAUPEL'S attempt [123] is further examined in Subsec. 5.4.2.

KIRILLOV AND KUZ'MIČEV [63, 64] One of the first comprehensive studies on the impact of PSCs on aerodynamics was published in the early 1960s by KIRILLOV AND KUZ'MIČEV [64]¹⁰. The work is based on experimental data and also considers an analytical approach. The authors [63] experimentally investigated a one-stage hot-air model turbine¹¹ with the rotor coupled by up to three wires in various arrangements and combinations (Fig. 1.7) by considering the energy balance between turbine inlet and outlet as well as by performing detailed probe measurements downstream of the rotor with PSCs. The results of configurations with lacing wire(s) were compared to results obtained with a configuration with free-standing rotor blades. Based on their experiments, KIRILLOV AND KUZ'MIČEV [63] come to the conclusion that the magnitude of loss due to the lacing wire is depending on its blade span position. The loss is particularly high for a wire mounted at low span position, i.e. closer to the hub, where in this case the lacing wire is subjected to a higher relative inflow velocity compared to upper span regions. According to the authors [63], this correlation is still valid for increasing mass flow rates, whereby the loss is increasing with increasing flow velocity.

⁸ $\zeta_T = 8 c_D \cos^2(\beta_2) (s/l_{PSC})^2 D_{PSC} d_{PSC} / (D_S^2 - D_H^2)$, TRAUPEL [123].

⁹No further details about experimental investigations in this field are given in Refs. [121–123].

¹⁰The original material [64] is published in Russian language. The present literature review of this article [64] is based on a version [63] translated into German.

¹¹Although KIRILLOV AND KUZ'MIČEV [63] do not make any statements about the type of investigated turbine, the given information points towards an HP turbine stage.

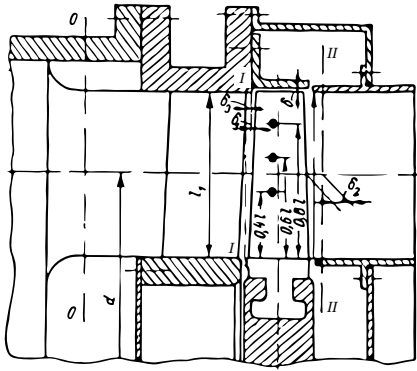


Figure 1.7 Test rig according to Ref. [64]

Based on the information given in Ref. [63], the measured efficiency drop due to a wire mounted at 60% span and blocking approximately 7% of the flow channel area is between 0.7 and 1 percentage point, depending on the load condition. Furthermore, KIRILLOV AND KUZ'MIČEV [63] conclude from their measurements that increasing the number of mounted wires inside the blade channel increases the measured loss. Interestingly, in this case the overall loss is higher compared to the summation of individual losses, which is due to the fact that the PSCs are interacting and thus in sum are causing higher losses. An additional phenomenon noticed by the authors [63] is the rise of degree of reaction¹² at mid-span due to the presence of the PSCs within the flow channel and corresponding blockage effects.¹³

Based on their flow field measurements, KIRILLOV AND KUZ'MIČEV [63] show that the lacing wire(s) cause(s) a radially inhomogeneous total pressure distribution downstream of the rotor, including the characteristic total pressure drop in the wake of the cylindrical element(s), whereby the inhomogeneous character of the flow properties is more pronounced at overload condition. According to the authors [63], this highly inhomogeneous flow is mixed out further downstream of the rotor blade row and leads to additional mixing loss, which increases with increasing mass flow rate. KIRILLOV AND KUZ'MIČEV [63] state that the described inhomogeneous outflow from the rotor could furthermore have a negative impact on the inflow condition of a downstream stator and in this case would lead to additional losses.

The authors [63] further note that for their test turbine, the loss induced by a simple wire mounted in span regions with strongly curved and convergent flow channel (at higher blade span position $\bar{l} = 0.8$, see Figs. 1.7 and 1.8) can

¹²According to KIRILLOV AND KUZ'MIČEV [63], the blade design follows the free vortex design, which is, according to BRÄUNLING [13], most common for "older" gas turbine designs. Here, c_z is kept constant along the span, i.e. $c_z = \text{const.} \neq f(r) \Rightarrow c_\theta r = \text{const.}$

¹³A general rise of the stage reaction and corresponding change of the rotor inflow conditions was also reported by HÄFELE ET AL. [54], who state that the inflow angle β is altered by up to 6°. Similar conclusions can be drawn from CFD predicted radial profiles of β (Fig. B.6, middle) and r_k (Fig. B.9, middle), whereby r_k at mid-span increases uniformly with the PSC blockage area.

be well predicted with the help of a correlation¹⁴ formulated by IDEL'ČIK [56] for plane-parallel flow around single smooth cylinders placed in a straight pipe, provided that a similar percentage of flow channel area is blocked by the PSC. In contrast, a wire mounted in a strongly curved blade channel with large attack angles and less accelerated or even decelerated flow (at lower blade span position $\bar{l} = 0.4$ (Fig. 1.7) with less convergent flow channel geometry, see Fig. 1.8) leads to higher drag and worse agreement with analytical results. In this case, the secondary loss induced by the PSC is increasing and according to Ref. [63] it is necessary to apply a correction factor larger than one within IDEL'ČIK's [56] common hydraulic equation.

Following these investigations of KIRILLOV AND KUZ'MIČEV [63], one can conclude that besides the size and shape of a PSC, the magnitude of loss is highly depending on the location where the PSC is mounted,

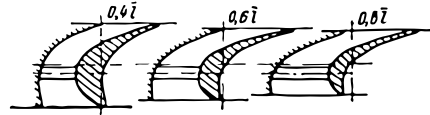


Figure 1.8 Flow channel geometry at different span positions \bar{l} , KIRILLOV AND KUZ'MIČEV [64]

i.e. the blade channel geometry (flow acceleration) and the corresponding flow conditions (inflow velocity and attack angle). This also implies a dependence of loss on the degree of reaction in the blade span region of the PSC.

RZHEZNIKOV AND TROSHCHENKOVA [98] Following the experimental and analytical study of KIRILLOV AND KUZ'MIČEV [64], RZHEZNIKOV AND TROSHCHENKOVA [98] carried out cascade measurements in air with two different LP steam turbine bladings¹⁵ coupled by lacing wire, whereby the free-standing versions of the rotor blades were also considered for comparison¹⁶. RZHEZNIKOV AND TROSHCHENKOVA [98] state that in contrast to the blading studied by KIRILLOV AND KUZ'MIČEV [64], the PSC in the considered LP steam turbine is usually mounted at span locations where the flow at the rotor inlet has much greater flow angles and in addition the outlet velocities are supersonic. The authors [98] focus on data derived from traverse measurements up- and downstream of the investigated cascade blades with and without lacing wire and show exemplary data in terms of span-wise outlet angle distribution in their paper. From their database they calculate

¹⁴ $\zeta_1 = \Delta p_{t,loss} / (\rho c_{ref}^2 / 2) \approx 1.15 c_D (A_{PSC} / A_{BP}) (1 - 2y/h)^{1/3} / (1 - A_{PSC} / A_{BP})^3$, IDEL'ČIK [56].

¹⁵The investigated blading is used in LMZ steam turbines K-300-240 and K-100-90 KhtGZ. Nowadays, LMZ is part of OJSC Power Machines.

¹⁶No data from measurements with the free-standing LP blades is shown in Ref. [98].

loss coefficients and present a correlation¹⁷ for the total pressure loss due to the lacing wire, which is an enhancement of the formulation provided by IDEL'ČIK [56] (see Ftn. 14 on the facing page) and relates the losses due to the PSC to the blade height, blade chord and furthermore accounts for relevant flow velocities up- and downstream the wire. Here, RZHEZNIKOV AND TROSHCHENKOVA [98] introduce the idea of taking into account the pitch-wise velocity distribution at the rotor inlet by averaging the values between blade pressure side (PS) and suction side (SS), which is later to some extent adopted in the correlation of DUNHAM AND PHILLIPSEN [31]. However, the authors [98] state that they did not succeed with their idea in describing the experimental data with the help of two empirical coefficients, one accounting for the flow around the wire and another one considering the mixing loss arising downstream of the wire and the blade. Furthermore, RZHEZNIKOV AND TROSHCHENKOVA [98] indicate that the derived loss coefficients have to be corrected by an empirical factor less than one ($\tau = 0.84$), which is in contradiction to the finding of KIRILLOV AND KUZ'MIČEV [64] and might be mainly attributed to the different type of investigated blading. According to Ref. [98], the comparison between calculated and experimentally derived loss coefficients shows absolute deviations in the range of -1.2% to $+0.9\%$, which means relative deviations of -33% to $+43\%$ when referred to the values derived by measurements, which is relatively large.

CRAIG AND COX [21] In their well known paper about performance estimation of axial-flow steam and gas turbines¹⁸, CRAIG AND COX [21] also briefly address the issue of loss due to lacing wires and present a simple correlation for estimating the total-total efficiency drop due to the presence of a wire within a blade passage. The authors [21] state that for wires with circular cross section, each corresponding 1% of passage area blocked by the wire increases the mean blade loss by approximately 1% of the local relative velocity head at the wire section. In their correlation¹⁹, CRAIG AND COX [21] add the wire drag coefficient only to account for wires with non-circular cross sections and thus assume $c_D = 1$ for circular ones. For wires with elliptical cross section having an aspect ratio of $d^*/d = 4$ they state that the loss will be decreased by 70% ($c_D = 0.3$). CRAIG AND COX [21] also note that the efficiency drop predicted with their loss correlation will strongly depend on the stage reaction. Further investigations of the authors [21] have revealed that the loss in real turbine stages shows a considerable scatter in comparison to the predicted one and

¹⁷ $\zeta_{RT} = \tau \zeta_I \left((w_{SS} + w_{PS})^2 / (4 w_2^2) \right) \sin^2(90^\circ + \beta_{PSC}) h / C$, RZHEZNIKOV AND TROSHCHENKOVA [98].

¹⁸It should be considered that the emphasis is on steam turbines rather than on gas turbines.

¹⁹ $\Delta\eta_{PSC} = c_D (A_{PSC} / A_{BP}) (w_{PSC}^2 / 2) / \Delta h_{t,s}$, CRAIG AND COX [21].

CRAIG AND COX [21] attribute this discrepancy on a reactive effect of the wire on the passage flow (see Ftn. 21 on Page 18), distinct from the loss due to fluid-dynamic drag. Unfortunately, the authors do not give any additional information about this issue nor references to further investigations.

However, of great interest is the informative discussion appended to the paper, especially the statements made by A. SMITH²⁰. He questions the meaning of applying a unit drag coefficient for circular cylinders and suggests that this would result in a considerable underestimation of loss, which he blames on the fact that additional losses are caused by the wire (boundary layer separation on the blade surfaces downstream of the wire)²¹ for which a drag coefficient of unity will not account for. Based on test results of his company (seven-stage turbine, 50 per cent reaction blading)²² he suggests a value in the range of $c_D = 2.5$ to 3.3, depending on the span position of the PSC, if loss is only considered in the form of fluid-dynamic drag. SMITH also refers to the publication of KIRILLOV AND KUZ'MIČEV [64] based on a lower reaction turbine stage and points out that these results would suggest a drag coefficient in the range of $c_D = 1.5$ to 3.4. However, SMITH indicates that in contrast to single-stage tests [64] additional loss is induced in a multi-stage turbine, where the PSCs can have a negative impact on the axial flow velocity profile.

NASA [35, 66, 71, 72, 93, 94] In the 1970s, extensive research has been published by the National Aeronautics and Space Administration²³ (NASA) in the field of transonic axial-flow compressor and fan blades connected with part-span dampers or shrouds (snubbers) and lacing wires. Although the subjects of Refs. [35, 66, 71, 72, 93, 94] are not on turbine blading and their outcomes are not directly applicable on the matter discussed here, the technical reports and papers from NASA are still worth mentioning at this point, since they represent the major research outcome available from this decade and field and possibly have influenced the work of KOCH AND SMITH, JR. [65].

KOCH ET AL. [66], LEWIS, JR. AND URASEK [72], LEWIS AND HAGER [71] as well as ESGAR AND SANDERCOCK [35] experimentally studied the efficiency drop and aerodynamic losses induced by PSCs and describe substantial effects of these elements on the performance and flow field. Following this, ROBERTS [94] analyzed further experimental data and presents a first correla-

²⁰CEng; FIMechE; affiliated with C. A. Parsons and Co. Ltd.; author of Refs. [110, 111].

²¹This is basically what CRAIG AND COX [21] mean by "reactive effect of the wire on the passage flow" (see Page 18), as they indicate in their respond to the discussion appended to Ref. [21].

²²HAVAKECHIAN AND GREIM [43] for example provide a thorough overview on key aerodynamic design issues of 50 per cent reaction steam turbines.

²³All measurements were carried out using an in-house test rig (see description in Ref. [35]) at the NASA Lewis Research Center in Cleveland, Ohio, USA.

tion for the total pressure loss due to part-span shrouds in compressor blading operating near design point.²⁴ This work is later continued and ROBERTS ET AL. [93] subsequently contribute a correlation for off-design conditions. According to WADIA AND SZUCS [133], who recently compared loss values predicted by ROBERT'S correlation [94] against results derived with 3D CFD, the correlation has found wide usage in industry. In a later work, ROBERTS [95] also presents design guidelines for part-span dampers.

KOCH AND SMITH, JR. [65] In their comprehensive work presented in the mid 1970s, KOCH AND SMITH, JR. [65] identify the presence of part-span shrouds as one of the four main loss sources²⁵ in axial-flow compressors. Consequently, the authors [65] present a loss correlation which they base on the concept of drag turned into an entropy rise²⁶. The drag is assumed to come from two sources, namely from the part-span shroud's profile and from the interference of the flow at the junction of part-span shroud profile and blade surface, whereby both drag coefficient formulations are based on correlations of HOERNER [47]. Based on a large number of experimentally investigated compressors, KOCH AND SMITH, JR. [65] state that the predicted magnitude of drag is generally too low and has to be increased by a factor of 1.8, in order to obtain a satisfying agreement with measurements.

DENTON [25] In his well known and recognized IGTI scholar lecture presented in 1993, DENTON [25] examines various loss mechanisms in turbomachines and also describes basic flow phenomena that are present in turbine or compressor blading joined by struts²⁷ at part-span in order to control blade vibration. He underlines the complex nature of the flow over the strut and sees an analogy of secondary flow generation on the strut to the one being induced near endwalls due to the static pressure gradient between blade PS and SS. According to DENTON [25], the loss behind the strut is clearly concentrated near the blade SS. In this context the author [25] points out the relevance of trailing edge shape for the magnitude of loss and states that especially the separated, low-energy fluid behind struts with blunt trailing edge like lacing wires will be subjected to the passage pressure gradient and subsequently move towards the blade SS, where it merges with the loss in the secondary vortex. Keeping this in mind, DENTON [25] concludes that in non-uniform

²⁴According to ROBERTS [94], several aerodynamic and geometric PSC factors can influence the loss in transonic rotors: MACH number, attack angle, thickness and chord, LE and TE thickness, blade span relative to the PSC geometry and blade geometry at the PSC location.

²⁵1) blade profile loss due to surface diffusion and trailing edge thickness; 2) losses due to endwall boundary layers and clearances; 3) shock losses; 4) losses due to part-span shrouds; [65].

²⁶This concept is also postulated by DENTON [25], as discussed below and in Sec. 5.1.

²⁷According to DENTON [25], lacing wires (circular rod) or part-span shrouds (airfoils).

flow the fluid-dynamic drag and entropy generation will strongly differ from the same scenario in uniform flow.

In his paper, DENTON [25] spends some thoughts on the relation of loss to drag and comes to the conclusion that for uniform flow, the drag of a strut can be expressed in terms of an entropy generation²⁸, whereby he also notes that in real flows there are considerable deviations from the assumptions made for uniform flow. However, to account for the loss induced by a strut in uniform flow, DENTON [25] presents a loss coefficient²⁹ in terms of drag coefficient of the strut based on its frontal area projected in relative flow direction and on an average relative flow velocity. He specifies the drag coefficient of order unity for lacing wires with circular cross section (compare to Ref. [21]) and $c_D = 0.1$ for airfoils. Interestingly, this approach is similar to the one pursued by CRAIG AND COX [21], as discussed on Page 17. However, here [25] the 1% of passage area blocked by the strut is referred to an average relative flow velocity and then transformed into an entropy change.

DENTON [25] furthermore discusses the entropy generation concept as an alternative method for predicting the boundary layer loss on a streamlined strut, i.e. an airfoil. One of DENTON's key messages is that the strut should be placed in a region where the relative flow velocity is low, i.e. near the blade leading edge (LE) when considering expanding flow in turbine blading. In contrast, a strut with blunt trailing edge (TE) and non-streamlined shape will show a large separated downstream region. For this scenario, DENTON [25] identifies the base pressure to be the main source of entropy. These tendencies basically correspond to the ones discussed on fluid-dynamic drag and the composition of drag force (skin friction drag and form drag) in Sec. 5.2 and shown in Tab. 5.1 on Page 97. Following the discussion above, it can be concluded that DENTON's work [25] incorporates useful definitions of coefficients to account for the various loss sources in turbomachinery, however, no universal loss correlation for PSCs is given.

DUNHAM AND PHILLIPSEN [31] In this paper, published in 2002, the application of a streamline curvature code to the design of turbochargers is focused on. The authors [31] state that even nowadays a throughflow calculation generally remains an important tool for designing turbocharger turbines, especially when considering the fact that usually a large number of geometrical configurations are investigated at several OPs to obtain one final design. According to DUNHAM AND PHILLIPSEN [31], turbocharger turbines are often coupled by a simple lacing wire in order to control the vibration level of the

²⁸ $T \Delta s = F_D / (\rho A_{BP})$, DENTON [25]. KOCH AND SMITH, JR. [65] use a similar approach.

²⁹ $\zeta = T \Delta s / (0.5 w_{avg}^2) = c_D A_{PSC}^* / A_{BP}^* = c_D A_{PSC}^* / A_{BP}^*$, DENTON [25].

blades. Interestingly, they state that "although lacing wires have been used in LP steam turbines, no prediction of the local losses caused by them appears to have been published". Due to the fact that TRAUPEL's [123] loss correlation for PSCs is based on various simplifications, DUNHAM AND PHILLIPSEN [31] present a new and more accurate method of modelling the aerodynamic losses due to lacing wires and blade reinforcements³⁰ in turbocharger turbines, which they parameterized using experimental data of a typical turbocharger. The correlation was finally implemented into SC90T [88].

With the help of 3D CFD analyses, the authors [31] were able to visualize the flow around the LW and BR and draw conclusions regarding the velocity distribution of flow approaching the PSC as well as the composition of loss due to the PSC. As indicated by other authors [21, 25, 64, 65, 98], DUNHAM AND PHILLIPSEN [31] conclude that downstream of blunt bodies like PSCs the separated flow in the wake is subjected to the blade pressure gradient and therefore a cross flow forms towards the blade SS, where it mixes with the local flow. This leads to a loss concentration at the intersection of PSC and blade SS, DENTON [25], which can be seen in terms of enhanced secondary flow formation. To account for the loss due to cross flow and the loss concentration on the blade SS, they [31] split their correlation into two loss parts, namely loss due to diffusion based on TRAUPEL's attempt [123] using a different reference velocity and loss due to cross flow along the PSC axis based on a mixing loss approach of DENTON [25]. According to the derivation of TRAUPEL's correlation [123], the diffusion loss, which is the main loss part, results from the drag force of the PSC. In contrast, the mixing loss due to cross flow along the PSC axis is mainly depending on the mass flow ratio of the mixing streams. Despite the fact that the correlation [31] was calibrated against experimental data, the general approach is of interest for the subject of this thesis and is further examined in Subsec. 5.4.3.

1.4.3 Experimental Investigations

In the following, publications with the focus on experimental approaches are reviewed and discussed.

ACCORNERO AND MARETTO [1], ACCORNERO ET AL. [2] In terms of providing experimental data of measurements downstream of rotors with PSCs in LP steam turbines, the publication of ACCORNERO ET AL. [2] and the more significant work of ACCORNERO AND MARETTO [1] has to be highlighted.

³⁰According to DUNHAM AND PHILLIPSEN [31], the holes for the lacing wire need reinforcements, in order to ensure sufficient low-cycle fatigue life.

ACCORNERO ET AL. [2] investigated a 320 MW full-scale multi-stage LP steam turbine during power plant operation³¹. Performed in the early 1980s, the focus of this work was a comprehensive aero-thermodynamic evaluation of the LP turbine with the goal of verifying an in-house (ANSALDO) throughflow code. According to the cross section of the turbine shown in Ref. [2] and statements provided later by ACCORNERO AND MARETTO [1], the LP section of this turbine features PSCs, namely tie wires and welded stubs³² in the penultimate and last rotor blade row, respectively. In their publication, ACCORNERO ET AL. [2] mainly focus on the presentation of the experimental

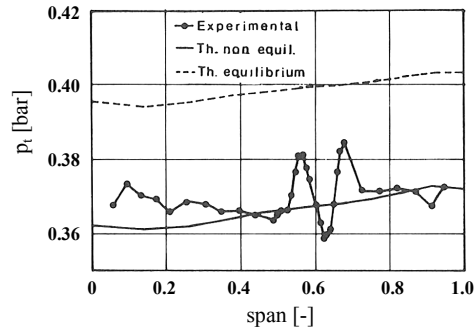


Figure 1.9 Total pressure behind rotor with PSC (tie wire), ACCORNERO AND MARETTO [1]

traverse data and the comparison to theoretical results, whereas the impact of the PSCs on the flow field is not discussed. As described in Ref. [2], flow field measurements were carried out in measurement planes downstream of the last four stages and in the diffuser by using spherical pneumatic multi-hole probes. Especially the experimental data obtained in planes downstream of the last and penultimate rotor is interesting to see, although it is hard to judge the level of significance of this data with respect to the influence of the PSCs, due to the relatively poor radial measurement point resolution³³ used.

More details about the steam turbine, based on additional measurements with higher radial measurement point resolution using three different kinds of probes³⁴, are provided by ACCORNERO AND MARETTO [1] a few years later. The presentation of experimental flow field data³⁵ is focused on the last stage of

³¹The steam turbine was developed by ANSALDO (today: ANSALDO Energia) and operated in the ENEL (Ente Nazionale per l'Energia Elettrica) power station in Vado Ligure, Italy.

³²According to NAUMANN [85], who provides a useful overview about lashing techniques used in the early 1980s, some manufacturers tend to weld stubs of several blades together, forming packages. He furthermore states that the cross section of these stubs should be elliptical rather than circular, which, according to NAUMANN [85], reduces the drag to one tenth.

³³9/14 measurement points along the span downstream of penultimate/last stage.

³⁴Disc probe for yaw/pitch angle and static pressure; Kiel probe for total pressure and total temperature; optical probe based on the extinction method for wetness measurement.

³⁵ACCORNERO AND MARETTO [1] state that measurements were carried out for several load conditions and condenser pressures. However, in Ref. [1] only data of one operating point is presented (except for the wetness fraction).

the LP turbine and is additionally compared to theoretical results derived with throughflow calculations, in order to check the confidence level of theoretical prediction methods, see also Ref. [126]. The authors [1] state that the aerodynamic effects of the PSCs could be resolved with the probe measurements. They find that the tie wire has a large impact on the flow field, which is obvious when regarding the measured radial total pressure distribution between last and penultimate stage, see Fig. 1.9. Here, the wake of the PSC (mounted at approximately 60% span) in terms of total pressure drop is properly resolved, whereby in span regions below and above the wire the total pressure has local maxima. In contrast, the authors [1] state that downstream of the last rotor blade row, the wake of the welded stubs³⁶ is less pronounced.

MAIER [77] In terms of identifying the efficiency drop due to PSCs in LP steam turbines by means of measurements, the work of MAIER [77] has to be highlighted, although the discussion made in Ref. [77] about this topic

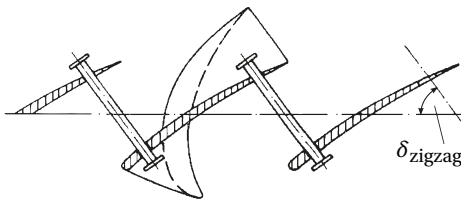


Figure 1.10 Coupled last stage blading design investigated by MAIER [77] and PFEIFFER [90]

is relatively short. Within an ITSM commemorative publication from 1985, MAIER [77] reports about efficiency measurements in an LP model steam turbine test rig at ITSM. Based on experiments with and without cylindrical damping pins³⁷ mounted in zigzag-configuration (compare to PFEIFFER [90] and NAUMANN [85]) within the blade passage of last stage LP blading

(Fig. 1.10), the author [77] presents efficiency curves for both configurations and identifies an efficiency drop of approximately two percentage points³⁸ at part and design load due to the presence of the PSCs. MAIER [77] assumes the steam flow to be congested upstream of the PSC, which leads to local blade incidence and additional blade profile loss. This assumption is later confirmed by numerical investigations of HÄFELE ET AL. [54]. Interestingly, the author [77] does not make any observations with regard to fluid-dynamic

³⁶Neither ACCORNERO ET AL. [2] nor ACCORNERO AND MARETTO [1] give information about the shape of these elements. However, based on statements made by NAUMANN [85] it is most likely that the cross section is elliptical, see Ftn. 32 on the preceding page.

³⁷Geometric details of the PSCs and the test rig as well as the vibrational behavior of the configurations are described by PFEIFFER [90].

³⁸Results of MAIER [77] for design load are in reasonable correlation to the outcome of HÄFELE ET AL. [54], as the relation of flow channel area blocked by the PSCs to efficiency drop is similar.

drag and corresponding loss induced by the PSCs. However, in contrast to part and design load conditions, the difference in efficiency vanishes towards extreme overload and both efficiency curves converge. MAIER [77] is of the opinion that in this operational range the negative impact of the choking diffuser is dominating the efficiency.

VÖLKER [132] In his PhD thesis published in 2006, VÖLKER [132] investigates various kinds of last stage blade designs used in LP steam turbines. Besides comparative experimental investigations carried out with two older SIEMENS blade designs, he focused on measurements in a model of a three-stage LP steam turbine³⁹ with newly developed shrouded LP titanium blades with snubbers⁴⁰ at part-span (Fig. 1.14). Although the aerodynamic performance of the PSCs is not the main focus of the work, VÖLKER [132] points out their impact on the downstream flow field.

Based on measurements with multi-hole cone-head probes downstream of the rotor with PSC, VÖLKER [132] presents circumferentially averaged radial traverse data of selected flow properties. Against the author's [132] expectation, the impact of the snubber on the radial static pressure distribution is not visible, which VÖLKER [132] blames on the relatively large distance between

³⁹The measurements were performed in an LP steam turbine test rig at ITSM, see Ref. [132].

⁴⁰According to Ref. [132] the snubber has an almost elliptical cross section shape with an aspect ratio of approximately 0.8 (compare to MISTRY ET AL. [82]). Thus, the flow characteristic around the snubber is comparable to the one around circular cylinders (*blunt* bodies, see Sec. 5.3.1).

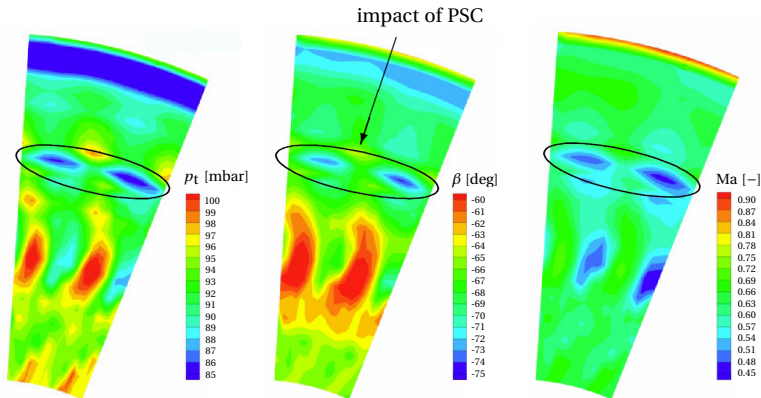


Figure 1.11 Measured, time-averaged flow field downstream of last stage rotor blading with PSC (snubber) in terms of total pressure, relative flow angle and absolute MACH number, according to VÖLKER [132]

measurement plane and snubber trailing edge. In contrast, the impact of the PSC is captured quite well in terms of total pressure and accordingly absolute velocity and MACH number, whereby these properties show increased values in the span region above and below the snubber and reduced values in the wake just downstream of the PSC. Compared to a blading without snubber, VÖLKER [132] points out that the measured flow angles above and below the snubber deviate by approximately $+4^\circ$ and -2° , respectively. The same tendency is reported in Ref. [54], whereby the deviation of relative flow angle above the PSC (FB & BR) is three times larger compared to the snubber investigated by VÖLKER [132]. According to HÄFELE ET AL. [54], this lowers the EULER work at this span region, because Δc_Θ is reduced.

Interesting to see are circumferentially and radially resolved measurement data based on probe measurements, presented in Ref. [132] in terms of contour plots (Fig. 1.11). VÖLKER [132] states that the impact of the snubber on the downstream flow field is not constant in circumferential direction but instead is partially diminished due to the wakes of the upstream stator blades.

The work [132] can be seen in the context of the trend arising in the first decade of the 21st century, switching in terms of blade material from steel to titanium due to the continuous increase of exhaust area (compare to Ftn. 4 on Page 6) and corresponding blade length. VÖLKER [132] points out that based on his measurements it is not feasible to determine the PSCs' influence on the turbine efficiency. However, he calculates the change of total pressure loss coefficient $\Delta p_{t,\text{loss}} / (0.5 \rho w_2^2)$ due to the presence of the snubber to the magnitude of 6×10^{-4} and concludes that compared to the gain of efficiency due to the increased exhaust area⁴¹ and corresponding reduced exhaust loss, the additional loss due to the snubber is negligibly small.

BOSDAS ET AL. [12] Time-resolved data, presented by BOSDAS ET AL. [12], reveal interesting details about the secondary flow structures in measurement planes downstream of the last (R4) and penultimate (R3) rotor blading of a

⁴¹Generally, the development trend towards increasing blade length in LP sections of steam turbines requires the introduction of coupling and damping elements in the last stages' rotor blading. Particularly the use of titanium as blade material requests the development of blades with integral shrouds, so-called *integrally shrouded blades* (ISB) or *continuous covered blades* (CCB), which often feature additional part-span shrouds (snubbers) at approximately mid-span. For example MACHIDA ET AL. [76], TANAKA ET AL. [119], HERMELER ET AL. [45] and later MURATA ET AL. [83], SHIBUKAWA ET AL. [105] and SENOO ET AL. [102, 103] reported the development of such blades in their works. However, with respect to these references and besides the mechanical integrity of the blades, only SHIBUKAWA ET AL. [105] also address the snubbers from the fluid-dynamical point of view within the development process, see Subsec. 1.4.4.

four stage LP model steam turbine⁴². In general, these flow structures are responsible for the unsteady aerodynamic blade loading and one source of possible blade excitation in turbomachinery. Both rotor bladings feature blade-integrated snubbers⁴³ with elliptical shape at approximately 50% span. The authors [12] used a newly developed FRAP-HTH⁴⁴ probe in order to resolve the unsteady wet steam flow field at OPs between part load and overload and show data of time-resolved relative flow angle and total pressure measurements in their paper. In terms of unsteadiness, one major finding of the paper is the fact that the secondary flow structures detected at the tip region downstream of the investigated rotors are the predominant sources. Although the focus of the paper [12] is not on the presence of the PSCs, some findings with respect to the PSCs are interesting to see.

By time-averaging the FRAP-HTH data and also comparing it to data obtained with conventional pneumatic five-hole probes (cobra shape), BOSDAS

⁴²The measurements were performed at the MHPS (MITSUBISHI HITACHI POWER SYSTEMS) steam turbine test facility in Hitachi City, Japan, see Ref. [12].

⁴³Based on a meridional view of the four-stage power plant LP steam turbine shown in Ref. [12], the span-wise extent of the PSCs can be approximated to 3.3% and 2.1% for rotors R3 and R4, respectively. This is relatively small, especially for the LSB, when comparing it to the geometry of the three-stage LP IST investigated in the present work (approximately 3.7% and 5.8% span for PSCs in rotors R2 and R3, respectively). Although it is not possible to quantify the blockage area from this data, it has to be kept in mind that, combined with the fact that the PSCs in Ref. [12] are located at approximately mid-span, the smaller radial extend and lower radial position might result in a considerably smaller relative blockage area and less intense flow interactions.

⁴⁴Based on the FRAP technology (Fast Response Aerodynamic Probe) developed at the Laboratory for Energy Conversion at ETH Zürich, this probe features a high temperature heated tip (tip temperature above saturation temperature) with two piezo-resistive sensors for measurements in wet steam flow, see Ref. [12].

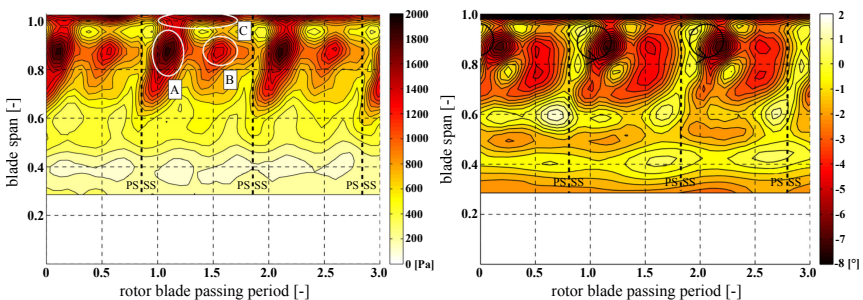


Figure 1.12 Time-resolved flow field at exit of rotor R3 with PSC (view in upstream direction): RMS value of the random part of the total pressure signal, indicating elevated aerodynamic losses (left) and relative yaw angle (right), BOSDAS ET AL. [12]

ET AL. [12] can confirm observations made by HÄFELE ET AL. [52, 54] regarding the two peaks of local flow overturning above and below the PSC, which are due to the vortex structure induced by the PSC (Fig. 5.15). Confirmed is also the fact that the absolute MACH number above and below the PSC is locally increased, which is due to the blockage effect of the PSC and the resulting redistribution of mass flow rate, as reported by HÄFELE ET AL. [50, 54]. These phenomena can also be seen in Fig. B.7.

By analyzing peak-to-peak fluctuations of a relative total pressure coefficient at several span-wise locations downstream of R3, BOSDAS ET AL. [12] found the highest amplitudes being present in the tip and shroud region. Moderate fluctuations are found in the mid-span region, whereby the variation increases with increasing mass flow rate, pointing towards more intense flow interactions with the PSC at overload condition. The authors [12] further analyze contour plots showing the time-resolved flow field at the rotor exit in terms of the RMS value of the random part of the total pressure signal and identify three major regions of elevated aerodynamic losses, see Fig. 1.12 (left): One is resulting from the tip passage vortex located near the suction side of the rotor blades (A), one is due to the tip passage vortex of the upstream stator (B) and a further region is related to the tip labyrinth leakage flow (C). It has to be noted that, compared to these major flow structures, the impact of the PSC (located at approximately 50% span) on the RMS value of the random part of the total pressure signal is relatively small and is not further discussed by the authors [12]. However, BOSDAS ET AL. [12] indicate that a small alternation of yaw angle ($\pm 1^\circ$) can be detected downstream of R3 and confirm observations of HÄFELE ET AL. [54] regarding the span-wise impact of the PSC on the flow field of approximately $\pm 10\%$ span, see Fig. 1.12 (right).

1.4.4 Numerical Investigations

In the following, publications with the focus on numerical approaches are reviewed and discussed.

RUBECHINI ET AL. [96] A paper of RUBECHINI ET AL. [96], presented in 2007, deals with aspects of CFD modelling in the analysis of an LP steam turbine. The focus of the study is on accounting for selected geometrical features and details of the flow path by simple models. In the following, only the simplified modelling for PSCs is reviewed. The actual full-scale reference turbine was experimentally investigated in situ throughout the 1980s, as described by ACCORNERO AND MARETTO [1] and ACCORNERO ET AL. [2], see Pages 21–23. RUBECHINI ET AL. [96] used this measurement data [1, 2] to validate their four stage equilibrium steam (EQS) 3D CFD calculations. However, they did

not include the actual PSC geometries in the passage model but instead considered the body force model of CHIMA [20] to apply a volume-weighted drag force⁴⁵ on appropriate grid cells representing and approximating in sum the volume of the PSC. The authors point out the simplicity of this approach with respect to grid generation and solving as well as the reduced CPU time and related costs. In contrast to CHIMA's model [20], which is able to consider both lift and drag force of a body, RUBECHINI ET AL. [96] limit their approach to the use of the drag force, which seems appropriate when considering the fact that PSCs with circular or slightly elliptical cross sections (lacing wires and elliptical-shaped welded stubs, see discussion on Pages 21–23 and Ftn. 36 on Page 23) and no airfoils are modelled.

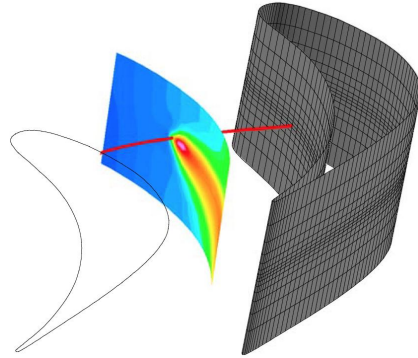


Figure 1.13 Entropy rise due to a lacing wire, modelled by RUBECHINI ET AL. [96]

The authors [96] performed additional 2D simulations with an isolated cylinder (same diameter as the PSC) subjected to similar flow conditions (MACH and REYNOLDS number) with respect to the blade row. Accordingly, the body forces were calibrated by adjusting the drag coefficient to match the drag force obtained from the 2D simulation. In Fig. 1.13, the loss generated downstream of the PSC within the blade passage is shown by an entropy rise. With regard to the validation, the authors found a generally satisfying agreement between measurements and CFD. However, they state that in measurement planes downstream of the rotors with PSC a relevant discrepancy is detected. Here, the absolute flow angle deviates up to -10° and the total pressure in span regions above the PSC is underpredicted.

The models presented in Ref. [96] are mainly intended for the usage within the design process, since basic physical effects are considered while the computational effort and time consumption for application is relatively low. The authors [96] point out the difficulty of including the PSC geometry in the computational mesh and yet present a simplified and smart way of modelling its impact and related losses. However, the presented approach does not account for the cross flow which naturally forms due to the blade passage pressure

⁴⁵ $\vec{F}_D = 0.5 \rho |\vec{w}|^2 c_{D, APSC} (V_c / \sum_{PSC} V_c) (\vec{w} / |\vec{w}|)$, RUBECHINI ET AL. [96]. \vec{F}_D is assumed parallel and opposed to the relative flow direction, in order to generate losses without turning the flow.

gradient along the PSC axis and carries the low-energy fluid in the wake of the PSC from blade PS to SS. Consequently, no related losses due to the interaction of the vortex system with the main passage flow or typically the blade SS are considered (compare to Fig. 5.15 on Page 126). Therefore, the model might probably underestimate the losses induced by the PSC.

WADIA AND SZUCS [133] A numerical study from WADIA AND SZUCS [133], published in 2008, examines the aerodynamic characteristics and differences of two very similar fan blades which can be generally found in the first stage of multistage fans of aircraft engines with low bypass ratio, whereby one of the investigated fans is equipped with a part-span shroud. The authors [133] applied three-dimensional CFD and carried out experimental validation for the shrouded fan at 95% (cruise) and 100% (design) speed by means of measurement data obtained from probes mounted along the LE of the downstream stator. A generally good agreement was found, whereby high discrepancies are visible at the span position of the snubber. As a result of the relatively poor radial measurement point resolution (5 points along the span), the impact of the PSC at the decisive span position is not captured by the data.

Surprisingly, a comparison of both fans' efficiencies in terms of level and radial distribution reveals that at design speed, the shrouded fan shows a better performance. The authors [133] argue that the boundary layer fluid at the blade suction side, centrifuged towards the tip, is blocked by the presence of the PSC. As a result, the interaction between shocks and the boundary layer is improved and therefore higher adiabatic efficiencies are obtained in the span region between PSC and blade tip (overall 1.9 percentage points). However, at cruise speed both fans show a similar overall efficiency. In the light of a reduced shock strength with corresponding reduction of shock boundary layer interaction and the fact that there is no more significant radial movement of fluid present in the suction side boundary layer of the shroudless fan, the blockage effect of the PSC and thus the efficiency gain in span regions above the PSC is only slight and is nullified by the severe efficiency drop in the vicinity of the PSC. Here and also at lower speeds, the part-span shroud induces a net additional loss. Furthermore, interesting to see is a comparison between radial efficiency loss distribution obtained by engine test data and CFD at 100% speed and the values predicted with a correlation of ROBERTS [94] for the fan with PSC.⁴⁶

⁴⁶MISTRY ET AL. [82] point out the significance of ROBERTS [93, 94] correlations and the work of WADIA AND SZUCS [133] for the application in transonic compressors but also state that these results cannot be transferred to the application of snubbers in the investigated LP steam turbine blading, since here the relative flow velocity upstream of the PSC is considerably lower.

SIGG ET AL. [107] The same model of a three-stage LP steam turbine analyzed by VÖLKER [132] is research object in a numerical and experimental study presented by SIGG ET AL. [107], whereby the LP section is considered at severe part load conditions only. The authors [107] carried out 3D CFD calculations using an EQS model and included the geometry of the snubber in the flow passage, which they discretized with hexahedral meshes, see Fig. 1.14. The CFD results are compared to flow field measurement data obtained with 7-hole probes in terms of radial traverses and meridional streamline plots combined with 2D velocity vectors, which show the separation area in the diffuser. Generally, a reasonable agreement between experiment and CFD was found. However, the focus of the study was not on the influence of the snubber but on the overall behaviour of the steam turbine during windage⁴⁷ condition. Therefore, no conclusive statements regarding the presence and impact of the PSC are made in the article.

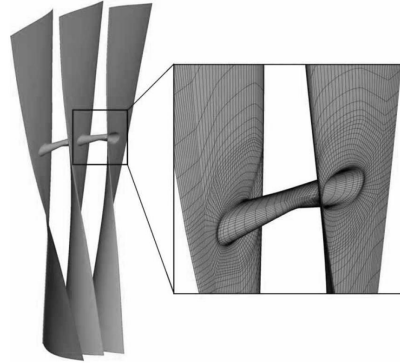


Figure 1.14 Snubber modelling in rotor R3, according to SIGG ET AL. [107]

MISTRY ET AL. [82] A CFD study with the focus on the effect of snubbers on the aerodynamic performance of 48-inch LSB utilized in GE steam turbines A15 and D11 and using perfect gas as working fluid was published by MISTRY ET AL. [82] in 2011. The snubber has a teardrop-shaped cross section (thickness to chord ≈ 0.83 , Fig. 1.15) and is mounted at 50% span. According to MISTRY ET AL. [82], $Ma_{rel} \approx 0.5$ upstream of the PSC. Due to the time-consuming methodology that applies for structured, hexahedral meshing of complex geometry parts, the authors [82] chose an unstructured tetrahedral mesh approach for the one-passage model, while tolerating limitations in the resolution of the prismatic boundary layer mesh. Unfortunately, no experimental validation of the presented CFD model was carried out.

The CFD results clearly reveal that the impact of the PSC on the flow within the blade passage cannot be reduced solely to boundary layer loss and mixing loss in the wake of the PSC. Moreover, the PSC induces a cross flow along the

⁴⁷Here, the steam is passing through the last rotor blades more radially than in axial direction. According to the authors [107] the snubber does not seem to impede this radial motion.

PSC axis, which interacts with the blade SS and the main flow, resulting in additional losses. This observation is confirmed by similar 3D CFD studies [31, 50, 52, 54, 74] and was also previously discussed in theory [21, 25, 64, 65, 98, 140]. A comparison of results obtained from simulations with and without the PSC shows that the presence of the PSC leads to a reduction of total-total stage efficiency of about 0.32 percentage points and to a redistribution of span-wise torque and mass flow rate. According to the authors [82], the presence of the PSC pushes the flow towards hub and shroud, resulting in lower torque around the span region of the PSC ($\pm 10\%$ span) and a slightly increased torque along upper and lower span positions. Besides this, MISTRY ET AL. [82] show that the fillet between blade and PSC affects the performance of the rotor. It can be concluded that out of the 0.32 percentage points mentioned above, 0.12⁴⁸ can be attributed to the presence of the fillet. Based on this, the authors [82] recommend a careful design of the fillet for loss reduction.

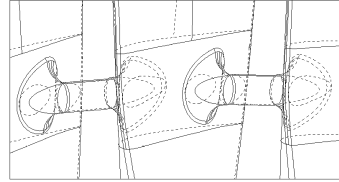


Figure 1.15 LSB with PSC [82]

WU ET AL. [137] In 2011, WU ET AL. [137] presented a multidisciplinary study on the design of snubbers in a SIEMENS gas turbine. The objective of this study is the optimization of the original snubber geometry in terms of minimizing the aerodynamic drag force while maximizing the fatigue life of the turbine blade. The swept snubber geometry is modelled in simplified form by two ellipses connected by straight lines.^{49,50} The main parameters are the snubber width (extent in span-wise direction) and the taper ratio.⁵¹ In addition, the fillet of the PSC is considered. The authors [137] state that the fillet supports the reduction of flow separation downstream of the snubber. For the CFD analysis, one blade passage is modelled as a linearized cascade and discretized with an unstructured tetrahedral grid, due to the complex snubber geometry and ease of use. WU ET AL. [137] point out the compromise between accuracy and CPU time and according to this, only a span-wise segment around the PSC is taken into account, whereby the domain boundaries in

⁴⁸MISTRY ET AL. [82] state that out of the overall efficiency drop (0.32 percentage points) due to the PSC, 0.20 percentage points is due to the fillet. However, based on a bar diagram shown in Ref. [82] it has to be concluded that this value is actually 0.12.

⁴⁹According to Ref. [137], a tilted and tapered snubber with cylindrical cross section and large fillet was originally implemented in the turbine blading at approximately mid-span.

⁵⁰The snubber contact surface in the middle of the flow channel is defined by a smaller ellipsis.

⁵¹The taper ratio is defined as the ratio of leading and trailing edge radius, see Ref. [137].

radial direction are treated as solid walls. Note that with this type of model an extensive radial movement of fluid, i.e. a redistribution of mass flow rate and corresponding torque due to the presence of the PSC (see Refs. [54, 74, 82]), is probably impeded, since only a relatively tight span-wise segment with solid endwalls above and below the PSC is considered. Furthermore, no details about validation aspects for the complex flow around the snubber simulated with a significantly simplified CFD model are discussed.⁵²

WU ET AL. [137] identify three major factors regarding design and positioning of the snubber with respect to aerodynamic issues. In order to reduce the drag of the PSC, small fillet radii are recommended. A similar statement is given by MISTRY ET AL. [82]. Moreover, tapered snubbers with smaller frontal surface area lead to a reduction of drag loss. Finally, placing the snubbers away from the blade leading edge results in more drag and less (blade) lift, since here, higher velocities are present in the investigated transonic turbine cascade flow. Regarding the latter, similar statements have been previously made for example by KIRILLOV AND KUZ'MIČEV [63] and DENTON [25].

The drag force is decreasing approximately linearly when increasing the taper ratio. However, a variation of the snubber width at constant taper ratio results in contrary findings. While the drag increases when increasing the snubber width at lower taper ratios, the drag force actually decreases at larger taper ratios, more for larger than for smaller widths. Unfortunately, the authors [137] only use the aerodynamic drag as a performance indicator and do not give further physical explanations regarding the flow structure induced by the different PSC variations.

SHIBUKAWA ET AL. [105] Published in 2011, this paper reflects the mechanical and fluid-dynamical considerations spent on a newly developed titanium 48-inch last stage blade for 60 Hz (3600 rpm) TOSHIBA steam turbines. According to the authors [105], this LSB has the world's so far largest⁵³ class exhaust annulus area (10.9 m²) and blade tip speed (766 m/s) for the application in up to 1400 MW thermal power plants. The blade features integral

⁵²WU ET AL. [137] state that the final snubbered blade geometry was tested in a low-speed wind tunnel and for the validation of the virtual design conclusions were drawn from the baseline snubber geometry through similarity analysis.

⁵³Similar details are given by SENOO ET AL. [102] with regard to newly developed titanium 50-inch and 60-inch HITACHI LSBs for the 60 Hz and 50 Hz market, namely exhaust areas of 11.5 m² respectively 16.5 m² and a blade tip speed of 786 m/s. An overview about the HITACHI steel and titanium LSB lineup is depicted in Fig. 1.16, whereby interesting to see is the part-span snubber as a mechanical design feature included in almost every pictured blade as well as the snubber's development in terms of shape, size and span-wise position with increasing blade length. An overview on MHI steel blades for 50 Hz turbines is provided by TANAKA ET AL. [119].

blade cover and a snubber connection at mid-span⁵⁴. Its underlying concept fits into the blade development progress in terms of increasing blade length and subsequent benefits mentioned in Ftns. 4 (Page 6) and 41 (Page 25). Besides the mechanical design and vibrational characteristic of the blade, the authors [105] discuss aerodynamic design features like the numerical optimization of the blade tip section⁵⁵ and particularly address the layout of the part-span snubber. However, the snubber was not included in the multi-stage 3D CFD flow path analysis but rather optimized separately by using a simplified numerical model.⁵⁶

SHIBUKAWA ET AL. [105] state that one of the drastic design alterations was the change from a sleeve⁵⁷ type PSC to a streamlined one. Accordingly, the challenge was finding an aerodynamically optimized snubber profile with still allowable compression stress. For this purpose, the maximum profile thickness and its chord-wise location were varied within a CFD-based parameter study. Similar to WU ET AL. [137], a span-wise limited blade section around the snubber was considered and the blade channel was approximated by two walls

⁵⁴Based on the blade depicted in Ref. [105], it can be estimated that the snubber is situated at approximately 60% span and has a span-wise extent of approximately 2.5%.

⁵⁵Along with the benefits resulting from increased exhaust area, see Ftn. 4 on Page 6, the transonic flow in the blade tip-span region with convergent-divergent profile (relative inlet and outlet MACH numbers of approx. 1.2 and 2 [105]) and corresponding losses have to be handled.

⁵⁶A review of publicly available literature reveals that PSCs in LP blading are normally not considered in industrial applications regarding the blade design process with 3D CFD.

⁵⁷According to the blade segment depicted in Ref. [105], an ellipsis with small aspect ratio.

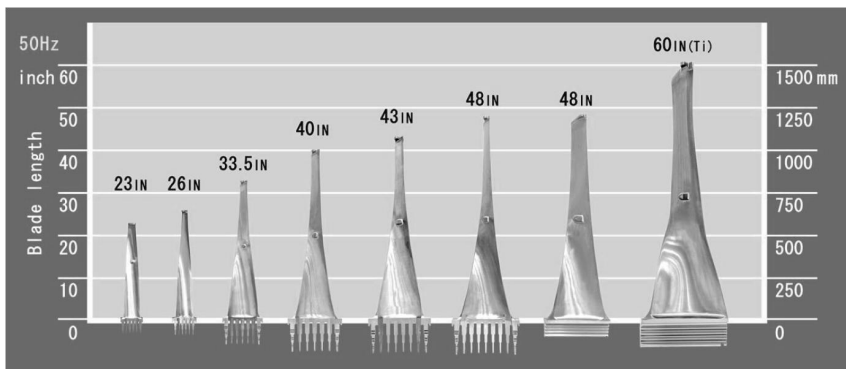


Figure 1.16 HITACHI Lineup of LSBs for 3000 rpm steam turbine, SENOO ET AL. [102]

of DE LAVAL nozzle⁵⁸ shape. According to Ref. [105], the boundary conditions were taken from the preliminary stage analyses without the PSC.⁵⁹

Under subsonic PSC inflow conditions, the loss increases with increasing MACH number and reaches a peak at $Ma_{rel} \approx 0.85$. Although the authors [105] do not explicitly discuss this, it is remarkable that at lower speed level the loss increase is only slight, whereas between $Ma_{rel} \approx 0.7 - 0.85$ the loss increases by a factor of almost three. Above $Ma_{rel} \approx 0.85$, the loss decreases approximately linearly and at $Ma_{rel} \approx 1.5$ it is below the level for the subsonic inflow. The authors [105] explain this loss peak with the presence of a normal shock wave containing strong expansion and compression waves downstream of the PSC.

SHIBUKAWA ET AL. [105] conclude that placing the maximum thickness of the streamlined shape close to the leading edge allows lowering the losses, while a snubber with thinner LE but thicker and thus blunt TE increases the losses. As explanation, the authors [105] mention the different TE wedge angle. Further results of loss versus PSC thickness show an approximately linear correlation. Solely a shape optimization from sleeve to streamlined leads to a loss reduction of over 20% with respect to the base sleeve design.

A consideration of radial loss profiles in evaluation planes just downstream of the PSCs shows that the two distinctive loss peaks representing the induced vortices (Sec. 5.6) are significantly reduced when changing from a conventional (sleeve type) to a streamlined shape. For this case, SHIBUKAWA ET AL. [105] estimate the stage efficiency enhancement to about 0.4%.

LI AND LI [74] In a recent publication, a numerical study on the performance of a three-stage LP steam turbine is presented and discussed. The LSB features a snubber with aerodynamic-shaped cross section and a draft angle, which means the snubber is tapered or swept towards the mid-channel (Fig. 1.17). For comparison, a configuration without PSC is also considered. LI AND LI [74] used hexahedral meshes for discretizing the one-passage model and carried out steady-state 3D CFD calculations while applying an EQS model. Unfortunately, no experimental validation is carried out.

The authors [74] stick closely to the investigations previously presented by MISTRY ET AL. [82] and HÄFELE ET AL. [54]. They generally confirm previous findings [54, 82] regarding the impact of the PSC on the flow field in LP steam turbines by briefly discussing aspects relevant for the blade design, like the

⁵⁸Named after Swedish engineer and inventor Karl Gustaf Patrik DE LAVAL (1845–1913), who contributed major findings to the design of steam turbines.

⁵⁹From the paper [105] it is not clear which kind of fluid model was used for the numerical investigations. However, considering the state-of-the-art in 2011, perfect gas or an equilibrium steam approach can be assumed, compare to Refs. [82, 107].

degree of reaction, the blade loading, the redistribution of torque and mass flow rate as well as the cross flow induced by the PSC. However, of greater interest is the fact that for the numerical investigations, the PSC is mounted at two different span locations, see Fig. 1.17. A comparison of total-total isentropic stage efficiency at design load reveals that case 1 drops the efficiency value by 0.2 percentage points, which is less than obtained by MISTRY ET AL. [82] or estimated by SHIBUKAWA ET AL. [105] for a similar type of LP blading.⁶⁰ Interestingly, a reallocation of the PSC to higher span reduces the efficiency drop to 0.11 percentage points, which is a considerable change. Unfortunately, LI AND LI [74] do not discuss details about the physical effects behind this quasi halving. However, they indicate that for case 2 the vortex below the PSC is weaker than for case 1. Considering part load condition, the authors [74] present slightly higher values for the efficiency reduction, whereby the difference between case 1 and 2 is decreased.

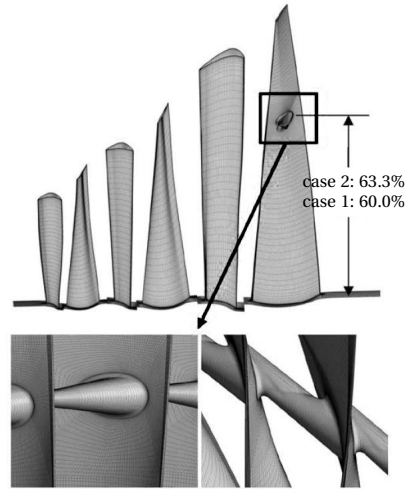


Figure 1.17 Modelling of PSC in last rotor blade, according to LI AND LI [74]

⁶⁰In this context it should be considered that the type of coupling and blading of modern power plant LP steam turbines investigated in Refs. [74, 82, 105] differs from the one of the typical LP IST studied in the context of the present work. Here, the presence of cylindrical PSCs reduces the stage efficiency by almost 4 percentage points at design load, see HÄFELE ET AL. [54] and compare to remarks on PSC blockage area and flow interactions in Ftn. 43 on Page 26.

2 | Industrial Steam Turbine Test Rig

Currently, steam turbine manufacturers like SIEMENS, GENERAL ELECTRIC (GE), MAN, MITSUBISHI HITACHI POWER SYSTEMS (MHPS) and TOSHIBA share the highly competitive global market for industrial steam turbines. While in the past the efficiency aspect has played a secondary role for these turbines and operational availability was of major interest, the latest

Table 2.1 Test rig specifications

Max. rotational speed (rpm)	17,000
Max. inlet pressure (bar)	30
Max. inlet temperature (°C)	350
Min. condensing pressure (bar)	0.05
Max. mass flow rate (t/h)	30
Max. power of brake (MW)	3.6

demands for resource conservation and environment protection have led to a change of priorities. In order to stick with the competitive battle, continuous developments and the introduction of technical innovations are mandatory to improve fuel utilization. To be able to quickly test new design developments, all manufacturers mentioned

above rely on appropriate test rigs. In this way, possible design problems or operational issues can be detected and fixed before market launch. At the Institute of Thermal Turbomachinery and Machinery Laboratory (ITSM) of the University of Stuttgart, a test facility is operated in cooperation with SIEMENS. This test rig, originally built as a prototype for a technical exposi-

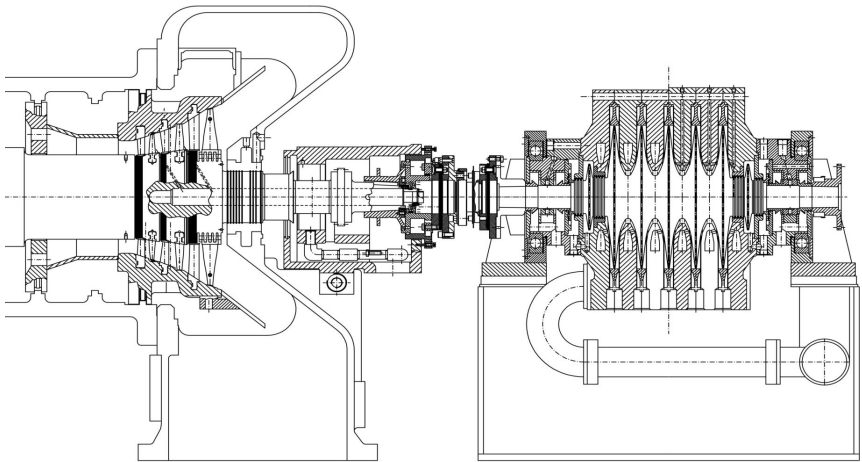


Figure 2.1 Industrial steam turbine test rig at ITSM (left: turbine; right: brake) [52]

tion, was installed at ITSM in the mid 1970s. Until the early 1990s it has been mainly used for pioneering experimental investigations on the vibrational behaviour of coupled blade systems [46, 61, 90, 136]. To meet nowadays needs for performance measurements as well as flow and vibration measurements, it has been recently updated with modern measurement equipment and new monitoring and control systems. Figure 2.1 shows a section of the test rig in its current configuration. It has to be considered that this turbine is not a model turbine but a 1:1 build of the last three stages of a multi-stage industrial steam turbine. The main characteristics of the facility are listed in Tab. 2.1.

For the basis of this thesis, the author carried out performance and flow field measurements in the industrial steam turbine test rig.¹ The measurement data are used as boundary conditions for the CFD calculations and also to validate the numerical models applied in Refs. [49, 51, 53, 54] and the present thesis, as discussed later. Basic features and relevant parts of the measurement equipment are briefly described in the first two sections of this chapter, followed by an introduction to the experimental investigations carried out. The last section deals with the evaluation of the measurement data.

2.1 Basic Features

The test rig for industrial steam turbines is operated with live steam supplied by the combined heat and power plant (HKW) of the University of Stuttgart, whereby the maximal live steam parameters are in the order of magnitude of $p_{\text{HKW}} \approx 70$ bar and $T_{\text{HKW}} \approx 350$ °C. The steam is reduced to an in-house pressure $p_{\text{ITSM}} \leq 30$ bar and the temperature can be additionally cooled down by injection of sprayed condensate using a two-substance-nozzle. The complete steam cycle is schematically depicted in Fig. C.1 on Page 213.

A constant condenser pressure, mandatory for the experimental investigations, is achieved with the help of three vacuum pumps, which allows a wide range of possible condensing pressures down to $p_{\text{con}} \approx 0.05$ bar and gives independence from the cooling water temperature used in the tube-bundle heat exchanger of the condenser.

The turbine casing is subdivided into inner and outer casing, both horizontally split, see Fig. 2.1 on the preceding page. Here, the inner casing is composed of three main components, namely a flow straightener, installed

¹In addition to the aerodynamic performance, the vibrational behaviour under real steam conditions has been evaluated for the investigated LP blades. Vibrational amplitudes and frequencies were measured in the test rig and the data is used to validate the FE models of rotors R2 and R3 with PSC, as presented in Refs. [27, 29].

in front of the first stage, the stator blade carrier and the inner ring of the axial-radial diffuser. The outer turbine casing consists of cast parts inclusive of valve casing along with a transition casing and the exhaust casing, forming the outer ring of the diffuser and guiding the steam flow into the condenser. The valve casing and the condenser are not depicted in Fig. 2.1. The type of installation in steam turbine facilities like the one at ITSM, where the condenser is mounted below the turbine, imposes an asymmetric exhaust hood design, see Figs. 2.1 and 2.4.

The turbine runner is embedded in tilting pad hydrodynamic bearings. In Fig. 2.1 only the back-side bearing (radial bearing) is shown, whereas the front-side bearing (axial-radial bearing) is not depicted. Variable power consumption can be achieved with a pendulum mounted water friction brake (HOFMANN ES4C), with which the torque (up to 2380 Nm) is measured in terms of a dynamometer. The pendulum mounting of the brake casing is realized with ball bearings, whereby the brake runner is embedded with hydrodynamic bearings into the brake casing. Brake and turbine are coupled by a flexible clutch (see Fig. 2.1) allowing longitudinal and lateral movements to be compensated. The brake has five chambers which can be independently applied with cooling water, depending on the range of power demand of the requested turbine operating point. The brake is supplied by cooling water (up to 1670 l/min) out of an elevated reservoir with constant fill level, preventing pressure fluctuations at the brake inlet. The pressure drop over the brake chambers can be adjusted by an inlet and outlet valve.

2.2 Measuring Equipment and Data Acquisition

2.2.1 Stage Pressures and Temperatures

Figure 2.2 shows a section of the test rig in its current configuration, which is a full-scale build of the last three stages of a multi-stage industrial steam turbine. As already mentioned, the turbine features conical friction bolts in the last rotor blade row (R3) and a lacing wire in the penultimate rotor blade row (R2). To determine the thermodynamic total state at the first stage's inlet, permanently installed total pressure (PITOT tubes) and total temperature probes are used, whereby one of each type is installed in the upper and lower part of the turbine and the measuring position is at approximately 50% span. This measurement setup is sufficient to determine the inlet conditions, as the steam is superheated at all investigated OPs (Sec. 2.3) and the flow straightener, installed in front of the first stage, guarantees a defined axial inflow direction. Static wall pressures are measured between stators and rotors and in the diffuser at six

circumferential positions (equidistantly distributed) at hub and shroud and are averaged using ring tubes. The same is valid for the condenser pressure, captured in the lower part of the exhaust casing at 12 equidistantly distributed positions in one streamwise plane. All operating pressures measured inside the turbine (inlet-, stage-, condenser pressure) are transformed into electrical signals using conventional SIEMENS Sitrans P pressure transducers. Operating temperatures are measured with RÖSSEL thermocouples (type K, diameter = 1 mm) at one stator blade per stage at approximately 25%, 50% and 75% span for stator S3 respectively 33% and 67% span for stators S2 and S1 at leading and trailing edges. Thermocouples are covered by shrinkage tubes, shielding the Inconel sheath of the elements against mechanical impacts and reducing the heat transfer between blade and thermocouple to a minimum. Additional temperature probes are installed downstream of rotor R3 and in the diffuser at five circumferential positions (equidistantly distributed) at hub and shroud.

- wall pressure measurement location at evaluation plane and outlet
- wall pressure measurement location along diffuser contour
- ⊕ total pressure and temperature measurement location
- — traversing plane

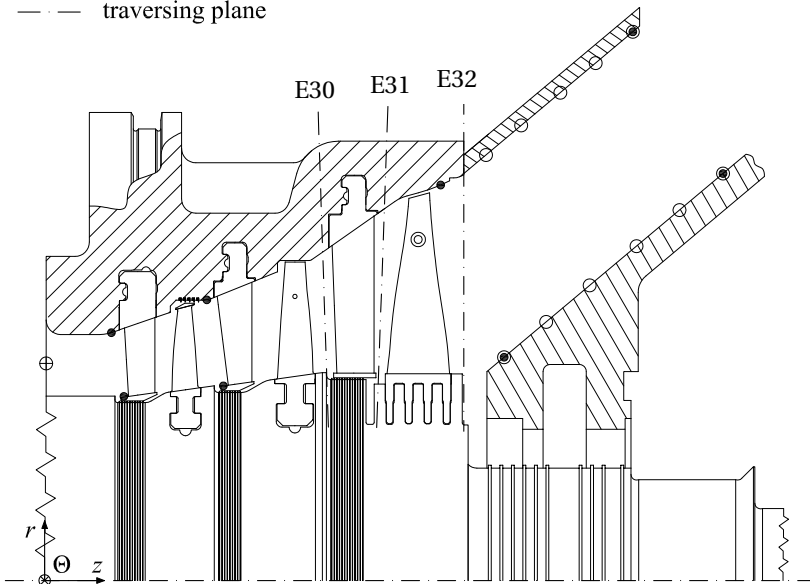


Figure 2.2 Section of the LP industrial steam turbine with PSCs, HÄFELE ET AL. [52]

2.2.2 Diffuser Pressure

In order to quantify the diffuser performance and draw conclusions regarding asymmetries of the flow field downstream of rotor R3, its inner and outer segments are equipped with pneumatic pressure measurement points (see Fig. 2.2). Here, wall pressures are measured at several measurement points along the diffuser contour at seven (inner diffuser) respectively eight (outer diffuser) circumferential positions. Pressure scanners (DMT 9116 type B with true reference) with a measurement range of 5 PSI (0.375 bar) are used to measure the diffuser wall pressures, whereby the condenser pressure p_{con} is used as reference for every single pressure tap.

2.2.3 Torque and Speed

As mentioned in Sec. 2.1 on Page 39, the torque is measured with the pendulum mounted water friction brake shown in Fig. 2.1 in terms of a dynamometer, that means a lever arm with defined length impinging a load cell. Speed measurement is carried out based on the pulse train signal measured with an inductive sensor on a sprocket and acquired by frequency counting.

2.2.4 Mass Flow Rate

The mass flow rate \dot{m} is measured with the help of a standard orifice plate according to ISO 5167-2:2003 [60]. Thus,

$$\dot{m} = \frac{C}{\sqrt{1-\beta^4}} \varepsilon \frac{\pi}{4} d^2 \sqrt{2 \rho_1 \Delta p_{\text{BL}}} . \quad (2.1)$$

Here, Δp_{BL} is the measured static pressure drop, ρ_1 is the density of the superheated steam upstream of the plate, C is the flow rate coefficient, $\beta = d/D$ is the diameter ratio (d : orifice plate diameter; D : tube diameter), $C/\sqrt{1-\beta^4}$ is the flow coefficient and ε the expansion number. Flow coefficient and expansion number are calculated based on polynomials given in Ref. [60]. Two measurement sections are available, see Fig. C.1. For the investigations of the present thesis only the larger one has been used to measure steam mass flow rates up to 30 t/h.

2.2.5 Bearing Oil Flow Rate and Temperature

In order to determine the power loss inside the tilting pad hydrodynamic bearings of the turbine, oil flow rate and temperature have to be measured. Temperature measurement is carried out with thermocouples arranged in

difference circuit and measuring at the oil intake and outlet of the axial-radial (front) and radial bearing (back), respectively (compare to Sec. 2.1). In addition, the oil inlet temperature is measured with one Pt-100 resistance thermometer. The oil flow rate is measured using conventional flow rate meters (MCD flow rate indicator 101A(i)).

2.2.6 Pneumatic 5-Hole Cone-Head Probes

Flow field measurements were carried out using miniature pneumatic 5-hole cone-head probes with a tube diameter of 0.4 mm, a head diameter of 2.5 mm and a stem diameter of 6 mm, as depicted in Fig. 2.3. Probes of this kind are known to be suitable for measuring in sub- to transonic, inhomogeneous steam flow field with moderate to high velocity gradients and have proven their applicability over the last decades, see e.g. Ref. [132]. The present miniaturized design developed at ITSM allows measurements with possibly low interference² of the probe with the measured flow field. Possible blockage effects with such probes in turbomachinery measurements are for instance

²It has to be considered that flow field measurement in near-wall or boundary layer regions is not meaningful with this type of probe.

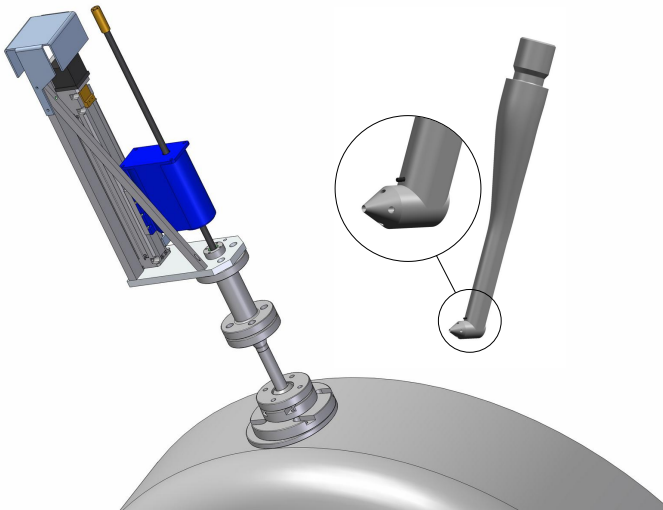


Figure 2.3 Pneumatic 5-hole cone-head probe (tube $\varnothing = 0.4$ mm, head $\varnothing = 2.5$ mm, stem $\varnothing = 6$ mm) with thermocouple ($\varnothing = 0.5$ mm) (right) and traversing system mounted on the exhaust hood (left), HÄFELE ET AL. [52]

described in Ref. [99]. The ratio of probe head diameter to blade pitch is approximately 0.06, considering rotor R3 at the radial position of the PSC. This magnitude gives an indication for the reasonable proportion between investigated blading and applied probes. With respect to the radial flow component present in the investigated LP steam turbine, the probe head has an inclination of -15° to the axial direction, which corresponds to the mean opening angle of the casing contour, see Fig. 2.2. The probes have been calibrated in air in the closed wind tunnel at ITSM at MACH numbers between 0.2 and 0.9 using a subsonic nozzle as well as at MACH 1.2 and 1.4 using supersonic nozzles. The wind tunnel and its features are properly described in Ref. [97]. For calibration, the static pressure has been set to 0.1 bar, which corresponds to the magnitude of the condenser pressure p_{con} used as backpressure for all experimental investigations within this thesis (compare to Sec. 2.3). This seems to be appropriate, considering the overall pressure level in the corresponding evaluation planes of the last stage during the experiments, see Fig. 2.2. The range of relative yaw and pitch angles used for calibration measurements is $\pm 10^\circ$ for the yaw angle and -15° to $+35^\circ$ for the pitch angle. After calculating the calibration coefficients for yaw and pitch angle, total, dynamic and averaged static pressures as well as the MACH number, the actual flow condition is determined by interpolation based on three-dimensional calibration fields, depicted e.g. in Ref. [99]. More details regarding the calibration procedure followed at ITSM are described in Refs. [34, 99, 132]. During the test rig measurements, the probes are oriented in approximate flow direction by nullifying the yaw angle pressures. In the case of a superheated steam flow, the total temperature can be approximated with the help of the miniature thermocouple ($\varnothing = 0.25$ mm) installed at the probe head (see Fig. 2.3) as well as the recovery factor which is determined within the probe calibration procedure. The same types of pressure scanners used for the diffuser wall pressure measurement (Page 41) are applied to acquire the probe pressures, whereby the condenser pressure p_{con} is used as reference for every single pressure tap.

2.2.7 Probe Traversing Systems

In Fig. 2.2 the probe traversing planes are indicated. Planes E30, E31 and E32 are equipped with probe traversing systems upstream of stator S3 (E30), between stator S3 and rotor R3 (E31) and downstream of rotor R3 (E32), allowing the thermodynamic states at any radial location to be evaluated. In planes E30 and E31, traversing systems are installed at one circumferential position, respectively (see Fig. 2.4). For measurements in plane E32, two traversing systems are used. It is known that the geometry of the exhaust hood leads to

circumferential asymmetries of the diffuser pressure field. A literature review on this topic has been recently given by BURTON ET AL. [16] and characteristics of the flow field in the present investigated turbine will be examined in detail later on. These asymmetries can lead to misinterpretations of the flow field measurements in combination with CFD calculations, where only one cyclic symmetric sector is modeled, see Sec. 3.3. Thus, one traversing system in the upper part E32 (OT) and one in the lower part E32 (UT) of the exhaust hood is installed. The probes in plane E32 are traversed radially. In order to reduce the blockage effect of the probe in plane E31, it is traversed with an inclination of $+15^\circ$ to the radial direction in circumferential direction (see Fig. 2.4 and Ref. [37]) and in addition -2° to the radial direction in axial di-

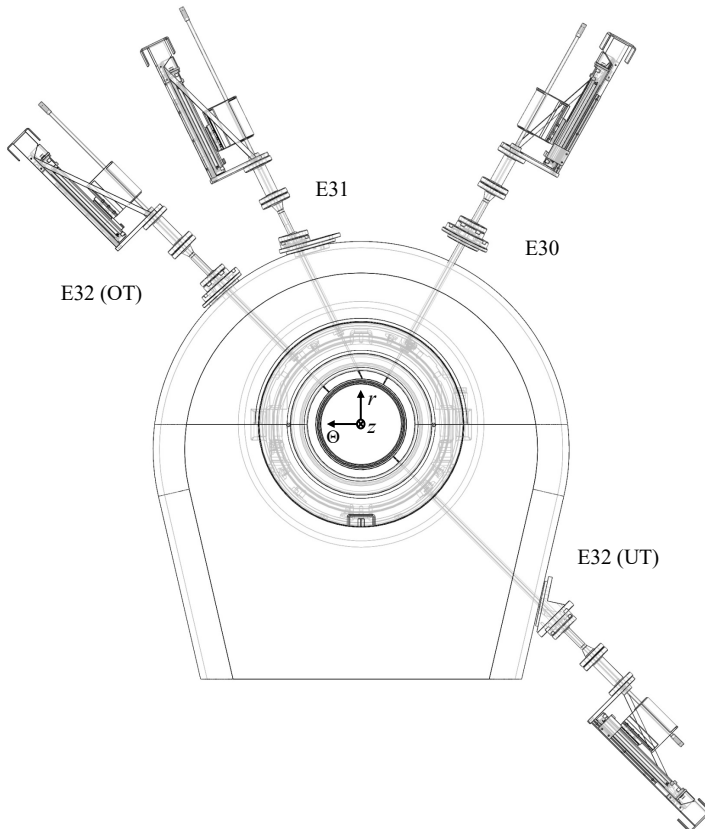


Figure 2.4 Exhaust hood with probe traversing systems [52]

rection (see Fig. 2.2). The probe in plane E30 is traversed with $+2^\circ$ inclination to the radial direction in axial direction. The probe traversing software and control devices used allow the traversing systems to be controlled separately and independently from each other. This allows a simultaneous traversing and measuring of radial flow distribution in all measurement planes. Due to their positioning at different circumferential locations (see Fig. 2.4), the probes are considered to be not affecting the flow field at the measurement locations of other probes in planes up- and downstream. The stepper motors of the linear and rotational modules of the traversing systems (see Fig. 2.3) allow a linear and rotational traversing in relatively small increments. For the present experimental investigation, a radial resolution of 40 measurement points along the span has been used. This results in a relatively long measurement time of approximately one hour for traversing all measurement points at one operating point, during which the operating condition of the turbine has to be kept constant. This high resolution ensures the complex structure of the flow field downstream of the rotors with PSC, which shows high gradients in flow values, to be resolved properly and allows a meaningful comparison with numerical results.

2.2.8 Continuous Purging

Pneumatic flow field measurement in condensing fluids like steam, especially wet steam, has ever been a challenging task. For most measurement scenarios the temperature inside the probe or pressure tubes is below the corresponding saturation temperature of the steam flow. In this case, condensation will set on, once the steam enters the tubes. Further pressure changes upstream of the probe head might lead to a movement of condensate droplets towards the pressure transducer, whereby capillary forces will hold the droplets inside the tubes. In order to avoid steam condensing in the probe or pressure tubes and subsequent blocking from condensate, a continuous purging procedure is used for all pneumatic pressure measurement points of the wall as well as the probe pressure measurement system at the test rig. The working principle of this purging procedure is properly described in Ref. [37] and will not be further discussed. In order to account for the resulting pressure offset, a purging correction according to HENEKA [44] is used, see Subsec. 2.4.2.

2.2.9 Blade Vibration

The test rig can also be used for investigations with variable rotational speed. For the purpose of blade dynamic investigations, strain gauges (S/G) are applied to several rotor blades of all three stage rows. Fig. 2.5 shows the appli-

cation on rotor blades of the last and penultimate stage, as considered in the investigations of DROZDOWSKI ET AL. [27, 29]. As indicated in Fig. 2.1, the signal leads from the strain gauges are guided through a center hole inside the rotor to a digital telemetry transmitter. The signals of 40 channels are transmitted simultaneously to the data evaluation system. The strain gauges are positioned close to the locations of maximum dynamic stress to keep the transmission factors low. A Fast FOURIER Transformation (FFT) is used to transform the time-resolved measurement data into the frequency domain (see measured CAMPBELL diagram³ in Fig. 1.3). Maximal amplitudes are obtained by filtering the time-resolved S/G signal with a band-pass filter of 5 Hz around the blade resonance frequency. In parallel to the S/G, a multi sensor tip timing (TT) measurement system is used to determine the vibration of the last stage rotor blades. By means of inductive probes installed in the casing above the blade tip, the frequency and amplitude of vibrational tip deflection is measured with the time-of-arrival-method. The blade tip edges have been magnetized and currency change signals are generated in the inductive probes when a blade is passing by.

³In order to observe blade resonant points at one fixed condenser pressure and mass flow rate level, the rotational speed is decreased with a relatively low speed gradient, starting from nominal speed down to machine standstill. As the turbine features realistic inlet and exhaust casing geometries (Fig. 2.1), both low order excitation in addition to the higher order excitation from the adjacent blade row is present. As a result, CAMPBELL diagrams are produced from the measured blade vibration frequencies and amplitudes, see DROZDOWSKI ET AL. [27, 29].

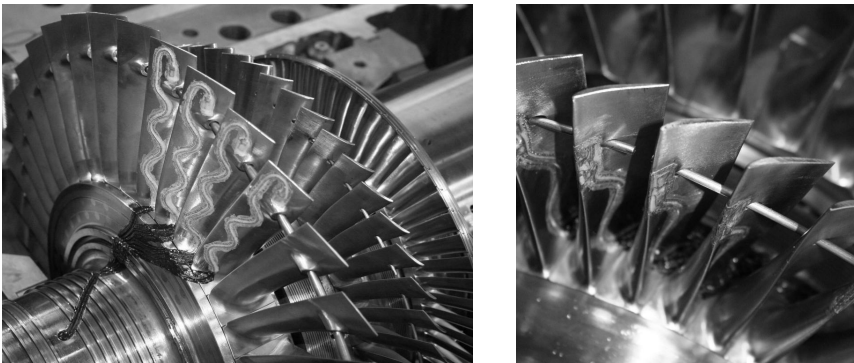


Figure 2.5 Strain gauges, applied to the last and penultimate rotor blade row, according to investigations of DROZDOWSKI ET AL. [27, 29]

2.3 Introduction to Experimental Investigations

Industrial steam turbines like the one investigated are normally operated between 60% and 100% nominal speed in a wide range of load conditions. One objective of the present study is the experimental aerodynamic evaluation of

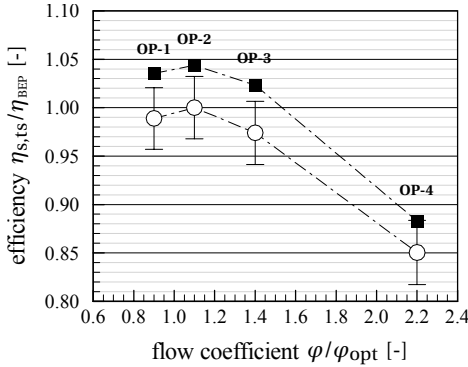


Figure 2.6 Normalized efficiency (2.3) of three-stage LP steam turbine (80% nominal speed) based on measurements ○ and 3D CFD (NES) ■ in moderate overload and OP-4 in extreme overload condition. Insight into the flow conditions at all four operating points is provided in Chap. 4 and Subsec. 5.7.2.⁴

the turbine running at 80% speed. Therefore, several operating points between part load and overload conditions along the corresponding speed-line were investigated in a measurement campaign with the industrial steam turbine test rig at ITSM. For the present thesis, experimental data and numerical results of four selected operating points at different load conditions are used to investigate the performance and flow field of the turbine. As indicated by Fig. 2.6 and Tab. 2.2, OP-1 is in slight part load, OP-2 is the best efficiency point (BEP), OP-3 is

In turbomachinery business, nondimensional parameters⁵ are commonly used for the sake of transferability of data, making different machines comparable. As it is common for operating test rigs of axial-flow turbines, often with down-scaled runners, the flow coefficient

$$\varphi = \frac{c_z}{u} = \frac{\dot{m}}{\rho_{32} A_{32} u_{32}} \quad (2.2)$$

⁴According to experimental investigations of HÄFELE [55], similar peak efficiencies $\eta_{s,ts}$ can be expected for 100% and 80% nominal speed, while for 60% a considerable drop occurs. Qualitatively, efficiency curves for 100% and 80% speed develop similar over the considered operating range, though for 80% the turbine performs slightly better towards overload.

⁵e.g. the head or pressure coefficient ψ , the flow coefficient φ , the work coefficient λ , the reaction ratio r_k (degree of reaction), to name a few, see VOGT AND CASEY [131].

as a similarity parameter⁶ in plane E32 (Fig. 2.2) is used as control variable defining the OP. Here, u_{32} is the blade velocity at the mean radius according to Eq. (5.31) and A_{32} the exhaust area in E32. Furthermore, the density ρ_{32} is needed. Since being a function of static pressure and specific enthalpy and thus not measurable inside the wet steam region, it is determined iteratively with the help of the continuity equation and a power balance between turbine inlet and plane E32. This method is commonly used at ITSM and is for example described in detail by VÖLKER [132]. Further control variables for operating the test turbine are the total temperature at the inlet, set to $T_{t,in} = 453.15$ K, as well as the condenser pressure, adjusted to $p_{con} = 0.1$ bar. Both are kept constant during the experiments, while the total pressure at the inlet $p_{t,in}$ is adjusted for each OP, in order to meet the power demand of the brake at constant rotational speed. Further details about the experiments, including a presentation of measurement data, are given in Sec. 2.4 and Chap. 4.

During testing, the performance of the turbine can be monitored online by means of the total isentropic efficiency

$$\eta_{s,ts} = \frac{P}{\dot{m} \Delta h_{s,ts}} = \frac{M\omega}{\dot{m}(h_{t,in} - h_{s,out})}, \quad (2.3)$$

including the diffuser domain in the balance. Here, M is the measured torque and ω the angular frequency (Subsec. 2.2.3). The mass flow rate \dot{m} is measured with the help of a standard orifice plate (Subsec. 2.2.4). Total enthalpy $h_{t,in} = f(p_{t,in}, T_{t,in})$ at the inlet and static enthalpy $h_{s,out} = f(p_{out}, s_{in})$, based on an isentropic expansion, are obtained from pressure and temperature measurements (Subsec. 2.2.1) and using the IAPWS-IF97 [134] standard. As already mentioned, the steam is superheated at all inlet conditions.

The definition of total efficiency $\eta_{s,ts}$ in Eq. (2.3), based on the generated torque, is applied in Fig. 2.6 for comparison of measurement data (including error bars) with 3D CFD results according to Subsec. 3.3.1, normalized to the experimental efficiency at BEP. Here, the calculation of measurement error of total efficiency $\eta_{s,ts}$ (approximately ± 2.6 percentage points at BEP) is based on the method of the least square error, as described e.g. in Refs. [55, 132]. The trend of the measured efficiency curve is predicted quite well by CFD. The overprediction of CFD efficiency sums up from several model-specific features, e.g. a steady-state simulation, using mixing planes as stage interfaces and neglecting most cavities and generally the sealings, see Sec. 3.3 for details.

⁶Note that the investigated test turbine is not a model but a 1:1 build of the last three stages of a multi-stage industrial steam turbine and keep in mind that the investigated blade design is also distributed in upscaled versions throughout the product portfolio of SIEMENS Steam Turbines SST-500, SST-600, and SST-800.

Table 2.2 Characteristic values of investigated operating points (OP) at 80% nominal speed, based on measurement data

	OP-1	OP-2 ^a	OP-3 ^a	OP-4
flow coefficient $\varphi/\varphi_{\text{opt}}$	0.90	1.10	1.40	2.20
mass flow rate $\dot{m}/\dot{m}_{\text{design}}$	0.70	0.89	1.16	1.82
pressure ratio $p_{t,\text{in}}/p_{\text{con}}$	7.22	9.14	12.08	18.93

^aExemplary blade profiles of last stage blading with flow velocity components, see Fig. 5.22.

Furthermore, any kind of asymmetry such as at the inlet or the outlet of the turbine cannot be modelled by a one-passage model. However, all these features contribute otherwise to lowering the efficiency, see HÄFELE ET AL. [54].

2.4 Evaluation of Measurement Data

2.4.1 Data Averaging

Generally, aero-thermodynamic quantities measured in the test rig are acquired as time-resolved raw data and further transformed into time-averaged values. Stagnation pressures and temperatures measured at the turbine inlet in the upper and lower casing at mid-span are arithmetically averaged, respectively. As mentioned above (Sec. 2.2), all stage wall pressures measured at hub and shroud are pneumatically averaged using ring tubes. For the comparison of averaged numerical and experimental data discussed in Sec. 4.2 (Tab. 4.1), 1D values in planes E10 and E20 (Fig. 3.5) are determined by linearizing⁷ the measured wall pressures between hub and shroud and area-averaging afterwards. In contrast, in planes E30 and E32 the calculation of mean static pressure, total pressure and flow angle values is done by area-averaging traversed probe data according to Figs. 4.8 to 4.11.

It should be noted that area-averaging of non-uniform flow is commonly used in the evaluation of turbomachinery measurement data, mainly for practical reasons, although it is only physically founded for static pressure averaging, see CUMPSTY AND HORLOCK [22]. However, the authors [22] state that often, the area average agrees surprisingly well with more rational averages, as long as the evaluation is not carried out in regions of separated flow blocking a significant portion of the flow channel while passing little mass

⁷3D CFD results show that the assumption of linear pressure distribution is valid in this case.

flow. Besides the fact that being the only practicable approach for the setup of the investigated three-stage turbine, considerations regarding the position of evaluation planes (Fig. 3.5) in combination with 3D CFD results allows to conclude that area-averaging of measurement data is appropriate here. It has to be considered that further discussion about averaging with the focus on CFD results can be found in Subsec. 3.4.1.

2.4.2 Purging Correction

The described issue of steam condensing inside pressure tubes and subsequent blocking from condensate results in the need for continuous purging and corresponding pressure correction in the evaluation procedure of the measurement data. Generally, the purging intensity can be adjusted with needle valves at the test rig, allowing controlled airflow into the machine. Due to the relatively large inner tube diameter ($\varnothing = 6$ mm) used for measuring the stage pressures, the resulting error is relatively small and it is legitimate to account for the pressure offset between *with* and *without* purging by a simple offset measurement at constant vacuum (machine standstill) and deduct Δp_{off} in the course of the data evaluation. However, another strategy is pursued for the pressure correction of the wall pressures along the diffuser contour (Subsec. 2.2.2) as well as the probe pressures (Subsec. 2.2.6), where pressure tubes with relatively small diameter ($\varnothing = 1.5$ mm) are used. For the offset measurement at machine standstill and constant condenser pressure $p_{\text{con,off}}$, the needle valves are adjusted to a pressure offset $\Delta p_{\text{off}} \approx 5$ mbar. According to HENEKA [44], the corrected absolute pressure can be calculated as⁸

$$p_{\text{abs}} = p_{\text{m}} + p_{\text{con,m}} - \Delta p_{\text{off}} \frac{p_{\text{con,off}}}{p_{\text{m}} + p_{\text{con,m}}} . \quad (2.4)$$

Here, p_{m} is the relevant measurement pressure and $p_{\text{con,m}}$ is the constant condenser pressure during the measurement.

2.4.3 Measurement Uncertainties

As already mentioned, the mass flow rate is measured with the help of a standard orifice plate and its measurement uncertainty is calculated to within $\pm 1\%$, according to ISO 5167-1:2003 [59]. In consequence of the high live steam

⁸HENEKA's [44] original approach, which additionally accounts for the difference in viscosity between offset and measurement scenario, is simplified by equating reference (offset) and measurement temperatures T_{off} and T_{m} . This simplification is commonly used in measuring practice and is valid, since pressure measurement in planes E30, E31, E32 and the diffuser (Fig. 2.2) takes place at generally moderate temperatures, resulting in negligibly small errors.

Table 2.3 Measurement uncertainties at mid-span, HÄFELE ET AL. [52]

Plane	Flow value	OP-1	OP-2	OP-3	OP-4
E30	total pressure p_t (%)	± 1.1	± 0.8	± 0.6	± 0.4
	static pressure p (%)	± 1.3	± 1.0	± 0.8	± 0.5
	flow angle α (°)	± 1.6	± 1.1	± 0.7	± 0.4
E32	total pressure p_t (%)	± 1.5	± 1.5	± 1.4	± 0.9
	static pressure p (%)	± 1.8	± 1.8	± 1.9	± 1.6
	flow angle α (°)	± 4.9	± 2.0	± 1.1	± 0.5

temperature of up to 350 °C, the thermal expansion of the orifice plate is accounted for in the measurement software. An estimation of the measurement uncertainties of all measured parameters is implemented in the evaluation procedure of the experimental data. Measurement uncertainties of probe measurements have been calculated using the GUM (guide to the expression of uncertainty in measurement) method according to DIN V ENV 13005 (ISO/IEC Guide 98-3:2008). Details about this method and the implementation into the probe evaluation software can be found in Ref. [34].

Measurement uncertainty quantities at mid-span are shown in Tab. 2.3. These magnitudes are representative for the uncertainty range of flow values captured by probe measurements at the corresponding evaluation plane and operating point, as the variation of uncertainty over the span is small. For plane E32, the mean values determined from the values at measurement locations at the upper and lower part of the turbine are shown.

2.4.4 Reproducibility

Data from test rig measurements were used to validate the numerical results predicted with the three-stage LP steam turbine CFD model, see Sec. 3.3 and Chap. 4. In order to claim reproducibility for these data, measurements have been repeated on independent measurement campaign days under the same operating conditions (Sec. 2.3) and a fairly good agreement can be reported. Fig. 2.7 exemplary shows the grade of reproducibility for radially traversed data at OP-3. Besides a generally good quantitative match, for the most part close to or within the uncertainty range (Tab. 2.3), Fig. 2.7 reveals a surprisingly well qualitative agreement regarding effects of complex flow structures measured in wet steam flow downstream of rotors with PSCs, see discussion on wakes and vortices in Chap. 4.

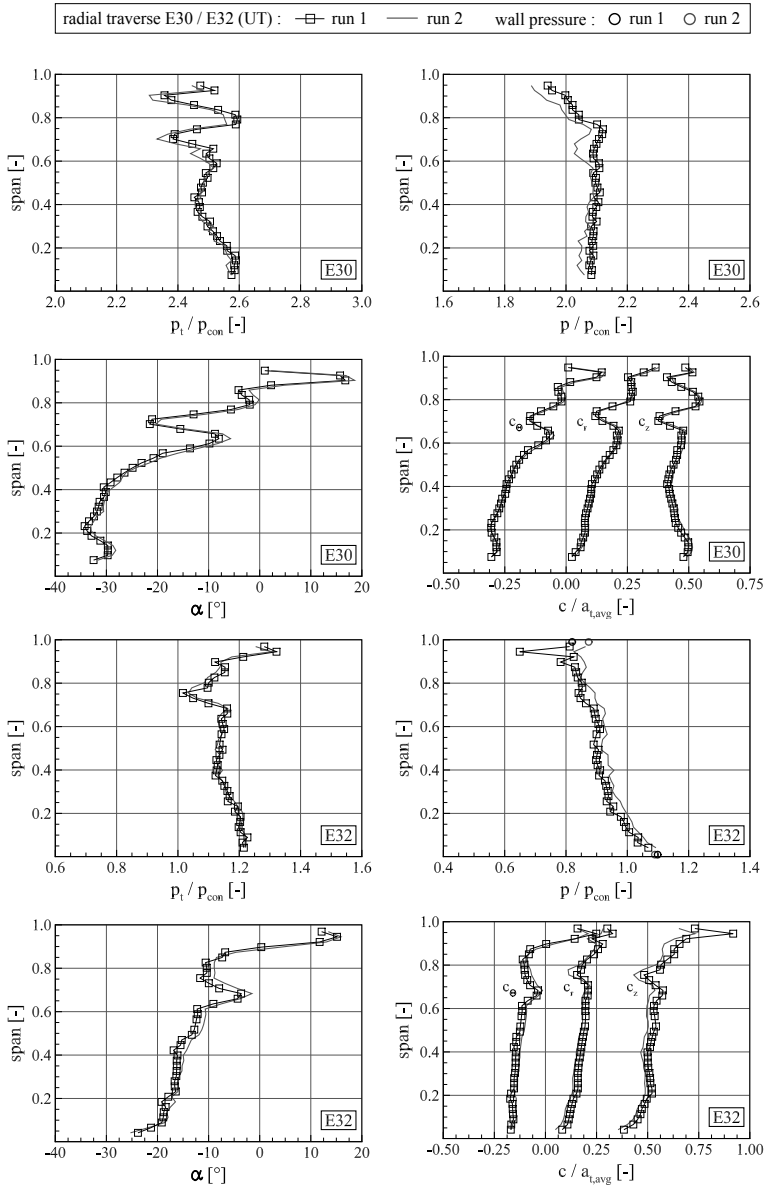


Figure 2.7 Reproducibility of measurement data in evaluation planes E30 and E32 (see Figs. 2.2 and 2.4) for operating point OP-3 (refer to Figs. 4.9, 4.11 and 4.14)

3 | Numerical Flow Simulation

For the present work, numerical methods were applied to gain deeper insights into the flow field inside the turbine and also to derive quantitative conclusions. These methods are mainly described within this chapter. First, a brief introduction to the relevant basics of computational fluid dynamics (CFD) is given. This is followed by a description of the developed and applied CFD models as well as details about the evaluation of CFD results. Their presentation and experimental validation is addressed in Chap. 4.

3.1 Introduction to Computational Fluid Dynamics (CFD)

The commercial solver ANSYS CFX 15.0 was employed for numerical flow simulation. The present section introduces relevant basics of CFD, whereby the flow solver and corresponding settings are addressed at appropriate positions.

3.1.1 Turbulent Flow Modelling

In thermal turbomachinery, compressible flow is being described by a system of nonlinear, partial differential equations, the so-called NAVIER-STOKES equations¹ (A.1). In their full forms they represent conservation laws of mass, momentum and energy in any considered spatial direction, see Sec. A.1 on Page 195. In contrast to the EULER equations², which govern adiabatic and inviscid flow, viscosity and thermal conductivity are regarded here. In principle, any flow phenomenon in continuum mechanics³ can be described by this set of equations [70]. Accordingly, laminar as well as turbulent flows can be characterized, both being of continuum mechanic nature. However, in many engineering applications the considered flow has mainly turbulent character. This is particularly true for thermal turbomachinery, where usually high flow

¹Named after French engineer and physicist Claude-Louis NAVIER (1785–1836) and Irish mathematician and physicist Sir George Gabriel STOKES (1819–1903).

²Named after Swiss mathematician, physicist, astronomer, logician and engineer Leonhard EULER (1707–1783). The EULER equations form the basis of gas dynamics, describing the relation between the fluid mechanical and thermodynamic state of a compressible fluid [70] and being a particular case of the compressible NAVIER-STOKES equations.

³The KNUDSEN number $Kn = \lambda_M/L$ (named after Danish physicist Martin KNUDSEN (1871–1949)), defined as the ratio of the molecular mean free path to a representative physical length scale, is used to set the boundary for continuum mechanic versus gas kinetic flows to the range of $Kn < 1 \times 10^{-2}$, LAURIEN AND OERTEL, JR. [70].

velocities are present, resulting in high REYNOLDS numbers⁴. This similarity parameter is defined as the ratio of *inertial* forces to *viscous* forces. Thus,

$$\text{Re} = \frac{\|\bar{c}\| L}{\nu}. \quad (3.1)$$

Here, \bar{c} is the absolute flow velocity vector, L is a representative physical length scale of the flow problem and ν is the kinematic viscosity of the fluid. Turbulent flow is generally characterized by the domination of inertial forces and accordingly high REYNOLDS numbers, whereby the *transition* from *laminar* to *turbulent* flow regime is defined by an individual critical REYNOLDS number. For pipe flows, $\text{Re}_{\text{crit}} \approx 2300$. Inherent characteristics of turbulent flows are irregular fluctuations superimposed onto the main flow, apparent as a formation of eddies of many different length and time scales, which come along with an increased presence of diffusion processes within the flow.

Thorough insights into turbulence modelling aspects for CFD are for example provided in a comprehensive work of WILCOX [135]. Limited to applications in turbulence scientific research, a Direct Numerical Simulation (DNS) generally aims at resolving the turbulent flow structures down to their smallest time and length scales (KOLMOGOROV microscales⁵, functions of solely dissipation rate ε and viscosity ν). This is applicable for relatively simple purpose like pipe flows with low REYNOLDS number, LAURIEN AND OERTEL, JR. [70]. However, since DNS requires the numerical model to be discretized appropriately fine in time and space, it is not feasible for industrial applications.

In engineering practice, a fairly simplified consideration for turbulent flow modelling is used instead. Since engineers are often only interested in averaged solutions, time-averaged quantities are calculated for defining a mean flow and turbulent fluctuations are considered as superimposing and affecting this time-averaged flow. This approach is based on the idea of REYNOLDS decomposition⁶. Together with subsequently time-averaging the NAVIER-STOKES equations (A.1), it results in the so-called REYNOLDS-averaged NAVIER-STOKES (RANS) equations which govern the mean flow. Time-averaging the nonlinear initial equations leads to additional mathematical terms in the RANS equations, which still contain turbulent fluctuations. These additional turbulent (REYNOLDS) stresses in the momentum equations and turbulent (REYNOLDS)

⁴Named after British engineer and physicist Osborne REYNOLDS (1842—1912), who discovered that transition from laminar to turbulent flow in a smooth pipe is depending on the fluid properties, namely the density ρ , the viscosity μ and the free stream velocity c_∞ as well as on the inner diameter of the pipe.

⁵Named after Soviet mathematician Andrey Nikolaevich KOLMOGOROV (1903—1987).

⁶For REYNOLDS decomposition, an instantaneous quantity ξ is decomposed into its time-averaged and fluctuating quantities $\bar{\xi}$ and ξ' , respectively: $\xi(x, y, z, t) = \bar{\xi}(x, y, z) + \xi'(x, y, z, t)$.

heat fluxes⁷ in the energy equation cause a need for supplementary expressions, which have to be modelled in order to close the system of equations. Hence, equations containing only mean flow values are obtained.

The closure problem described above resulted in the development of a variety of turbulence models over the years, which can be basically classified into REYNOLDS stress and eddy viscosity models. Here, the latter ones are less time-consuming and more appropriate for engineering applications, LAURIEN AND OERTEL, JR. [70]. For the present work, the Shear Stress Transport (SST) model of MENTER [81], implemented in ANSYS CFX 15.0, has been adopted. It combines the advantages of the $k-\varepsilon$ [80] and $k-\omega$ [79] models, both of the two-equation model type, which are able to consider turbulent length as well as time scales. Here, transport equations for the turbulent kinetic energy k , the dissipation rate ε and the turbulent frequency ω are solved. These transport equations consider production, convection, diffusion and dissipation of turbulence. A blending function, modelled in dependence of local flow quantities, controls the application of each of the two models within the SST approach, whereby the $k-\varepsilon$ model is established for the core flow and the $k-\omega$ model for the flow in close vicinity to the walls (boundary layer).

3.1.2 Flow Discretization

In the absence of general analytical solutions for the NAVIER-STOKES or RANS equations, they are commonly treated using numerical discretization methods⁸. Discretization means transferring the continuous equations to discontinuous ones, which enables a numerical solution of the flow problem. Here, the partial derivation equations are transferred to finite differences, which are solved for discrete points on a user defined mesh⁹ or grid representing the fluid domain. Generally, the mesh quality has to be appropriate for the considered flow and type of investigation and several preconditions have to be respected, described for example in best practice guidelines for CFD, as it is done by CASEY AND WINTERGERSTE [18]. Applying a discretization scheme leads to a linear system of equations.

Structured high-resolution hexahedral meshes were set up for the discretization of the flow domains of the LP steam turbine investigated in the present work, see Fig. 3.3. A conventional one-passage model approach was

⁷If heat transfer is important, the initial time-dependent energy equation is time-averaged as well, CASEY AND WINTERGERSTE [18].

⁸Three basic methods are available, whereby in the following list, flexibility decreases while accuracy rises: Finite Element Method (FEM), Finite Volume Method (FVM), Finite Difference Method (FDM). In ANSYS CFX 15.0, an element-based FVM is used, see Ref. [6].

⁹Here, the terms *mesh* and *grid* are both used without distinction.

chosen, as it is suitable for an industrial design process and appropriate to investigate the impact of PSCs with engineering accuracy, see Sec. 3.3. ANSYS Turbogrid 15.0 with automated topology and meshing (ATM) option was used for grid generation of stator and rotor domains without PSC. ANSYS ICEM CFD 15.0 was used to generate the grid of blade passages with PSC and the axisymmetric section of the diffuser. The basic meshes were applied in several student theses [3, 14, 23, 38, 86] proposed and supervised by the author of the present work and have been adopted for the investigations within this PhD thesis. Here, H-Grids¹⁰ are used for the core flow and O-Grids for the boundary layer regions around blades and PSC profiles (see Fig. 3.1), enabling a high and reproduceable mesh quality and resolution. By using hexahedral grids, the quality and resolution of the boundary layer grid can be well controlled. In contrast, within a tetrahedral meshing methodology the boundary layer is normally discretized with prismatic layers and it is more tricky to get a high quality boundary layer grid on complex geometry parts (compare to MISTRY ET AL. [82]). For meshing, common quality requirements according to Ref. [18] were considered. Figure 3.2 shows a model of rotor R3 and the surface mesh. Generally, aerodynamic blade profiles with airfoil pre-twist were used to built up the flow passage models of rotors with PSC, whereby the geometry of the PSCs has been incorporated into the CAD model. Structured meshing of complex geometry parts like these LP blades with PSC is generally

¹⁰DENTON [24] points out that complicated blade features like e.g. part-span shrouds can be easily accommodated by the H-Grid type. In this context it is however surprising that not many published documents can be found dealing with CFD investigations where the PSCs in the flow channel are included, and it seems that still nowadays, industrial 3D blade design processes predominantly do not consider these elements, compare to the literature review in Subsec. 1.4.4.

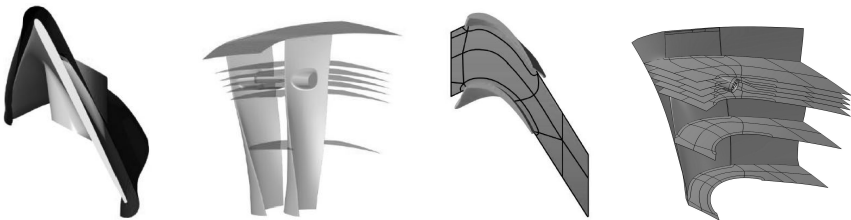


Figure 3.1 Geometry preparation in CAD for hexahedral grid generation of rotor R3 with PSC [53]. Left to right: Offset surface around blade and reinforcement (O-Grid); supplementary radial surfaces in blade channel; master topology on radial surface; radial surfaces with master topology and offset surface around friction bolt (O-Grid)

challenging and very time consuming. A detailed tutorial about the hexahedral grid generation for LP blades with PSC is provided by HÄFELE ET AL. [53].

In order to numerically resolve the boundary layer flow instead of using wall functions¹¹, a sufficient number of nodes is necessary within the boundary layer mesh, see Ref. [6] for further details. As indication for judging the appropriate minimum distance of nodes adjacent to the walls, the dimensionless wall distance

$$y^+ = \frac{c_\tau y}{\nu} \quad (3.2)$$

is commonly used. Here, y is the distance of the wall nearest node normal to the wall and c_τ is the wall friction velocity, defined with the wall shear stress τ_W as

$$c_\tau = \sqrt{\frac{\tau_W}{\rho}}. \quad (3.3)$$

For Low-REYNOLDS models, the y^+ -values should be appropriately small for a proper resolution of the viscous sublayer of the boundary layer. CASEY AND WINTERGERSTE [18] propose values less than four and preferably close to unity for this purpose. y^+ -values as well as boundary layer thickness δ can be only checked in the post-processing, after performing the CFD simulation.

In order to figure out the sufficient grid resolutions for accurate numerical results, several grid independency studies have been accomplished, comparing the impact of grid fineness on results of relevant flow and performance

¹¹According to CASEY AND WINTERGERSTE [18], this is most common in industrial practice.

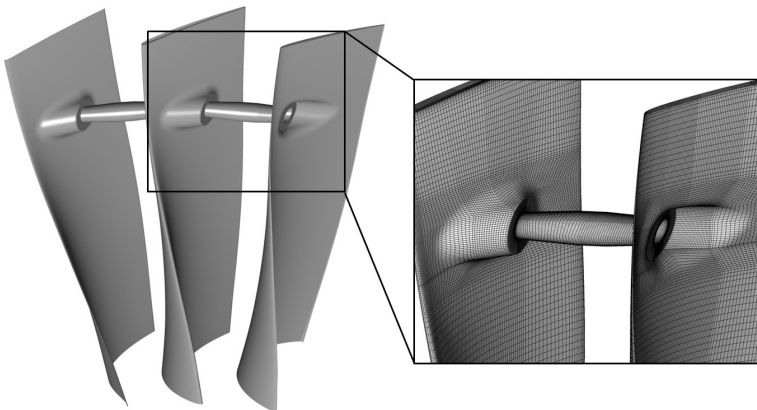


Figure 3.2 Surface mesh on rotor R3 with PSC, HÄFELE ET AL. [50, 52]

values. Based on these studies, accomplished with a three- and two one-stage CFD models presented in Subsecs. 3.3.1 and 3.3.2, relatively fine grids with approximately eight respectively two million hexahedral elements and area-averaged y^+ -values of approximately two were used for the final CFD simulations. In Sec. A.2, findings from these studies are exemplary shown.

3.2 Wet Steam Effects in LP Steam Turbines and Modelling with ANSYS CFX

The expansion characteristic of the flow in multi-stage LP steam turbines like the investigated one is particularly characterized by the final expansion point laying within the so-called wet steam region, a coexistence of water in its liquid and vaporous state. The final wetness¹² fraction y is thereby depending on the operating condition of the turbine and this is also the case for the count of LP stages operating in dry or wet steam. As schematically illustrated in Fig. 3.4, the expansion into the wet steam region causes a fall below the saturation line ($x = 1$), which is a fictive process and solely used to demonstrate the condensation of steam in the state diagram of water (MOLLIER-diagram). It re-

¹²The terms *liquid mass fraction* or *wetness fraction* y as well as *vapor mass fraction* or *dryness fraction* x are equally used within this work, respectively, whereby $x + y = 1$.

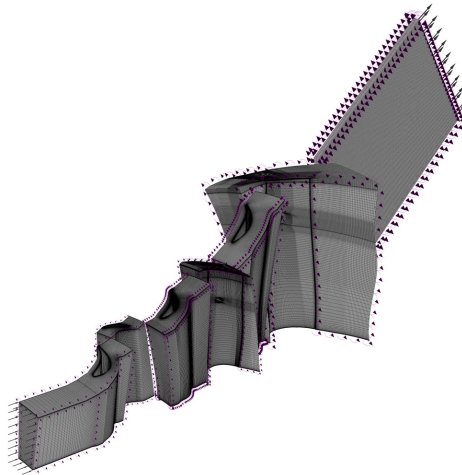


Figure 3.3 Structured, hexahedral meshes for discretization of one-passage CFD model of LP industrial steam turbine with PSCs (no. of elements $\approx 8 \times 10^6$ and $y^+ \approx 2$)

sults in immediate starting of condensation and thus droplet formation, when assuming the steam flow being in thermodynamic equilibrium during the expansion process. In ANSYS CFX 15.0, this idealized equilibrium expansion is accounted for by an equilibrium steam (EQS) model. This model describes the real gas behavior of superheated as well as saturated equilibrium steam and is based on the IAPWS-IF97 [134] standard, which is referred to in table form during the solver run. For this equilibrium condensation, the vapor mass fraction x can be directly taken from the MOLLIER h, s -diagram (Fig. A.2).

LP stages operating in wet steam are generally subjected to additional energy dissipation resulting from the condensation process and the droplets being present within the flow domain. Historically, this efficiency drop was accounted for by the well-known empirical correlation named BAUMANN rule¹³, which is nowadays still used for a rough estimation of wetness loss quantity. Based on experiments with steam turbines carried out in the early 1920s, BAUMANN [8] originally proposed the dry isentropic efficiency of a turbine stage to be reduced by one percentage point for each one percentage of mean wetness fraction, whereby this BAUMANN factor of unity ($\alpha_B = 1$) developed over the years and was later identified to be in the range of 0.4 – 2.5, based on further turbine testing (see e.g. LEYZEROVICH [73] or PETR AND KOLOVRATNIK [89]). Since then, a lot of struggle has been undertaken in engineering science for a better understanding of the loss formation and composition related to wetness in LP stages. The first physically consistent approach for the 1D evaluation of wetness loss was introduced in GYARMATHY's [42] theory for wet steam turbines in the early 1960s, followed by others and more recently resulting in the development of 2D and 3D methods¹⁴. According to GYARMATHY [42], wetness loss can be split into three main contributors, namely *thermodynamic loss* (due to irreversible heat transfer between liquid and gaseous phase), *kinematic relaxation loss* (due to frictional effects between droplets and steam) and *breaking loss* (due to the impact of coarse water droplets on the rotor blades), whereby large droplets can also lead to severe erosion damage at the rotor blades' leading edges, see AHMAD [4].

Because it is relatively simple to apply and resource-friendly, the conventional EQS approach is still quite common in the technical steam turbine community nowadays. However, since a two-phase mixture is considered and no separate conservation equations are solved for each phase, a calculation of wetness loss is not possible with this numerical scheme.

¹³ $\eta_{\text{wet}} = \eta_{\text{dry}}(1 - \alpha_B y_{\text{mean}})$, where y_{mean} is an average steam wetness and α_B is an empirical coefficient named BAUMANN factor.

¹⁴A comprehensive overview about the development of these models and the state-of-the-art can be found in the PhD thesis of STARZMANN [112]

For real steam turbine flow, the fall below the saturation line leads to a temporary thermodynamic non-equilibrium, characterized by supersaturation S or subcooling ΔT , which are defined as

$$S = \frac{p}{p_s(T_g)} \quad \text{and} \quad \Delta T = T_s(p) - T_g. \quad (3.4)$$

Here, $p_s(T_g)$ is the saturation pressure at the temperature of the gaseous phase and $T_s(p)$ is the saturation temperature at the pressure¹⁵, see Fig. 3.4. This non-equilibrium state results in a delayed onset of condensation and is due to the fact that in steam turbines, high expansion rates

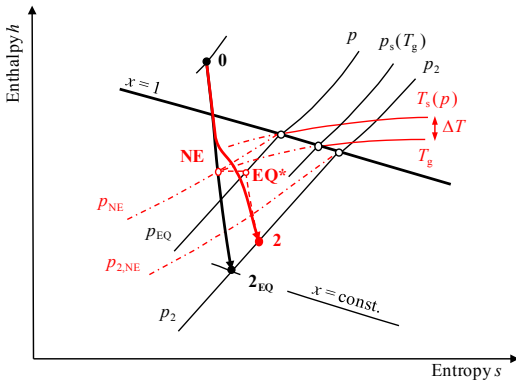


Figure 3.4 Equilibrium (0-2_{EQ}) and non-equilibrium (0-2) expansion process, according to STARZMANN [112] and based on TRAUPEL [123]

In steam turbines, homogeneous (spontaneous) nucleation is the main contributor, triggered by random collisions of water molecules within the steam flow path. In contrast, heterogeneous nucleation, triggered by flow past particles¹⁷ or the flow path's endwalls¹⁸ (film condensation), is of minor

¹⁵In wet steam modelling it is common to assume that the gaseous and the liquid phase share the same pressure field.

¹⁶In the following, solely the term *subcooling* is used to express the level of thermodynamic non-equilibrium. Accordingly, the term *supersaturation* is not further applied.

¹⁷Depending on the steam purity, heterogeneous condensation might play a minor role, see STARZMANN [112]. Similar to the model steam turbine considered in Ref. [112], a high steam purity can be assumed for the investigated industrial steam turbine, since live steam is supplied by the combined heat and power plant (HKW) of the University of Stuttgart, which is tied to certain regulations considering steam purity [112]. Furthermore, the fact that high expansion rates are present throughout the relatively small-scale turbine encourages the assumption of mainly homogeneous nucleation, see also remarks in Ftn. 21 on Page 61.

¹⁸According to GYARMATHY [42], in reality endwalls or blade surfaces are not cooled down enough to discharge the latent heat that is being released during heterogeneous condensation.

$$\dot{p} = -\frac{1}{p} \frac{dp}{dt} \quad (3.5)$$

are present, meaning comparatively fast relative pressure change per time. With progressing expansion of non-equilibrium steam (NES), ΔT is further increased until a sufficient subcooling¹⁶ level for the formation of stable nuclei and a corresponding transition to thermodynamic equilibrium is reached.

relevance for turbomachinery flow, GYARMATHY [42]. Condensate is being deposited at stable nuclei and accordingly, latent heat is released, allowing the subcooling level to collapse. Subsequently, no further droplet formation is usually taking place and wetness is increased solely by droplet growth.

The NES model of GERBER [39], implemented in ANSYS CFX 15.0 and used for this investigation, accounts for these wet steam effects. This EULER-EULER¹⁹ model is able to consider the non-equilibrium process of droplet formation and droplet growth. Here, the classical homogeneous nucleation model, see BAKHTAR ET AL. [7], and the droplet growth model according to YOUNG [138] are used. Details of the condensation model are given in the appendix A.3. The NES model has been used in several investigations at ITSM and a lot of expertise has been built up, see GRÜBEL ET AL. [41]. While generally being a mono-disperse model, it allows several different liquid phases to be defined for different domains. This enables the consideration of different droplet diameters²⁰ and might be useful in cases where solely calculating a mean droplet diameter does not lead to a sufficient representation of the droplet spectrum²¹. For this work, however, only one liquid phase was used in addition to one gaseous phase throughout all domains. This is mainly done to reduce computational effort and is accepted because the droplet growth and the origin of droplet groups were not of interest in this investigation. The real gas handling is based on IAPWS-IF97 [134], which includes the extrapolation into the metastable steam region, as it is indicated in Fig. 3.4.

It has been already mentioned that the NES approach used for this investigation is able to consider the non-equilibrium process of droplet formation and droplet growth. The RANS equations are supplemented by these additional wet steam models. It is common that the gaseous and the liquid phase share the same pressure field and for the small fog droplets it is also allowed

¹⁹The EULER-EULER approach considers the conservation equations of both liquid as well as gaseous phase in a stationary system of reference and is commonly used in the calculation of wet steam flow in steam turbines, see STARZMANN [112]. The EULER-LAGRANGE framework is another method common for multiphase flow simulation. Here, the gaseous phase is defined as carrier phase and the gas flow is discretized in a stationary system of reference. In contrast, the dispersed (liquid) phase is solved within a system moving with the carrier phase.

²⁰The droplet size is determined by the volume fraction of the liquid phase and the droplet number and thus is uniform for each liquid phase.

²¹The droplet spectrum present in model steam turbines is for example discussed in the work of STARZMANN [112], based on numerical simulations and a comparison to wetness measurement data. The author [112] states that in down-scaled steam turbines, higher (according to the scale factor) expansion rates are present, resulting more likely in a mono-disperse droplet spectrum, compared to the steam turbines' full-scale versions. It is therefore appropriate to assume a similar behavior for the investigated industrial steam turbine, when considering the size and operating conditions in relation to the turbine described in Ref. [112].

to assume that there is no slip between the phases, see Ref. [42]. The enthalpy h_m and entropy s_m of the mixture can be calculated as follows.

$$h_m = (1 - y) h_g + y h_l \quad \text{and} \quad s_m = (1 - y) s_g + y s_l \quad (3.6)$$

The heat and mass transfer between the phases strongly depends on the temperature of the gaseous phase and the surface temperature of the droplets. For the gaseous phase an own equation for energy conservation is solved. However, in order to reduce the computational effort an algebraic equation according to Gyarmathy [42] is used to determine the temperature of the liquid phase. This means that no conservation equation for the energy of the liquid phase is solved and the enthalpy (and also entropy) is calculated from GYARMATHY's droplet temperature.

In ANSYS CFX 15.0, the described NES model is the closest, feasible approach available to model condensing steam flow in LP steam turbines.²² In contrast to the EQS approach, it is generally able to take into account wetness losses²³. A comprehensive overview about wetness loss prediction for LP steam turbines using CFD was recently given by STARZMANN ET AL. [114]. Besides a more physical representation of the expansion characteristic and flow field in the turbine – with respect to the EQS modeling approach, see STARZMANN [112] – it holds the advantage of being able to model wet steam effects induced by the PSCs, as discussed in Sec. 5.5. Furthermore, boundary conditions (BC) for the parameter study based on one-stage CFD calculations (see Subsec. 3.3.2) can be directly extracted from the three-stage CFD results, which have been validated against experimental data, see Chap. 4. This leads to the consideration of more realistic OPs for the one-stage calculations than three-stage EQS results would give, as discussed in Subsec. 3.3.2. These advantages are accompanied by the disadvantage that for NES a simple calculation of the mixed-out state is not possible so far. Therefore, no mixed-out quantities are calculated but instead conventional averaging methods are used. This topic is discussed in more detail in Sec. 3.4.

²²Fundamental findings about EQS versus NES modelling are provided in the research works of SIGG [108] or STARZMANN [112], for example. A comparison between these models goes beyond the scope of the present thesis and is therefore not accomplished here.

²³Among the three main contributors to wetness loss according to GYARMATHY [42], the present numerical scheme only considers thermodynamic loss. Investigations with a similar LP steam turbine like the present one showed that it accounts for over 90% of the total wetness loss, see STARZMANN ET AL. [114]

3.3 LP Steam Turbine CFD Models with PSCs

In steam turbine facilities like the one investigated at ITSM (see Figs. 2.1 and 2.2), where the condenser is mounted below the turbine, both diffuser and exhaust hood have a significant impact on the overall turbine performance and strongly interact with the LSB. This is why a lot of effort is normally put into optimizing these components with respect to increasing the amount of recovered kinetic energy. BURTON ET AL. [16] give a general, comprehensive overview about LP steam turbine exhaust hood and diffuser studies. Besides the aerodynamic optimization, one difficulty can be seen in a proper CFD prediction of the resulting turbine performance and flow field. With increasing computational power over the last decades, one trend in CFD modelling has been towards using highly sophisticated 360 degree models of LSB/diffuser and performing transient coupled calculations, normally including the geometry of the exhaust hood. While being the most accurate, this method is also the most expensive one and often not feasible for industrial applications and the design process. More simplified coupling approaches have been developed recently, focusing on reducing the computational effort without compromising the accuracy, see e.g. Refs. [15, 115]. While being simplified, these methods still require relatively high computational power and are not appropriate for the scope of the present investigation, as discussed below.²⁴

Despite the fact that most accurate CFD results are only obtained with the LSB/diffuser/exhaust hood coupled to each other and hence allowing flow interaction, a different approach is pursued here. In general, conventional one-passage CFD models with mixing planes²⁵ between rotating and stationary domains are considered for the steady-state CFD calculations, as commonly used in industrial 3D blade design processes. This simplified consideration results from one of the objectives of this thesis, which is to provide a validated, affordable modelling approach sufficient for engineering practice but still well able to predict the wet steam flow in coupled LP steam turbine blading.²⁶ In this way, a first comprehensive investigation on thermodynamic and fluid

²⁴BEEVERS ET AL. [9] and STEIN ET AL. [115] included PSCs in their 360 degree models, using ideal gas as working fluid, but none of the works provides insights into PSC modelling aspects. Furthermore, the impact of PSCs on aero-thermodynamics or related losses is not discussed.

²⁵The mixing plane method was first introduced by DENTON AND SINGH [26] and has become the industry standard treatment for rotor-stator interfaces in steady-state CFD simulations. The method considers circumferentially averaging of flow properties at the interface plane between rotating and stationary blade rows, while suppressing any transient rotor-stator interaction (RSI).

²⁶HÄFELE ET AL. [54] showed an analysis of the flow in LSB with PSC applying an NES approach and the publication of HÄFELE ET AL. [52] concentrates on validating such a CFD model with experimental data.

dynamic effects of PSCs in LP steam turbines can be conducted. Transient flow effects, however, are not captured by such a modelling approach as this would require a lot more computational power. This in turn is in contradiction to the development and validation of an engineering tool within this dissertation. Accordingly, aspects of unsteadiness, as discussed e.g. by BOSDAS ET AL. [12] on an experimental base for the wet steam flow downstream of rotors with PSCs (see Subsec. 1.4.3, Pages 25–27), are not in focus of this work.

3.3.1 Three-Stage Model

According to the statements made above, a conventional one-passage CFD model is used to simulate the flow in a three-stage steam turbine configuration shown in Fig. 2.2. The model is divided into seven domains, see Fig. 3.5, whereby stage interfaces²⁷ between rotating and stationary domains are used. The no-slip condition is set for all solid boundaries. Considering the cyclic symmetrical blade passages, a rotational periodicity interface model with 1:1 mesh connectivity is applied for each of the seven domains.

As can be seen in Fig. 3.5, the radial gaps between the rotor tip and the casing of rotor R3 and rotor R2, including the backward facing step²⁸, are considered in the numerical model. However, a comparison between Figs. 2.2 and 3.5 shows some simplifications that apply and which are relevant for

²⁷In ANSYS CFX 15.0, a mixing plane interface is called *stage interface*.

²⁸Investigations of SIGG ET AL. [107] showed that this is essential for predicting the radial pressure gradient behind a rotor with backward facing step.

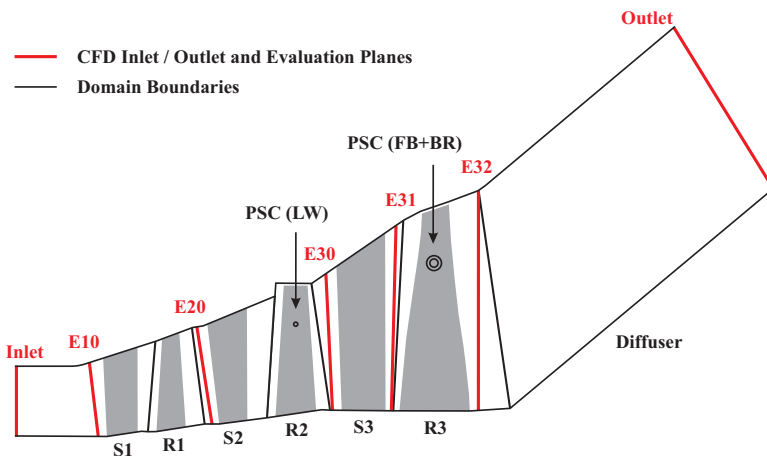


Figure 3.5 Sketch of the three-stage LP steam turbine CFD model, HÄFELE ET AL. [52]

further interpretation of the flow field: The radial clearances between the hub of stators S3, S2, S1 and the rotor as well as the shroud of R1 and the casing are equipped with gap sealings and are not included in the model, as well as the cavities in these regions. In addition, the cavities in the hub region between S3 and R3 as well as between R3 and the inner diffuser ring are not modelled. Furthermore, the small step at the casing behind rotor R3, near the wall pressure measurement location (see Fig. 2.2), is not considered.

The steady-state boundary conditions for the three-stage CFD calculations are derived from experimental data acquired with the three-stage LP steam turbine configuration according to Fig. 2.2, whereby subsonic flow conditions predominate at the inlet and outlet of the turbine for all investigated OPs. At the CFD outlet, a linear distributed static pressure between hub and shroud is used, based on circumferentially averaged wall pressure measurement data (see Sec. 2.2). At the CFD inlet, constant total pressure and total temperature profiles between hub and shroud are applied, based on circumferentially averaged measurement data from probes located at 50% span. As already mentioned, the steam is superheated at all inlet conditions ($x = 1$). Due to the flow straightener installed in front of the three-stage configuration (see Fig. 2.1) the flow is considered to be without swirl at the CFD inlet ($c_r = c_\theta = 0$). The rotational speed is set to 80% nominal speed of the turbine.

With the setup described above, steady-state 3D CFD calculations were performed with the commercial solver ANSYS CFX 15.0 for four OPs introduced in Sec. 2.3 (see Fig. 2.6 and Tab. 2.2). For all simulations, physical timescales in the range of 1×10^{-5} to 1×10^{-6} have been chosen.²⁹ All calculations achieved sufficient convergence with RMS residuals less than 1×10^{-5} for momentum and mass. It should be noted that the total pressure at the inlet of the three-stage configuration had to be slightly (+1%) adjusted for the CFD calculations of OP-1 and OP-2, in order to meet the measured mass flow rate with the calculated one. Here, the mass flow rate was used as indicator because it is measured very accurately (uncertainty range of $\pm 1\%$). This behavior can be explained by the present asymmetries at the inlet and outlet of the turbine, which cannot be modelled by the introduced one-passage model.

3.3.2 One-Stage Models

In order to study aerodynamic optimization issues of PSCs in the last stage of the investigated turbine and the losses induced by these elements, two different one-stage CFD models (sketched in Fig. 3.6) with parameterized

²⁹In contrast to a transient simulation, the timescale chosen here does not have any physical meaning for the flow itself but is only relevant for convergence issues.

PSC geometry have been applied. CFD model *PSC-1* basically corresponds to the setup of last stage and diffuser used in the three-stage model (compare to Fig. 3.5), whereby in contrast, the inlet domain boundary of S3 is shifted downstream to evaluation plane E30. The same applies for CFD model *PSC-2*, whereas in contrast to *PSC-1*, rotor R3 and diffuser share the same domain.³⁰ While *PSC-1* enables a PSC variation based on a real geometry of coupled SIEMENS steam turbine blading, *PSC-2* represents a virtual case with the same airfoil geometry but different kind of PSC, namely a simple lacing wire which allows a more fundamental study of the flow-impact of PSCs compared to the complex PSC geometry used in *PSC-1*. The basic models were applied in the student theses of BRÜGGEMANN [14] and NIEDERER [86], proposed and supervised by the author, and have been adopted. For these studies [14, 86] the underlying material was part of the work elaborated in the present thesis. Regarding the choice of modelling the real blade channel geometry, it should be recalled that most CFD studies on the influence of PSC parameters found in literature (see Subsec. 1.4.4) do only consider a span-wise segment of the real blading or a linear cascade, which is however compromising on accuracy, due to the fact that not all effects of the PSC can be covered.

³⁰This has general advantages and enables for example a more reasonable study of the diffuser flow, since no numerical interface mixing occurs between rotor with PSC and diffuser. This feature was added in the course of the development process of the one-stage CFD model and is, however, not included in the first version of the parameterized model (*PSC-1*).

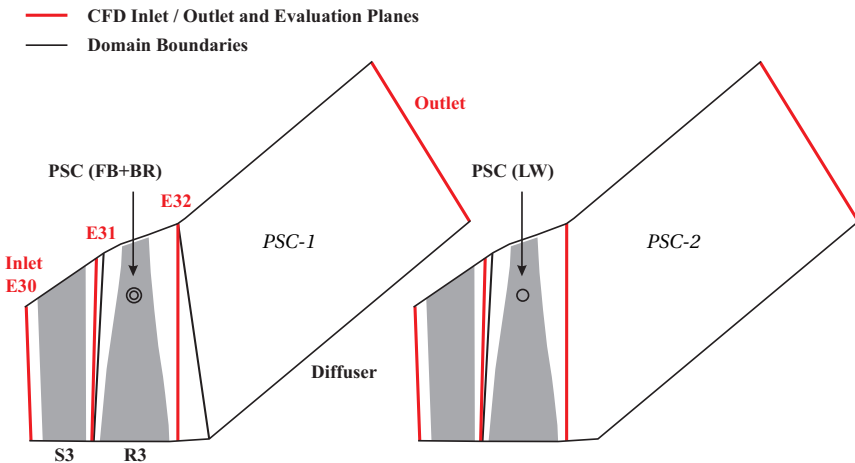


Figure 3.6 Sketch of one-stage LP steam turbine CFD models with parameterized PSC geometries (left: CFD model *PSC-1* with friction bolt (FB) and blade reinforcements (BR) according to HÄFELE ET AL. [50]; right: CFD model *PSC-2* with lacing wire (LW))

In order to perform a study on the aerodynamic effects of geometrical variations of PSCs using hexahedral meshes, the CAD model and meshing procedure which have been formerly used (introduced in Subsec. 3.1.2 and more detailed described in Ref. [53]), need to be adjusted. Because of the time-consuming grid generation, it is inconvenient to build a new mesh for every single PSC configuration. This means, the method of choice is using one existing mesh and updating the linked associations of the blocking structure with the new geometric information. To ensure this automatic update of the blocking to be successful, it is necessary to keep all geometric variations within a certain range. Due to general limitations in ANSYS ICEM CFD 15.0, it is essential that no additional points and curves are created in CAD when adjusting the PSC parameters. The generation of the blade passage with free-standing airfoils and endwalls as well as the parameterized modelling of the PSCs have been realized using the CAD system Solid Edge ST6. More details about the parameterization methodology is provided in Refs. [14, 86].

In Fig. B.1, a sketch of the LP blade (rotor R3) of CFD models *PSC-1* and *PSC-2* is depicted, including all relevant PSC parameters. The blade reinforcements, including fillets between blade and PSC, are generated as solid bodies in CAD. Their cross section profiles are modelled as B-splines and controlled via the corresponding control points and the two diameters d_{BR} and d_{BR}^* of the main axes. The fillet radius R_{PSC} as well as the axial and radial positions Z_{PSC} and D_{PSC} are also parameterized and can be adjusted. The friction bolt has a cylindrical mid-section and – due to mechanical reasons – conical sections on both sides. To gain additional flexibility regarding the realization of various friction bolt (*PSC-1*) and lacing wire (*PSC-2*) profiles, they are not modelled as solid but as surface bodies. Table curves are used to define the cross section profiles and the paths for extrusion. For this study, circular, elliptical and teardrop-shaped cross section profiles have been used, see Tabs. B.1 to B.4, defined by the parameters d_{FB} and d_{FB}^* respectively d_{LW} and d_{LW}^* .

The geometrical PSC parameters and chosen PSC configurations are described in Sec. 5.7.³¹ It should be noted that the blade geometry of the model is fixed and has not been varied for the parameter study. This means, only the influence of the PSC variation is considered. Tabs. B.1 to B.4 show the cross sections and parameters used for this study. These shapes and values were chosen due to aerodynamic aspects and do not consider any mechanical

³¹In a master thesis proposed and supervised by the author of this PhD thesis, TRAXINGER [125] investigates the loss due to PSCs in LP steam turbine blading. The focus of the study is on the derivation of a mixed-out approach for equilibrium steam flow. TRAXINGER [125] considered five of the same PSC configurations (V1.1, V1.4, V1.5, V1.8 and V1.9 in Tab. B.1) by applying CFD model *PSC-1* (Fig. 3.6, left) and performing EQS simulations for an OP similar to OP-3 (see Tab. 5.4), whereby the underlying material was part of the work elaborated in the present thesis.

constraints. With CFD model *PSC-1*, eleven PSC configurations (V1.1–V1.11) are investigated. Furthermore, CFD model *PSC-2* allows to study the complex flow phenomena and loss induced by PSCs by means of a simplified PSC geometry and additionally provides a wider range of possible PSC positions and geometries to be investigated. Thus, 31 additional PSC configurations (V2.1–V2.31) are considered with the help of *PSC-2*. In addition, a one-stage domain assembly with rotor R3 without PSC (V0) is used for comparison.

The steady-state BCs for the one-stage CFD calculations are adopted from the investigations with the three-stage model introduced in Subsec. 3.3.1. The same conditions are used regarding the CFD outlet and rotational speed. The BCs applied at the CFD inlet (E30) are extracted from the three-stage calculations with PSCs³², more precisely, circumferentially averaged radial profiles of total pressure p_t , total temperature T_t , absolute flow direction (c_r , c_θ , c_z) as well as turbulent kinetic energy k and turbulent eddy dissipation ε . Since NES simulations are performed, the volume fractions of both liquid and gaseous phases as well as the droplet number have to be evaluated from the three-stage simulations and specified in the form of radial profiles as well.³³ However, it has to be noted that virtually no wetness³⁴ is present in plane E30 for the investigated OP-2 and OP-3. As it is the case for the three-stage model, all inlet and outlet conditions are in the subsonic flow regime.

For the present work, only steady-state solutions of the flow field are regarded. For all numerical flow simulations performed, physical timescales in the range of 1×10^{-5} to 1×10^{-6} have been chosen. With the numerical setups and PSC configurations described above, steady-state 3D CFD calculations were performed with the commercial solver ANSYS CFX 15.0 for operating points OP-2 and OP-3 (Tabs. 2.2, 5.4 and Figs. 2.6, 5.22). These representative OPs were chosen because they cover a wide operating range of the turbine from BEP up to moderate overload condition³⁵ and allow to study the loss due PSCs not only geometry-dependent but also dependent on the flow conditions in the last turbine stage. All calculations achieved sufficient convergence with RMS residuals less than 1×10^{-5} for momentum and mass.

³²SHIBUKAWA ET AL. [105] e.g. state that their boundary conditions were taken from preliminary stage analyses without the PSC, which might result in inaccuracies due to the fact that the presence of the PSC can lead to a change of rotor inflow conditions, HÄFELE ET AL. [54].

³³All properties are extracted from the gaseous phase, except liquid volume fraction and droplet number, which are derived from the liquid phase.

³⁴The area-averaged wetness fraction is approximately 0.3% for OP-2 and 0.9% for OP-3.

³⁵The OP investigated by HÄFELE ET AL. [50] differs from the ones considered here and is located between OP-2 and OP-3 in terms of flow coefficient, mass flow rate and pressure ratio ($\varphi/\varphi_{\text{opt}} = 1.25$, $\dot{m}/\dot{m}_{\text{design}} = 1$, $p_{t,\text{in}}/p_{\text{con}} = 10.6$, compare Tabs. 2.2 and 5.4) at the same rotational speed. In order to obtain dry steam conditions in plane E30 during the measurements, $T_{t,\text{in}}$ has been increased by 20 K, which leads to a condensation onset downstream of E30, see Subsec. 5.7.2.

3.4 Evaluation of CFD Results

3.4.1 Data Averaging

To utilize steady-state 3D CFD results for comparison with experimental data and the outcome of loss correlations, the non-uniform flow field in the turbine has to be represented by one-dimensional values which can be gained by averaging. Different averaging approaches are shown in the literature, see e.g. GREITZER ET AL. [40] or CUMPSTY AND HORLOCK [22]. Each of them will conserve different information and properties of the flow field and can lead to various faults and misinterpretations. This results from the well-known fact that a non-uniform flow cannot completely be represented and matched by any derived uniform flow. In other words, "no uniform flow exists which simultaneously matches all the significant stream fluxes, aerothermodynamic and geometric parameters of a nonuniform flow", as stated by PIANKO AND WAZELT [91], who contributed the most extensive report on averaging in recent times. According to CUMPSTY AND HORLOCK [22] it is therefore important to identify the most appropriate averaging method for each individual purpose in terms of preserving the essential flow features.

Accordingly and consistent with former work [50, 52–54], the basic ideas of mass, momentum and energy conservation were considered, in order to get meaningful average values. Generally, CFD static pressure values were area-averaged and total pressure as well as flow angle values were mass-averaged.³⁶ This is particularly valid for the comparison of 1D values with experimental data shown in Tab. 4.1 as well as radial profiles of computed flow values in evaluation planes E30 and E32 (Figs. 4.8 to 4.11), which were evaluated on 200 span-wise equidistant, circumferential surfaces and circumferentially averaged afterwards. For comparison with measured flow velocities in Fig. 4.14, the axial velocity component was calculated as an area average and the circumferential and radial components were determined as mass averages (Subsec. 3.4.4). As it is valid for span-wise CFD pressures and flow angles described above, radial profiles of absolute velocity components in planes E30 and E32 (Fig. 4.14) are also based on circumferentially averaged data.

³⁶ $\bar{q} = \frac{1}{A} \int q \, dA$ and $\bar{q} = \frac{1}{\dot{m}} \int q \, d\dot{m}$, where q is the physical quantity considered for averaging. As stated above for the evaluation of measurement data (Subsec. 2.4.1), area-averaging of static pressure is physically founded, derived from the net force $F = pA$. Moreover, CUMPSTY AND HORLOCK [22] state that generally, the given possibility of defining a flux of physical quantity results in reasonable averaging definitions, usually referred to as mass averages. However, despite the fact that there is no pressure flux, it is common to consider mass-averaging as the appropriate approach for the total pressure, see Ref. [22].

3.4.2 Determination of Static Enthalpy

To compare the analytical loss coefficients of TRAUPEL [123] (5.20) and DUNHAM AND PHILLIPSEN [31] (5.21) with a CFD-based loss approach (5.15), the static enthalpy loss

$$\Delta h_{\text{loss,PSC}} = \bar{h}_{\text{withPSC}} - \bar{h}_{\text{w/oPSC}} \quad (3.7)$$

has to be determined from averaged CFD results. The best method for this would be a mixed-out approach, resulting in an imaginary flow which would contain the complete losses caused by the PSC, independent of averaging location. However, published literature shows that there is only an established method known for perfect gas, see DZUNG [33] or PRASAD [92].³⁷ Therefore and in accordance with HÄFELE ET AL. [50], for the present investigation of non-equilibrium steam the basic ideas of mass, momentum and energy conservation are considered in order to get meaningful average values for the study of loss due to PSCs, compare to Subsec. 3.4.1. Consequently, while NES is being the most appropriate modelling approach for wet steam flow within LP turbines, no simple calculation of the mixed-out state is possible.³⁸ Accordingly, it has to be coped with the deficiency of using location-dependent averaging techniques and the resulting inaccuracies. Thus, only losses arising upstream of the corresponding evaluation plane are captured.

In order to determine the static enthalpy downstream of rotor R3, the basic definition of total enthalpy $h_t = h + c^2/2$ was used. The static enthalpy at the rotor outlet (2) in plane E32 was determined by subtracting the work output of the rotor (Subsec. 3.4.3) and the kinetic energy at the rotor outlet (Subsec. 3.4.4) from the stagnation enthalpy at the stator inlet (0) in plane E30, whereby, based on energy conservation, the stagnation enthalpy was generally mass-averaged. Thus,

$$\bar{h}_2 = \bar{h}_{t,0} - w - \frac{\bar{c}_2^2}{2}. \quad (3.8)$$

This approach seems to be more feasible than calculating the static enthalpy directly, because for the presented NES simulations, the droplet temperature was calculated using an algebraic equation proposed by GYARMATHY [42]

³⁷Recently, TRAXINGER [125] followed these concepts [33, 92] within his master thesis and derived a mixed-out approach for equilibrium steam (EQS) flow. Within a sensitivity study, the author [125] compares CFD results based on area- and mass-averaged as well as mixed-out flow in several evaluation planes between rotor R3 and E32 (Fig. 3.6). TRAXINGER [125] shows the scattering of area and mass-averaged results along the axial position and confirms – for the investigated rotor R3 with and without PSC – their dependency on the averaging location.

³⁸A method like the one developed by CHANDLER ET AL. [19] is associated with high implementation effort and was therefore not further pursued for the present study.

instead of a separate energy conservation equation, compare to Sec. 3.2, which results in small inaccuracies in the calculation of the enthalpy h_1 of the liquid phase (Eq. (3.6)).

3.4.3 Determination of Work Output

The work output of the rotor is evaluated in CFD based on the generated torque M transferred on blade and hub surfaces. Thus,

$$w = \frac{M\omega}{\dot{m}}. \quad (3.9)$$

Here, ω is the angular frequency and \dot{m} the evaluated mass flow rate. For the PSC parameter study presented later, w/w_{V0} is used as performance indicator for the assessment of PSC designs (Sec. 5.8), whereby w is the work output of each individual PSC configuration and w_{V0} the output of configuration V0 with freestanding blades.

3.4.4 Determination of Kinetic Energy

Generally, kinetic energy of three-dimensional flows in turbomachinery can be characterized by the corresponding flow velocity components in axial, circumferential and radial direction. Determination of the absolute velocity at the rotor exit (2) in plane E32 was done by averaging the three different components separately³⁹ and calculating the mean velocity as

$$\bar{c}_2 = \sqrt{\bar{c}_r^2 + \bar{c}_\theta^2 + \bar{c}_z^2}. \quad (3.10)$$

According to mass conservation, the axial velocity \bar{c}_z was calculated as an area average and based on momentum conservation, the circumferential and radial components \bar{c}_θ and \bar{c}_r were determined as mass averages. In consequence of Eq. (3.10), the mean kinetic energy $\bar{c}_2^2/2$ downstream of rotor R3 can be determined.⁴⁰

³⁹DZUNG [32] indicated the need for averaging the flow velocity components differently, depending on their direction relative to the blade row. The author [32] is thereby following the central idea that only state variables which obey a certain conservation law are eligible to be integrated for averaging purpose across the flow section. Based on this principle, DZUNG also regarded thermodynamic state variables in a later publication [33].

⁴⁰The same is valid for relative velocity \bar{w}_2 and its components as well as kinetic energy $\bar{w}_2^2/2$.

4 | Experimental Validation of LP Steam Turbine CFD Model

The experimental validation of numerical results obtained with the three-stage CFD model described in Chap. 3 is subject of discussion in the following. This discussion is based on data previously published [52] and corresponds to the argumentation of HÄFELE ET AL. [52], however, is presented here in a more comprehensive form. Background information about the test rig measurements is provided in Chap. 2. **Four major validation aspects** are considered.

1. 1D FLOW VALUES – A comparison of area-averaged 1D flow values in quasi-axial inter-stage evaluation planes ...
 - quantifies the overall deviation between measurement and CFD.
 - allows conclusions regarding the match of measured and predicted expansion characteristic of the three-stage turbine.
2. DIFFUSER PRESSURE FIELD – A consideration of the measured circumferentially non-uniform diffuser wall-pressure field ...
 - supports the interpretation of flow field measurement data obtained by radial traversing and the comparison to CFD results derived with a one-passage model.
3. RADIAL FLOW PROFILES – A comparison of measured and CFD predicted flow profile values downstream of rotors with PSC ...
 - allows to capture the local and span-wise degree of agreement of the complex 3D flow field.
4. VORTEX SYSTEMS – A study of the secondary flow structures in rotors with PSC by means of 3D CFD ...
 - contributes to the understanding of measured total pressure drops due to wakes and vortices downstream of rotors with PSC.
 - is useful for the comparison of circumferentially averaged radial CFD profiles versus experimentally traversed data.

4.1 Basic Overview

In this section, a basic overview of the experimental data and the comparison to CFD is given. Details will be discussed in the subsequent sections. The plots in Figs. 4.8 to 4.11 and 4.14 show this comparison for several OPs according to Tab. 2.2 by means of radial total pressure, static pressure, absolute flow angle and velocity profiles as well as wall pressures at hub and shroud.

In evaluation plane E32 downstream of rotor R3 with FB & BR, the CFD model is generally able to predict the measured flow values quantitatively and also in their radial distribution pattern (Figs. 4.8 and 4.9). It is remarkable that the wake of the PSC is captured very accurately in terms of total pressure reduction. However, general differences between measurement data in the upper and lower casing, induced by the asymmetric pressure field in the diffuser, are noteworthy and further examined in the next sections. This deviation is also obvious for the static pressure p and the flow angle α . For both p as well as α , a generally good agreement between measured and computed values is found. However, it is obvious that in the span region around the PSC the deviation of α is higher, which implies that the complex flow structure in the wake of the PSC or in other words the composition of the velocity field (c_r , c_θ , c_z) is predicted with some inaccuracies (Fig. 4.14).

Regarding the results in evaluation plane E30 downstream of rotor R2 with LW (Figs. 4.10 and 4.11), ambivalent statements have to be made. On the one hand, a very good agreement can be observed in the wake of the PSC, when considering the total pressure profile. Furthermore, the flow pattern in upper span regions and the deviation between experiment and CFD can be explained with the help of the three-dimensional CFD results. Here, several vortex structures are present (Figs. 4.6 and 4.7). Related modelling as well as measurement issues are discussed in Sec. 4.4. However, on the other hand it is obvious that the drop in total pressure between 20% and 60% span is not captured by the three-stage CFD model. Here, the total pressure p_t based on CFD results is significantly higher. Since the measured static pressure is constant at this span region, the curve shape of measured p_t corresponds to the reduction in kinetic energy, mainly axial flow velocity c_z (Fig. 4.14). As it is obvious for all investigated OPs, the measured static and total pressures are significantly lower than the CFD results. This offset in plane E30 can be associated with an enlarged CFD static pressure downstream of rotor R3 and is further discussed in Sec. 4.5.

4.2 Comparison of 1D Values

To capture the general deviation between experiment and CFD, area-averaged values in planes E10, E20, E30 and E32 are used, see Tab. 4.1. Mean values in CFD were gained by averaging on the corresponding planes, see Fig. 3.5 and Subsec. 3.4.1. Average values of measurement data were calculated according to Subsec. 2.4.1. The comparison shows a satisfying agreement across all OPs, whereby the deviation rises from part load to overload (OP-1 to OP-4), see Tab. 4.1. According to this comparison, the static pressure in the different

Table 4.1 Comparison of 1D values: Deviation between area-averaged experimental data and CFD results in quasi-axial inter-stage planes (Fig. 3.5), HÄFELE ET AL. [52]

Plane	Flow value	OP-1	OP-2	OP-3	OP-4
E10 ^a	static pressure p (%)	-0.4	-1.4	+0.1	-0.5
E20 ^a	static pressure p (%)	+2.1	+1.9	+1.6	+2.0
E30	total pressure p_t (%)	+0.5	-0.6	-0.6	-1.6
	static pressure p (%)	-1.5	-3.5	-4.6	-4.9
	flow angle α (°)	+1.6	+2.1	+4.0	+7.1
E32 (UT)	total pressure p_t (%)	+0.5	+0.1	-0.2	-5.5
	static pressure p (%)	-0.2	-0.7	-3.7	-3.8
	flow angle α (°)	+2.8	+5.4	+3.6	+3.3

^aFor qualitative comparison only; measured wall pressures are linearized between hub and shroud for area-averaging of static pressure, see Subsec. 2.4.1.

planes shows that the average expansion path within the turbine can be captured quite well with the applied CFD model. Furthermore, a good agreement concerning the total pressure can be seen in Tab. 4.1 except for the value in plane E32 (UT) at OP-4.¹ Apart from this noticeable deviation, the good agreement of total pressure 1D values leads to the conclusion that the loss due to the PSC in the last stage can be captured with the applied numerical model. According to Tab. 4.1, also the absolute flow angle shows satisfying results, whereby the deviation of 1D values in E30 would be lower without the opposite trend of experimental and CFD radial traverses above 90% span (Figs. 4.10 and 4.11), caused by the vortex structure and discussed in Sec. 4.6.

4.3 Pressure Field in the Diffuser

The exhaust hood design in steam turbine facilities like the one investigated at ITSM with the condenser mounted below the turbine (Fig. 4.1) imposes an asymmetric pressure field at the diffuser outlet and further upstream and thus impacts the operation of the diffuser and the expansion characteristic of the LP turbine stages. A literature review of this topic was recently given by BURTON ET AL. [16]. This common phenomenon also influences the interpretation of results shown in the present work and is therefore discussed below.

¹A comparison of experimental data and CFD results for p_t at OP-4 (Fig. 4.9) shows that the difference can be drawn back to the different manifestation of the tip jet above 90% span.

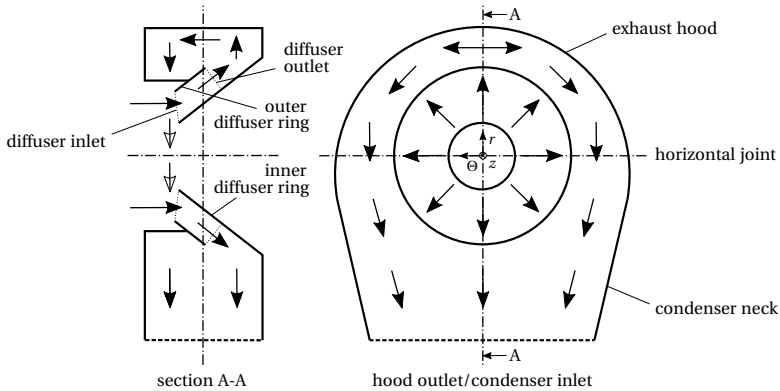


Figure 4.1 Schematic flow structure in the exhaust hood of the industrial steam turbine test rig at ITSM (Figs. 2.1 and 2.4) in accordance with BURTON ET AL. [16]

Based on measurement data obtained in the test rig, Figs. 4.2 and 4.3 show that the circumferential asymmetry of the wall pressure field is slight in part load and increases with increasing loading. At extreme overload condition (OP-4), a distinctive circumferentially non-uniform pressure field is present. In addition to the increasing asymmetry, a rotation of the pressure field can be observed in Fig. 4.2, depending on the load condition and the given swirl at the exit of rotor R3 (compare to flow angle α in plane E32, Figs. 4.8 and 4.9). However, for the one-passage model used in this investigation a linear static pressure profile at the CFD outlet, based on circumferentially averaged static pressures at the hub and the shroud, has been applied. This certainly leads to inaccuracies and deviations in general, depending on the load condition.

4.4 Total Pressure Profile Downstream of PSCs

In Figs. 4.8 to 4.11 the radial profiles of total pressure in planes E32 and E30 downstream of rotors with PSC are shown. Fig. 4.4 gives additional, exemplary insights into the CFD predicted total pressure (stationary frame of reference). In plane E32, between approximately 70% and 85% span, the wake of FB & BR can be seen in terms of total pressure reduction. Due to the influence of the asymmetric pressure field in the diffuser, the measured total pressure level is slightly different for both locations E32 (OT) and E32 (UT). However, the level

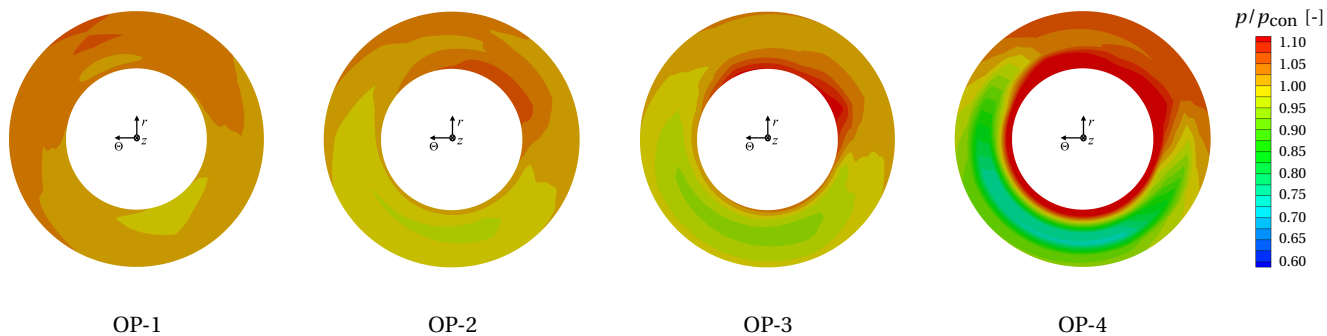


Figure 4.2 Measured wall pressures at the inner diffuser ring (see Fig. 2.2), projected on an axial plane, HÄFELE ET AL. [52]

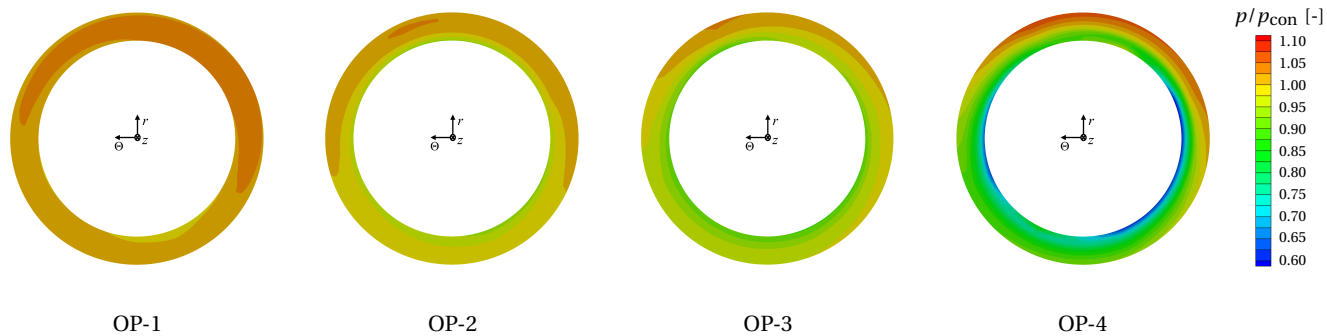


Figure 4.3 Measured wall pressures at the outer diffuser ring (see Fig. 2.2), projected on an axial plane

of total pressure drop is similar and in good agreement with the predicted one. For OP-1 to OP-3 the drop between 70% and 85% span is caused by the combined wake and vortex structure due to the PSC and is similar in shape and magnitude. At OP-4 the CFD profile shows two total pressure drops in this span region. This is due to the fact that wake and vortices induced by the PSC occur next to each other, whereby the lower drop corresponds to the wake. In plane E30, between approximately 60% and 80% span, the wake of the LW can be seen and an even better agreement between experiment and CFD is found. The radial position and shape of the wake contour as well as the strength of the total pressure loss is captured very well by the numerical model and basically lies within the uncertainty range of the measurements. For OP-4 the drop in p_t is slightly underpredicted by CFD, see Fig. 4.11.

4.4.1 Remarks on Vortices in Turbomachines

Vortices are secondary² flow structures which generate losses due to their dissipative character. Different types of vortices occur in turbomachinery, whereby the tip, passage and horseshoe vortex are the most common ones and are caused by the basic geometry of the blading and the passage pressure gradient between blade PS and SS.

²LANGSTON [69] cites the telling example that "a turbine designer might well define secondary flows as those three-dimensional flow effects in a turbine that he had not planned on."

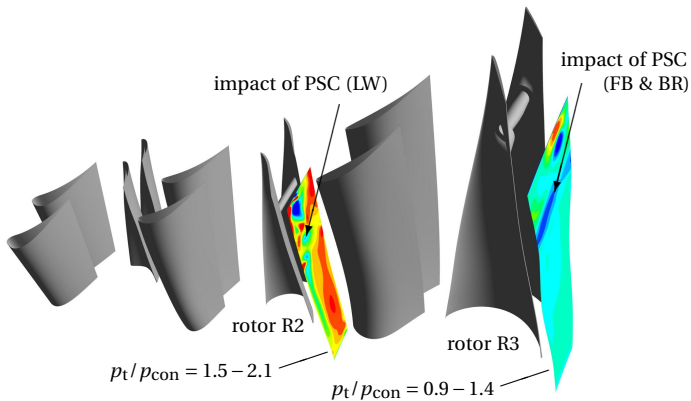


Figure 4.4 CFD predicted total pressure contours (OP-2) on planes downstream of rotors with PSC, complementary to radial traverse data of p_t/p_{con} in Figs. 4.8 to 4.11

The generation of horseshoe and passage vortices is illustrated in Fig. 4.5 while the basic formation of a tip vortex can be learned from Fig. 4.6 (right). According to LANGSTON [69] and Fig. 4.5, the two-legged horseshoe vortex forms due to inlet boundary layer separation. While the suction-sided leg is situated in the SS endwall corner, the pressure-sided one merges with the passage vortex. The tip vortex on the other hand occurs at the gap between the blading and the casing and forms continuously from the leading to the trailing edge, see Figs. 4.6 and 4.7.

In the investigated IST three supplementary vortex sources appear in addition to the basic ones. These sources are the backward facing step upstream of rotor R2, the lacing wire in rotor R2 and the friction bolts and blade reinforcements in rotor R3 (see Fig. 3.5). The loss due to vortices induced by these sources can be seen in total pressure drops in the corresponding planes E30 and E32 (Figs. 4.8 to 4.11). These flow phenomena and corresponding effects on the flow field are subjects of discussion in the following two subsections. The purpose of this brief introduction is to enhance the understanding of CFD results³ and measurement data obtained in planes downstream of the PSCs. A detailed examination of the flow effects in rotor R3 is done in Chap. 5.

³Nowadays, the use of conventional EQS as working fluid for CFD modelling of LP steam turbines is still quite common. In contrast, an NES model was primarily used for the present investigation. Based on a comparison between 3D CFD results obtained with each of both modelling approaches it can be reported that at least for the present case the use of NES in CFD modelling does not show any significant impact on the vortex structure and vorticity.

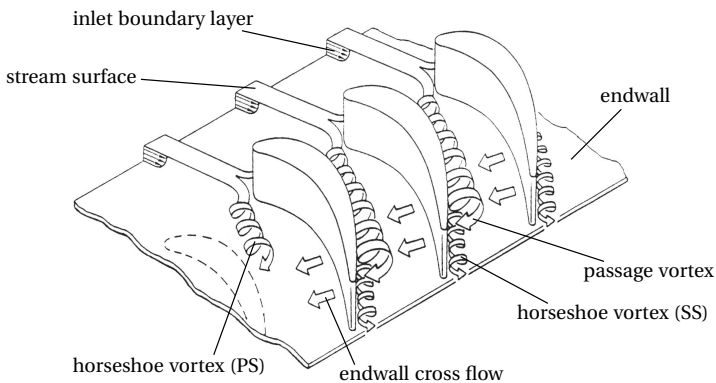


Figure 4.5 Sketch of secondary flow features in a plane cascade of turbine airfoils according to LANGSTON [69]

4.4.2 Vortices in R2 and Effect on Total Pressure in E30

In rotor R2 and downstream, four different vortices can be found with the help of 3D CFD results and measurement data. Their formation is caused by the tip clearance, the backward facing step and the lacing wire. A sketch of the vortex system is depicted in Fig. 4.6 (right). In addition, the sketch in Fig. 4.6 (left) shows the CFD domain boundary downstream of rotor R2 and the evaluation plane E30 which is located in the CFD domain of stator S3 (see Fig. 3.5). The squares in plane E30 correspond to the probe measurement points and the colored markers match the highlighted ones in Figs. 4.10 and 4.11.

At the gap between the blading and the casing a tip vortex occurs, resulting from the pressure gradient between blade PS and SS, see Figs. 4.6 and 4.7. The tip vortex forms continuously from LE to TE and is a typical vortex structure in turbomachinery. Moving down the span, a second vortex can be detected with the help of 3D CFD. This vortex forms along the SS of the blading and it can be drawn back to the wake space at the backward facing step upstream of rotor R2. The low-energy fluid is caused by the discontinuous opening of the casing and is the source of the second vortex which has a large extent in radial as well as circumferential direction and interacts with the tip vortex downstream of the TE (see Fig. 4.7). In addition to these vortices caused by

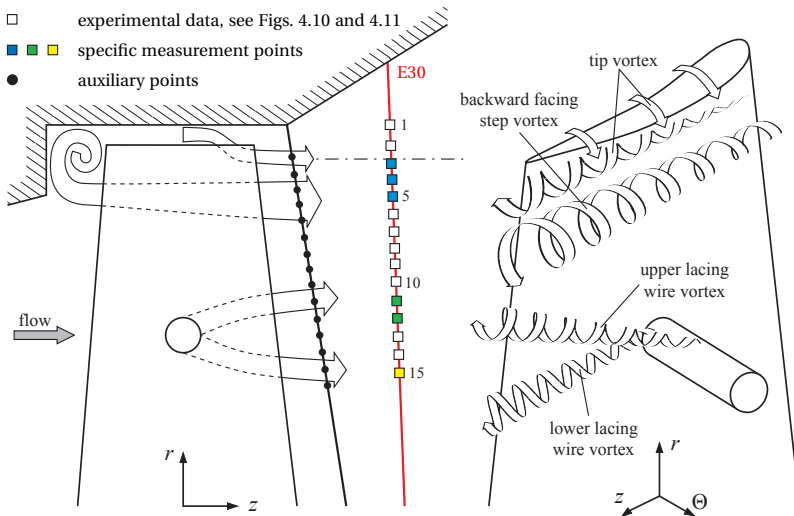


Figure 4.6 Sketches of the vortex system in rotor R2 with PSC, HÄFELE ET AL. [52]

the casing contour, two further vortices which are induced by the lacing wire, compare to Figs. 4.7 and 4.12 (left), appear in the considered flow field. The upper one separates approximately at the middle of the LW between blade PS and SS and is oriented in positive r -direction. The other one appears at the intersection of the lacing wire and the suction side of the blading.

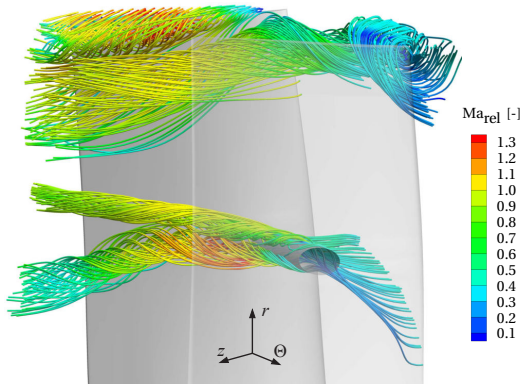


Figure 4.7 Vortex system in rotor R2 with PSC visualized by means of streamlines with 3D CFD (top down: tip vortex, backward-facing step vortex, upper and lower lacing wire vortex), HÄFELE ET AL. [52]

Effects of the described vortex system in rotor R2 can be partially found downstream in the radial profiles of flow values at plane E30 (see Figs. 4.10 and 4.11). In the span region above 80% (markers 1 to 7) a deviation between CFD results and measurement data can be seen in total pressure. Within an OP, the total pressure loss has the same magnitude for both CFD and measurement but occurs at different span position. The points 3, 4 and 5 in Figs. 4.10 and 4.11 (blue colored) show the measured total pressure drop, whereby in CFD the drop appears within the range of markers 1 to 3. The numerical mixing at the stage interface due to the domain change from rotor R2 to stator S3 and the opening of the casing contour downstream of the domain interface leads to the above described local, span-wise deviation of total pressure drop. This is due to the fact that the flow channel between domain interface and E30 only carries the mixed flow of the domain interface towards plane E30.

Beside the deviations due to interface mixing, further flow phenomena in conjunction with the described vortex system can be seen in the p_t profiles at plane E30 (Figs. 4.10 and 4.11). The lower vortex caused by the LW according to Figs. 4.6 and 4.7 can be found approximately at the measurement point 15 (see Figs. 4.10 and 4.11, yellow colored markers). The total pressure drop due to this vortex can be seen in CFD results as well as in the measurement data of the different OPs. The total pressure loss due to the upper vortex of the lacing wire cannot be seen in the radial traverses because it collapses with the wake of the wire (see Figs. 4.10 and 4.11, green colored markers).

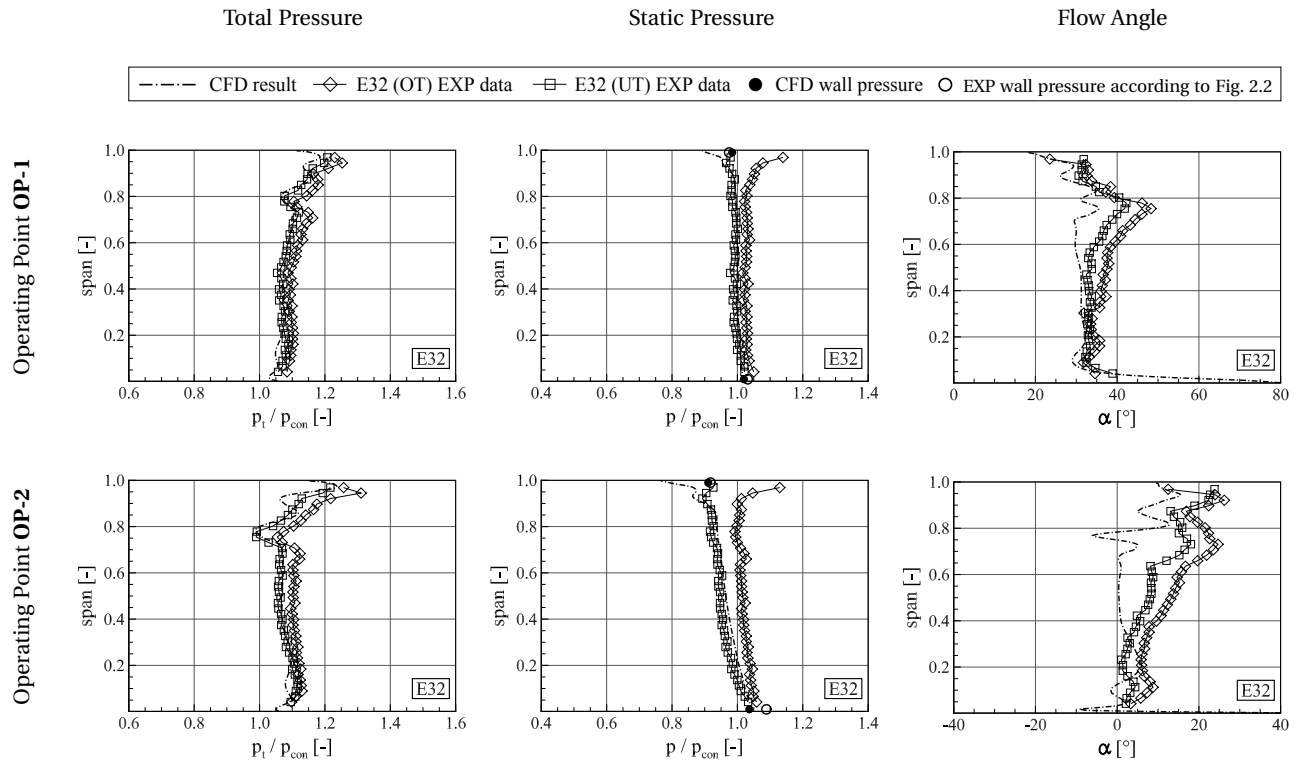


Figure 4.8 Comparison of measured and CFD predicted radial profiles of total pressure, static pressure and absolute flow angle in evaluation plane **E32** (see Figs. 2.2, 2.4 and 3.5) for operating points **OP-1** and **OP-2**, HÄFELE ET AL. [52]

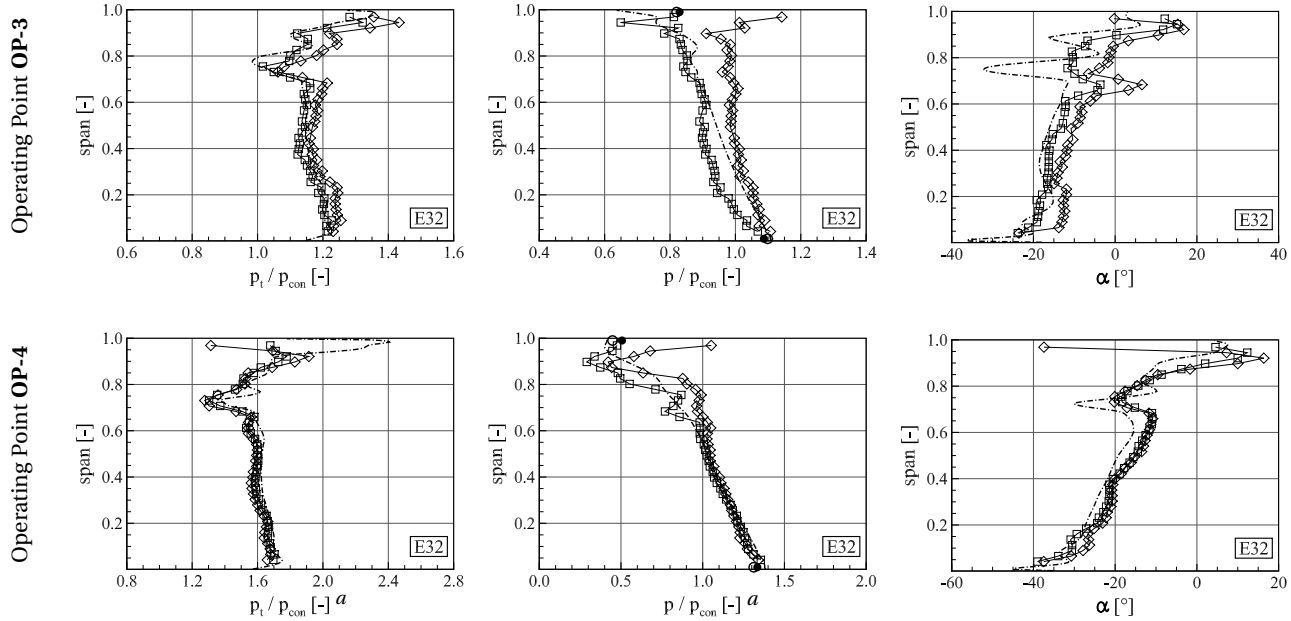


Figure 4.9 Comparison of measured and CFD predicted radial profiles of total pressure, static pressure and absolute flow angle in evaluation plane **E32** (see Figs. 2.2, 2.4 and 3.5) for operating points **OP-3** and **OP-4**, HÄFELE ET AL. [52]

^aNote that the pressure range is doubled, compared to other diagrams of total pressure respectively static pressure in Figs. 4.8 and 4.9.

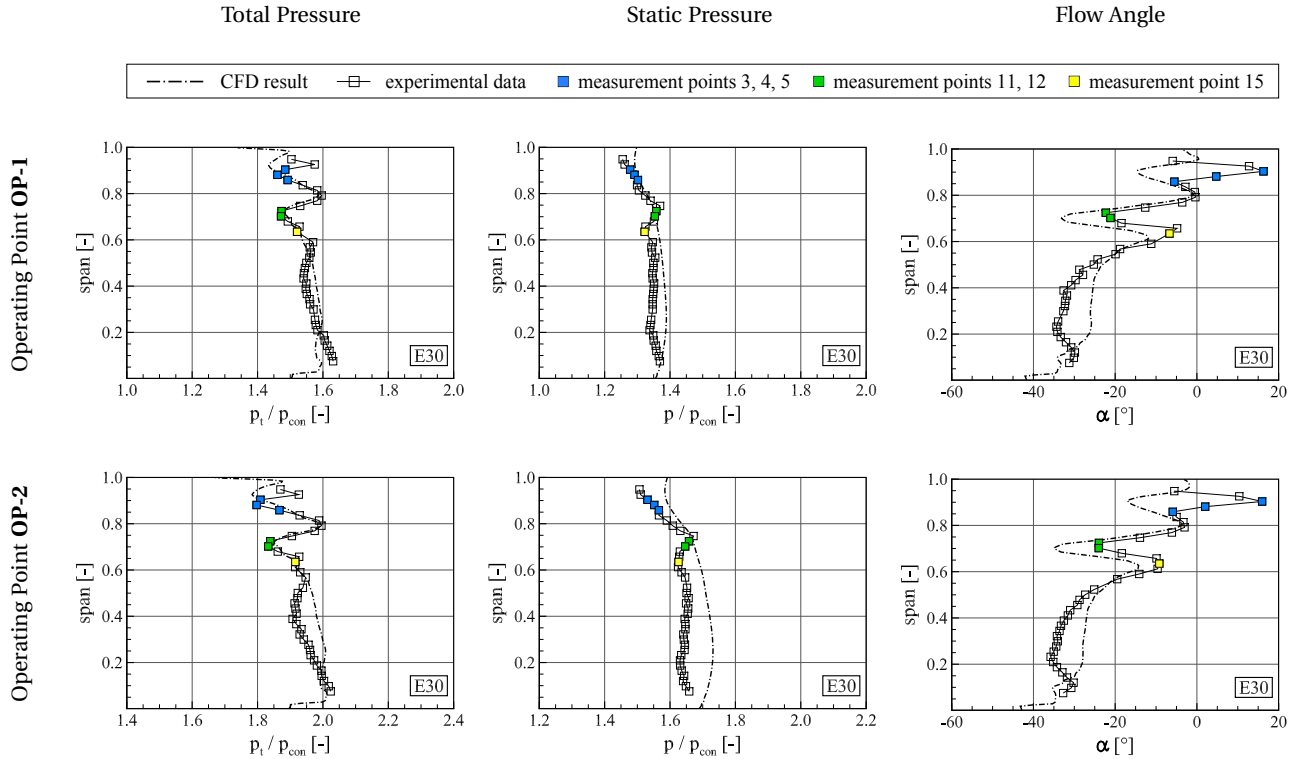


Figure 4.10 Comparison of measured and CFD predicted radial profiles of total pressure, static pressure and absolute flow angle in evaluation plane E30 (see Figs. 2.2, 2.4 and 3.5) for operating points OP-1 and OP-2, HÄFELE ET AL. [52]

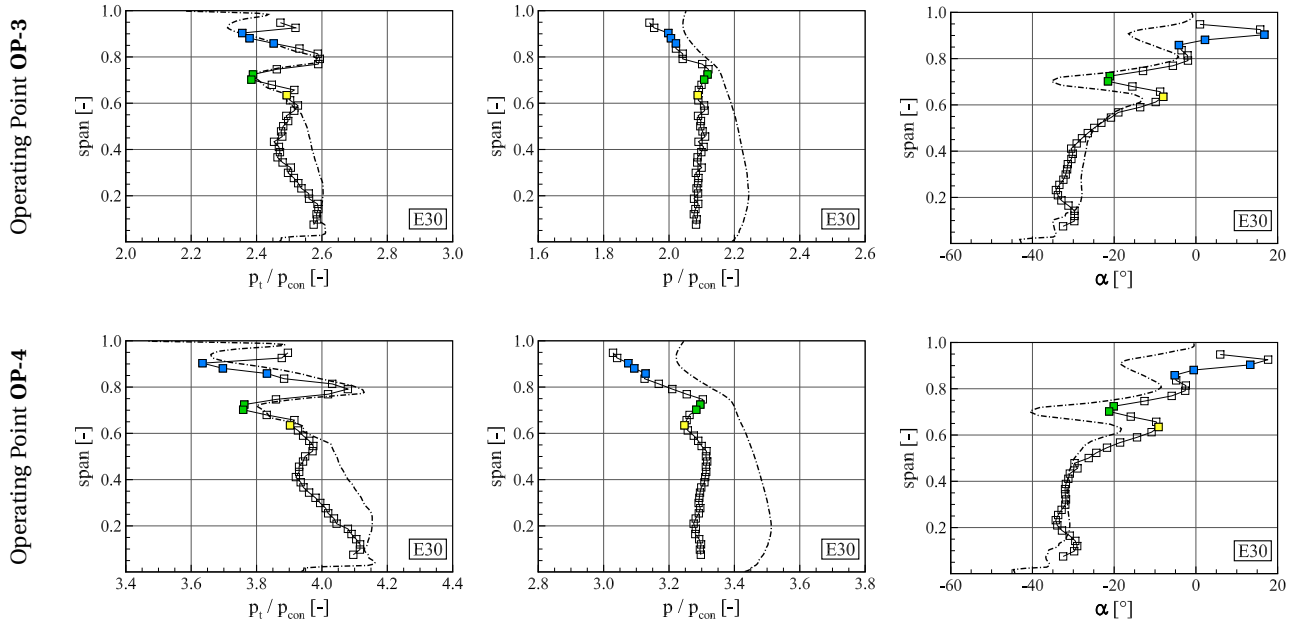


Figure 4.11 Comparison of measured and CFD predicted radial profiles of total pressure, static pressure and absolute flow angle in evaluation plane E30 (see Figs. 2.2, 2.4 and 3.5) for operating points **OP-3** and **OP-4**, HÄFELE ET AL. [52]

4.4.3 Vortices in R3 and Effect on Total Pressure in E32

The vortex system leaving the rotor R3 has similarities with the one downstream of rotor R2 discussed in the paragraph above. Due to the fact that there is no domain interface between rotor R3 and plane E32, no numerical mixing occurs and therefore the complete information is carried towards plane E32. Based on the explanations above and on 3D CFD results, four vortices can be found downstream of rotor R3. The first one is the tip vortex, which can be detected in Figs. 4.8 and 4.9 between 85% and 95% span for all investigated OPs. The comparison of CFD results and measurement data shows that CFD slightly overpredicts the tip vortex and therefore leads to a higher total pressure loss. This might be mainly due to uncertainties in modelling the tip gap between the blading of rotor R3 and the casing and might suggest that the modelled gap height is too large. The other three vortices (see Figs. 5.15 and 5.17 as well as associated description) are caused by the FB & BR, explained in more detail by HÄFELE ET AL. [50] and also discussed in Secs. 5.6 and 5.8. They appear next to each other and are not split like the ones caused by the lacing wire in rotor R2 (see Fig. 4.6). Therefore, these vortices occur in or next to the wake of the PSC, respectively. For OP-1 to OP-3 the total pressure loss due to the PSC can thus be found as a single, pronounced drop in the region around 80% span (see Figs. 4.8 and 4.9). Only for OP-4 the vortices induced by the PSC are pulled above the wake and can be seen as a single drop in total pressure at 80% span, which is only obvious in the CFD results. Here, the wake of the PSC can be seen at approximately 70%-75% span.

In addition to these vortices caused by the tip gap and the PSC, a drop in total pressure occurs at the span region of 5% to 15% for the CFD results only. An analysis of the flow field in 3D CFD showed a small horseshoe vortex in the stator S3 and a slight passage vortex in the rotor R3. Both contribute to the mentioned additional loss in CFD total pressure, which is getting obvious in plane E32 by the drop at 5% to 15% span. The additional loss can also be

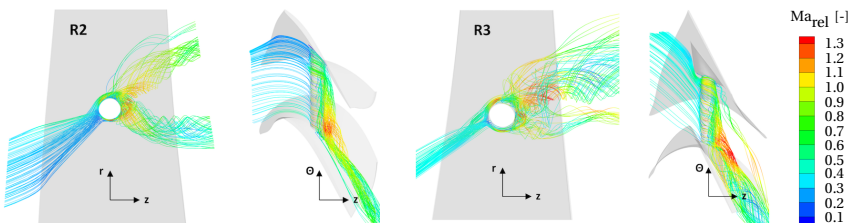


Figure 4.12 Secondary flow structures due to PSCs, HÄFELE ET AL. [54]

seen in a deviation of the flow angle α in Figs. 4.8 and 4.9 or in a reduced axial and circumferential velocity due to dissipation in Fig. 4.14.

4.5 Static Pressure Profile Downstream of PSCs

In Sec. 4.3, the asymmetric pressure field in the diffuser is introduced. Based on this short discussion, the radial profiles of the static pressure downstream of rotors R2 and R3 are analyzed in the following.

4.5.1 Static Pressure in E32

In Figs. 4.8 and 4.9, data of probe measurements in plane E32 at the upper (OT) and lower (UT) part of the turbine are shown. It is clearly evident that the measured static pressure along the span is different for both measurement locations and the magnitude and radial distribution of the deviation also depends on the investigated OP. This variation of static pressure is a result of the asymmetric pressure field downstream of rotor R3, see Figs. 4.2 and 4.3. According to Figs. 4.8 and 4.9, the deviation in static pressure is maximal at the shroud, because here the asymmetry of the exhaust hood has its biggest impact on the pressure field, whereas the pressure values do converge towards the hub, where the pressure field is more equalized. Therefore, a more or less linear static pressure distribution between the shroud of the upper and the shroud of the lower part of the turbine can be seen. In part load (OP-1) the overall deviation is generally small, however, the deviation of static pressure in the upper casing part E32 (OT) is already obvious. The ratio of area-averaged static pressure of E32 (OT) to E32 (UT) is approximately 1.05. This ratio rises within the operating points OP-2 and OP-3. For OP-2 it is 1.08 and for OP-3 it is 1.13. At OP-4 the pressure offset almost disappears in the span region below 60%, which is also reflected in Figs. 4.2 and 4.3. This corresponds to a generally high swirl in this span region. Although the deviation between E32 (OT) and E32 (UT) is relatively high above 60% span, the area-averaged static pressure ratio decreases to approximately 1.12, which is mainly due to the similar radial pressure distribution below 60% span (see Figs. 4.8 and 4.9).

In addition to these deviations of the measured static pressure in the lower and upper turbine casing, the tendency of static pressure for CFD and measurement is different above 90% span. The CFD static pressure decreases, whereas the measured static pressure rises. This can be explained by the fact that the small step at the casing behind rotor R3 is not included in the CFD model, compare Figs. 2.2 and 3.5. Therefore, the flow in the model is not disturbed and a local minimum of the static pressure can be found due

to the deflection into the diffuser. In the real geometry, the step leads to a locally detached flow, which causes the static pressure to rise and the axial velocity respectively the total pressure to decrease, see Figs. 4.8, 4.9 and 4.14. In this context it should be considered that the positions of wall pressure measurement points do not exactly match with traversing plane E32, see Fig. 2.2. However, the CFD wall pressure, averaged in circumferential direction, has been evaluated at the position of the wall pressure measurement points and according to Figs. 4.8 and 4.9 the measured and computed pressures at hub and shroud match quite well.

When considering the flow angle distributions in Figs. 4.8 and 4.9, it is noticeable that the offset between measured static pressures in the upper and lower part of the turbine correlates to some extent with the swirl at the exit of rotor R3. This is also reported by BURTON ET AL. [16] and MUSCH ET AL. [84], who state that swirl of the last stage has a first order effect on the flow field in the diffuser. The interdependency of static pressure field downstream of R3 and swirl is also obvious when comparing the plots in Figs. 4.2 and 4.3.

The present investigation shows that data of probe pressure measurements in E32 (UT) seem to be more representative for the overall pressure field in plane E32, since these data match the measured wall pressures at both hub and shroud very closely, see Figs. 4.8 and 4.9. This is also the result when comparing probe measurement data of E32 (UT) and the radial CFD distribution. Thus, the success of a comparison between one-passage CFD results and experimental data is dependent on the measurement location.

4.5.2 Static Pressure in E30

In plane E30 at 75% span and below, the measured static pressure is lower than the one predicted with CFD, slightly for OP-1 (approximately 3.5% at 20% span) and more significantly for OP-2 to OP-4 (maximal 7% for OP-3 at 20% span). This is in contrast to the generally higher measured static pressure in plane E32 in the upper part of the casing (see experimental data of E32 (OT) in Figs. 4.8 and 4.9), which would give rise to the expectation that in plane E30 the measured static pressure level will be higher, too. When regarding CFD results on an axial plane at the TE region of stator S3 (Fig. 4.13) it is found that portions of the flow channel are choked in the span region of 75% and below, partly at OP-1 and almost completely at OP-2 to OP-4. According to VERSTRAETE ET AL. [129] and BURTON ET AL. [16], a choked stator limits the circumferential variation of flow properties to a minimum. Thus, it can be assumed that the static pressure in E30 is nearly independent of circumferential position. Together with the facts that the CFD static pressure in E32

is higher than the measured one in the lower part for all OPs (see Figs. 4.8, 4.9 and Tab. 4.1) and that the lower part of the turbine is representative for the expansion within the considered turbine, the higher CFD static pressure in E30 can be mainly drawn back to the enlarged static pressure level in E32. The overprediction results from the assumption of linearized static pressure boundary condition at the diffuser exit (Subsec. 3.3.1), which manifests itself in a nearly linear distribution of CFD static pressure in plane E32 for all investigated OPs, see Figs. 4.8 and 4.9.⁴ The coupling of static pressure in planes E32 and E30 is also confirmed by the comparison between averaged CFD results and measurement data in Tab. 4.1, where the deviation rises from part load to overload.

At the span region around 70%, the already discussed total pressure drop due to the wake of the lacing wire can be seen for both measurement data as well as CFD results. For the static pressure a rise occurs, which can be drawn back to the high swirl caused by the cross flow along a PSC from the blade pressure to the suction side, see e.g. Fig. 5.15. The rise can only be seen within the measurement data, resulting from the lower static pressure level. Due to the proximity of rotor R2 and plane E30, a slight drop in static pressure appears in the measurement data above and below the wake. In CFD results this reduction cannot be seen due to the mixing at the stage interface between rotor R2 and stator S3 (Figs. 3.5 and 4.6).

⁴Aside from the explanation given here, an impact of wet steam effects and possible deficiencies in NES modelling in this regard cannot be completely ruled out and might additionally influence the offset in static pressure in plane E30. Interestingly, a similar OP-dependent discrepancy between measurements and CFD in terms of magnitude and tendency has also been observed applying the same NES modelling in another LP steam turbine, see SCHATZ ET AL. [100].

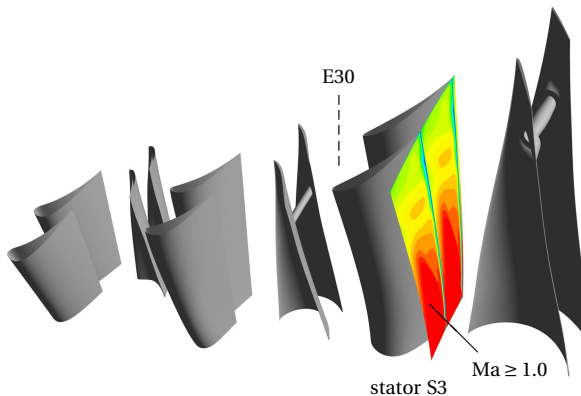


Figure 4.13 Partly choked flow channel of stator S3 (contour plot with $\Delta Ma = 0.05$)

4.6 Flow Angle and Velocity Profile Downstream of PSCs

The agreement between predicted and measured flow angles is examined in the following. The analogy between flow angle α and the velocity components c_θ and c_z is clarified by comparing Figs. 4.8 to 4.11 with Fig. 4.14.

4.6.1 Flow Angle and Velocity in E30

Figs. 4.10 and 4.11 show that the predicted flow angle distribution generally follows the radial pattern of measured values. The trend is reproducible for all investigated OPs. However, some discrepancies are obvious. In the wake of the lacing wire at approximately 70% span the magnitude of α is generally predicted too high. Basically, this is due to the fact that the magnitude of the circumferential velocity component c_θ is predicted too high in this span region, see Fig. 4.14. This can be allocated to the influence of the cross flow along the lacing wire from blade pressure to suction side (Fig. 4.12, left), which seems to be overpredicted by the numerical simulation. The deviation between CFD results and the experimental data for span regions above 85% can be explained with the help of the present vortex system in rotor R2 and downstream in plane E30, see Figs. 4.6 and 4.7. A change in sign occurs for the measured flow angle α at the measurement points 3, 4 and 5 (blue colored). Figure 4.7 shows that this effect can be drawn back to the tip and the backward facing step vortex, which interact and form a complex vortex structure. This change in sign was also observed in 3D CFD at the downstream domain interface of rotor R2, but the information is lost due to mixing at the stage interface between rotor R2 and stator S3 and therefore is not apparent in the CFD results of flow angle α at plane E30 (Figs. 4.10 and 4.11). Below 50% span the magnitude of α is underpredicted and this corresponds to the deviation of velocity components c_θ and c_z (see Fig. 4.14).

4.6.2 Flow Angle and Velocity in E32

In evaluation plane E32, downstream of the rotor R3 with friction bolts and blade reinforcements, the basic trend of absolute flow angle α is captured with satisfying agreement (see Figs. 4.8 to 4.9). The shift in flow angle between the measurements in the upper and the lower part of the turbine can be directly explained with the deviation of the static pressure, as discussed in Sec. 4.5. The good agreement between computed and measured total and static pressure profiles implies that the kinetic energy downstream of R3 is well predicted

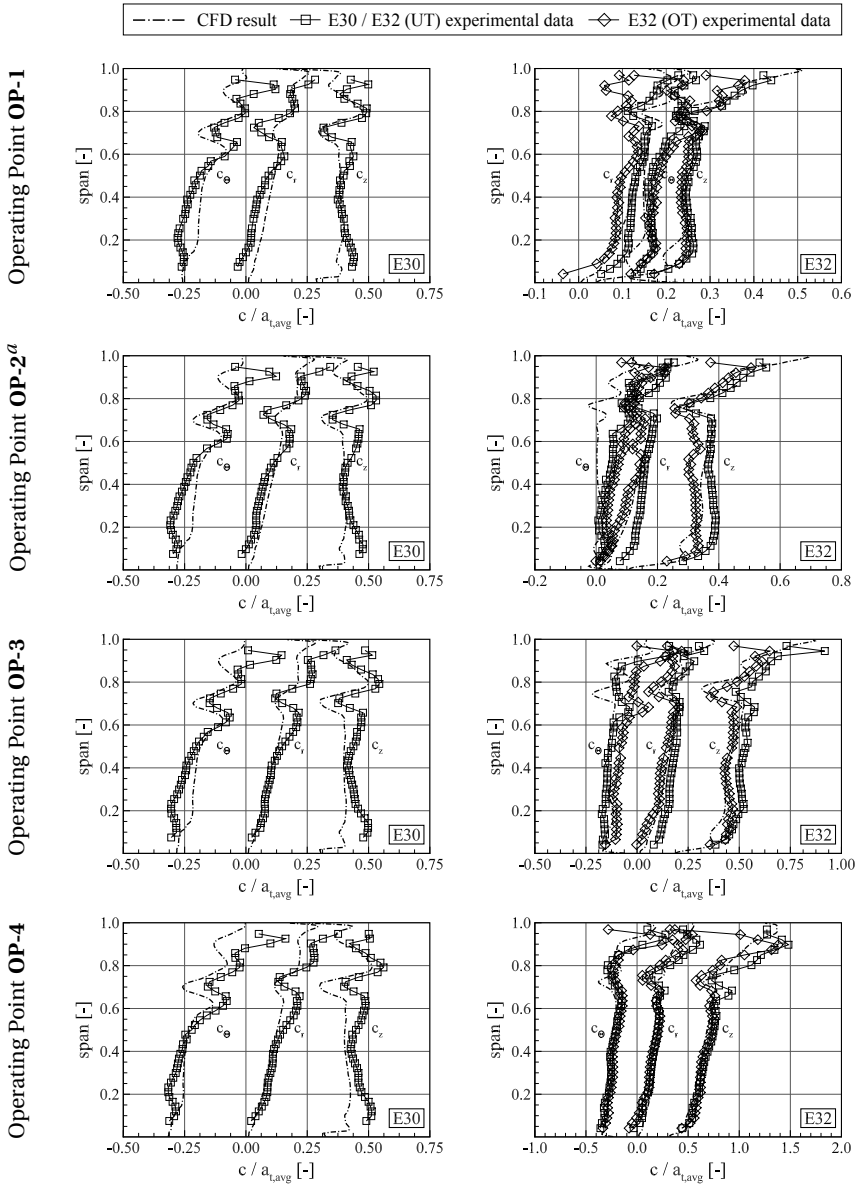


Figure 4.14 Radial profiles of absolute flow velocity components in evaluation planes E30 and E32 (see Figs. 2.2, 2.4 and 3.5) for operating points OP-1 to OP-4

^aCFD results and experimental data in E30 / E32 (UT) published by HÄFELE ET AL. [52].

by the CFD model. However, the complex flow pattern in evaluation plane E32 due to vortices cannot be fully reproduced by the model. Discrepancies in the velocity component c_θ are mainly responsible for the deviation of the flow angle, compare to Fig. 4.14. This again can be mainly traced back to an overprediction of the cross flow along the PSC in R3, shown in Fig. 5.15.

4.7 Key Points on the Experimental Validation

The three-stage CFD model according to Subsec. 3.3.1 was developed to investigate the impact of PSCs with engineering accuracy, suitable for an industrial design process. The numerical model was validated with experimental data obtained from extensive test rig measurements with a full-scale LP industrial steam turbine at ITSM under real steam conditions.

- 1) The comparison shows a generally good agreement between CFD results and measurement data at different load conditions along the investigated speed line. According to these results, the present investigation leads to the conclusion that using a conventional one-passage CFD model is valid to capture the three-dimensional flow field in LP steam turbine blading with PSC and is therefore sufficient for engineering practice.
- 2) The CFD model is able to capture the total pressure reduction due to PSCs with a very good agreement to measured values. Furthermore, the predicted static pressure shows a generally good agreement at this span region. Nevertheless, the predicted velocity components respectively the flow angle α downstream of the PSC deviates moderately from the measured data.
- 3) The vortex systems in rotors R2 and R3 with PSCs have been studied and a comparison of CFD and experiment shows that the total pressure losses due to wakes and vortices can be captured very well in magnitude and location with the help of 3D CFD, which implies that CFD based evaluation of total pressure loss caused by PSCs is suitable for this case. This is also obvious when comparing area-averaged 1D values.
- 4) An asymmetric pressure distribution downstream of the last rotor blade row and in the diffuser is shown by the experimental data. The comparison of probe measurement data in the upper and lower part of the turbine with CFD indicates a good agreement between the data of the lower measurement location and the one-passage CFD model.

5 | Loss due to Part-Span Connectors in LP Steam Turbine Blading

Loss in turbomachinery can be generally classified into three main mechanisms: 1) *Profile loss* is usually assigned to arise in the blade boundary layers and normally includes loss generated at the blade TE regions. 2) *Endwall loss* is usually in distance to profile loss and sometimes referred to as secondary loss, because it arises partly from the secondary flows induced by the annulus boundary layers passing through the blade rows, depicted e.g. in Ref. [68, p. 324]. According to DENTON [25], however, this "loss does not arise directly from the secondary flow but is due to a combination of many factors." 3) *Tip leakage loss* originates from the leakage flow through radial clearances between the blade tip or shroud and the casing as well as between the hub of the stator blades and the runner. However, these loss mechanisms are seldom independent from each other and it is often difficult to separate them, DENTON [25], also because there is sometimes strong loss interaction present. It is common to state that for many turbomachines, each of the three mechanisms accounts for approx. $1/3$ of the total loss. Depending on the type of machine and details of the blading, a different distribution might be present.¹

¹In condensing steam turbines, additional wetness loss arises, as discussed in Sec. 3.2.

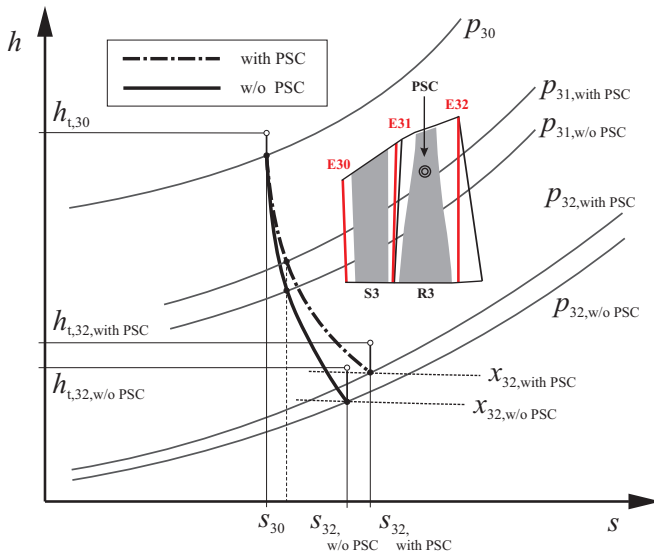


Figure 5.1 Schematic expansion characteristic in the last stage of a low-pressure industrial steam turbine with/without part-span connectors (PSC), HÄFELE ET AL. [54]

According to DENTON [25], "any flow feature that reduces the efficiency of a turbomachine" can be called loss. PSCs are sources of such flow features and it is accepted that these elements reduce the efficiency of the turbine. This efficiency drop is e.g. indicated in Fig. 5.1. By blocking parts of the blade passage, the PSC in rotor R3 causes an upstream static pressure rise² and eventually results in a change of expansion characteristic of the whole last stage. Summing up, the work done by the blading is lower in this

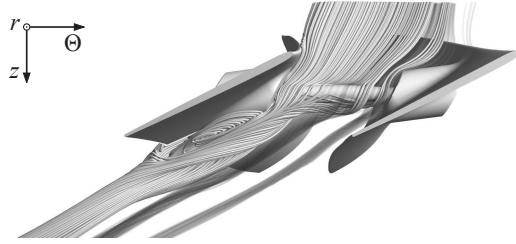


Figure 5.2 Flow around a PSC, HÄFELE ET AL. [50]

case. The EULER turbomachinery equation $w = u_2 c_{\Theta,2} - u_1 c_{\Theta,1}$ indicates that this results in a change of the flow field, which is also obvious with respect to the degree of reaction $r_k = \Delta h_{R3} / (\Delta h_{S3} + \Delta h_{R3})$. According to this, fundamental blade design parameters are changed, as discussed in Ref. [54]. Moreover, the fluid is span-wise redistributed, resulting in altered blade loading.

An aerodynamic optimization of the PSC configuration can lead to less impact on the flow field and reduce the losses. In the flow field, the loss manifests in terms of pronounced secondary flow structures. The most significant ones are shown in Fig. 5.2. This includes vortices induced by the PSC as well as strong interaction of the flow around and downstream of the PSC with the main passage flow and the blade profile boundary layer.³ Besides these major, predominantly aerodynamically-governed effects, HÄFELE ET AL. [54] identified a change in wetness loss due to the presence of the PSC, arising in wet steam due to thermodynamic non-equilibrium (Sec. 5.5).

The present chapter gives a comprehensive overview about loss sources that are directly associated with PSCs and moreover, discusses ideas of roughly capturing related losses induced in the last stage of an LP steam turbine by means of simplified analytical correlations (Sec. 5.4), which are validated by

²MAIER [77] briefly reflected on this topic and a general effect on the rotor inflow conditions as cause for his measured efficiency drop. Regarding the flow angles upstream of rotor R3 with PSC, HÄFELE ET AL. [54] showed that this effect leads to more incidence at part and design load but improves the rotor inflow angle at overload. Thus, adjusting the inlet of rotor R3 or the outlet of stator S3 with regard to the influence of the PSC could improve the rotor inflow conditions. However, it has to be kept in mind that this type of turbine is normally operated over a wide range of loading and rotational speed. Globally, this effect is of minor relevance.

³The loss behind the PSC is clearly concentrated near the blade suction side. In this context, DENTON [25] points out the relevance of PSC trailing edge shape for the magnitude of loss.

CFD results in Sec. 5.9. It is the main purpose of Secs. 5.2 and 5.3 to channel the relevant knowledge about fluid-dynamic drag towards this discussion. The aerodynamic performance of various PSC configurations from a CFD-based parameter study (Sec. 5.7) is comprehensively assessed in Sec. 5.8.

5.1 General Definition of Loss Coefficients

In order to predict losses in fluid mechanics, various definitions of loss coefficients are available for regular use, see DENTON [25]. The most common ones are based on the total or stagnation⁴ pressure loss $\Delta p_{t,\text{loss}}$, the energy or enthalpy⁵ loss Δh_{loss} and the dissipation j , compare to Fig. 5.3. The total pressure loss coefficient

$$Y = \frac{\Delta p_{t,\text{loss}}}{p_{t,1} - p_1} = \frac{p_{t,0} - p_{t,1}}{p_{\text{dyn},1}} \quad (5.1)$$

is commonly used in hydraulics and often applied when investigating cascade flows in thermal turbomachinery. In the latter discipline it owes its popularity to the fact that it is easy to calculate from cascade test data.

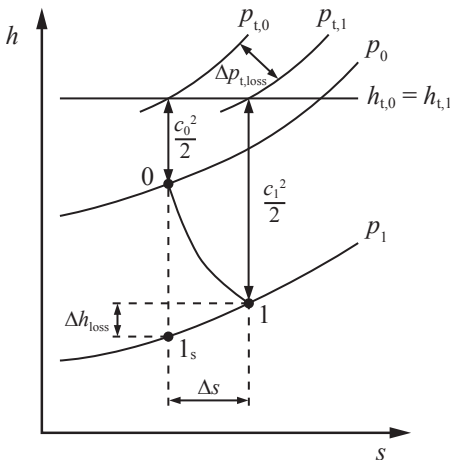


Figure 5.3 Expansion process in a stator

From the blade designer's point of view, the enthalpy-based loss coefficient

$$\zeta = \frac{\Delta h_{\text{loss}}}{h_{t,1} - h_1} = \frac{h_1 - h_{1,s}}{c_1^2/2} \quad (5.2)$$

offers a preferable formulation, where $h_{1,s}$ is obtained in an isentropic expansion to the same final process pressure (Fig. 5.3). DENTON [25] addresses the issue that both Y (5.1) as well as ζ (5.2) can result in fault interpretations when applied to rotating blade rows. This is due to the fact that between blade inlet and outlet, $p_{t,\text{rel}}$ as well as $h_{t,\text{rel}}$ can vary without

⁴In this work, the equal term *total* is predominantly used to describe the *stagnation* quantity.

⁵DENTON [25] uses both terms equally; in the further progress of this thesis, the term *enthalpy loss* is used to express a drop of enthalpy Δh and to label the corresponding loss coefficient ζ .

any change of loss but only due to a variation of radius.⁶ Due to this imaginary loss, DENTON [25] proposes to determine all loss based on the entropy. In a closely adiabatic flow, which is an appropriate assumption for most turbomachines, entropy is primarily produced by irreversibilities. This in combination with the fact that entropy is independent from its reference system makes it a reasonable justification for considering the entropy, which is, according to DENTON [25], "the only rational measure of loss in an adiabatic machine". Following this, the entropy loss coefficient ζ_s , based on the dissipation $j = \int T ds$, can be defined. Thus,

$$\zeta_s = \frac{j_{01}}{h_{t,1} - h_1} \approx \frac{T_1 \Delta s}{c_1^2/2}, \quad (5.3)$$

whereby according to DENTON [25] and based on Fig. 5.3 the dissipation between the states 0 and 1 can be approximated with $T_1 \Delta s$ and $c_1^2/2$ is the kinetic energy at the stator exit.⁷ As discussed by DENTON [25], enthalpy and entropy loss coefficients can be equated⁸ and thus equally used. In the given context it is obvious that the enthalpy loss Δh_{loss} closely equates to the dissipation $T_1 \Delta s$, see Eqs. (5.2) and (5.3).

Above, all loss coefficients have been defined for a stator blade row. The same kinds of coefficients can be derived for rotor blading, namely the total pressure loss coefficient⁹

$$Y = \frac{p_{t,\text{rel},1} - p_{t,\text{rel},2}}{p_{\text{dyn},2}}, \quad (5.4)$$

the enthalpy loss coefficient

$$\zeta = \frac{\Delta h_{\text{loss}}}{h_{t,\text{rel},2} - h_2} = \frac{h_2 - h_{2,s}}{w_2^2/2} \quad (5.5)$$

and the entropy loss coefficient

$$\zeta_s = \frac{j_{12}}{h_{t,\text{rel},2} - h_2} \approx \frac{T_2 \Delta s}{w_2^2/2}. \quad (5.6)$$

⁶In a rotor's relative system, rothalpy $I = h_t - u c_\Theta = h + w^2/2 - u^2/2$ is being conserved.

⁷For turbine blading it is common to normalize loss coefficients to the dynamic pressure (Y) or kinetic energy (ζ , ζ_s) at the blade row exit.

⁸ $\zeta_s - \zeta \approx 0.25 (\kappa - 1) \text{Ma}^2 \zeta \zeta_s$. According to DENTON [25], the difference between enthalpy and entropy-based loss coefficients is negligibly small, being of order 10^{-3} . This is due to the fact that the difference $\zeta_s - \zeta$ is depending on the product $\zeta_s \zeta$.

⁹Here, $p_{t,\text{rel}}$ is used according to HORLOCK'S [48] definition of stagnation losses Y for rotor blading. Alternatively, the rothalpy-based total pressure could be used, see discussion above.

5.2 Basics on Fluid-Dynamic Drag

Aero- and hydrodynamic drag or resistance¹⁰ of bodies with all kind of shapes plays an important role in everyday fluid flows. The fluid-dynamic drag force acting on a body, e.g. a car or an aircraft, is commonly used to determine the lost performance. In turbomachinery flows, the idea of drag has been adopted to some degree. However, in contrast to external fluid flows the flow direction in blade rows is not obvious at all and it is sometimes difficult to define the main direction the drag is acting. In addition, there are issues concerning interactions, non-uniformities and compressibility effects of the flow. It is DENTON's [25] opinion that "the concept of drag is of little use in turbomachinery and should be replaced by the concept of entropy generation".

However, several examples in literature can be found where the given relationships between drag and loss, in fact only valid for uniform flow, have been successfully applied for turbomachinery flows, as discussed in Subsec. 5.4.1. One scope of application is examined in the present work. It is the loss induced by a part-span connector, which arises due to the drag of the PSC

¹⁰According to HOERNER [47], the term *drag* is preferred in aviation, whereas *resistance* is commonly used in marine engineering.

Table 5.1 Composition of drag force $F_D = F_{D,\text{friction}} + F_{D,\text{form}}$ depending on body shape and flow pattern, according to SIGLOCH [109]

Body shape and flow pattern	$F_{D,\text{friction}}$	$F_{D,\text{form}}$
	$\approx 100\%$	$\approx 0\%$
	$\approx 90\%$	$\approx 10\%$
	$\approx 10\%^a$	$\approx 90\%$
	$\approx 0\%$	$\approx 100\%$

^aRule of thumb: For blunt bodies the skin friction drag is approximately one magnitude smaller than the form drag, SIGLOCH [109].

and manifests itself in an impulse loss according to NEWTON's second law of motion¹¹. According to SIGLOCH [109], the drag force acting on a body is depending on parameters like the type of fluid, the relative velocity between fluid and body, the surface finish as well as the shape of the body. However, two crucial contributors can be clearly distinguished, namely body surface and shape, resulting in *skin friction* drag¹² and *form* drag¹³ (viscous pressure drag, caused by boundary layer separation). Thus, the total drag force can be written as

$$F_D = F_{D,\text{friction}} + F_{D,\text{form}} = c_D \frac{\rho_\infty}{2} c_\infty^2 A, \quad (5.7)$$

see Ref. [109, p. 322]. The separation between skin friction and form drag is often difficult and accordingly hard to measure, SIGLOCH [109]. Tab. 5.1 gives an overview about the composition of total drag F_D for different body shapes and flow patterns. Generally, for streamlined shapes the skin friction drag is decisive, whereas for blunt bodies the form drag is most relevant for the total loss. As a rule of thumb it is found that for blunt bodies the skin friction drag is approximately one magnitude smaller than the form drag. Hence, the form drag is the principal cause for the drag arising in flow around circular cylinders¹⁴ and moreover around the type of PSCs investigated in the present thesis. However, as mentioned above, according to SIGLOCH [109] a strict isolation of both drag force parts is often not possible and it becomes apparent that for the considered PSC shapes (Tabs. B.1 to B.4) friction between PSC surface and fluid must not be ignored. This results from the fact that besides flow deceleration, skin friction is one reason for flow separation¹⁵ along the cylinder and contributes to the extent of the corresponding region of detached flow in the wake (compare to Fig. 5.4). This again induces the dominant form drag for these kinds of shapes. Thus, it is meaningful to consider the optimization conditions and interaction of both parts.

¹¹Named after English physicist and mathematician Sir Isaac NEWTON (1643–1727).

¹²Induced from friction between body skin and fluid passing by and calculated by integrating the fluid shear stress $\vec{\tau}$ on covered body surface area A . Thus, $\vec{F}_{D,\text{friction}} = \int_A \vec{\tau} dA$, see Ref [109].

¹³Results from pressure gradient on surface area A and is calculated as $\vec{F}_{D,\text{form}} = -\int_A p d\vec{A}$, where p is the static pressure on the body surface area and \vec{A} is an area vector, see Ref [109]. The form drag becomes larger with the wake downstream of the body stronger pronounced.

¹⁴This is valid for technical applications like flow around PSCs in LP steam turbine blading, where moderate to large REYNOLDS numbers are found. In contrast, the skin friction is dominant in creeping flows ($0 < \text{Re}_{\text{Cyl}} < 4$ to 5, see Tab. 5.2) around cylinders.

¹⁵In contrast to flow separation along sharp edges, the position of starting *pressure-induced* separation (separation line) on the cylinder surface is very sensitive to flow conditions.

The approach in Eq. (5.7) is based on the law of BLASIUS for flat plates¹⁶ (see Ref. [109, p. 181]) and can be used to calculate the fluid-dynamic drag forces acting on bodies with any kind of shape, provided that the drag coefficient c_D is given. In the rightmost part of Eq. (5.7), $\rho_\infty/2 c_\infty^2$ is the incompressible dynamic pressure of the undisturbed flow. c_D is dimensionless and – for ideal and incompressible fluid flow – depending on the REYNOLDS number and body shape (Sec. 5.3). The value of c_D is normally based on measurements and in daily practice can be derived by empirical correlations, see HOERNER [47]. The definition of reference area A is depending on the investigated case. For the present consideration of flow around circular cylinders $A = d \times l$ is the projected cross section area normal to the direction of the undisturbed flow, whereby d is the cylinder diameter and l the cylinder length.

5.3 Drag Coefficient of a Circular Cylinder

Because cylindrical PSCs with mostly circular cross sections are under investigation in the present thesis, the drag coefficient of a circular cylinder is focused on in the following. Drag coefficients derived from experiments are the foundation of several loss correlations for PSCs found in literature, of which two are discussed in Sec. 5.4. This popularity is possibly due to the fact that the drag coefficient c_D is a crucial part of the drag force F_D defined in Eq. (5.7) and contains all parts of F_D that cannot be described analytically. Thus, the value of c_D provides the general relationship between drag force and investigated body shape. The following brief analysis is mainly based on the compendium works of ZDRAVKOVICH [140, 141] and HOERNER [47]. It includes discussions about ideal incompressible as well as compressible flow around circular cylinders, considerations on CFD approaches and furthermore thoughts on the applicability of derived c_D -values for real flow applications.

5.3.1 Incompressible Flow

Fluid flow past a cylinder is always to a certain extent inducing regions of disturbed flow around the body. Bluff¹⁷ or blunt bodies like circular and elliptical cylinders normally generate a particularly large and usually unsteady flow pattern. Fig. 5.4 shows a subdivision of the disturbed flow into four flow

¹⁶Named after German physicist Paul Richard Heinrich BLASIUS (1883—1970).

¹⁷For example a brick, a cylinder or an airfoil at large angle of attack is referred to as *bluff* body, whereas an airfoil at small attack angle is called *streamlined*. In literature, the term *blunt* body is often used equally to *bluff* body, however, indicating a *bluff* body with *blunt* front and rear face. In this work, *blunt* body is used to denote cylinders with circular or elliptical cross sections.

regions, whereby these can be characterized by the magnitude of local time-averaged velocity c and its relation to the free stream velocity c_∞ . In contrast to bodies with sharp edges, for round cross section shapes like circle or ellipsis the (pressure-induced) flow separation is not occurring at a fixed position but the point of separation can move, depending on the flow structure in the separated region. According to ZDRAVKOVICH [140], this flow structure is similar for flow around blunt bodies and its development is therefore a common feature of them. Out of the four regions depicted in Fig. 5.4, the wake¹⁸ has received most attention in research work

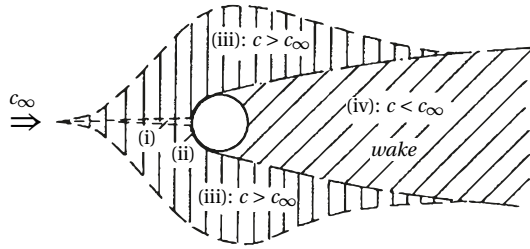


Figure 5.4 Regions of disturbed flow, according to Ref. [140]; (i): retarded flow; (ii): attached boundary layer; (iii): displaced and accelerated flow; (iv): downstream region of separated flow called *wake*

so far, see Ref. [140]. As already mentioned above, the appearance of this region is mainly responsible for the magnitude of form drag, which is governing the overall drag force for flow around cylinders (see Sec. 5.2, Tab. 5.1).

Incompressible flow is commonly characterized by the fact that the magnitude of free stream velocity c_∞ is negligibly small compared to the sound velocity a . Considering incompressible and disturbance-free flow past a cylinder, the governing similarity parameter is the REYNOLDS number

$$\text{Re}_{\text{Cyl}} = \frac{c_\infty d}{\nu}, \quad (5.8)$$

defined as the ratio of *inertial* forces to *viscous* forces. Thus, for this type of flow c_D is only a function of Re_{Cyl} . For flow around cylinders, the cylinder diameter d is used as characteristic dimension. In fluid mechanics it is common to categorize flow regimes depending on their magnitude of REYNOLDS number into *laminar*, *transitional* and *turbulent*. The same applies for flow around cylinders, whereby in Ref. [140] a further categorization of the above stated basic regimes is proposed, see Tab. 5.2. Here, further sub-regimes are classified depending on their inherent flow phenomena. The transition regime in particular is subdivided into three zones (1)–(3), namely transition in wake (TrW), transition in shear layer (TrSL) and transition in boundary layer (TrBL),

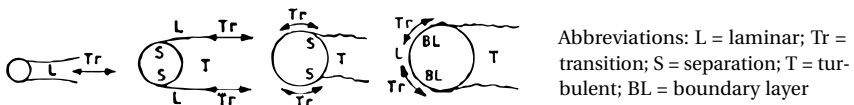
¹⁸According to ZDRAVKOVICH [140], the term *wake* was originally used for the narrow trail left behind a hull of a ship.

Table 5.2 Flow regimes for flow around cylinders depending on the REYNOLDS number Re_{Cyl} , according to ZDRAVKOVICH [140]

REYNOLDS number Re_{Cyl}		Flow regime	TrZ
lower limit	upper limit		
0	4 – 5	L1	
4 – 5	30 – 48	L2	
30 – 48	180 – 200	L3	
180 – 200	220 – 250	TrW1	(1)
220 – 250	350 – 400	TrW2	
350 – 400	$1 - 2 \times 10^3$	TrSL1	(2)
$1 - 2 \times 10^3$	$20 - 40 \times 10^3$	TrSL2	
$20 - 40 \times 10^3$	$100 - 200 \times 10^3$	TrSL3	
$100 - 200 \times 10^3$	$300 - 340 \times 10^3$	TrBL0	(3)
$300 - 340 \times 10^3$	$380 - 400 \times 10^3$	TrBL1	
$380 - 400 \times 10^3$	$0.5 - 1 \times 10^6$	TrBL2	
$0.5 - 1 \times 10^6$	$3.4 - 6 \times 10^6$	TrBL3	
$3.5 - 6 \times 10^6$	-	TrBL4	
-	-	T1	
-	∞	T2	

Abbreviations: L = laminar; TrZ = transition zone; TrW = transition in wake; TrSL = transition in shear layer; TrBL = transition in boundary layer; T = turbulent

each notation indicating the location of transition. According to Fig. 5.5 the transition zone is approaching the cylinder with increasing REYNOLDS number and for $Re_{Cyl} = 100 \times 10^3 - 200 \times 10^3$ (TrBL (3) – lower Re_{Cyl} limit) it is situated in the region of the separation point. When further increasing Re_{Cyl} it can be found within the boundary layer of the cylinder (TrBL (3) – towards higher Re_{Cyl}). In the latter, the shift from subcritical to supercritical flow con-



Abbreviations: L = laminar; Tr = transition; S = separation; T = turbulent; BL = boundary layer

Figure 5.5 Transition zones depending on Re_{Cyl} , see Tab. 5.2 and Ref. [140]. Left to right: TrW (1); TrSL (2); TrBL (3) – lower Re_{Cyl} limit; TrBL (3) – towards higher Re_{Cyl}

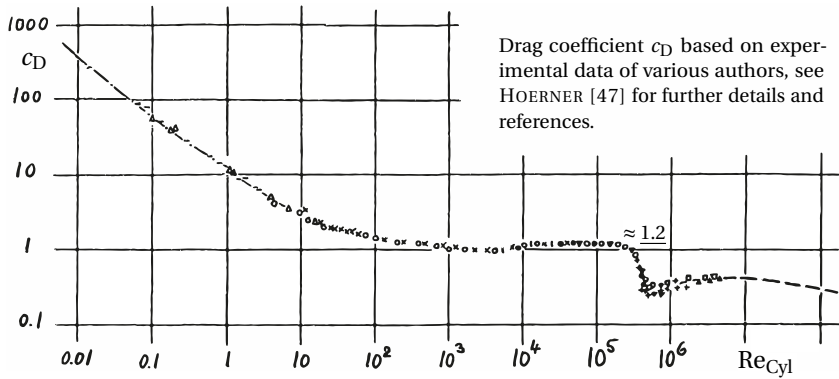


Figure 5.6 Drag coefficient c_D of a circular cylinder in ideal incompressible flow as a function of the REYNOLDS number Re_{Cyl} , according to HOERNER [47]

dition is taking place at a critical REYNOLDS number $Re_{Cyl}^* \approx 3 \times 10^5 - 4 \times 10^5$, HOERNER [47], leading to a crisis in drag force. In Fig. 5.6 this critical state can be found as a drop of the drag coefficient c_D at the critical REYNOLDS number Re_{Cyl}^* . It is accompanied by the formation of separation bubbles on the surface of the cylinder, see Ref. [140]. Due to the fact that the transition takes place close to the cylinder surface, the flow is able to follow the contour more persistently and flow separation is shifted further downstream, compare Fig. 5.5. The pressure recovery around the cylinder is higher and thus a smaller wake downstream of the cylinder is forming. This actually leads to a smaller drag force F_D , in this case mainly caused by the considerably smaller form drag, compare Eq. 5.7, and manifests itself in the drag crisis shown in Fig. 5.6.

It has to be noted that for technical applications like the investigated PSCs, the magnitude of Re_{Cyl} is normally situated below the critical REYNOLDS number, in the present case at approximately 1×10^4 (subcritical regime TrSL (2)), compare to Subsec. 5.3.3. In this range the drag coefficient c_D (5.9) according to Fig. 5.6 is approximately 1.2.

$$c_D = \frac{2 F_D}{\rho_\infty c_\infty^2 A} \quad (5.9)$$

In contrast to the considered idealized disturbance-free flow around cylinders, where the REYNOLDS number has been identified to be the governing parameter, a set of considerably governing and influencing parameters are

found in real flow applications¹⁹. These parameters represent and quantify the wide variety of disturbances that are usually present in this type of flow. It is shown in Ref. [140] that all transition states discussed above can be basically described by the REYNOLDS number, however, their premature initiation and possible modification is dependent on the relevant influencing parameters. In some transition states it is possible that an influencing parameter becomes the governing one, in case it exceeds a certain magnitude. In terms of disturbances, the free stream turbulence is the most common one in practical applications, followed by the surface roughness of the cylinder, possible wall blockage effects and oscillations of the cylinder itself, to name a few. For PSCs the *end effect* becomes apparent, due to the presence of the side walls (blade PS and SS). Here, the aspect ratio of cylinder length to diameter might be an influencing parameter considerable for the transition states.

5.3.2 Compressible Flow

Above, the drag coefficient for fluid flow considered as incompressible has been discussed. This would generally apply for hydraulic turbomachinery as well as gaseous flow for which the magnitude of free stream velocity c_∞ is negligibly small, compared to the sound velocity a . It has been further stated that a governing similarity parameter for the incompressible and disturbance-free flow past circular cylinders is the REYNOLDS number Re_{Cyl} (5.8), which can be used to categorize the flow into laminar, transitional and turbulent.

In most thermal turbomachines the flow is compressible and thus the variability in density has to be considered. Compressible flow is characterized by c_∞ being less, comparable or greater than a , that means an additional similarity parameter arises, which is the MACH number²⁰

$$Ma = \frac{c_\infty}{a}. \quad (5.10)$$

Correspondingly, a flow can be termed subsonic ($Ma < 1$), transonic ($Ma \approx 1$) and supersonic ($Ma > 1$). Transonic flow, characterized by the appearance of supersonic regions within subsonic flow or vice versa, can spread over a wide range of Ma . In particular flow around circular cylinders shows an

¹⁹In Tab. 5.2, the lower and upper limit of the flow regimes are specified by a set of Re_{Cyl} -values, because their definitions are based on experimental data obtained from measurements for which influencing parameters (probably small) are normally being present and thus the actual flow can only be considered as *almost* disturbance-free. A fixed range would only apply for *genuinely* disturbance-free flow, see Ref. [140].

²⁰Named after Austrian physicist and philosopher Ernst MACH (1838–1916), who investigated the motion of objects at supersonic velocity and corresponding sound effects.

extremely wide transonic range from $Ma^* \approx 0.4$, the so-called critical MACH number at which first supersonic regions locally appear near the cylinder surface, up to high supersonic MACH numbers. Fig. 5.7 shows a classification of compressible flow regimes and the corresponding c_D -value according to ZDRAVKOVICH [140]. For $Ma > Ma^*$ compressibility effects start to occur and small regions of supersonic flow arise around the cylinder. In contrast to incompressible flow, no continuous deceleration but discontinuous shock waves are found at the transition between super- and subsonic regions. In accordance with Fig. 5.7, intermittent shock waves, alternating between both sides of the cylinder, are first appearing. Thus, the corresponding separation is moving and triggers a roll-up of free shear layers just downstream of the cylinder, ZDRAVKOVICH [140], which leads to an increase of c_D in regime (2). Within this cycle the shock waves are triggering the flow separation and this is in contrast to incompressible flow around circular cylinders, where the flow separation is governed by deceleration of the flow near the cylinder surface. The elongation of the eddy formation region downstream of the cylinder is responsible for the decrease of c_D in regime (3), see Fig. 5.7. Here, the shock waves are attached to both sides of the cylinder at the same time and during one cycle they only vary in strength but not in location. In regime (4)

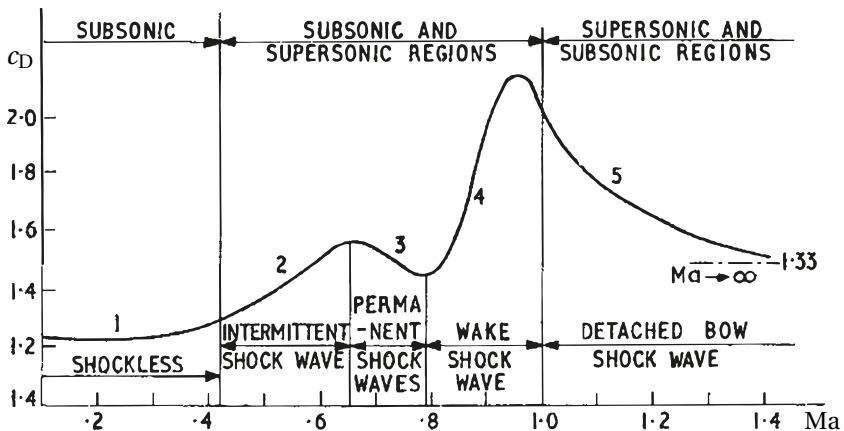


Figure 5.7 Drag coefficient c_D of a circular cylinder in ideal compressible flow as a function of the MACH number Ma and classification of flow regimes, according to ZDRAVKOVICH [140]. (1) "shockless" subsonic flow regime strongly dependent on Re_{Cyl} ; (2) intermittend shock waves alternate on two sides of cylinder; (3) permanent shock waves on both sides; (4) wake shock waves behind tapered near-wake; (5) detached bow shock wave upstream from cylinder

shock waves are present in the wake of the cylinder and basically lead to a strong increase of c_D . For supersonic flow ($Ma > 1$) one final regime (5) can be identified, characterized by a shock wave upstream from the cylinder. In contrast to bodies with sharp LE, for blunt bodies like circular or elliptical cylinders this shock wave is detached and begins to bow with increasing MACH number. This deformation is the reason for the decreasing drag coefficient in this regime, as the flow incidence is decreasing due to the increasing bending. For $Ma \rightarrow \infty$ the drag coefficient is approaching $c_D \approx 1.33$, see Fig. 5.7.

5.3.3 REYNOLDS and MACH Numbers in LP Blading with PSC

In order to classify the investigated steam turbine flow around *circular* PSCs, REYNOLDS and MACH numbers have been evaluated. For Eq. (5.8), the averaged relative inflow velocity w_1 and kinematic viscosity ν_1 in front of R3 at the radial PSC position as well as d_{PSC} were adopted. For the given database (Tabs. B.1 and B.2), the values of Re scatter around an average of 9.3×10^3 (OP-2) and 1.2×10^4 (OP-3). The values of rotor inlet and exit relative MACH number, mass-averaged on evaluation planes E31 and E32 (V1.1), are 0.47/0.50 (OP-2/OP-3) and 0.79/0.98 (OP-2/OP-3), respectively (Tab. 5.4 on Page 131).

5.3.4 Applicability of c_D for Real Flow Applications

Following the above discussions about drag coefficients for circular cylinders in incompressible as well as compressible flow, some additional thoughts on the applicability of these values are necessary, since they are derived from experiments considering an almost disturbance-free (ideal) flow and in contrast are adopted for real flow applications.²¹

From the literature reviewed in Sec. 1.4 it is interesting to learn that lots of authors adjusted their theoretical findings based on experienced deviations from measurements. The outcome of Refs. [21, 31, 50, 64, 65, 123] indicates that the drag coefficients assumed are generally too low and do not sufficiently cover the real flow phenomena and corresponding drag losses. This is e.g. reflected by a statement of TRAUPEL [123], who doubled his theoretical attempt to get better agreement with experimental data (Subsec. 5.4.2). DUNHAM AND PHILLIPSEN [31] on the other hand used an empirical calibration factor to adjust their correlation to reality. Furthermore, they conclude that in their practice, calculations showed that c_D needed to be a function of the MACH number, in order to get acceptable agreement with experiments (Subsec. 5.4.3).

²¹Regarding loss due to PSCs in turbomachinery, DENTON [25] points out that in non-uniform flow the fluid-dynamic drag will strongly differ from the same scenario in uniform flow.

With respect to TRAUPEL's [123] analytical loss correlation and comparisons with CFD, both DUNHAM AND PHILLIPSEN [31] as well as HÄFELE ET AL. [50] certify that the drag coefficient ($c_D = 1.2$) proposed by TRAUPEL [123] for circular PSCs, does by far not account for the real loss magnitude when applied with TRAUPEL's correlation. The same is true regarding c_D -values for PSCs with elliptical cross sections, derived by a correlation of HOERNER [47], see Ref. [50]. The uncertainty on the choice of appropriate c_D -values is also reflected in the paper of CRAIG AND COX [21]. In particular the discussion appended to Ref. [21] implies that c_D -values greater than three (2.5 to 3.3, depending on the radial PSC position) might be necessary to account for the drag losses in 50 per cent reaction blading under real steam flow conditions. In this context, A. SMITH [21] states that for the experimental results of a lower reaction turbine investigated by KIRILLOV AND KUZ'MIČEV [64], needed correction values scatter in the range of 1.5 to 3.4. Based on a large number of experimentally investigated compressors, KOCH AND SMITH, JR. [65] report that the magnitude of drag predicted by their correlation is generally too low and has to be increased by a factor of 1.8.

To conclude the above mentioned uncertainty on the choice of appropriate c_D -values it has to be pointed out that statements like the one of A. SMITH [21] (Subsec. 1.4.2) are rare to find in open literature. Up to the current knowledge, there is no published data available which could be properly used to validate the given correlations or quantify deviations for applications in LP steam turbines. The discussion in Sec. 5.9 will contribute to this field.

5.3.5 Consideration on Numerical Approaches of c_D

Since the numerical assessment of c_D is still fairly inaccurate nowadays, drag coefficients are usually determined based on measurements. With the advent of sophisticated numerical schemes in combination with affordable computing power and also progress in turbulence modelling, a number of publications considering CFD of incompressible flow around circular cylinders for technically relevant REYNOLDS numbers were published in recent years.²²

Out of these, BENIM ET AL. [11] for example performed 2D RANS predictions of incompressible, turbulent flow past a circular cylinder ($Re = 1 \times 10^4$ to 5×10^6) utilizing the standard $k-\varepsilon$ and the SST turbulence model. According to the authors [11], there is still need for applying such economical methods for industrial purposes. A comparison with measurement data shows that even with the SST model the drag coefficients are underestimated to $c_D \approx 0.8$ ($Re = 1 \times 10^4$ to 1×10^5), while qualitatively the drag crisis over the critical regime

²²An overview is given e.g. by BENIM ET AL. [10] and more recently by YUCE AND KAREEM [139].

can be reproduced with this technique, provided that the near-wall region is adequately resolved. The authors [11] blame this deficiency to the fact that the RANS-SST approach does not take into account the organized transient motion. In a subsequent article, BENIM ET AL. [10] present a more comprehensive study by applying various turbulence modelling strategies while keeping the focus on the predictability of c_D . At a REYNOLDS number of 1×10^4 the 2D RANS simulation under-predicts the experimental value, see Fig. 5.8. In contrast, a 2D URANS calculation seemingly over-predicts the drag coefficient. According to BENIM ET AL. [10], this points towards the intimate relationship between the organized transience and three-dimensionality. Thus, the consideration of transient effects within 2D CFD does not necessarily improve the results. On the other hand, 3D transient simulations like 3D URANS, LES and DES showed a substantial improvement, whereby the best agreement was found for LES (Fig. 5.8). Besides these integral results, BENIM ET AL. [10] show the importance of including three-dimensionality in the CFD calculation with respect to the flow structures induced by the cylinder.

Literature shows that the numerical modelling of flow around cylinders is still a challenging task in engineering practice, setting high demands on the CFD model applied. Nevertheless, the given results have mainly indicative meaning, since academic test cases are considered. For the present study, a 3D RANS-SST approach has been chosen, extended by an NES model in order to consider wet steam effects. In the context discussed above, the strategy of using fine structured hexahedral meshes for the blade passages with O-grids around the cylindrical PSCs (Fig. 3.2) in order to properly control the boundary layer grid seems to be the right choice. Details on the numerical modelling strategy and the general approach chosen in this thesis are given in Sec. 3.3. In the light of today's affordable computing power, performing 3D URANS simulations for the investigated LP steam turbine with PSCs is feasible but still highly challenging and was not the scope of this work, in fact disagrees with the concept of providing a simplified CFD model with PSCs for engineering purpose. It is yet an approach that could be investigated in subsequent studies.

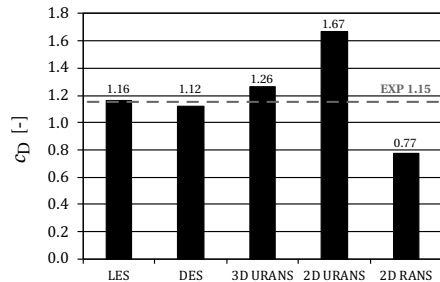


Figure 5.8 CFD results for time-averaged c_D ($Re = 1 \times 10^4$) obtained by different modelling strategies, according to BENIM ET AL. [10]

5.4 Introduction to Loss Correlations for PSCs

In Sec. 1.4, several loss correlations that can be found in literature and aim at estimating the loss induced by PSCs in rotor blading of turbomachines have been introduced. All given approaches are intended for the use in the mean line prediction method²³ and express either the dissipation j , the enthalpy loss Δh_{loss} or the total pressure loss $\Delta p_{t,\text{loss}}$.

In preliminary considerations, the correlations of TRAUPEL [123], DUNHAM AND PHILLIPSEN [31], CRAIG AND COX [21] as well as KOCH AND SMITH, JR. [65] have been identified to have potential relevance for the prediction of loss induced by PSCs in LP steam turbine blading, see KRAUS [67] and TRAXINGER [125]. All mentioned references [21, 31, 65, 123] consider the loss due to a PSC as dissipation j or enthalpy loss Δh_{loss} ²⁴. In contrast, the correlations of DENTON [25], KIRILLOV AND KUZ'MIČEV [63] as well as RZHEZNIKOV AND TROSHCHENKOVA [98] are based on the total pressure loss $\Delta p_{t,\text{loss}}$. These approaches is not given further attention here, since they differ from the above mentioned ones and furthermore, according to the presentations of the authors [25, 63, 98], no satisfying agreement between experimentally or numerically derived results and the corresponding correlation can be expected, compare to Ref. [125] and to the literature review given in Sec. 1.4.

With respect to Refs. [21, 31, 65, 123] it has been found that only the approaches of TRAUPEL [123] and DUNHAM AND PHILLIPSEN [31] can capture the loss due to PSCs in the investigated LP steam turbine rotor blading with acceptable quantitative agreement to 3D CFD results ($\zeta_{\text{PSC,CFD}}$), which is one major outcome of TRAXINGER [125] (Ftn. 31 on Page 67), see Eq. (5.11).

$$\boxed{\zeta_{\text{PSC,CFD}} > \zeta_{\text{PSC,DP}} > \zeta_{\text{PSC,T}}} > \zeta_{\text{PSC,KS}} > \zeta_{\text{PSC,CC}} \quad (5.11)$$

Thus, the present thesis is focusing on these two correlations solely and the approaches of CRAIG AND COX [21] as well as KOCH AND SMITH, JR. [65] are not further pursued. It has to be noted that the principle derivation of these loss correlations [31, 123], as shown in the following subsections, is also partly

²³A mean line velocity triangle calculation is usually performed early in the design process. According to KACKER AND OKAPUU [62] it is "based on the assumption that the thermodynamic process undergone by the working fluid can be represented by velocity triangles at midspan." Such a calculation must naturally also account for aerodynamic losses, in order to output a most realistic flow path. Regarding this matter, KACKER AND OKAPUU [62] state that the mean line loss system of AINLEY AND MATHIESON [5] is perhaps the best known and most completely documented one (later updated by DUNHAM AND CAME [30] and the authors [62] themselves).

²⁴KOCH AND SMITH, JR. [65] consider the dissipation as basis for their correlation and the other authors use the enthalpy loss coefficient (DUNHAM AND PHILLIPSEN [31], TRAUPEL [123]) or an efficiency approach (CRAIG AND COX [21]) to derivate their correlations, see Ref. [125].

included in the publication of HÄFELE ET AL. [50] and more comprehensively in the master thesis of TRAXINGER [125].

5.4.1 Relation of Loss to Drag

The correlations of TRAUPEL [123] and DUNHAM AND PHILLIPSEN [31] are based on the drag force F_D of a circular cylinder in uniform flow. According to Eq. (5.7), the drag force of a PSC can be defined as

$$F_D = 0.5 \rho w_{\text{ref}}^2 c_D A_{\text{PSC}} \approx 0.5 \rho w_{\text{ref}}^2 c_D D_{\text{PSC}} \pi d_{\text{PSC}}. \quad (5.12)$$

Here, w_{ref} is a relative reference velocity, c_D is the drag coefficient of the PSC and A_{PSC} is the blade passage area blocked by the PSC. This blockage area can be approximated with the circular ring area $A_{\text{PSC}} \approx D_{\text{PSC}} \pi d_{\text{PSC}}$ (see Fig. 5.9). The ratio of power loss $P_{\text{loss,PSC}} = F_D w_{\text{ref}}$ (based on the drag force of the PSC (5.12)) to mass flow rate \dot{m} can be used to estimate the enthalpy²⁵ loss, thus

$$\Delta h_{\text{loss,PSC}} \approx T_2 \Delta s = \frac{P_{\text{loss,PSC}}}{\dot{m}} = \frac{F_D w_{\text{ref}}}{\dot{m}}. \quad (5.13)$$

The mass flow rate is calculated with $\dot{m} = \rho A w_{\text{ref}}$, whereby A is the circular ring area defined with hub and shroud diameters D_H and D_S , thus $A = (D_S^2 - D_H^2) \pi / 4$. w_{ref} is assumed to be normal to A . This in combination with Eqs. (5.12) and (5.13) leads to the simplifying approach

$$\Delta h_{\text{loss,PSC}} \approx T_2 \Delta s = 2 c_D w_{\text{ref}}^2 \frac{D_{\text{PSC}} d_{\text{PSC}}}{D_S^2 - D_H^2}. \quad (5.14)$$

As a result, the estimated loss depends on the drag coefficient c_D , the chosen reference velocity w_{ref} as well as the geometry of the investigated rotor and PSC design, see Fig. 5.9. Accordingly, the correlations of TRAUPEL [123] and DUNHAM AND PHILLIPSEN [31], presented and discussed in Secs. 5.4.2 and 5.4.3, solely differ in the definition of c_D and w_{ref} . It has to be considered that all equations presented in the following have been modified to meet the angle convention used at ITSM, see Fig. 5.9. Furthermore, in the present study the shroud diameter D_S instead of the blade tip diameter is used to determine the mass flow rate. Following the general definition in Eq. (5.5) for a rotor blad-

²⁵It has to be noted that in accordance with HÄFELE ET AL. [50], the enthalpy loss $\Delta h_{\text{loss,PSC}}$ due to a PSC is regarded here. In contrast, the loss is considered as dissipation $T_2 \Delta s$ in the derivation of TRAXINGER [125]. Both approaches are equally valid, following the fact that enthalpy and entropy loss coefficients can be equated, see Sec. 5.1.

inlet velocity w_1 is used as reference velocity w_{ref} . With this specification, the coefficient can be formulated as

$$\zeta_{\text{PSC}} = 4 c_{\text{D}} \left(\frac{w_1}{w_2} \right)^2 \frac{D_{\text{PSC}} d_{\text{PSC}}}{D_{\text{S}}^2 - D_{\text{H}}^2}. \quad (5.16)$$

Here, the ratio of rotor inlet to outlet velocity w_1/w_2 can be determined by applying mass conservation

$$\dot{m} = \rho_1 w_1 l_{\text{PSC}} \left(\frac{D_{\text{S}}}{2} - \frac{D_{\text{H}}}{2} \right) = \rho_2 w_{z,2} s (R_{\text{S}} - R_{\text{H}}) = \rho_2 w_2 \cos(\beta_2) s (R_{\text{S}} - R_{\text{H}}) \quad (5.17)$$

and the assumption $\rho_1 = \rho_2$, which is valid for incompressible flow. In addition, a swirl-free inlet condition and a rectangular blade channel is assumed, whereby the channel height equals $R_{\text{S}} - R_{\text{H}}$ and the channel width is approximated with the PSC length l_{PSC} at the channel inlet and the blade pitch s at the channel outlet. Following these simplifying assumptions, the ratio of rotor inlet to outlet velocity w_1/w_2 can be expressed with the relative flow angle β_2 at the rotor outlet, the blade pitch s and the PSC length l_{PSC} . Thus,

$$\frac{w_1}{w_2} = \cos(\beta_2) \frac{s}{l_{\text{PSC}}}. \quad (5.18)$$

Putting Eq. (5.18) into Eq. (5.16) delivers the enthalpy loss coefficient

$$\zeta_{\text{PSC}} = 4 c_{\text{D}} \cos^2(\beta_2) \left(\frac{s}{l_{\text{PSC}}} \right)^2 \frac{D_{\text{PSC}} d_{\text{PSC}}}{D_{\text{S}}^2 - D_{\text{H}}^2}. \quad (5.19)$$

TRAUPEL [123] doubled this theoretical attempt to get better agreement with experimental data. This correction arises from the applied simplifications of an incompressible flow, a swirl-free flow at the inlet ($w_1 = w_{z,1}$), the lacing wire placed shortly behind the inlet and a blade with constant height and pitch. Thus, in the present study TRAUPEL's final approach [123] is used to predict the loss coefficient due to the presence of a PSC in a rotor:

$$\zeta_{\text{PSC,T}} = 8 c_{\text{D}} \cos^2(\beta_2) \left(\frac{s}{l_{\text{PSC}}} \right)^2 \frac{D_{\text{PSC}} d_{\text{PSC}}}{D_{\text{S}}^2 - D_{\text{H}}^2} \quad (5.20)$$

This approach is only dependent on geometrical values and the drag coefficient c_{D} of the PSC. According to the incompressible flow assumption, TRAUPEL [123] suggests a drag coefficient $c_{\text{D}} = 1.2$ for a lacing wire with circular cross section and a reduced coefficient between 0.4 and 0.8 for a lacing

wire with elliptical cross section ($d_{\text{PSC}}^*/d_{\text{PSC}} = 4$). As discussed in Sec. 5.3 and based on Figs. 5.6 and 5.7, these values are only valid for incompressible, subcritical flow and do therefore not account for the compressible, non-uniform flow upstream and around the PSC. For this type of flow, the drag coefficient would be higher and this is the main reason why the correction with a factor of two is required. Another reason is the missing consideration of the cross flow along the PSC axis, as accounted for in the correlation of DUNHAM AND PHILLIPSEN [31], which is discussed in the next section.

5.4.3 Loss Correlation of DUNHAM AND PHILLIPSEN [31]

In their paper, DUNHAM AND PHILLIPSEN [31] identify TRAUPEL's attempt (Subsec. 5.4.2) to be the first published correlation estimating loss due to PSCs. The authors [31] briefly report about their experience with applying this method and conclude that in their practice, calculations showed that the drag coefficient of the PSC needed to be a function of the MACH number, in order to get acceptable agreement with experimental data.

DUNHAM AND PHILLIPSEN [31] split their approach into two loss parts²⁶, namely loss due to diffusion resulting from the flow around the PSC – which is the main loss part – and loss due to the cross flow along the PSC axis and corresponding mixing of the fluid flow near the blade suction side.

$$\zeta_{\text{PSC,DP}} = \zeta_{\text{PSC,DP,diff}} \quad (5.25) + \zeta_{\text{PSC,DP,cross}} \quad (5.30) \quad (5.21)$$

These two basic flow phenomena and corresponding loss sources could be also identified by means of 3D CFD for the LP steam turbine investigated in the present thesis and have been introduced in an earlier publication of HÄFELE ET AL. [54] for condensing steam flow around PSCs. In Figs. 5.15 and 5.16 on Page 126, this flow constellation in rotor R3 with PSC is exemplarily depicted and it is obvious that flow phenomena are present which deviate from TRAUPEL's simple model, as also stated by DUNHAM AND PHILLIPSEN [31] with regard to the investigated turbocharger turbines.

Loss due to Diffusion In order to predict the loss part that results from the drag of the PSC, the authors [31] based their concept on the derivation of

²⁶DUNHAM AND PHILLIPSEN [31] state that their CFD results show the formation of weak shock surfaces above and below the investigated lacing wire on the blade suction side. However, the authors [31] conclude that the additional entropy generation due to these normal shocks does not justify the implementation of a separate modelling approach. This observation and conclusion can be basically confirmed for the LP steam turbine with PSCs investigated here.

TRAUPEL [123], see Eq. (5.19), which basically means a reduction to the general, theoretical loss approach²⁷ described by Eq. (5.14). The decisive contrast to TRAUPEL's theoretical approach is the determination of the reference velocity w_{ref} . Unlike TRAUPEL [123], who assumes a uniform rotor inlet velocity w_1 as reference, the authors [31] consider a pitch-wise variation of the velocity. Based on considerations of the blade loading, DUNHAM AND PHILLIPSEN [31] choose a linear velocity distribution between blade PS and SS. Thus, $\bar{w} = \bar{w}_{\text{PS}} + \left(\frac{\bar{w}_{\text{SS}} - \bar{w}_{\text{PS}}}{l_{\text{PSC}}} \right) y$, whereby the mathematical integration is simplified by considering the Cartesian coordinate y instead of the circumferential direction Θ . Based on the assumption of an incompressible, loss-free flow in a section of unit height, DUNHAM AND PHILLIPSEN [31] derive the tangential force F_{Θ} acting on the blade by using three different approaches, one being the principle of linear momentum between rotor inlet and outlet, one being the pressure force acting on the blade surface and one being the circulation around the profile surface contour, see Ref. [31] for further details. Based on this, the relative mean velocities of the flow around the PSC on blade PS and SS can be formulated.

$$\bar{w}_{\text{PS}} = w_2 \left(\frac{L}{C_z} \cos(\beta_2) - \frac{1}{2} \frac{s}{L} \left(\tan(\beta_1) \cos(\beta_2) - \sin(\beta_2) \right) \right) \quad (5.22)$$

$$\bar{w}_{\text{SS}} = w_2 \left(\frac{L}{C_z} \cos(\beta_2) + \frac{1}{2} \frac{s}{L} \left(\tan(\beta_1) \cos(\beta_2) - \sin(\beta_2) \right) \right) \quad (5.23)$$

Here, L is the blade profile length²⁸ and C_z is the axial blade chord. With respect to the basic loss approach in Eq. (5.14), DUNHAM AND PHILLIPSEN [31] define the reference velocity w_{ref} as root mean square of the local mean velocity \bar{w} along the PSC axis, thus

$$w_{\text{ref}} = \sqrt{\frac{1}{l_{\text{PSC}}} \int_0^{l_{\text{PSC}}} \left(\frac{\bar{w}_{\text{PS}}}{l_{\text{PSC}}} + \frac{\bar{w}_{\text{SS}} - \bar{w}_{\text{PS}}}{l_{\text{PSC}}} y \right)^2 dy}. \quad (5.24)$$

²⁷It has to be noted that DUNHAM AND PHILLIPSEN [31] reference to the PhD thesis of TRAUPEL [120], where this particular loss approach is, however, not traceable. Even so, the correlation for the drag loss given in Ref. [31] can be reduced to the theoretical derivation of the loss coefficient shown in Ref. [123], see Eq. (5.19), whereby the doubling of TRAUPEL's theoretical attempt (5.20) is neglected by DUNHAM AND PHILLIPSEN [31].

²⁸DUNHAM AND PHILLIPSEN [31] assume that $L \approx L_{\text{PS}} \approx L_{\text{SS}}$ and state that its value can be approximated with sufficient accuracy by means of a polygon course along the blade suction side based on distinctive locations (trailing edge, throat, maximum profile thickness, leading edge). According to the authors [31], this approximation is used in SC90T [88] and results in an expression of L/C_z which is only dependent on basic profile parameters.

Applying this definition (5.24) to Eq. (5.14), the coefficient for loss due to diffusion²⁹ can be specified as

$$\zeta_{\text{PSC,DP,diff}} = 4 \frac{c_D}{l_{\text{PSC}} w_2^2} \int_0^{l_{\text{PSC}}} \frac{D_{\text{PSC}} d_{\text{PSC}}}{D_S^2 - D_H^2} \left(\overline{w_{\text{PS}}} + \frac{\overline{w_{\text{SS}}} - \overline{w_{\text{PS}}}}{l_{\text{PSC}}} y \right)^2 dy. \quad (5.25)$$

In contrast to TRAUPEL's correlation (5.20) this approach allows the consideration of PSCs with different diameter or radial extent d_{PSC} along the PSC axis, which is meaningful for the investigated rotor blading with friction bolt and blade reinforcements, see Fig. B.1 (left/middle). Unlike TRAUPEL [123], DUNHAM AND PHILLIPSEN [31] do unfortunately not provide any suggestions regarding the choice of meaningful c_D -values. However, they introduce an empirical calibration factor³⁰ for adjusting their correlation to experimental data, which is not done in the present study. Here, the correlation of loss due to diffusion is considered in its plain form.

Loss due to Cross Flow In order to predict the loss part that results from the cross flow along the PSC axis from blade pressure to suction side and corresponding mixing of fluid flow at the blade suction side, DUNHAM AND PHILLIPSEN [31] utilize a mixing loss approach for perfect gas [25]. Accordingly, two fluid streams with mass flow rates \dot{m}_{cross} and \dot{m}_{SS} , mixing under an angle $\gamma = \arcsin(C_z/C)$, are considered in the following. If $\dot{m}_{\text{cross}} \ll \dot{m}_{\text{SS}}$, which is obviously valid for turbomachinery blading with PSC, a simplified formulation for the entropy rise due to mixing presented by DENTON [25] can be applied, whereby the theory for this simplified approach goes back to SHAPIRO [104]. With the relations $c_p = c_v + R$ and $\kappa = c_p/c_v$ as well as additionally assuming the two mixing streams to have the same total temperature leads to the following definition of specific entropy rise.

$$\Delta s_{\text{cross}} = \kappa R \text{Ma}_{\text{rel,SS}}^2 \left(1 - \frac{w_{\text{cross}} \cos(\gamma)}{w_{\text{SS}}} \right) \frac{\dot{m}_{\text{cross}}}{\dot{m}_{\text{SS}}} \quad (5.26)$$

DUNHAM AND PHILLIPSEN [31] further simplify this approach by assuming uniform total flow conditions at the rotor inlet, thus the cross flow expands to the local flow velocity at the blade suction side and $w_{\text{cross}} \approx w_{\text{SS}}$. The authors [31] moreover assume that the ratio of mixing mass flow rates can be

²⁹It has to be noted that this formulation differs from the one given in Ref. [31], which is due to the fact that DUNHAM AND PHILLIPSEN [31] abstain from normalizing the derived enthalpy loss to the relative kinetic energy at the rotor outlet, resulting in a dimensional coefficient.

³⁰DUNHAM AND PHILLIPSEN [31] do not state the magnitude of the calibration factor.

approximated with the ratio of PSC cross section area and blade channel area, whereby both areas are simplified considered as rectangles. Hence,

$$\frac{\dot{m}_{\text{cross}}}{\dot{m}_{\text{SS}}} = \frac{d_{\text{PSC}}^2}{(R_S - R_H) s}. \quad (5.27)$$

In Eq. (5.26) the mixing angle γ can be expressed with the help of the blade chord length C respectively its decomposition in y - and z -direction and in such a way as

$$\cos(\gamma) = \frac{C_y}{C} = \frac{\sqrt{C^2 - C_z^2}}{C} = \sqrt{1 - \frac{C_z^2}{C^2}}, \quad (5.28)$$

which finally results in the definition of entropy rise applied by DUNHAM AND PHILLIPSEN [31]

$$\Delta s_{\text{cross}}^{31} = \kappa R \text{Ma}_{\text{rel,SS}}^2 \left(1 - \sqrt{1 - \left(\frac{C_z}{C} \right)^2} \right) \frac{d_{\text{PSC}}^2}{(R_S - R_H) s}. \quad (5.29)$$

In their paper, DUNHAM AND PHILLIPSEN [31] consider the loss generated in terms of entropy rise and abstain from calculating a loss coefficient. However, in the present work a comparison in terms of loss coefficients is carried out. The entropy rise Δs_{cross} due to the mixing of cross flow and main flow at the blade suction side can be directly considered within the formulation of the entropy-based loss coefficient (5.6). With $\zeta \approx \zeta_s$ (Sec. 5.1), the enthalpy-based coefficient can be finally written as

$$\zeta_{\text{PSC,DP,cross}} \approx 2 \frac{T_2}{T_{\text{SS}}} \frac{\overline{w_{\text{SS}}}^2}{w_2^2} \left(1 - \sqrt{1 - \left(\frac{C_z}{C} \right)^2} \right) \frac{d_{\text{PSC}}^2}{(R_S - R_H) s}, \quad (5.30)$$

whereby the relative MACH number is expressed as $\text{Ma}_{\text{rel,SS}} = \overline{w_{\text{SS}}} / \sqrt{\kappa R T_{\text{SS}}}$.

³¹It has to be noted that in contrast to this definition of Δs_{cross} , DUNHAM AND PHILLIPSEN [31] included an empirical calibration factor for adjusting the formulation out of theory to experimental data, which is not meaningful for the present study and thus is neglected here.

5.4.4 Evaluation of Loss Correlations

In Sec. 5.9, a detailed comparison of CFD results to the analytical loss correlations of TRAUPEL [123] and DUNHAM AND PHILLIPSEN [31] is carried out. To evaluate the correlations and to compare them to the CFD results afterwards, geometric parameters of the PSC and the turbine as well as averaged values of the CFD results are required.

Basic Turbine Data According to TRAUPEL [123] and based on Fig. 5.9, blade pitch s as well as blade inlet and exit angles β_1 and β_2 have been taken at the mean radius (also referred to [13] as EULER radius)

$$R_{\text{mean}} = \sqrt{\frac{R_H^2 + R_S^2}{2}}, \quad (5.31)$$

dividing the annulus area into two ring cross-sections of the same area. Hub and shroud diameters D_H and D_S have been evaluated at the axial reference³² position $Z_{\text{PSC,ref}}$ (Fig. B.1) of the standard configuration V1.1 (Tab. B.1). In addition, the blade profile length³³ L and blade chords C and C_z have been captured at the mean radius.

PSC Parameters The PSC length l_{PSC} and the radial position D_{PSC} have been directly taken from the rotor design.

Due to the fact that the PSC in CFD model *PSC-1* consists of a friction bolt and blade reinforcements, the PSC diameter or extent is actually not constant. Therefore, in order to evaluate TRAUPEL's correlation (5.20), equivalent quantities d_{eqv} and d_{eqv}^* , based on the cross section areas normal to the axial and radial direction as well as the overall PSC length, have been introduced (Fig. B.1 and Tab. B.1). By this means, the complex PSC geometry of *PSC-1* is virtually transformed to a simple lacing wire with the same blockage area. Accordingly, the equivalent diameter d_{eqv} replaces the PSC diameter d_{PSC} in Eq. (5.20). However, the lacing wire configuration in *PSC-2* features constant diameters and thus d_{LW} and d_{LW}^* have been used for the loss prediction.

In contrast, DUNHAM AND PHILLIPSEN's [31] correlation (5.25) for loss due to diffusion allows to consider a PSC with different diameter levels and thus an approximation to the real PSC geometry of *PSC-1* shown in Fig. B.1 (middle). For evaluating Eq. (5.25), the PSC is split into three parts. However, since the part diameters are actually not constant (conical friction bolt and fillet at

³²All values referring to the standard configuration V1.1 are indexed with *ref*.

³³In their derivation of $\overline{w_{\text{PS}}}$ (5.22) and $\overline{w_{\text{SS}}}$ (5.23), DUNHAM AND PHILLIPSEN [31] assume that $L_{\text{PS}} \approx L_{\text{SS}}$. For the blading investigated in the present work, the lengths at blade pressure and suction side have been measured in CAD and an averaged value $L = (L_{\text{PS}} + L_{\text{SS}})/2$ is used.

the junction of reinforcement and blade), separate equivalent diameters are calculated for each part, using the corresponding blockage area and length. It has to be mentioned that for each part also the drag coefficient is considered separately, see determination of drag coefficients in the next paragraph. In contrast to *PSC-1*, the actual diameters d_{LW} and d_{LW}^* of the lacing wire are applied for predicting the loss of PSC configuration *PSC-2*.

As mentioned above, DUNHAM AND PHILLIPSEN'S [31] correlation (5.30) for loss due to cross flow considers the ratio of PSC cross section and blade channel area, simplified as rectangle, in order to approximate the ratio of mixing mass flow rates. For evaluating this loss part it has to be considered that for PSCs with elliptical cross sections, generally $d_{PSC} \times d_{PSC}^*$ is used instead of d_{PSC}^2 . Furthermore, a particular thought has to be spend on configuration *PSC-1*. Since only the friction bolt considerably contributes to the loss due to cross flow³⁴, and its presence gives shelter to the downstream low-energy fluid that is carried towards the blade suction side, only the equivalent diameters of the bolt are used in Eq. (5.30). For configuration *PSC-2* the original diameters d_{LW} and d_{LW}^* of the lacing wire are applied.

Drag Coefficients For PSCs with circular cross section, a drag coefficient $c_D = 1.2$ according to TRAUPEL [123] is used, which is valid for incompressible and subcritical ($Re < 3 - 4 \times 10^5$) flow. The drag coefficients for PSCs with elliptical cross section were determined according to an empirical correlation of HOERNER [47, p. 3–11] as

$$c_D = 2 \times 0.0075 \left(1 + \frac{d_{PSC}^*}{d_{PSC}} \right) + 1.1 \frac{d_{PSC}}{d_{PSC}^*}, \quad (5.32)$$

which is valid for incompressible and subcritical flow. This attempt was chosen because TRAUPEL [123] only suggests a drag coefficient in the range of 0.4 to 0.8 for PSCs with elliptical cross sections and an aspect ratio of $d_{PSC}^*/d_{PSC} = 4$.³⁵ Similar to the use of equivalent PSC diameters in TRAUPEL'S loss correlation (5.20) when considering *PSC-1*, d_{eqv} and d_{eqv}^* replace the PSC

³⁴The pressure-sided blade reinforcement might, however, have the potential to support the formation of cross flow. As indicated by MISTRY ET AL. [82], the fillet radius between the blade and a PSC with roughly constant radius and continuous geometry (no steps), provides a platform for this secondary flow, which was investigated in an LSB with teardrop-shaped snubbers by means of 3D CFD, see Subsec. 1.4.4. However, no cross flow will form if only the blade reinforcements are present within the flow channel of the turbine investigated in the present work.

³⁵This aspect ratio can be recalculated to $c_D = 0.35$ using HOERNER'S [47] correlation (5.32). Vice versa, TRAUPEL'S upper boarder $c_D = 0.8$ leads to an aspect ratio $d_{PSC}^*/d_{PSC} \approx 1.5$, which corresponds to the largest aspect ratio of elliptical PSC configurations investigated in the present work, see Tabs. B.1 and B.3.

diameters d_{PSC} and d_{PSC}^* in HOERNER's correlation (5.32). With respect to the fact that $\zeta_{\text{PSC,DP,diff}}$ (5.25) is evaluated separately for the friction bolt and each blade reinforcement, the drag coefficient for each of the three PSC parts has to be determined. For the lacing wire of CFD model *PSC-2*, d_{LW} and d_{LW}^* are used to evaluate Eq. (5.32).

Aero-Thermodynamic Data TRAUPEL's correlation (5.20) is just a function of the blade, PSC and flow channel geometry, whereas DUNHAM AND PHILLIPSEN (5.21) also consider aero-thermodynamic quantities. On the one hand, this results from the fact that a different approach for the inlet velocity is used. On the other hand it is associated with the additional consideration of loss due to cross flow. Thus, thermodynamic state variables and velocity components have to be extracted from the CFD results.

Determination of the relative velocity w_2 at the rotor exit (evaluation plane E32) was done as described in Subsec. 3.4.4. The static temperature T_2 of the wet steam flow at the rotor exit was gained by area-averaging the static pressure p_2 on plane E32 and applying IAPWS-IF97 [134] afterwards. Finally, the static temperature T_{SS} is needed, which was extracted as an area-averaged value on the blade suction side.³⁶

5.5 Non-Equilibrium Condensation Effects

Nowadays, there is the ambition to consider wetness in the design process of LP steam turbine blading and aside from aerodynamic issues, also optimize the turbines towards decreasing wetness losses, see e.g. LI ET AL. [75]. For the present work, the non-equilibrium condensation of steam was modeled by applying an NES model within the CFD code. As discussed in Sec. 3.2, this enables the consideration of wetness loss (here: thermodynamic loss) that arises in LP stages of condensing steam turbines. Up to the current knowledge, HÄFELE ET AL. [54] were the first to apply such a model for LP steam turbines with PSCs. Although it is a state-of-the-art modelling approach for wet steam, the use of conventional EQS is still very common in industrial practice.

The present section is based on the discussion in Ref. [54] on non-equilibrium condensation effects due to the presence of PSCs and further clarifies the significance of this additional feature compared to the overall PSC loss, which is predominantly governed by aerodynamic effects. This is done especially with the focus on the PSC parameter study presented later.

³⁶In evaluation plane E32, static pressure and temperature of the two-phase flow are coupled, see Fig. A.2. In contrast, on the blade SS surface the fluid is superheated, due to local dissipation.

Table 5.3 CFD-based, volume-averaged/maximum values of subcooling ΔT (≥ 0)

	OP-1	OP-2	OP-3	OP-4
ΔT [K] in S2	– / 20.9	– / 25.7	– / 29.9	1.9 / 44.1
ΔT [K] in R2	0.1 / 45.0	5.0 / 48.6	8.0 / 51.4	5.9 / 46.1
ΔT [K] in S3	3.8 / 28.2	3.8 / 35.7	3.0 / 33.7	1.3 / 26.5
ΔT [K] in R3	1.0 / 25.5	1.0 / 48.8	1.5 / 49.9	2.2 / 50.0

5.5.1 Overview on Condensation in Three-Stage LP Turbine

As discussed in Sec. 3.2, in real steam turbine flow the fall below the saturation line leads to a temporary thermodynamic non-equilibrium, characterized by subcooling ΔT (Fig. 3.4). This non-equilibrium state results in a delayed onset of condensation. A maximum of droplet formation per volume and time can

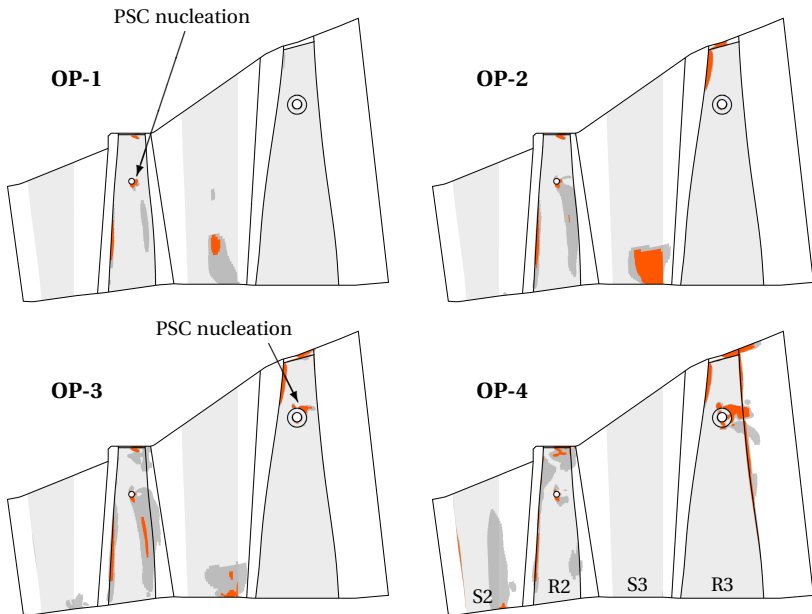


Figure 5.10 Meridional view of last and penultimate LP stage with PSC, including regions of CFD results with high nucleation rates $J \geq 1 \times 10^{15}$ [$\text{m}^{-3} \text{s}^{-1}$] ■ and $J \geq 1 \times 10^{22}$ [$\text{m}^{-3} \text{s}^{-1}$] ■

be expected in regions of maximum subcooling. Concerning nucleation within the investigated turbine, Fig. 5.10 gives an overview for all investigated operating points (note that only the last two stages are depicted). High nucleation rates J are present throughout the rotor R2 and in the hub region of stator S3, which is valid for OP-1 to OP-3. For OP-4 the main regions of high nucleation are shifted upstream and can be found in the hub to mid-span region of stator S2 and in rotor R2 between the lacing wire and the shroud. Further notable nucleation occurs in the hub section of rotor S3. Due to the presence of the PSCs, additional regions of high nucleation rates can be found just downstream of the PSCs. This supplementary *PSC nucleation* is discussed below. Besides these nucleation phenomena, the analysis of the CFD results shows area-averaged wetness fractions $\gamma \approx 1\%$ (OP-1), 2.8% (OP-2), 4.3% (OP-3) and 7.5% (OP-4) downstream of rotor R3 in evaluation plane E32.

5.5.2 PSC Nucleation

Present CFD results (Fig. 5.10) and conclusions from Ref. [54] indicate that non-equilibrium condensation of steam is affected by the presence of PSCs. Accordingly, it is recommended to include the PSCs within the numerical model, if nucleation and corresponding losses are of interest.

Rotor R2 The following discussion considers the lacing wire in rotor R2 according to Ref. [54]. The cross flow along the PSC axis, strongly accelerating from blade PS to SS, and the vortices formed (Fig. 4.12) lead to wetness phenomena which originate in the wake of the PSC. In order to evaluate the impact of the PSC on non-equilibrium condensation, additional computations without the wire in rotor R2 have been performed by the authors [54]. Fig. 5.11 shows the nucleation rates on a span-wise plane at the radial PSC position for the cases with and without lacing wire (note that a logarithmic scale is used). In the region of the cross flow (Fig. 4.12), near the blade suction side, the high pressure drop in the wake leads to high expansion rates and the nucleation rates are pushed to magnitudes two orders higher than for the case without PSC. The same behavior is found when looking at re-

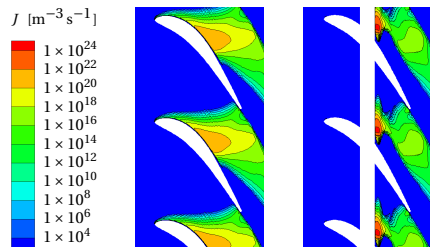


Figure 5.11 PSC nucleation: Comparison of nucleation rates in rotor R2 with and without lacing wire, HÄFELE ET AL. [54]

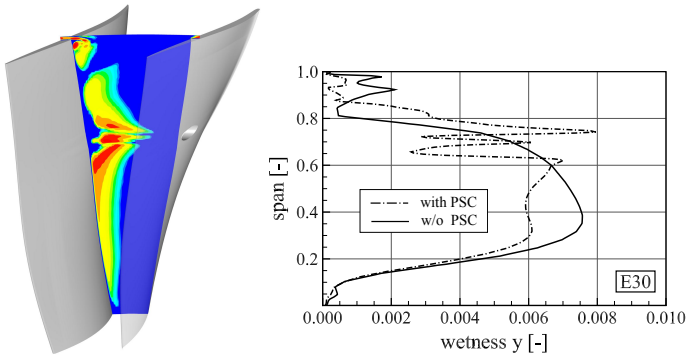


Figure 5.12 Nucleation in rotor R2 just downstream of the lacing wire (contour labels according to Fig. 5.11) and wetness in plane E30, HÄFELE ET AL. [54]

gions below and especially above the radial position downstream of the lacing wire, see Fig. 5.12 (left). When considering the radial wetness distribution in evaluation plane E30 (Fig. 5.12, right), three significant wetness peaks can be seen, which correspond to high nucleation rates within the blade passage at these span heights. Overall, the wetness y in plane E30 is found to be lower for the case with lacing wire. This corresponds to higher pressure and enthalpy in this plane.

Rotor R3 Fig. 5.10 shows local conglomerations of high J in proximity to the PSC in R3 (near the blade SS) for all OPs except for OP-1 (denoted with *PSC nucleation*). The principle context regarding their origination can be transferred from the considerations with the LW in rotor R2, see explanation above. However, the effect is less pronounced in rotor R3. CFD results show that here, the overall level of thermodynamic non-equilibrium is lower than in R2 (see Tab. 5.3), since latent heat is released due to condensation on already existing droplets (the onset of condensation is further upstream), allowing the subcooling level to collapse. Typically, no further significant droplet formation is taking place and wetness is increased solely by droplet growth.

By means of Fig. 5.13 it can be seen that the liquid mass fraction y in front and behind rotor R3 is lower for the case with PSC. This corresponds to higher pressure and enthalpy in these planes. It was found by HÄFELE ET AL. [54] that the expansion of the steam in stator S3 occurs at a lower pressure ratio i.e. higher backpressure in plane E31 due to the presence of the PSC in R3, which causes blocking of the steam flow and the mean static pressure in plane E31 to rise. Fig. 5.1 schematically shows the change of expansion characteristic in the LSB. Besides this general wetness shift, the pattern of the wetness distribution

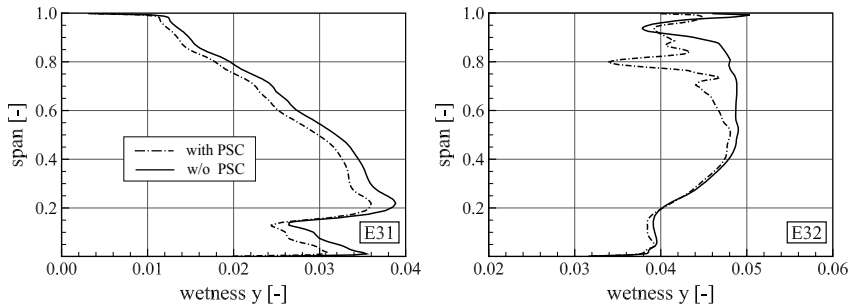


Figure 5.13 Span-wise wetness distribution up- and downstream of rotor R3 (OP-3)

in E32 can be drawn back to local changes due to wakes and vortices in the flow. When consulting 3D CFD results on an axial plane just downstream of the PSC, local wetness peaks and drops can be detected. However, this information is lost in Fig. 5.13 (right) due to averaging. In contrast to rotor R2, no significant wetness peak in this circumferentially averaged data can be clearly attributed to the detected supplementary PSC nucleation.

5.5.3 Thermodynamic Wetness Loss

Among the three main contributors to wetness loss according to GYARMATHY [42], the present numerical scheme only considers thermodynamic loss, as discussed in Sec. 3.2. Since the liquid and the gaseous phase share the same velocity field, a consideration of kinematic relaxation loss and breaking loss is not feasible with this CFD approach.³⁷

The calculation of thermodynamic wetness loss follows the *entropy method* based on the second law of thermodynamics, see Ref. [113]. Here the condensing flow through the turbine is considered as adiabatic with internal heat exchange between the phases. The mass specific thermodynamic loss j_{th} is calculated by entropy production rate \dot{S}_{th} times a mean temperature T_m between the vapor and liquid phase, evaluated for each control volume and integrated over the whole domain. Thus,

$$j_{th} = \frac{1}{\dot{m}} \int_{vol} T_m \dot{S}_{th} dV = \frac{1}{\dot{m}} \int_{vol} T_m \left(\frac{\dot{Q}}{T_c} - \frac{\dot{Q}}{T_d} \right) dV. \quad (5.33)$$

³⁷Besides thermodynamic loss, the release of condensation heat leads to a reduction of flow velocity and a change of flow angles, relevant for the incident flow of the downstream blade row, STARZMANN ET AL. [113]. This can induce additional aerodynamic loss and might be relevant for the design process, since the use of an EQS model will predict differing operating points.

Here, \dot{Q} is the heat flux between the droplets with a temperature T_d and the vapor with a temperature T_c . The heat flux is given by the latent heat L multiplied by mass transfer rate $\dot{m}_{c/d}$ per volume, see STARZMANN ET AL. [114]. The consequence of Eq. (5.33) is a low thermodynamic loss generation, if the thermal non-equilibrium and thus the subcooling level of the steam is small.

CFD-based results of the thermodynamic loss j_{th} discussed below are considered in relation to the aerodynamic loss j_{aero} of the corresponding stage (normalized to the difference in aerodynamic loss Δj_{aero} between both cases).³⁸ j_{aero} is calculated as difference between specific isentropic dissipation loss j_s and the thermodynamic loss. Thus,

$$j_{aero} = j_s - j_{th} . \quad (5.34)$$

Following the schematic expansion process depicted in Fig. 5.3, the specific isentropic dissipation loss is basically defined as

$$j_s = \Delta h_{loss} = h_{out} - h_{out,s} . \quad (5.35)$$

Rotor R2 The following results are derived from the three-stage CFD calculations with and without the lacing wire in rotor R2, compare to Ref. [54]. Because wetness is low in the penultimate stage, the thermodynamic losses are relatively small here and there is almost no difference in j_{th} when comparing both cases (j_{th} is slightly higher for the configuration with LW, see Fig. 5.14). In the last stage, thermodynamic losses are generally higher than in the penultimate stage. However, the presence of the LW in the penultimate stage actually leads to a reduction of thermodynamic loss in the last stage and also when balancing over both stages combined. This can be explained by the higher nucleation rate within the blade passage in the wake of the wire, see Fig. 5.11, which leads to a larger number of droplets per volume (N) and also to smaller droplets (droplet diameter D)

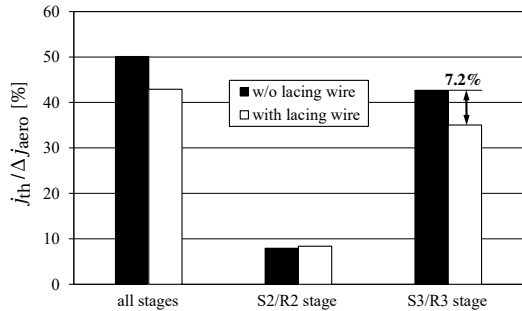


Figure 5.14 Thermodynamic wetness loss in three-stage LP steam turbine with and without PSC in rotor R2, HÄFELE ET AL. [54]

³⁸The normalization to Δj_{aero} is meaningful because as such, the overestimation of j_{aero} can directly be shown.

in plane E30. When considering the interfacial area density $\beta_1 = N\pi D^2$, which represents the area of droplet surface per volume, the reduction in thermodynamic wetness loss can be understood. The numerical results downstream of rotor R2 show that β_1 is significantly higher in case the wire is present. Thus, in the last stage, where the droplet growth takes place, the heat transfer between the liquid and gaseous phase is improved. This leads to condensation at lower subcooling ΔT in the last stage. As a result, the thermodynamic loss in the last stage is reduced. This also means that if the lacing wire in the penultimate stage is not present, the subcooling and in conclusion the entropy production rate \dot{S}_{th} (see Eq. 5.33) is higher than for the setup with wire. Consequently, in the investigated case the described scenario leads to an overestimation of aerodynamic loss j_{aero} ($\Delta j_{th}/\Delta j_{aero} \approx 7.2\%$, see Fig. 5.14), when modelling non-equilibrium condensation without taking into account the PSC of the penultimate stage in the CFD model.

Rotor R3 With regard to the PSC study in the last stage carried out for OP-2 and OP-3 (Sec. 5.7) it is important to know that the presence of the PSC in R3 affects the non-equilibrium condensation process, leading to additional small nucleation zones. The major effect of the PSC on the thermodynamic wetness loss is the general shift to lower wetness in this stage due to a change of expansion characteristic, as mentioned above. Overall, less thermodynamic loss is being produced in the LSB when FB & BR are accounted for in the CFD model, in average $\Delta j_{th}/\Delta j_{aero} \approx 3.5\%$ (OP-2) and 4.5% (OP-3) among the investigated configurations. However, regarding the variation of $\Delta j_{th}/\Delta j_{aero}$ among V1.1 to V1.11 it is found that the deviations are limited to approximately 1%. Compared to the overall loss, the thermodynamic loss in the last stage is still relatively small ($j_{th} \approx 0.1 j_s$). Hence, a separate detailed evaluation for each PSC configuration is not justified, at least not for the present study, and is therefore not examined in the following section. Still, it has to be kept in mind that this loss part is inherent in the presented CFD results.

5.6 Vortex System in Rotor R3 with PSC

Chap. 5 deals with loss due to PSCs in LP steam turbine blading. Vortices, which form downstream of blunt bodies like PSCs, are an indicator for this additional loss and its magnitude. Some remarks on vortices in turbomachines have been already given in Chap. 4. There, major vortex sources in the investigated turbine are identified and the flow phenomena and corresponding effects on the flow field downstream of rotors with PSCs are discussed. It

is found that the loss due to vortices induced by these sources can be seen downstream in total pressure drops in the corresponding evaluation planes (Figs. 4.8 to 4.11). Furthermore, the comparison between experimental and numerical results shows that the CFD model is well able to capture the wake and vortices in rotors with PSC in terms of total pressure reduction in appropriate span regions. In consequence, this fairly good agreement implies that CFD based evaluation of total pressure loss caused by PSCs is suitable for this case, which is also obvious when comparing area-averaged 1D values (Tab. 4.1). Following the discussion in Chap. 4, the present section covers a more detailed examination of the PSC-related vortices in rotor R3 with FB & BR or a simple LW. This prepares the reader towards the performance assessment of different PSC designs in Sec. 5.8.

5.6.1 Friction Bolt (FB) & Blade Reinforcements (BR)

According to HÄFELE ET AL. [50], the vortex structure induced by the FB & BR in rotor R3 (Figs. 5.15 and 5.17) can be divided into three different main vortices, whereby their size, interaction and orientation varies depending on the PSC geometry. Out of the three vortices, the vortex at the blade suction side (PSC Vortex SS) is the biggest one. It is mainly caused by the BR as well as the cross flow along the PSC axis and encloses a wake downstream of the BR. The second vortex (PSC Vortex FB) is caused by the FB and rolls up at approximately mid channel position. The smallest vortex forms at the blade pressure side (PSC Vortex PS) and is caused by FB & BR.

5.6.2 Lacing Wire (LW)

According to Figs. 5.16 and 5.18, the vortex structure induced by the LW in rotor R3 differs from the one discussed in the paragraph above and can be divided into four different main vortices, whereby their size, interaction and orientation varies depending on the PSC geometry. Out of the four vortices, the biggest one (Lower LW Vortex) rolls up near the blade suction side. It is mainly caused by the cross flow along the PSC axis and primary fed from fluid pushed below the PSC. The second vortex (Upper LW Vortex) rolls up at approximately mid channel position, partly supplied by cross flow fed from below and enhanced by fluid stream above the PSC. In addition, two smaller vortices form at the blade suction side (Upper & Lower SS Vortex).³⁹ While the Lower SS Vortex is mainly caused by the cross flow along the PSC axis

³⁹In contrast to rotor R3 with LW, the Upper & Lower SS Vortex is not pronounced in rotor R2 with LW and thus not depicted in Fig. 4.7.

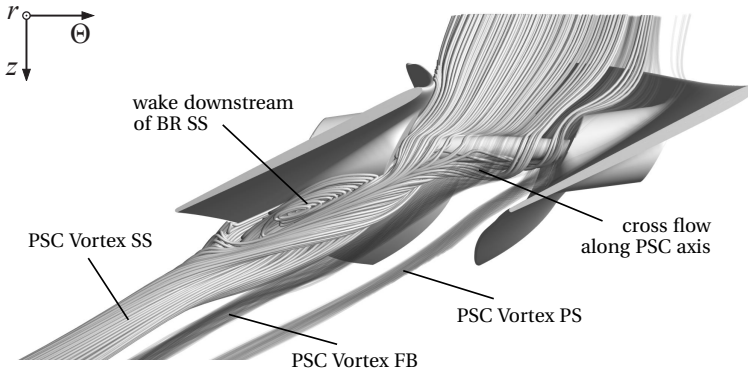


Figure 5.15 Flow around a friction bolt (FB) and blade reinforcements (BR) in rotor R3 (top blade view), HÄFELE ET AL. [50]

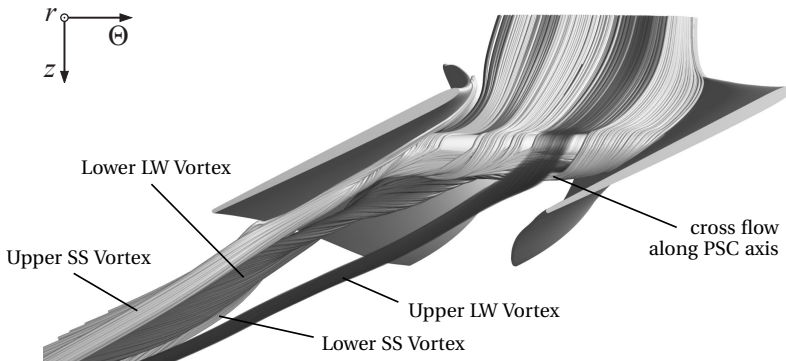


Figure 5.16 Flow around a lacing wire (LW) in rotor R3 (top blade view)

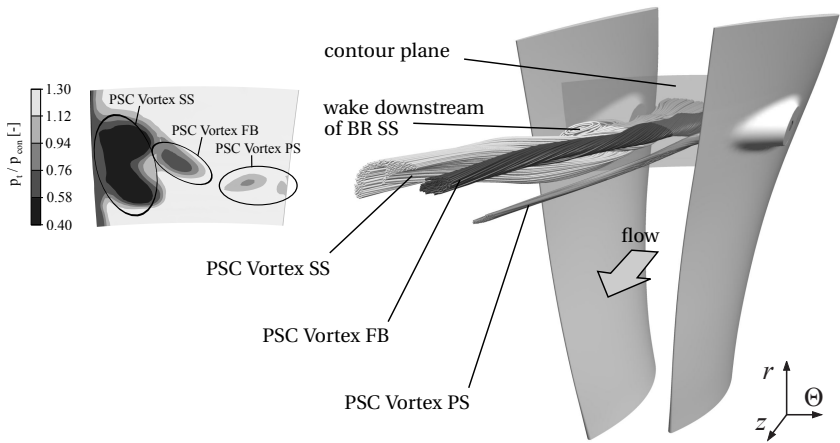


Figure 5.17 Flow around a friction bolt (FB) and blade reinforcements (BR) in rotor R3 (isometric blade view) and total pressure downstream of the PSC, HÄFELE ET AL. [50]

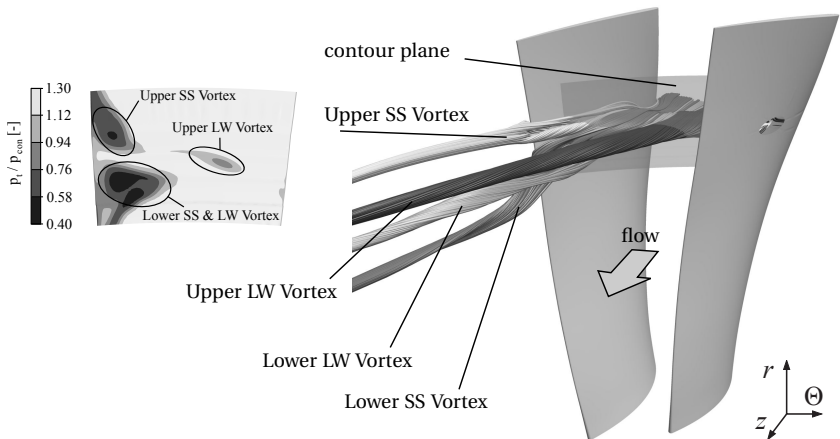


Figure 5.18 Flow around a lacing wire (LW) in rotor R3 (isometric blade view) and total pressure downstream of the PSC

and pushed down to lower span when leaving the rotor, the Upper SS Vortex is straight and predominantly caused by fluid passing the PSC in main flow direction. Upper & Lower SS Vortex interact near the blade SS and can be seen as a single loss agglomeration in the total pressure contour plot just downstream of the PSC (Fig. 5.18) before leaving the blade passage.

5.7 Introduction to PSC Parameter Study

In the further course of this work, a huge variety of PSC configurations is analyzed and assessed in terms of lost work output compared to a freestanding blade configuration. This is done with the main focus on the available potential for efficiency improvements and in order to analyze the loss sensitivity on global PSC parameters (Sec. 5.8). Moreover, 3D CFD results are compared to analytical loss correlations from literature (Sec. 5.9). The built up database provides thorough insights into the loss due to PSCs in LP steam turbine blading. It is the purpose of the present section to briefly introduce the variations of PSC configurations and OPs investigated within this PSC parameter study.

5.7.1 Review of Investigated PSC Variations

The basic relation of loss to drag, as derived in Subsec. 5.4.1, identifies the main PSC parameters which have a first order effect on the magnitude of generated loss. Accordingly, the following preliminary conclusions relevant for the choice of PSC parameters and the results presented later can be drawn. Based on Eq. (5.14), the loss $\Delta h_{\text{loss,PSC}}$ due to a PSC will be reduced by ...

- decreasing the **PSC diameter** d_{PSC} .
- adjusting the **cross-sectional PSC shape** to decrease c_D .
- mounting it at a lower **radial PSC position** D_{PSC} .

In addition to these three major variations of PSC configurations, two additional ones of subordinate importance, namely a variation of *axial PSC position* and *zigzag PSC angle*, are presented.

Details of the parameterized PSC models are given in Subsec. 3.3.2. Two different, basic PSC concepts are considered in this work. One is the friction bolt (FB) mounted between blade reinforcements (BR) \rightarrow *PSC-1* and the other one is the lacing wire (LW) \rightarrow *PSC-2*. Results and conclusions derived with the latter, more simplified PSC geometry can be used to supplement findings with the first one and also allow to make more generalizing statements. As a basis,

the present work adopts the geometrical FB & BR variations considered by HÄFELE ET AL. [50], see Tab. B.1 and Fig. B.1 (left). Moreover, this is extended by numerous LW variations, see Tabs. B.2 to B.4 and Fig. B.1 (right). Aforementioned figures and tables provide a thorough overview on the geometrical PSC parameters, cross sections and corresponding drag coefficients. All presented PSC variations were chosen solely due to aerodynamic aspects and do not consider any mechanical constraints.⁴⁰

PSC Diameter A variation of PSC diameter at constant span is conducted to investigate the influence of PSC blockage area on the loss. In order to evaluate this relationship, three different LW diameters are studied in addition to the configurations of FB & BR. The diameters d_{LW} are equivalent to the ones derived from the blockage area of three different FB & BR configurations, see Tabs. B.1 and B.3 and compare Figs. 5.38 and 5.39.

Cross-Sectional PSC Shape A variation of PSC cross section shape aims at revealing the effectiveness of streamlined PSCs (ellipsis and tear-drop) in complex 3D flow in LP turbine blading. The elliptical shape is additionally investigated as a configuration inclined to the meridional flow direction.

Besides the PSC diameter and shape, the PSC position within the flow channel plays a major role. This is due to the fact that for one thing it can affect the PSC blockage area and on the other hand it governs the velocity i.e. kinetic energy the PSC is facing.⁴¹

Radial PSC Position A variation of radial PSC position aims at the varying flow conditions along the span of the highly twisted and tapered LP blade (Fig. 1.5, left) and in this context the span-wise variation of blade profile (Fig. 5.22) and degree of reaction (Fig. B.9). Furthermore, this modification affects the blockage area, whilst keeping the PSC diameter constant. Due to geometric limitations in the parameterized CFD model *PSC-1*, FB & BR are varied over a relatively small span portion while the configuration with LW considers a wider span-wise variation of the PSC position down to mid-span.

⁴⁰PSC diameter and position are key parameters related to the dynamic behavior of the blade system. While considering relevant mode shapes of the LSB, the axial and radial PSC position have to be chosen carefully. The focus of mechanical FB and LW design normally is on optimal structural damping and blade coupling and thus contact forces between blade and PSC, mainly resulting from a combination of PSC mass (PSC dimension and material) and radial PSC position.

⁴¹ESTABROOK AND LEGER [36] for example report about IST improvements for GE's 20-inch last stage bucket and mention loose tie wires relocated to a lower velocity region for improved performance and increased structural damping as one design enhancement.

In addition, the variation of *axial PSC position* at reference span is investigated, in order to draw conclusions regarding the impact of chord-wise PSC location on the stage performance. Finally, a *zigzag PSC configuration* at reference span is studied. Such zigzag mounting of the PSC is an alternative blade coupling concept (Fig. 1.10) with aerodynamic features rarely investigated.

5.7.2 Review of Investigated Operating Points

As a first approximation it is valid to claim that generally speaking, loss due to PSCs is increasing with turbine operating parameters such as pressure ratio, mass flow rate or outlet MACH number, i.e kinetic energy the PSC is facing, as indicated e.g. by KIRILLOV AND KUZ'MIČEV [64]. To account for this tendency, the loss due to PSC variations introduced in Subsec. 5.7.1 is investigated for two different operating points **OP-2** and **OP-3**, whereby OP-2 shows almost swirl-free outflow (Figs. 4.8 and 5.22) and OP-3 has an approximately 30% higher mass flow rate (Tab. 2.2). These representative OPs were chosen because they cover a wide, relevant operating range of the turbine from BEP up to moderate overload condition (see Fig. 2.6) and allow to study the loss due PSCs not only geometry-dependent but also dependent on the flow conditions in the last turbine stage. Tab. 5.4 summarizes basic stage parameters. For the complex flow in the investigated blading it is, however, not obvious at all that the loss variation can be directly scaled or reduced to these parameters. Besides direct effects on the loss quantity it is moreover obvious that the varying flow conditions affect the characteristic of the vortex system and thus the loss composition, see Fig. 5.19.

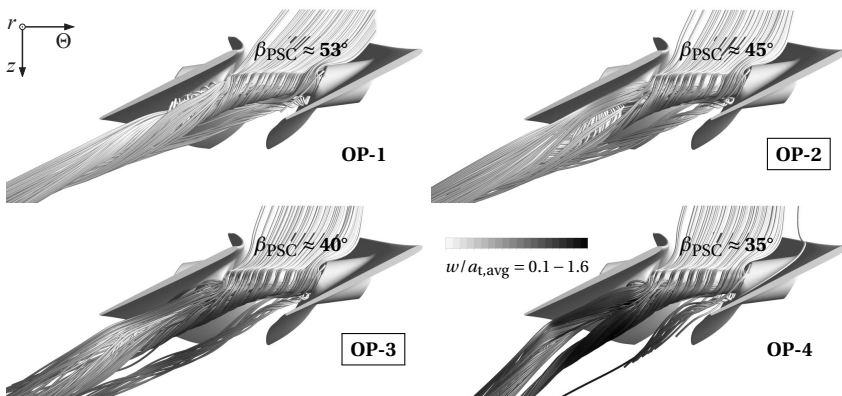


Figure 5.19 Vortex systems for reference PSC configuration V1.1

Table 5.4 Characteristic values of operating points OP-2 and OP-3 as well as of OPs investigated by HÄFELE ET AL. [50] and TRAXINGER [125] at 80% nominal speed, based on CFD results of one-stage configuration V1.1 (Tab. B.1)

	OP-2	OP-[50]	OP-3	OP-[125]
flow coefficient $\varphi/\varphi_{\text{opt}}$	1.10	1.25	1.40	1.40
mass flow rate $\dot{m}/\dot{m}_{\text{design}}$	0.89	1.00	1.16	1.16
pressure ratio $p_{t,30}/p_{32}$	2.03	2.33	2.73	2.75
pressure ratio $p_{t,30}/p_{t,32}$	1.78	1.94	2.17	2.15
MACH number $\text{Ma}_{\text{rel},31}$	0.47	0.49	0.50	0.51
MACH number $\text{Ma}_{\text{rel},32}$	0.79	0.89	0.98	1.02
steam model (CFX)		NES		EQS

According to Figs. 5.19 to 5.21, the distinctive flow features described in Sec. 5.6 can be basically found for all four OPs.⁴² Nevertheless, it is evident that the manifestation of vortex structures is different across the investigated operating range. Based on these results three major characteristics in vicinity to the PSC can be detected. 1) With increasing OP the inflow angle β_{PSC} just upstream of the PSC gets steeper, corresponding to an increasing axial flow velocity due to increasing turbine capacity (volume flow rate). 2) Interesting to see is the bending and redirecting of stagnation streamlines approaching the cylindrical PSC. Similar observations are described by ZDRAVKOVICH [141, p. 966] for visualization of stagnation streamlines by means of smoke. According to the author [141] the streamlines gradually bend as they approach the stagnation line of a yawed cylinder in incompressible flow ($\text{Re} = 3.1 \times 10^3$) and pass the cylinder at almost right angle to the cylinder axis. While in the present case (Fig. 5.19) the PSC inflow angle (β_{PSC}) strongly depends on the

⁴²In order to get the full picture, part load (OP-1) and extreme overload (OP-4) is also regarded.

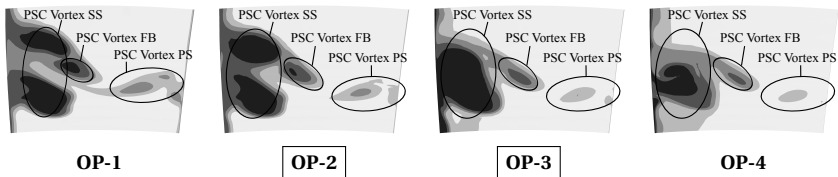


Figure 5.20 Total pressure contour (67.5% to 87.5% span, see Fig. 5.17) downstream of PSC, scaled from plane-wise $p_{t,\text{max}}$ to $p_{t,\text{min}}$ at the respective OP

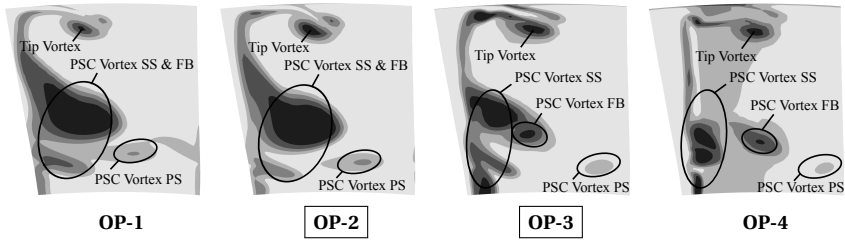


Figure 5.21 Total pressure contour on axial plane (67.5% to 100% span) $1.3 d_{BR}^*$ downstream of PSC, scaled from plane-wise $p_{t,max}$ to $p_{t,min}$ at the respective OP

OP and decreases from approximately 53° to 35° with increasing OP, the PSC passing angle is only moderately altered (approximately 25° to 15°), meaning the redirecting of stagnation streamlines gets lesser towards overload.⁴³ 3) Downstream of the PSC, the wake space is narrow at part load and vortices are concentrated near the blade SS. Towards overload the wake gets broader. Here, vortices are more bended towards the PS and slightly pulled apart, leading to less interaction between FB and SS Vortex. From Figs. 5.20 and 5.21 it is evident that the relative strength of FB⁴⁴ and PS Vortex is reduced. Here the relative pressure drop from plane-wise $p_{t,max}$ (0% drop) to $p_{t,min}$ (100% drop) at the respective OP is plotted.

As indicated earlier, the pressure gradient between blade PS and SS is the main driving force for the cross flow. Generally speaking, as the blade loading increases with increasing OP, compare to plots of chord-wise blade loading in the blade span region of the PSC (Fig. B.5), the cross flow gets stronger. However, especially at part load this driving force is low, as here the pressure gradient is low. Nevertheless, the flat relative inflow angle β_{PSC} pushes mass flow and the whole vortex system towards the blade SS, see Fig. 5.19 (top left). This leads to the conclusion that the system is sensitive to the inflow direction and towards part load, the cross flow is enhanced by the yawed inflow direction.

Two additional OPs have to be examined here. 1) TRAXINGER [125] based his CFD investigations on an operating point corresponding to OP-3. However, the author [125] performed EQS simulations, resulting in slightly different operating conditions (see STARZMANN [112]) and no consideration of wetness loss. 2) HÄFELE ET AL. [50] performed experimental and numerical investigations with an OP between OP-2 and OP-3. However, the authors [50] chose a

⁴³Both flow angles are being measured to the perpendicular of the PSC axis.

⁴⁴Note that the FB Vortex is an indicator for the relative strength of the cross flow.

higher inlet temperature (+20 K in plane E10) for their experiments in order to obtain superheated steam conditions in probe traversing plane E30 (CFD inlet boundary). Tab. 5.4 compares most relevant stage parameters.

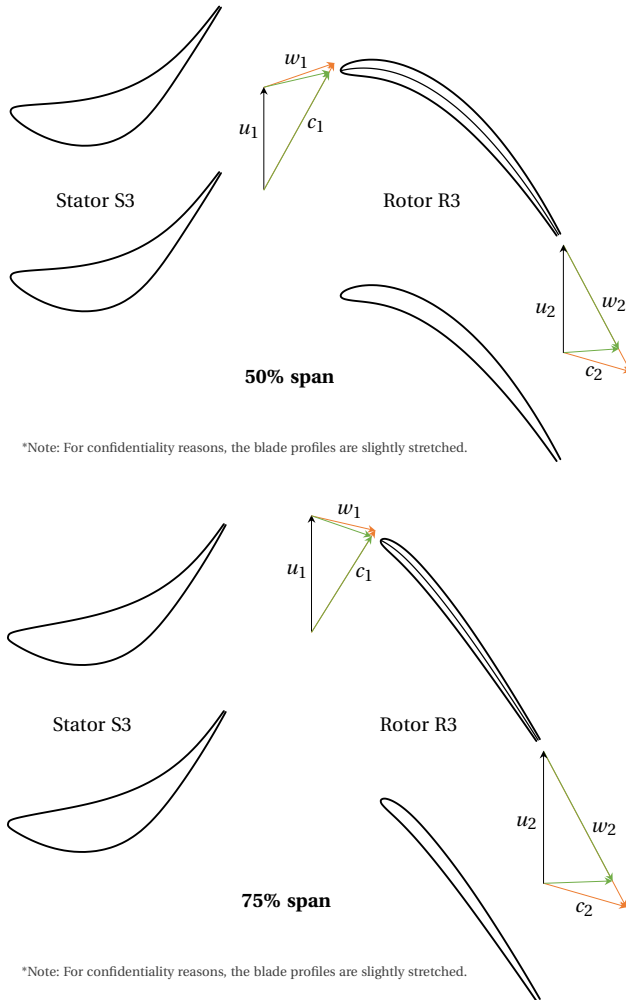


Figure 5.22 Exemplary blade profiles at 50% ($D_{\text{PSC}}/D_{\text{PSC,ref}} = 0.67$) and 75% span ($D_{\text{PSC}}/D_{\text{PSC,ref}} = 1$) with flow velocity components at **OP-2** (BEP) and **OP-3** (overload)

5.8 Performance Assessment of PSC Designs

Following the introduction to the PSC study in Sec. 5.7, a huge variety of PSC designs is analyzed and assessed in the following. This is done with the main focus on the available potential for efficiency improvements and the loss sensitivity on global PSC parameters. The built up database provides thorough insights into the loss due to PSCs in LP steam turbine blading.

The specific work output w/w_{V0} (Subsec. 3.4.3) was chosen as performance indicator, since being a direct measure of PSC loss and thus the preferable quantity for evaluating the given 3D CFD results. As a basis, the outcome of w/w_{V0} from HÄFELE ET AL. [50] and TRAXINGER [125] (Tab. 5.4) is summarized in Fig. 5.23. The reduction of work output due to a PSC is between 2.5% and 5%. Details will be discussed in the following, whereby these former findings are merged to the given extended study. The PSC geometry V1.1 of a typical SIEMENS LP IST blade (Fig. 1.5, left) is considered as reference PSC configuration. Fig. 5.24 shows that for OP-2 (BEP) the work output is reduced by 3.6%, while at overload condition OP-3 the work output is diminished by 4.9%. Besides these reference values, CFD results of w/w_{V0} are ranging from 1.3% to 3.6% for OP-2 and 1.5% to 4.9% for OP-3, see Figs. 5.24 to 5.28.

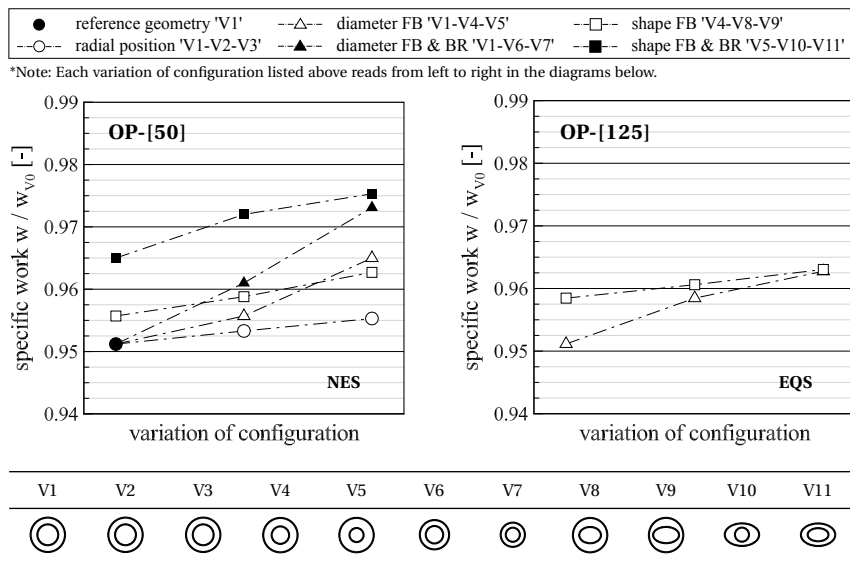


Figure 5.23 Comparison of work output for PSCs investigated by HÄFELE ET AL. [50] and TRAXINGER [125] – V1 to V11 correspond to V1.1 to V1.11 according to Tab. B.1

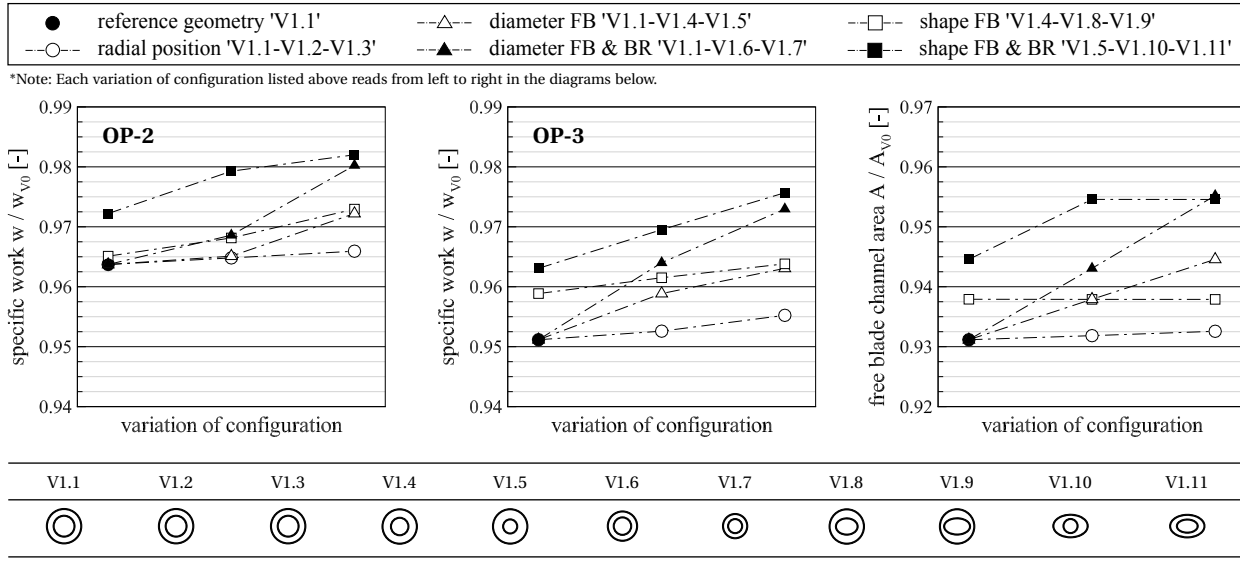


Figure 5.24 Work output at operating points **OP-2** and **OP-3** and free blade channel area for PSC configurations with friction bolt (FB) and blade reinforcements (BR) according to Tab. B.1 and HÄFELE ET AL. [50]

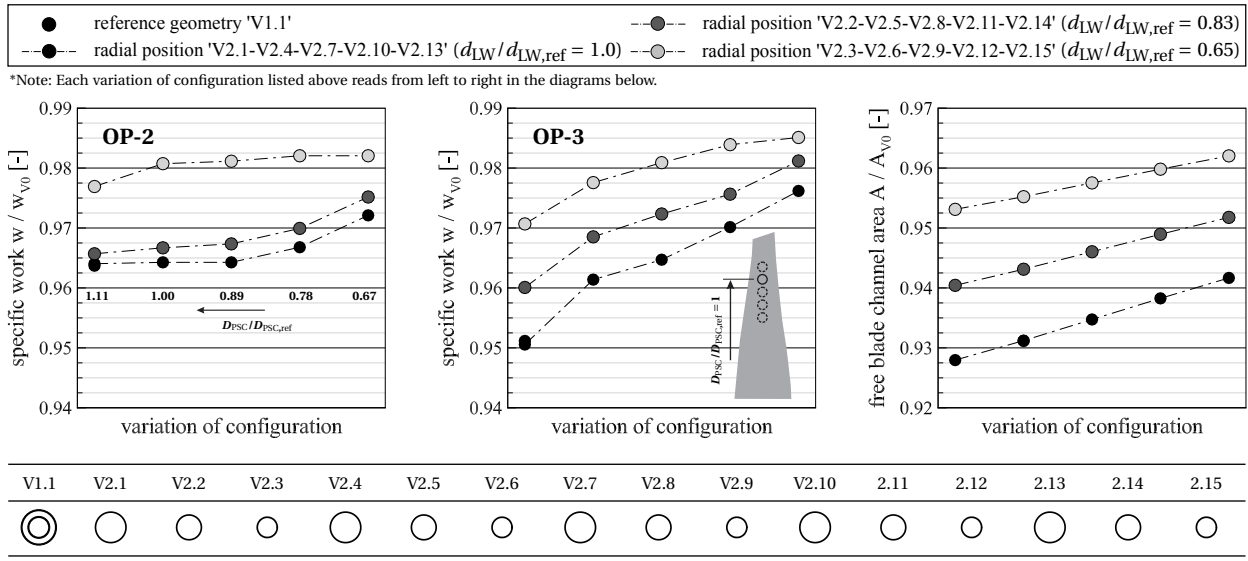


Figure 5.25 Work output at operating points **OP-2** and **OP-3** and free blade channel area for PSC configurations with lacing wire (LW) according to Tabs. B.2 and B.3 – Variation of **radial PSC position** $D_{PSC}/D_{PSC,ref} = 1.11, 1, 0.89, 0.78$ and **0.67** at **three** PSC diameters $d_{LW}/d_{LW,ref} = 1.0, 0.83$ and 0.65

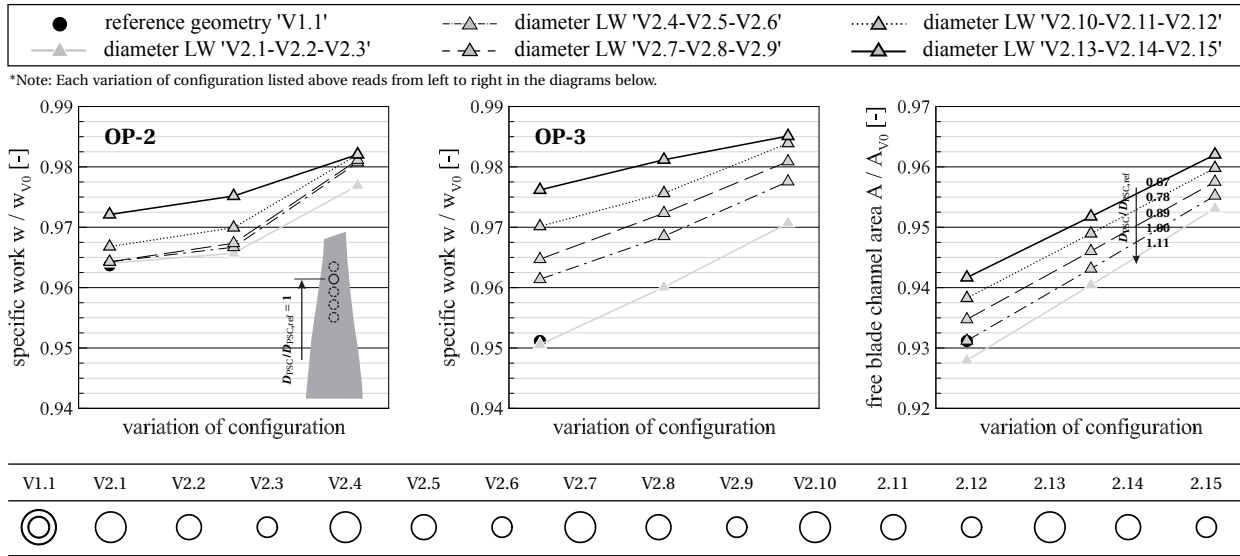


Figure 5.26 Work output at operating points **OP-2** and **OP-3** and free blade channel area for PSC configurations with lacing wire (LW) according to Tabs. B.2 and B.3 – Variation of PSC diameter $d_{LW}/d_{LW,ref} = 1.0, 0.83$ and 0.65 at **five** radial PSC positions $D_{PSC}/D_{PSC,ref} = 1.11, 1, 0.89, 0.78$ and 0.67

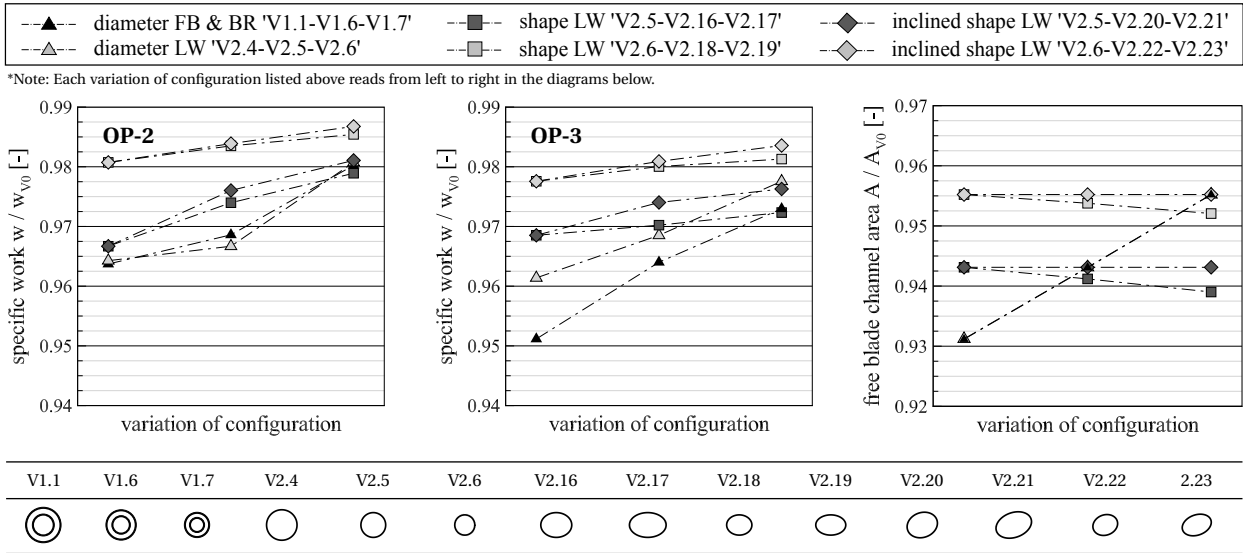


Figure 5.27 Work output at operating points **OP-2** and **OP-3** and free blade channel area^a for PSC configurations with lacing wire (LW) according to Tabs. B.2 and B.3

^aFor elliptical LWs the blockage area is derived by projection on a plane inclined by 20° to an axial plane. With increasing aspect ratio of the ellipse, the blockage area is increased.

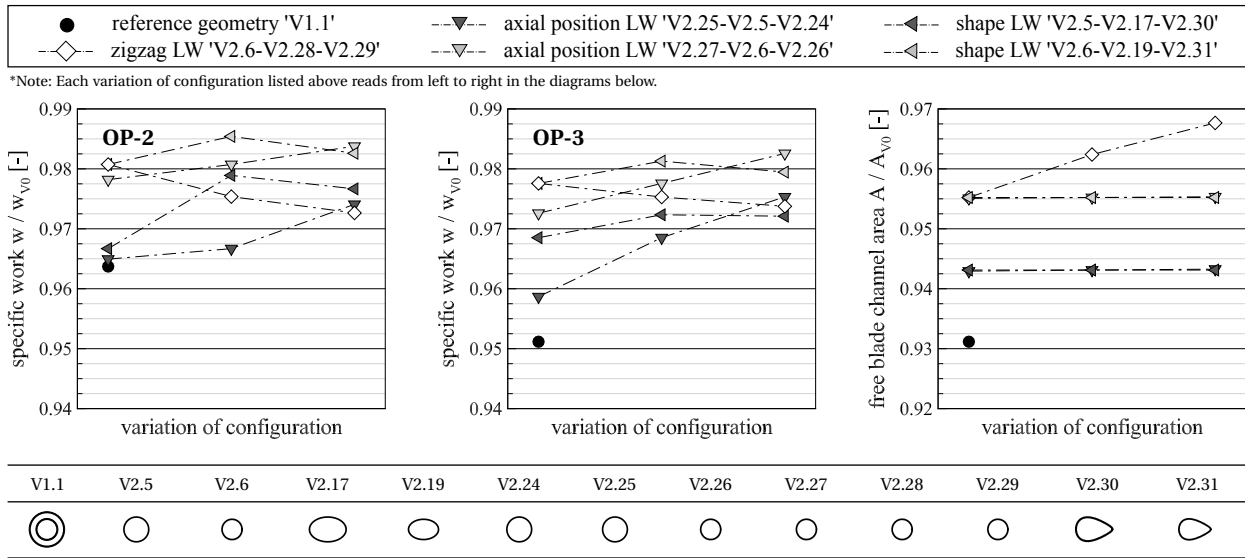


Figure 5.28 Work output at operating points **OP-2** and **OP-3** and free blade channel area for PSC configurations with lacing wire (LW) according to Tabs. B.3 and B.4

5.8.1 Radial PSC Position

Regarding a modification of radial PSC position, two key messages can be extracted from preceding investigations [50]. **1)** According to Fig. 5.23 (left), a lowering of the radial PSC position ('V1-V2-V3') increases the work done linearly. **2)** This loss reduction can be mainly drawn back to a decrease of the blockage area, compare to Fig. 5.24 (right).

Friction Bolt (FB) & Blade Reinforcements (BR) Regarding the two statements given above, it has to be considered that HÄFELE ET AL. [50] covered only a relatively small span range of approximately 4% span ($D_{PSC}/D_{PSC,ref} = 1.0/0.99/0.98$) by their radial PSC variation within CFD model *PSC-1* (FB & BR). Basically, their results can be confirmed by the present study, compare Figs. 5.23 (left) and 5.24. For OP-3, a positioning of the PSC at 4% lower span ('V1.1-V1.3') gives a gain in work output of approximately 0.4%, which corresponds well to Ref. [50] and the linear decrease of blockage area. For OP-2 (BEP) the increase of work is less (approx. 0.2%).

Lacing Wire (LW) A more generalizing view can be gained from results with CFD model *PSC-2* (LW), where the span-wise extent of PSC variation is considerably larger ($D_{PSC}/D_{PSC,ref} = 1.11/1.0/0.89/0.78/0.67$). Fig 5.25 shows that obtained CFD results have to be treated with diversity in such a wide span range. For both OPs the magnitude of loss due to the LW is depending on its blade span position and is particularly high for a wire mounted at high span, i.e. closer to the shroud.⁴⁵ This implies a dependence of loss on the degree of reaction, compare to Fig. B.9.⁴⁶ Globally, the proclaimed linearity can be confirmed for OP-3, while for OP-2 obvious deviations from a roughly linear trend exist. Overall, losses for OP-2 are less sensitive to a change of radial PSC position than for OP-3.

The streamline plots exemplary depicted in Figs. 5.29 and 5.30 for 50% and 75% span show that the PSC is exposed to varying flow conditions. At mid-span the PSC is facing a steeper inflow angle β_{PSC} compared to the reference span position (see also Fig. B.6, middle). Furthermore, the vortex system is altered. Similar observations (yawed versus unyawed cylinder) can be made when altering the OP (Fig. 5.19) or considering a zigzag PSC (Fig. 5.55).

⁴⁵This is in contrast to KIRILLOV AND KUZ'MICEV [63] who obviously investigated an HP turbine stage in hot air with an "older" blade concept following the free vortex design (see Ftn. 12 on Page 14) with stage reactions of 0.10 and 0.48 at hub and shroud, respectively.

⁴⁶In the investigated LSB, the stage reaction decreases linearly from shroud towards mid-span, according to Fig. B.9. Fig. 5.22 exemplary shows the corresponding change of blade profile from a high reaction passage to a typical 50 per cent profile within the considered span range.

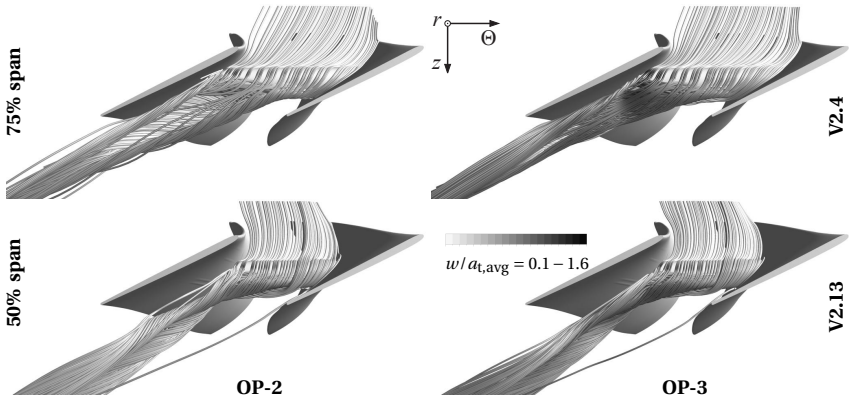


Figure 5.29 Vortex systems for radial PSC variation ($d_{LW}/d_{LW,ref} = 1.0$)

Besides the span-wise variation of aerodynamic stage parameters (Figs. B.6 to B.9), the change of PSC blockage area or free blade channel area is obviously governing the loss.⁴⁷ Fig. 5.25 shows that a strong linear correlation exists for moderate overload condition (OP-3). When keeping the PSC diameter constant, the linear decrease of blockage area is synonymous with a linear decrease of PSC length l_{PSC} , compare to Tabs. B.1 to B.3.

Compared to OP-3, the overall work gain at OP-2 when lowering the radial PSC position is less (Fig. 5.25, left). Here, in contrast to OP-3, the average slope is less. Thus, as stated above, the PSC loss is less sensitive to the radial PSC position. Furthermore, an erratic increase of w/w_{V0} between curves for $d_{LW}/d_{LW,ref} = 0.83$ and $d_{LW}/d_{LW,ref} = 0.65$ can be observed. The same behavior is visible in Fig. 5.26 (left) when plotting these results as a function of d_{PSC} and is discussed in Subsec. 5.8.2 on PSC diameter variation.

OP-Dependency (Inversed Loss Tendency) From basic fluid dynamic considerations it would be normally expected that at OP-3 the normalized specific work output w/w_{V0} is generally lower than at OP-2, i.e. losses due to PSCs are higher because of increased stage parameters (e.g. higher mass flow density, MACH number, stage reaction, etc., compare to Tab. 5.4 and radial traverse data in Sec. B.2). The general tendency of increasing PSC loss with increasing turbine operating parameters is pointed out in relevant literature, see e.g. KIRILLOV AND KUZ'MIČEV [63] and was also experienced in previous

⁴⁷As stated by HÄFELE ET AL. [50], the increase in specific work when lowering the radial PSC position can be mainly drawn back to an increase of free blade channel area, Figs. 5.23 and 5.25.

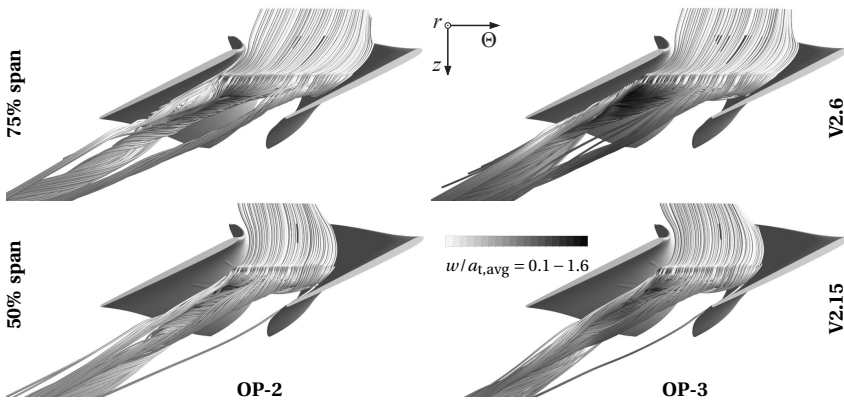


Figure 5.30 Vortex systems for radial PSC variation ($d_{LW}/d_{LW,ref} = 0.65$)

numerical investigations [54] with the reference geometry V1.1. Moreover, this trend is confirmed for the majority of PSC variations at reference span ($D_{PSC}/D_{PSC,ref} = 1.0$) investigated in the present work. However, from specific work plots in Fig 5.25 it can be learned that this tendency is not generally followed along the span and is only valid for higher radial PSC positions ($D_{PSC}/D_{PSC,ref} \geq 0.89$, depending on the PSC diameter $d_{LW}/d_{LW,ref}$). For lower spans down to mid-span this relation is inverted and subsequently w/w_{V0} is higher for OP-3, meaning PSC losses are lower. These observations (Fig 5.25) are confirmed by the net blade torque in Figs. 5.32 (right) and 5.33 (right).

The reason for this *inversed loss tendency* can be found in a span-wise redistribution of the steam flow due to the presence of the PSC and corresponding altered torque generation. This PSC-related effect was already pointed out by HÄFELE ET AL. [54]. For evaluation of span-wise 1D values, the blade span has been divided into 13 segments in order to meet the pattern of radial PSC variation. The plots in Figs. 5.31 to 5.33 show the span-wise (re-)distribution of averaged mass flow rate and torque.

In the following, the PSC diameter $d_{LW}/d_{LW,ref} = 1.0$ is discussed. Similar conclusions apply to PSC diameter $d_{LW}/d_{LW,ref} = 0.83$. At OP-2 and $D_{PSC}/D_{PSC,ref} = 1.10$ the local torque reduction (i.e. at the span segment where the PSC is located) is larger than at OP-3, see Fig. 5.32 (red-colored bars). This is obviously valid for all radial PSC positions (red, orange, yellow, green, blue). In return, torque is recovered over a wide span range, while at OP-3, torque is solely recovered in the blade tip region and even reduced at lower spans. Overall, at $D_{PSC}/D_{PSC,ref} = 1.10$ this results in less net torque reduction for OP-2

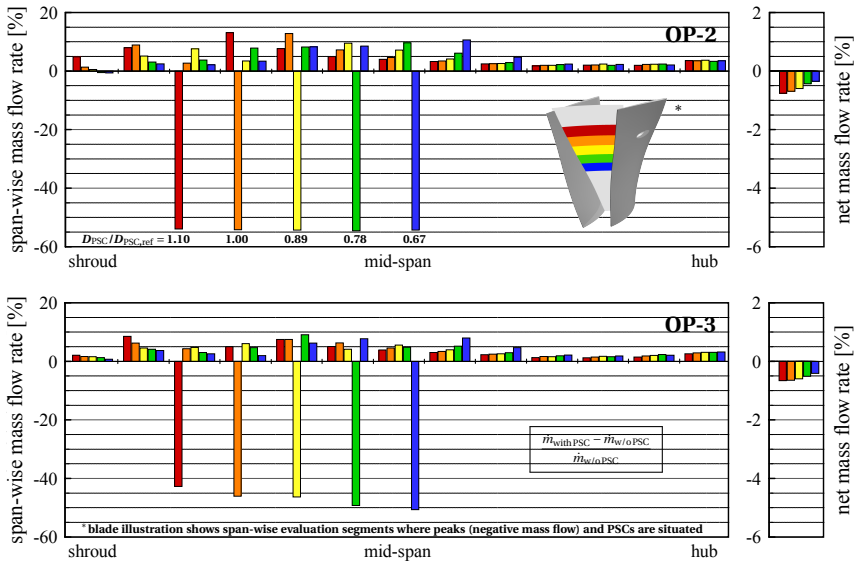


Figure 5.31 Relative mass flow rate for radial PSC variation ($d_{LW}/d_{LW,ref} = 1.0$)

than for OP-3 (Fig. 5.32, right) and accordingly higher work output. When lowering the radial PSC position down to mid-span, this torque tendency is altered and the relation of net torque is inverted for $D_{PSC}/D_{PSC,ref} = 0.67$, meaning higher output for OP-3.

This redistribution of torque can be mainly attributed to a span-wise redistribution of mass flow rate. From Fig. 5.31 it gets obvious that for OP-2 the mass flow rate locally blocked in the region of the PSC stays more or less constant for all radial PSC variations and thus is independent from the radial PSC position. This is different for OP-3. Here, a proper linear increase of the local PSC blockage effect can be detected when lowering the radial PSC position down to mid-span. Although the local blocking effect at OP-2 and $D_{PSC}/D_{PSC,ref} = 1.10$ is larger, the redistribution of mass flow rate is more advantageous for torque generation than it is at OP-3. For OP-2 and $D_{PSC}/D_{PSC,ref} = 0.67$ the opposite effect takes place and leads to a disadvantageous torque distribution with understated specific work output.

For PSC diameter $d_{LW}/d_{LW,ref} = 0.65$ slightly different conclusions have to be drawn. While at OP-3 the trend of work versus radial PSC position is similar for all PSC diameters (Fig. 5.25, middle), at OP-2 the specific work output for the smallest diameter develops different along the span (Fig. 5.25, left). Except

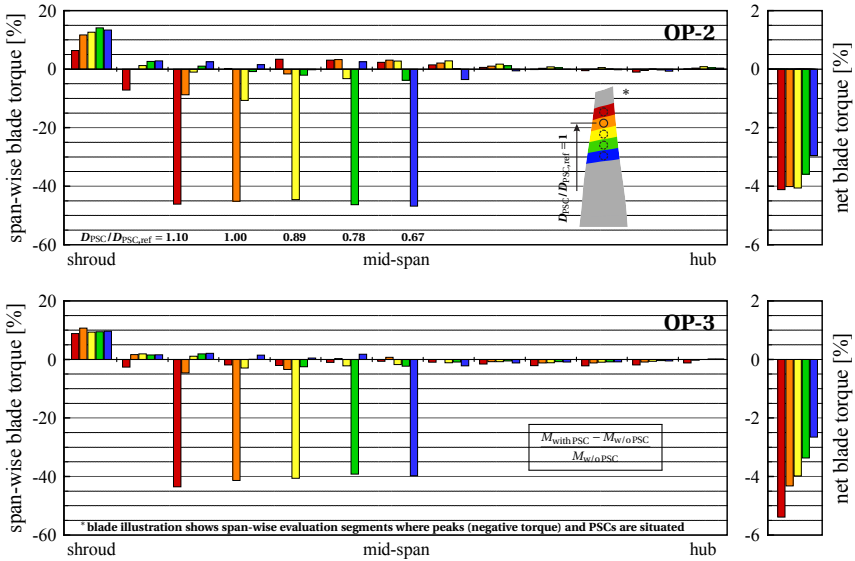


Figure 5.32 Relative blade torque for radial PSC variation ($d_{LW}/d_{LW,ref} = 1.0$)

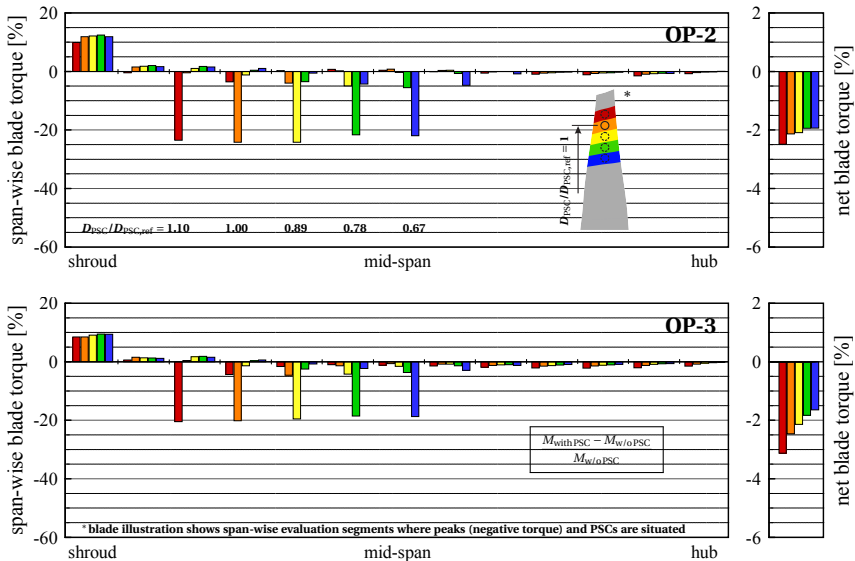


Figure 5.33 Relative blade torque for radial PSC variation ($d_{LW}/d_{LW,ref} = 0.65$)

for the drop at the highest radial PSC position, a fairly linear trend can be seen. In contrast to OP-3 the slope is less, meaning the PSC loss is less sensitive to the radial PSC position. The plot of span-wise torque provides insights into this specific feature. At OP-2 the local torque reduction at the respective radial PSC position is generally larger than at OP-3, see Fig. 5.33. The same was found for $d_{LW}/d_{LW,ref} = 1.0$ discussed above and this is obviously valid for all radial PSC positions, whereby the magnitude of local drop is rather independent from the radial position for both OP-2 and OP-3. While for the largest PSC diameter torque is recovered over a wide span range (see discussion above) at OP-2, this effect cannot be confirmed for the smallest diameter and here torque recovering is limited to the shroud area.

Furthermore, at **OP-2** an erratic increase of w/w_{V0} between curves for $d_{LW}/d_{LW,ref} = 0.83$ and 0.65 can be observed (Fig. 5.25, left). Overall the local torque reduction for $d_{LW}/d_{LW,ref} = 0.65$ (Fig. 5.33) is significantly lower than for PSC diameters $d_{LW}/d_{LW,ref} = 1.0$ and 0.83 (Figs. 5.32), which corresponds to the higher specific work output in Fig. 5.25. Nevertheless, the torque recovering in the shroud area is at a comparable level in terms of absolute values (bar height), meaning a relatively higher recovering effect for small PSC diameters. For the radial PSC position $D_{PSC}/D_{PSC,ref} = 1.10$ (red-colored bars) at OP-2 the recovering is disproportionately reduced at the shroud, corresponding to the kink in the slope of w/w_{V0} for the PSC mounted at the highest radial position (Fig. 5.25, left). This drop in performance can also be detected in the net blade torque shown in Fig. 5.33 (right).

In contrast, at **OP-3** the offset between specific work curves in Fig. 5.25 (middle) is more balanced. Thus, when plotted as a function of the PSC diameter, a more or less linear slope is visible (Fig. 5.26, middle) for all radial PSC positions, well corresponding to the free blade channel area (Fig. 5.26, right). Like for OP-2, the recovering in the blade shroud area is still large. However, in contrast to OP-2, here torque is also consistently reduced at lower blade span.

5.8.2 PSC Diameter

Regarding a modification of PSC diameter, preceding investigations [50] revealed **1)** a nonlinear increase in work output due to FB diameter adjustment 'V1–V4–V5', see Fig. 5.23 (left), whereby the blockage area normal to the z-direction is reduced linearly (Fig. 5.24, right). According to HÄFELE ET AL. [50], this nonlinear increase results from the fact that d_{FB} affects both loss due to diffusion and loss due to cross flow. **2)** A modification of FB diameter was found to be more effective than reducing the size of BR diameter.

Friction Bolt (FB) & Blade Reinforcements (BR) Fig. 5.24 shows that for the present study, the effect of nonlinear increase of w/w_{V0} due to FB diameter reduction can be found only for OP-2 and is even more pronounced here, see 'V1.1–V1.4–V1.5'. In this context it should be considered that OP-[50] lies between OP-2 and OP-3 (see Tab. 5.4). In contrast, at moderate overload (OP-3) an approximately linear, slightly regressive increase in work output can be seen.⁴⁸ The explanation for this OP-related tendency is given below.

As a consequence of d_{FB} reduction a lower portion of fluid is disturbed, which manifests itself in a reduced size of FB and PS vortex and a decreasing interaction of FB and SS vortex, see Fig. 5.35. Furthermore, the reduction of d_{FB} leads to a lowering of the cross flow along the PSC axis and therefore to a reduced mixing loss at the blade SS. The link between FB diameter and cross flow loss arises from the fact that the blockage area of the FB acts as a shelter for the flow along the PSC axis from blade PS to SS, depicted in Fig. 5.15. As reported in Subsec. 5.7.2 for reference geometry V1.1, the relative strength of FB and PS vortices is decreased towards overload. It was also found that the interaction between FB and SS vortex and the wake is mitigated. This behavior is also visible for variation 'V1.1–V1.4–V1.5' (Fig. 5.35). Both FB and PS vortices are stronger proportionally pronounced at OP-2, i.e. they lead to a locally higher relative total pressure drop. Moreover, the region of disturbed flow near the blade SS is larger. Generally, there is more alteration in the vortex structure across the PSC diameter variation at OP-2, see Fig. 5.35. In contrast, at OP-3 the vortex structure stays more similar. Thus, in the light of diminishing impact of loss due to cross flow and increasing dominance of diffusion loss

⁴⁸This corresponds to TRAXINGER [125], who investigated the same configuration for a similar OP (Fig 5.23, right). Regarding an FB diameter reduction, the author [125] pointed to the difference between the outcome of Ref. [50] (nonlinear, progressive increasing specific work) and results based on his own CFD investigations (nonlinear, slightly regressive increase of w/w_{V0}). According to TRAXINGER [125] the cause of this deviation (related to OP or wet steam modelling approach EQS/NES) could not be finally clarified. However, based on the results presented here the different behavior is rather OP-related (Figs. 5.23, 5.24 and 5.26).

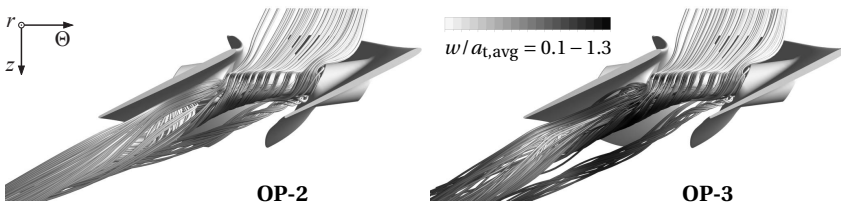


Figure 5.34 Vortex systems for reference PSC configuration V1.1

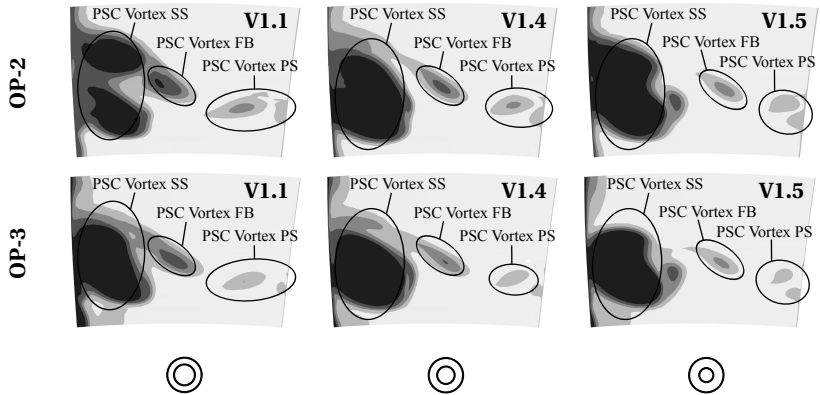


Figure 5.35 Total pressure contour (67.5% to 87.5% span, see Fig. 5.17) downstream of PSC, scaled from plane-wise $p_{t,max}$ (light) to $p_{t,min}$ (dark) at the respective OP

at overload, a more linear increase of specific work at OP-3 is reasonable and vice versa, a disproportionate growth of w/w_{V0} must be expected for OP-2 when decreasing the FB diameter (blockage area) linearly (Fig. 5.24).

A further increase in work output can be gained by reducing both FB and BR diameter, see Fig. 5.24 ('V1.1–V1.6–V1.7'). At OP-2 the contributions of the adapted FB and BR 'V1.1 to V1.6' to the overall loss reduction ('V1.1 to V1.7') is smaller than of the modification 'V1.6 to V1.7'. At OP-3 this allocation is reverse. Further, HÄFELE ET AL. [50] report an approximately even loss contribution for both modifications (Fig. 5.23) at OP-[50]. This supports the statement that the impact of loss due to cross flow is diminishing from OP-2 towards overload (Tab. 5.4), see discussion above. Nevertheless, the comparison of configurations 'V1.1 to V1.5' and 'V1.1 to V1.7' shows that a decrease of d_{FB} tends to be more effective than a reduction of d_{BR} and this is true for all discussed OPs. As stated before, this is due to the fact that the BR diameter may only affect the diffusion loss whereas the FB diameter affects both diffusion loss and loss due to cross flow along the PSC axis. The fact that the adaption of the BR has only a local impact can be seen in Figs. 5.35 and 5.36. Here, for 'V1.5 to V1.7' (adjustment of d_{BR}) only the SS vortex respectively the wake downstream of the BR vary in size, whereas the FB and PS vortices stay nearly unaffected. This is valid for both OPs and was also reported for OP-[50].

Lacing Wire (LW) The findings discussed for FB & BR regarding an OP-dependent nonlinear (OP-2) and linear (OP-3) increase in work output due

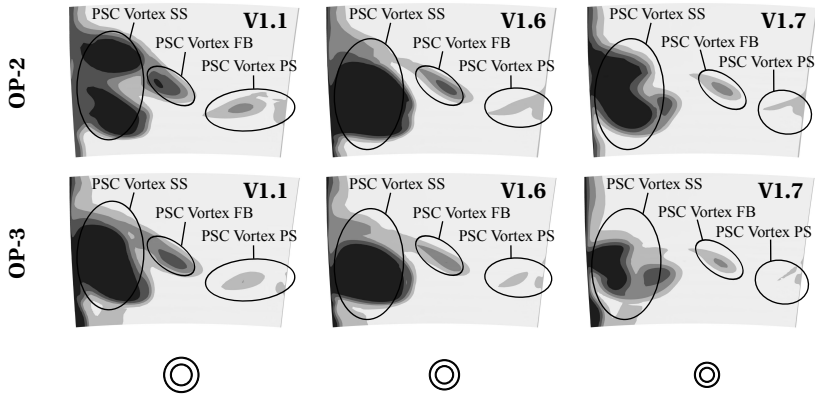


Figure 5.36 Total pressure contour (67.5% to 87.5% span, see Fig. 5.17) downstream of PSC, scaled from plane-wise $p_{t,max}$ to $p_{t,min}$ at the respective OP

to PSC diameter reduction are confirmed by the CFD results for the LW in a qualitative manner for all radial PSC positions, see Fig. 5.26. The principal vortex system induced by a simple lacing wire in LP steam turbine blading, however, is different to the one that can be found in a rotor with FB & BR (see Sec. 5.6 and Figs. 5.15 to 5.18). It is therefore not surprising that the work output for comparable PSC configurations does not exactly correlate. Nevertheless, the phenomena that are indicative for a diminishing impact of loss due to cross flow and predominantly responsible for the difference in work increase are related and can be seen in Fig. 5.37. According to Sec. 5.6, all vortices but the Upper SS Vortex are partly or completely related to the cross flow from blade PS to SS. From the contour plots in Fig. 5.37 it is obvious that their formation and interaction is proportionally stronger pronounced at OP-2. Moreover, the region of disturbed flow near the blade SS is larger.

Remarks on Equivalent Diameters HÄFELE ET AL. [50] proposed the study of loss by means of equivalent⁴⁹ PSC diameters (Subsec. 5.4.4). With this simplification, a comparison of CFD results to the analytical loss correlation (5.20) of TRAUPEL [123] was possible even for LP blades with complex PSC geometries (FB & BR). In order to check the applicability of this approach and also to

⁴⁹Equivalent quantities d_{eqv} and d_{eqv}^* , based on the cross section areas normal to the axial and radial direction as well as the overall PSC length, have been introduced (Fig. B.1 and Tab. B.1). By this means, the complex PSC geometry of *PSC-1* is virtually transformed to a simple lacing wire with the same blockage area.

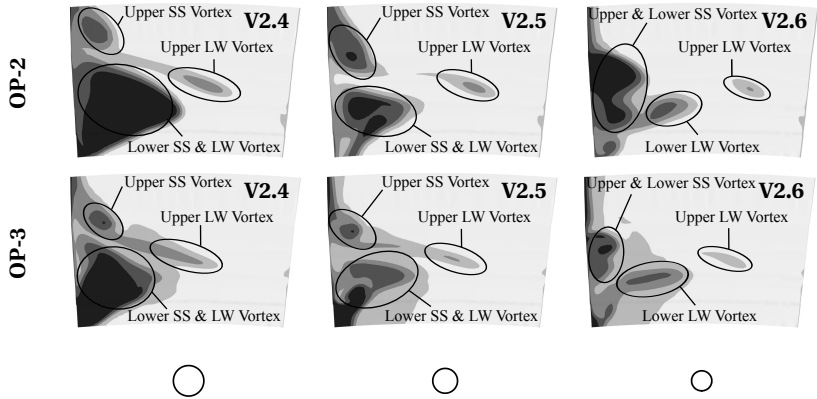


Figure 5.37 Total pressure contour (67.5% to 87.5% span, see Fig. 5.18) downstream of PSC, scaled from plane-wise $p_{t,max}$ to $p_{t,min}$ at the respective OP

allow a more fundamental study of the flow-impact of PSCs compared to the complex PSC geometry with FB & BR, a simple lacing wire geometry ('V2.4–V2.5–V2.6', see Fig. 5.39) with diameters covering the equivalent diameters of PSC variation 'V1.1–V1.6–V1.7' (Fig. 5.38) was introduced in Subsec. 3.3.2 (see also Tabs. B.1 and B.3). Advantageous is the fact that a broader audience can benefit from the given results, since this type of PSC is still very common in steam turbine applications, DROZDOWSKI ET AL. [29].

Due to the obviously more complex PSC geometry of FB & BR one must suspect a rather higher potential for loss generation than compared to a simple, cylindrical LW with equivalent diameter ($d_{LW} = d_{eqv}$) and also stronger pronounced nonlinear effects. It is therefore not surprising that the work output does not exactly correlate. However, according to Fig. 5.27 a fairly good agreement can be found for OP-2. Nevertheless, for OP-3 a deviation of approximately 1% is obvious for reference geometry V1.1 versus V2.4. Towards decreasing PSC diameter, this offset is diminished to approximately 0.5%, compare 'V1.1–V1.6–V1.7' versus 'V2.4–V2.5–V2.6' in Fig. 5.27 (middle).



Figure 5.38 Variation of PSC diameters d_{FB} and d_{BR}



Figure 5.39 Variation of PSC diameter $d_{LW} = d_{eqv}$

Although the concept of FB & BR has shown strong performance and proven its reliability from a mechanical point of view (see e.g. Refs. [27, 116]) it has two key disadvantages considering fluid dynamics. First, the blade surface covered by the relatively large cross section of the BR ($d_{BR} > d_{LW}$) directly contributes to a reduced torque generation i.e. work output.⁵⁰ Furthermore, because of the relatively large BR diameter combined with the fact that the PSC faces the highest kinetic energy close to the blade SS, the diffusion loss in this region is significantly enlarged, which is also indicated by means of analytical results later in this work, compare to loss composition in Tab. 5.5 on

⁵⁰See Subsec. 5.8.3 (Page 153), where the shape of the BR is varied from circular to elliptical and a decrease of specific work is detected due to the enlarged blade surface covered by the BR.

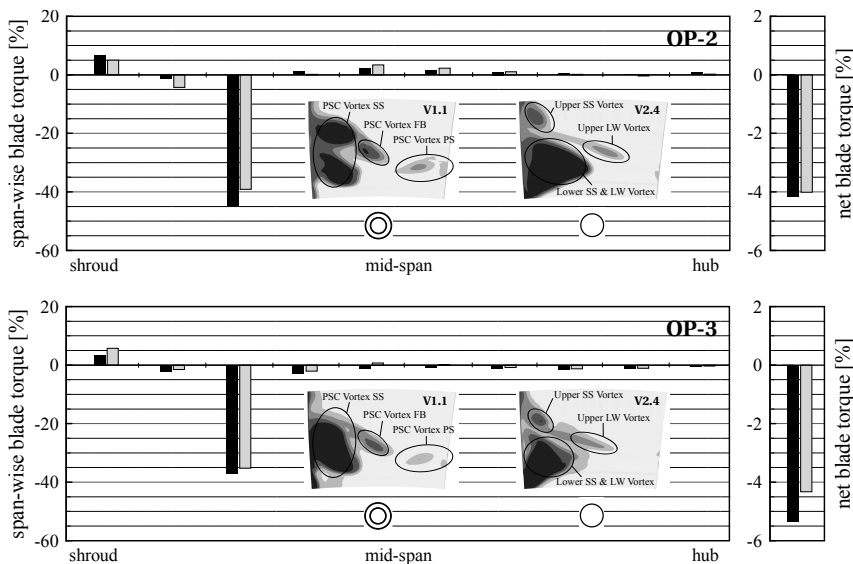


Figure 5.40 Relative blade torque (compare to Fig. 5.32) and total pressure contour downstream of PSC (compare to Figs. 5.35 and 5.37) for reference PSC geometry V1.1 ■ and equivalent PSC diameter V2.4 ■ ($d_{LW}/d_{LW,ref} = 1.0$) at OP-2 and OP-3

Page 164. This manifests itself in the PSC vortex and wake downstream of the BR SS (Fig. 5.15) and also results in a stronger disturbance of the boundary layer flow near the blade SS.

These effects can be verified by means of span-wise torque and total pressure contours shown in Fig. 5.40. Here, the blade torque for reference PSC geometry V1.1 and corresponding equivalent PSC diameter $d_{LW}/d_{LW,ref} = 1.0$ (V2.4) is depicted.⁵¹ The general OP-dependent span-wise (re-)distribution of torque and mass flow rate was already addressed earlier on Page 142 (see Figs. 5.31 and 5.32). In addition to this, the characteristic difference of the two PSC concepts and moreover the disadvantage of the BR can be seen. At both OPs the BR has a locally more negative impact, due to the effects mentioned above. Based on Fig. 5.40, the reason for the large deviation of approximately 1% performance at OP-3 can be mainly attributed to the large recovering effect in the blade shroud area for the configuration with LW. Conversely, the fact that the FB & BR concept can compete with the LW in terms of aerodynamic performance at OP-2 can be traced back to a larger torque recovering mainly in the same blade span area. Further evaluations have shown that this tendency is also given for the remaining equivalent diameters $d_{LW}/d_{LW,ref} = 0.83$ and 0.65 at reference span position (V1.6/V2.5, V1.7/V2.6).

5.8.3 Cross-Sectional PSC Shape

In addition to the modifications of the blockage area (variation of PSC diameter & radial PSC position), a change of PSC cross section from circular to elliptical and teardrop-shaped is considered in the present work. Based on Fig. 5.23 (left) and HÄFELE ET AL. [50], **1**) a friction bolt with elliptic cross-sectional shape lowers the losses ('V4–V8–V9'). **2**) In contrast, a blade reinforcement with elliptical cross section increases the losses ('V7 to V10').

Friction Bolt (FB) & Blade Reinforcements (BR) Fig. 5.24 shows that for the present study, the introductory statements can be confirmed for both investigated OPs. Within the variation of configuration 'V1.4–V1.8–V1.9' the FB shape is modified, whereby variation 'V1.4 to V1.8' shows the effect of the change from circular to elliptical shape and 'V1.8 to V1.9' the effect when further increasing the aspect ratio d_{FB}^*/d_{FB} of the ellipse. According to Fig. 5.24 both modifications show an approximately similar loss reduction, which corresponds to the decrease of the drag due to a more streamlined shape. Results also reveal that the overall gain potential for 'V1.4–V1.8–V1.9' is largest at

⁵¹In contrast to Fig. 5.32 and according to HÄFELE ET AL. [54] only 10 span-wise segments were chosen in order to capture the full BR geometry within one segment.

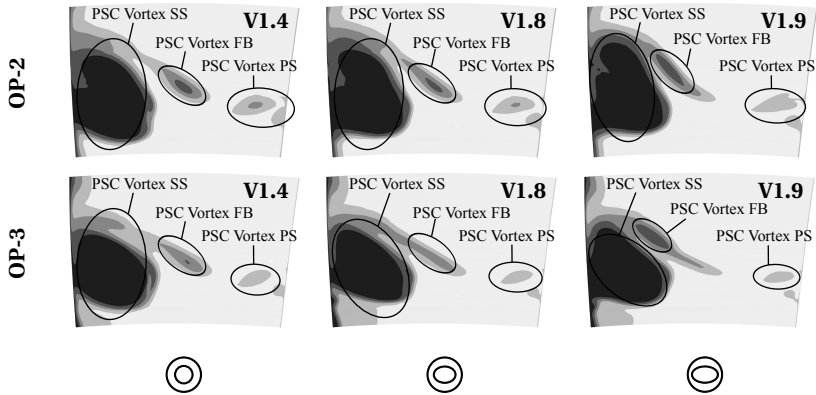


Figure 5.41 Total pressure contour (67.5% to 87.5% span, see Fig. 5.17) downstream of PSC, scaled from plane-wise $p_{t,max}$ to $p_{t,min}$ at the respective OP

OP-2 and diminishes towards overload (OP-[50], OP-3). Besides this, a good agreement of CFD results at OP-3 (Fig. 5.24, middle) with the outcome of TRAXINGER [125] (Fig. 5.23, right) is found, who performed this variation for a similar working point using a different steam model (EQS), compare Tab. 5.4.

The reduction in drag and thus reduced disturbance of the flow leads to a smaller size of the PSC Vortex FB and to a stronger bending of this vortex towards the blade SS, compare V1.4 and V1.9 in Fig. 5.41. Concerning the PSC Vortex FB, Fig. 5.41 misleads about the fact of different vortex sizes for V1.4 and V1.9. However, 3D CFD results and Fig. B.2 show that a reduced size of PSC Vortex FB leads to the fact that the PSC Vortex SS as well as the enclosed wake are less affected and disturbed by the PSC Vortex FB. These effects mainly cause the increase in work output. According to Figs. 5.41 and B.2, the PSC Vortex PS stays nearly unaffected of the FB shape modification, whereby its alteration with increasing aspect ratio of the ellipse is larger for OP-2.

Besides these main influences on the vortex structure, it has to be considered that the velocity field has a radial component (see Fig. 4.14). Hence, the flow direction upstream of the PSC is not parallel to the major axis of the ellipse (approximately 20 degree incidence). According to HÄFELE ET AL. [50], the gain due to an elliptical shaped FB ('V1.4-V1.8-V1.9') is therefore slightly⁵² diminished. Nevertheless, 3D CFD analyses show that the flow can basically follow the PSC structure and no severe premature separation compared to the

⁵²Results for the lacing wire (Fig. 5.45) indicate that only for large PSC diameters and overload condition this effect gets considerably large.

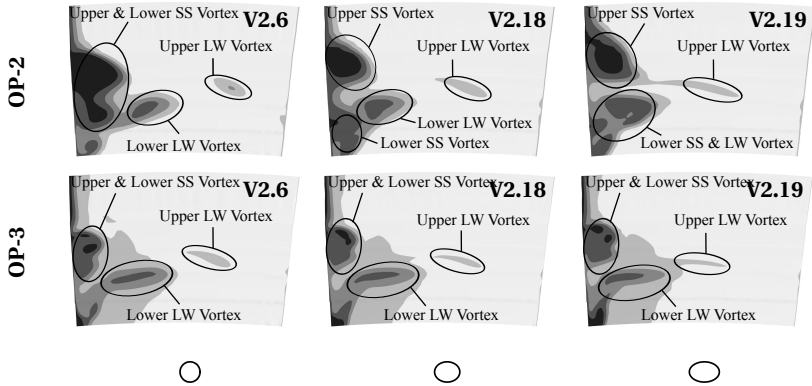


Figure 5.42 Total pressure contour (67.5% to 87.5% span, see Fig. 5.18) downstream of PSC, scaled from plane-wise $p_{t,max}$ to $p_{t,min}$ at the respective OP

circular shape can be found, which results from the low aspect ratio and thus high incidence tolerance (indicated in Fig. 5.46 for an LW).

According to the loss reduction due to FB shape adjustment 'V1.4–V1.8–V1.9', the comparison of modifications 'V1.10–V1.11' and 'V1.4–(V1.8)–V1.9' from HÄFELE ET AL. [50] shows a decrease of the gain potential for elliptical cross section at a lower FB diameter (see Fig. 5.23, left). Results of the present work (Fig. 5.24, left) show that this relation is also found for OP-2 and is even stronger pronounced there. For OP-3 (Fig. 5.24, middle), however, the opposite is the case, meaning an increase of the gain potential for elliptical FB at lower diameter. This OP-dependent increasing effectiveness of PSC variation 'V1.10–V1.11' is clearly outlined when regarding the slope of 'V1.5–V1.10–V1.11', whereby it is obvious that the kink between 'V1.5–V1.10' and 'V1.10–V1.11' is largest at OP-2 and vanishes towards overload (OP-[50], OP-3). Thus, with increasing OP the gain potential for an elliptical shape modification at small diameter ($d/d_{LW,ref} = 0.55$) is increasing and for larger diameter ($d/d_{LW,ref} = 0.69$) it is reduced. This tendency is further refined and confirmed with a simple LW, see next paragraph (in particular Fig. 5.44).

The comparison of V1.7 and V1.10 indicates that an elliptical BR increases the losses. This results from the strongly enlarged cross section of the BR. Thus, a higher amount of blade surface is covered by the BR and the work done is reduced due to this larger coverage. For OP-2 and OP-[50] this *blade surface coverage effect* is of approximately the same magnitude whereas at OP-3 the loss increase is more than doubled, compare Figs. 5.23 and 5.24. The

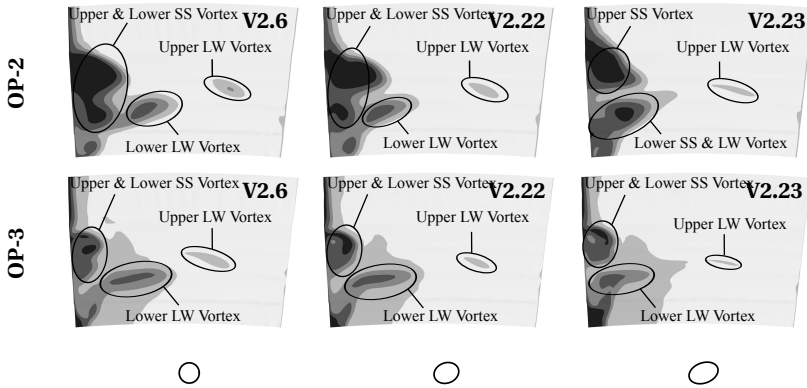


Figure 5.43 Total pressure contour (67.5% to 87.5% span, see Fig. 5.18) downstream of PSC, scaled from plane-wise $p_{t,max}$ to $p_{t,min}$ at the respective OP

detrimental performance of an elliptical BR is also responsible for the only slight loss reduction within modification V1.7 to V1.11, where the gain of work output due to the elliptical FB is reduced by the elliptical shape of the BR.

Lacing Wire (LW) – Ellipse The results derived with CFD model *PSC-2* for a simple lacing wire confirm the global trend of loss reduction found for friction bolts (*PSC-1*) when changing the cross section shape from circular to elliptical with max. aspect ratio $d_{LW}^*/d_{LW} = 1.5$, compare modifications 'V1.4–V1.8–V1.9' and 'V1.10 to V1.11' in Fig. 5.24 to 'V2.5–V2.16–V2.17' and 'V2.6–V2.18–V2.19' in Fig. 5.27 and see discussion above. However, for LWs a consistently slightly decreasing effectiveness towards higher aspect ratios can be seen.

Based on Fig. 5.27, the gain potential for a modification of elliptical cross section for both investigated LW diameters ($d_{LW}/d_{LW,ref} = 0.83$ and 0.65) is lower at OP-3 than it is at OP-2. This is e.g. indicated in Fig. 5.42, where at OP-3 the vortex structure near the blade SS is not changed significantly within the PSC variation, whereas at OP-2 an obvious rearrangement of vortices is visible (separation of Upper & Lower SS Vortex and merging of Lower SS & LW Vortex). As also found for the PSC Vortex of an elliptical FB (see paragraph above), the Upper LW Vortex is significantly reduced in size (mostly visible in Fig. B.3) and bended towards the blade SS, due to a reduction in drag and thus mitigated disturbance of the flow, see Figs. 5.42 and B.3.

In order to compare results from *PSC-1* and *PSC-2*, the diameters d_{FB} and d_{LW} considered for elliptical shape variation of FB and LW have been reduced to a reference diameter $d_{LW,ref}$ (Tabs. B.1 and B.3). According to Fig. 5.44, the reduction divisor R_D describing the change of gain potential from OP-2 to OP-3 for increasing PSC diameter follows an approximately linear, slightly progressive slope. According to this trend, the gain in work output for variations with PSC diameter $d_{norm} > 0.625$ will be reduced by a reduction divisor of $R_D > 1$. Vice versa, the gain in work output for variations with $d_{norm} < 0.625$ will be increased by $R_D < 1$. The disproportional increase of R_D for larger PSC diameters (see Fig. 5.44, slightly progressive slope) can be partly attributed to the *blade surface coverage effect* already described for a modification of BR from circular to elliptical cross section. As reported in the paragraph above, despite a streamlined BR shape, loss is increased within V1.7 to V1.10 (Fig. 5.24) and for OP-3 the magnitude is even doubled in comparison to OP-2. For an elliptical LW basically the same problem arises and increasing the aspect ratio d_{LW}^*/d_{LW} of the ellipsis leads to a nonlinear increase of covered blade surface which directly reduces the generated blade torque (see discussion on Page 150) and diminishes the gain in work output.

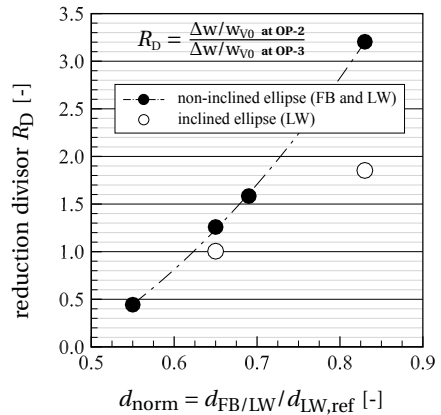


Figure 5.44 Reduction divisor R_D describing the change of work gain potential OP-2/OP-3 for variation of PSC cross section from circular to elliptical ($d_{PSC}^*/d_{PSC} = 1.5$)

Lacing Wire (LW) – Inclined Ellipse In order to assess the performance of elliptical cross sections inclined towards the flow direction, the PSC was rotated about 20 degree, which corresponds to the average flow angle γ upstream of the PSC. CFD results in Fig. 5.27 clearly reveal that for the present case an inclined elliptical shape generally performs better compared to its non-inclined counterpart. When comparing the total pressure contour downstream of the PSC of individual configurations non-inclined versus inclined (Fig. 5.42 versus 5.43 and Fig. B.3 versus B.4) one can see that besides small alterations of the vortex structure near the blade SS, the Upper LW Vortex is reduced in size, corresponding to a reduced PSC blockage area (Fig. 5.27, right) and accordingly less shelter for the low energy fluid feeding the cross

flow and the Upper LW Vortex. This tendency is also indicated by Figs. 5.46 and 5.47 (V2.19 versus V2.23). The contour plot of meridional velocity w_m shows that the wake downstream of the inclined ellipse is smaller, mainly resulting from the separation line on the upper PSC surface being shifted further downstream. Accordingly, the plot of circumferential velocity w_Θ indicates a weaker pronounced cross flow.

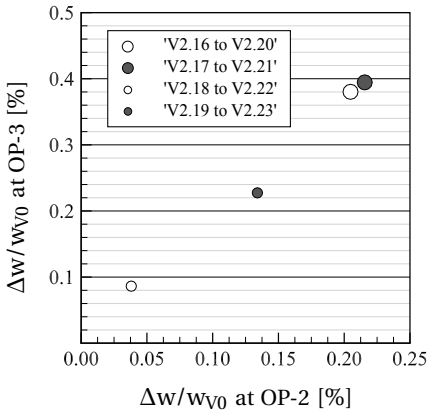


Figure 5.45 Specific work gain for variation *non*-inclined to inclined ellipse (see Tab. B.3)

the same for aspect ratios $d_{LW}^*/d_{LW} = 1.25$ ('V2.16 to V2.20') and 1.5 ('V2.17 to V2.21'), whereas for smaller diameter the gain is more than two times (OP-3) and three times (OP-2) increased, 'V2.18 to V2.22' versus 'V2.19 to V2.23'.

Besides this it is quite satisfactory that the effect of diminishing gain in work output (due to circular versus *non*-inclined elliptical PSC cross section) when increasing the OP can be reproduced with CFD for inclined PSCs. However, due to the fact that the impact of an inclination is significantly enlarged at OP-3, R_D is reduced accordingly, see Fig. 5.44 (○). Thereby, the reversal point at $R_D(d_{norm}) = 1.0$ is shifted to slightly higher d_{norm} (Fig. 5.44).

Lacing Wire (LW) – Droplet As already indicated, the CFD model with lacing wire (PSC-2) provides more feasible PSC variations. MISTRY ET AL. [82] report about the application of teardrop-shaped PSCs and LI AND LI [74] also applied snubbers with aerodynamic-shaped cross section in LP steam turbine blading. From empirical correlations⁵³ of HOERNER [47] it can be learned that

⁵³It has to be considered that these correlations are based on experimental data derived for geometries in incompressible flow with ideal inflow conditions at relatively low REYNOLDS numbers.

The performance increase of inclined shapes gets also obvious from Fig. 5.45, where an approximately linear dependency between OP-2 and OP-3 can be seen ($\Delta w/w_{V0}$ at OP-3 $\approx 1.77 \times \Delta w/w_{V0}$ at OP-2). For the smallest LW diameter ($d_{LW}/d_{LW,ref} = 0.65$) the magnitude of work gain is small ('V2.18 to V2.22' at OP-2 $\approx 0.04\%$) but increases with increasing PSC diameter and operating point ('V2.17 to V2.21' at OP-3 $\approx 0.4\%$), see Figs. 5.45 and 5.27. Figs. 5.45 and 5.27 also show that for the larger PSC diameter the impact of an inclined ellipsis is nearly the

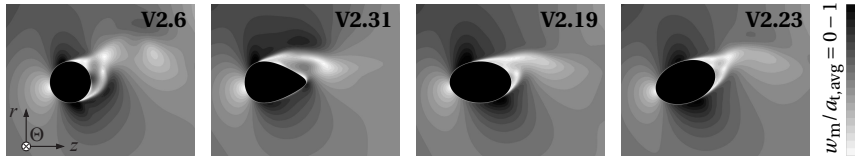


Figure 5.46 Meridional velocity contour on a meridional plane ($\Theta = \text{const.}$) in distance $1/3 l_{\text{PSC}}$ from blade suction side (OP-2)

such profiles tend to have drag coefficients smaller than elliptical cross sections, compare Eqs. (5.32) and (5.36). According to HOERNER [47], streamline shapes are generally tapered towards the trailing edge in order to avoid flow separation. For such shapes the form drag (viscous pressure drag) is reduced, see Tab. 5.1 and refer to SIGLOCH [109]. While some marine applications prefer a sharper forebody, it is popular in aviation to apply rounded leading edges and thus high incidence tolerance of the profile due to a wide range of attack angles. Examples for streamline section shapes are e.g. depicted in Ref. [47, p. 6–8] for a thickness to chord ratio of 0.4.

HOERNER [47, p. 6–6] presents an approach for c_D based on experimental data of predominantly streamline wires and compression struts⁵⁴ having NACA cross sections (e.g. 4-digit series family of airfoil sections), amongst others ($\text{Re} = 1 - 5 \times 10^4$). Thus,

$$c_D = 2 \times 0.0077 \left(1 + \frac{d_{\text{PSC}}}{d_{\text{PSC}}^*} \right) + \left(\frac{d_{\text{PSC}}}{d_{\text{PSC}}^*} \right)^2, \quad (5.36)$$

where the last term accounts for the viscous pressure drag. It is obvious that for larger thickness to chord ratios, this drag component becomes predominant, compare to Tab. 5.1.

⁵⁴Streamline wires and compression struts are used e.g. in the wing sections of double decker propeller aircrafts.

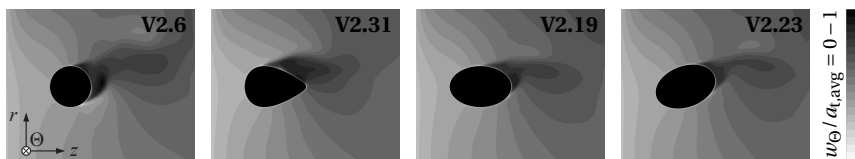


Figure 5.47 Circumferential velocity contour on a meridional plane ($\Theta = \text{const.}$) in distance $1/3 l_{\text{PSC}}$ from blade suction side (OP-2)

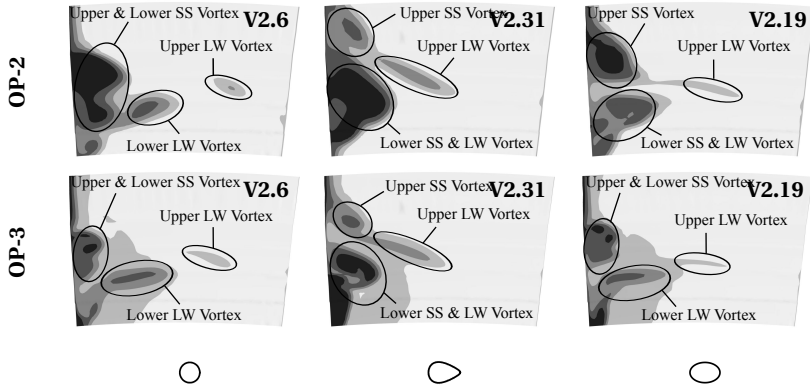


Figure 5.48 Total pressure contour (67.5% to 87.5% span, see Fig. 5.18) downstream of PSC, scaled from plane-wise $p_{t,max}$ to $p_{t,min}$ at the respective OP

In order to check the performance of such PSC designs against an elliptical PSC in real steam turbine flow under non-ideal inflow conditions, a droplet-shaped profile with an aspect ratio $d_{LW}^*/d_{LW} = 1.5$ has been chosen (Tab. B.4). CFD results in Fig. 5.28 ('V2.17 to V2.30' and 'V2.19 to V2.31') show that for the investigated LP blading and flow conditions a teardrop-shaped PSC performs slightly worse than an elliptical one, depending on the OP and PSC diameter. For OP-2 the deviation is largest (max. 0.25%) and diminishes for OP-3.

According to Fig. 5.46, severe premature separation is present on the upper PSC side of V2.31, resulting in a larger wake downstream of the PSC and a stronger pronounced cross flow (Fig. 5.47). One reason for this might be the too blunt leading edge of the shape chosen here (compared to an ellipse), resulting from a large thickness to chord ratio of 0.667, which is relatively high for streamlined shapes, see HOERNER [47]. In the contour plots depicted in

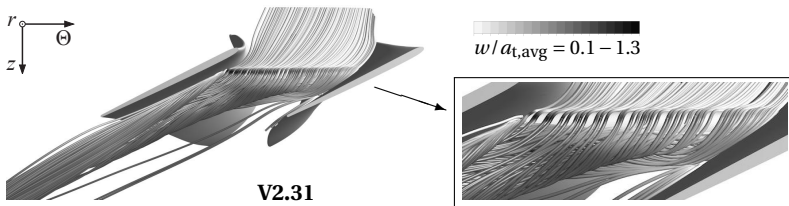


Figure 5.49 Vortex system for teardrop-shaped PSC cross section (OP-2)

Fig. 5.48, the fluid downstream of the PSC is found to be more disturbed than resulting from an elliptical cross section with the same aspect ratio, which manifests itself in a larger wake and stronger pronounced vortices (Lower SS Vortex, Upper & Lower LW Vortex). Furthermore, these plots indicate that the whole vortex system is shifted towards higher span. A closeup look to the streamline plot in Fig. 5.49 (right) gives additional insights and reveals that towards the blade SS the cross flow tends to form more and more on the upper surface of the PSC, seeking towards the PSC leading edge, see also contour plot of w_Θ for V2.31 in Fig. 5.47. According to Fig. 5.46 (V2.31) and 5.49 it is obvious that for the main flow the tendency for premature separation on the upper PSC surface is increasing towards the blade SS. Thus, the shape of a streamlined PSC cross section in LP turbine blading should be chosen carefully, especially with respect to large inflow pitch angles (here: $\gamma \approx 20$ deg).

5.8.4 Axial PSC Position

As stated before, the axial PSC position Z_{PSC} (Fig. B.1) within the flow channel plays an important role for the magnitude of PSC loss. This is due to the fact that for one thing it can affect the PSC blockage area and on the other hand it governs the velocity i.e. kinetic energy the PSC is facing. Based on the experimental work of KIRILLOV AND KUZ'MIČEV [63] from the early 1960s, one can conclude that besides the size and shape of a PSC, the magnitude of loss is highly depending on the location where the PSC is mounted. In this context it is desirable for turbine blading to place the PSC close to the leading edge and for compressor blading close to the trailing edge, ROBERTS [95]. A similar advice can be found in Ref. [25]. According to DENTON [25] a strut should be positioned in a region where the relative flow velocity is low, i.e. near the blade leading edge when considering expanding flow in turbine blading. Another source comes to a similar conclusion. Based on CFD, WU ET AL. [137] found that placing snubbers away from the blade leading edge results in more drag and less (blade) lift, since here, higher velocities are present in the investigated transonic turbine cascade flow.



Figure 5.50 Variation of axial PSC position

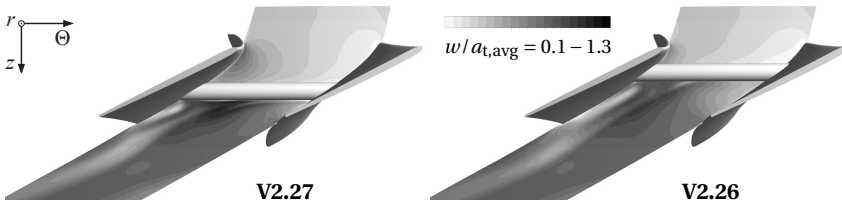


Figure 5.51 Contour plots on constant span for axial PSC variation (OP-2)

In order to check the sensitivity and gain potential of such variations for simple wires in LP steam turbine blading, PSCs with two different diameters ($d_{LW}/d_{LW,ref} = 0.83$ and 0.65) were axially shifted about $\pm 13\%$ of $C_{z,PSC}$ (axial blade chord length at the radial PSC position) from reference PSC position, see Fig. 5.50 and compare to Tab. B.4. CFD results in Fig. 5.28 show that mainly a rather linear loss variation can be expected when relocating the PSC within this axial range.⁵⁵ For OP-2 the magnitude of loss variation is small for the smaller PSC diameter ('V2.27 to V2.26' \rightarrow 0.6%) and increases for the larger one ('V2.25 to V2.24' \rightarrow 0.9%). For overload condition OP-3 these individual gains are almost doubled. Near the blade TE (V2.25, V2.27) the PSC shows a strong OP-dependency and loss is increased towards overload by approx. 0.5%. In contrast, for the axial PSC position near the blade LE (V2.24, V2.26) the sensitivity is small and work output is only slightly scattered ($\pm 0.1\%$).

Fig. 5.51 shows that shifting the PSC position upstream results in an overall lower inflow velocity for the PSC. Both Fig. 5.51 and streamline plots in Fig. 5.52 suggest that the gain of placing the PSC towards the blade LE might be diminished due to the wake and vortices downstream of the PSC (near the blade SS) being more effective within the flow channel in this case (V2.26), leading to additional disturbance of the suction-sided boundary layer flow.

⁵⁵This general tendency for loss versus axial PSC position correlates to the statements given by DENTON [25], ROBERTS [95] and WU ET AL. [137].

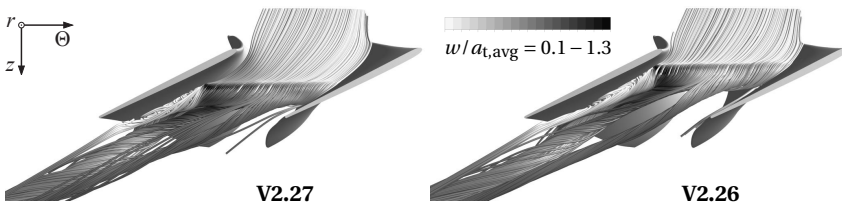


Figure 5.52 Vortex systems for axial PSC variation (OP-2)

5.8.5 Zigzag PSC Angle

Due to mechanical reasons, turbine blades are occasionally coupled by a zigzag PSC arrangement, see Fig. 1.10 and refer to NAUMANN [85]. In this setup, the flexible trailing edge and the stiffer leading edge of adjacent blades are connected by damping pins or wires. According to PFEIFFER [90] and compared to a setup with FB and BR (Fig. 1.6) this joining technology is softer, leading to less blade frequency rise.

MAIER [77] carried out test rig measurements with PSCs arranged in zigzag configuration, see Page 23. In order to check the performance of a similar arrangement and the sensitivity of work output on the PSC rotation angle δ_{zigzag} (Fig. 1.10) for the investigated LP blading, additional CFD calculations with $\delta_{\text{zigzag}} = 7.5^\circ$ and 15° have been performed for the smallest PSC diameter ($d_{\text{LW}}/d_{\text{LW,ref}} = 0.65$), see Fig. 5.53 and compare to Tab. B.4. CFD results in Fig. 5.28 reveal that from fluid-dynamical point of view arranging the PSC in zigzag configuration has a negative impact on the stage performance and lowers the specific work output. For OP-2 a change of δ_{zigzag} from 0 to 15 degree increases the lost work by 0.8%, compare to Fig. 5.28 (left). For OP-3 the reduction of w/w_{V0} within modification 'V2.6–V2.28–V2.29' is halved (0.4%), see Fig. 5.28 (middle). Thus, the negative impact of rotating the PSC is diminishing towards overload but is still considerable. This mitigated OP-dependency can be mainly blamed on the loss increase of base configuration V2.6 towards overload, whereas w/w_{V0} of V2.28 and V2.29 varies only slightly. Regarding the sensitivity of w/w_{V0} on δ_{zigzag} it can be reported that for the investigated configuration and angle range an approximately linear, slightly progressive relation is found, see Fig. 5.28.

In contrast to the mechanical properties of the coupled blade system [90], very little on fluid dynamics can be found about this topic in literature. ZDRAVKOVICH [141] discusses some aspects on yawed cylinders in incompressible flow for regimes TrSL and TrBL (Tab. 5.2), whereby *yawed* means positioning the cylinder non-perpendicular to the free stream.⁵⁶ When com-

⁵⁶According to Fig. 5.53 the PSC arrangement V2.6 (cylinder axis coincides with the circumferential direction) is considered as *yawed*, whereas V2.29 is approaching an unyawed constellation.



Figure 5.53 Variation of zigzag PSC angle

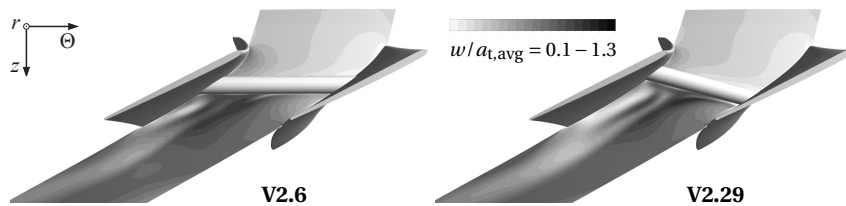


Figure 5.54 Contour plots on constant span for variation of zigzag PSC angle (OP-2)

paring both streamline plots in Fig. 5.55 it gets obvious that a yawed PSC (V2.6) reshapes the circular cross section in the plane of the free stream velocity to an elliptic one.⁵⁷ This is also mentioned by ZDRAVKOVICH [141] and the question is raised if there is an analogy between flow around yawed cylinders and unyawed elliptic cylinders. However, the author [141] expects that this analogy does not hold. Nevertheless, regarding Figs. 5.54 and 5.55 it is evident that the wake SS downstream of the PSC is significantly larger for the unyawed PSC configuration (V2.29). Furthermore, regarding the vortex system in Fig. 5.55 it is obvious that especially the lower LW vortex is enlarged. Both effects can be attributed to the fact that a PSC in zigzag arrangement (Fig. 5.55, right) faces a steeper relative inflow angle compared to the PSC in reference position (Fig. 5.55, left), resulting in less mass flow getting pushed towards the suction side. This effect is related to the one described for varying operating conditions in Subsec. 5.7.2. Overall, due to the *unyawed* PSC (V2.29) a bigger portion of the flow channel is affected by the wake and vortices and this leads to the mentioned reduction in work output,⁵⁸ although the free blade channel area is increased (see Fig. 5.28, right).

⁵⁷Interesting to see is the bending and redirecting of stagnation streamlines approaching the cylindrical PSC in Fig. 5.55 (compare to the discussion in Subsec. 5.7.2 on Page 131), while the relative redirection angle is comparable for both cases V2.6 and V2.29.

⁵⁸ZDRAVKOVICH [141, p. 976] presents results of measured drag coefficients in incompressible flow ($Re = 2 \times 10^4$). For a cylinder with end plates (here: blade PS and SS) c_D is decreasing with increasing yaw angle. This basically corresponds to the trend of CFD results in Fig. 5.28.

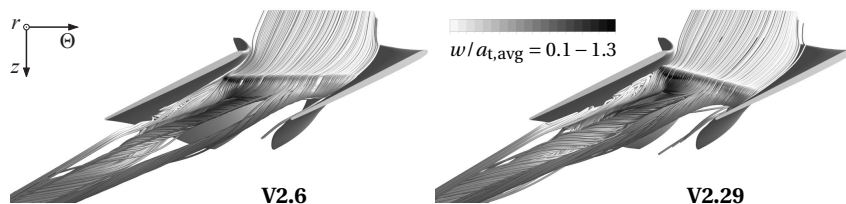


Figure 5.55 Vortex systems for variation of zigzag PSC angle (OP-2)

Regarding the statements given above on the inflow velocity the PSC is facing (Page 160), it has to be noted that for a zigzag PSC variation a mixed effect is present. While at the blade PS the PSC is shifted towards the blade trailing edge, a shift towards the leading edge takes place at blade SS. While overall the averaged velocity decreases towards the channel inlet, a local peak can be found near the leading edge at blade SS, see Fig. 5.54.

5.9 Comparison of CFD Results to Analytical Loss Correlations

In the previous section the aerodynamic performance of various PSC variations is evaluated. As performance indicator the specific work output was chosen, as it is a direct measure of PSC loss and the preferable quantity for evaluating the given 3D CFD results. Within the early design process such data is naturally not available and blade designers often rely on simple correlations to estimate the deteriorating effect of PSCs on the stage efficiency. Loss correlations like the one of TRAUPEL [123] or DUNHAM AND PHILLIPSEN [31] are commonly used in industrial practice. However, it is known that these simplified approaches are fraught with uncertainties. Accordingly, their applicability for LP steam turbine blading has to be tested.

In the present section, CFD results of selected PSC configurations are compared to the outcome of these analytical loss correlations. This is done on the basis of an enthalpy-based loss coefficient ζ_{PSC} defined by Eq. (5.15).⁵⁹ OP-2 is used for this evaluation, as it comes closest to the design point.

5.9.1 Overview on Loss Correlation Results

A discussion on loss composition and the cause of main deviations between TRAUPEL [123] and DUNHAM AND PHILLIPSEN [31] is conducted in the following. Fig. 5.57 gives an overview on the evaluation results of loss correlations by means of $\zeta_{\text{PSC,CFD}}/\zeta_{\text{PSC,T}}$ and $\zeta_{\text{PSC,CFD}}/\zeta_{\text{PSC,DP}}$. According to Ref. [125] and confirmed by this extended database it can be reported that the main deviation of $\zeta_{\text{PSC,DP}}$ from TRAUPEL's correlation can be attributed to the more realistic representation of the mean velocity based on a linear distribution between blade PS and SS, leading to a significant increase of predicted loss due to diffusion (compare Fig. 5.57, $\zeta_{\text{PSC,T}}$ versus $\zeta_{\text{PSC,DP,diff}}$). For the present case the mean velocities on pressure and suction side w_{PS} (5.22) and w_{SS} (5.23),

⁵⁹Besides deviations resulting from inaccuracies due to compromises resting in the averaging approach (Subsec. 3.4.1 and 5.4.4) the general trend of w/w_{V0} is captured by $\zeta_{\text{PSC,CFD}}$.

Table 5.5 Composition of loss due to PSCs based on the correlation of DUNHAM AND PHILLIPSEN [31] for CFD models *PSC-1* and *PSC-2* with equivalent diameters (OP-2)

	BR,SS	FB/LW	BR,PS	FB/LW	
V1.1	35.2%	48.0%	7.2%	9.6%	⊙
V1.6	36.2%	48.4%	7.4%	8.0%	⊙
V1.7	37.3%	48.8%	7.7%	6.2%	⊙
V2.4	–	84.4%	–	15.6%	○
V2.5	–	86.8%	–	13.2%	○
V2.6	–	89.3%	–	10.7%	○
	$\zeta_{\text{PSC,DP,diff}}$			$\zeta_{\text{PSC,DP,cross}}$	

derived within DUNHAM AND PHILLIPSEN's approach, spread approximately by a factor of three, whereby w_{PS} is in the range of inlet velocity w_1 and w_{SS} approaches the magnitude of outlet velocity w_2 . In this context it must be recalled that for the derivation of the enthalpy loss coefficient $\zeta_{\text{PSC,T}}$ based on the idea of TRAUPEL [123], the rotor inlet velocity w_1 is used as reference velocity w_{ref} , see Subsec. 5.4.2.

For CFD model *PSC-1* with FB and BR, loss due to diffusion $\zeta_{\text{PSC,DP,diff}}$ is integrated along the individual lengths of pressure and suction-sided BR as well as FB. This results in the fact that $\zeta_{\text{PSC,DP,diff}}$ is split into three different loss parts, see Tab. 5.5 (V1.1/V1.6/V1.7) and Fig. 5.56 (top). It is evident that out of these three, the FB and suction-sided BR are the main loss contributors. This is due to the fact that the FB covers approximately 45% of the overall PSC blockage area and the BR,SS faces the highest kinetic energy at relatively high PSC diameter. Similar proportions have been reported by TRAXINGER [125], whereby the author [125] presents values averaged among five investigated PSC configurations. In CFD model *PSC-2*, lacing wires with $d_{\text{PSC}} = \text{const.}$ are being investigated, resulting in only one integral value for $\zeta_{\text{PSC,DP,diff}}$, see Tab. 5.5 (V2.4/V2.5/V2.6) and Fig. 5.56 (middle/bottom).

Furthermore, the consideration of loss due to cross flow ($\zeta_{\text{PSC,DP,cross}}$) accounts for approximately 6–16% of the overall loss for circular PSCs at reference span and further affects the quantitative agreement. From Tab. 5.5 and Fig. 5.56 the general trend of decreasing loss due to cross flow when lowering the PSC diameter can be detected for both *PSC-1* and *PSC-2*. It is further obvious that $\zeta_{\text{PSC,DP,cross}}$ is always considerably larger for the configuration with lacing wire when comparing the FB & BR concept with its equivalent LW diameter. Both observations can be reduced to the definition in Eq. (5.27) for

the ratio of mixing mass flow rates – i.e. the PSC cross section approximated as rectangle by means of d_{PSC}^2 (more precisely $d_{\text{FB}} \times d_{\text{FB}}^*$ and $d_{\text{LW}} \times d_{\text{LW}}^*$, whereby $d_{\text{FB}} < d_{\text{LW}}$, refer to Subsec. 5.4.4 on the evaluation of loss correlations and applied PSC diameters) – and the idea of the PSC giving shelter to the low energy fluid in the wake, which is carried from blade PS to SS, HÄFELE ET AL. [50]. In this context it is questionable if the approach from Eq. (5.27), proposed in Ref. [31], is also meaningful for cross sections other than circular, since this results in a growth of $\zeta_{\text{PSC,DP,cross}}$ with increasing aspect ratio of elliptical PSCs (see e.g. 'V2.4–V2.16–V2.17' and 'V2.5–V2.18–V2.19' in Fig. 5.56, middle). Accordingly, it does not correlate with the statement of HÄFELE ET AL. [50] and the concept that PSCs with similar radial extent will cause comparable loss due to cross flow. Related observations have been reported in Ref. [125] and this topic is further discussed in the next section.

The choice of c_{D} has no effect on the deviation between both correlations, since basically the same drag coefficients are applied.⁶⁰ However, if scaling the correlation results by an appropriate c_{D} -value, the scaling effect will be damped for $\zeta_{\text{PSC,DP}}$, since DUNHAM AND PHILLIPSEN's formulation is split into two parts, whereby the part for loss due to cross flow is independent from c_{D} . Accordingly, the drag coefficient has mainly a global impact on the deviation between correlation results and CFD, see discussion below.

5.9.2 Numerical Validation of Loss Correlations

In-depth numerical validation of both loss correlations is discussed at this point. This is done on the basis of one-stage CFD models *PSC-1* and *PSC-2* (Subsec. 3.3.2), derived from the experimentally-validated three-stage CFD model (Subsec. 3.3.1 and Chap. 4). Fig. 5.57 gives an overview on the quantitative agreement between CFD and analytical results while Figs. 5.58 to 5.60 put the focus on a more qualitative comparison. Both presentations are further discussed below.

Brief Overview on Quantitative Agreement The comparison for PSCs located at reference span (Fig. 5.57, top/middle) shows that TRAUPEL's correlation significantly underestimates the CFD predicted loss up to two times (in average $\zeta_{\text{PSC,CFD}}/\zeta_{\text{PSC,T}} \approx 1.68$), although TRAUPEL [123] introduced a correction factor of two in the final version of his correlation in order to account for

⁶⁰Only for variations V1.8, V1.9, V1.10 with mixed cross section shapes marginal deviations exist, since for the correlation of TRAUPEL [123] averaged values according to Tab. B.1 are used, whereas for evaluating the correlation of DUNHAM AND PHILLIPSEN [31] individual values for each PSC part are applied.

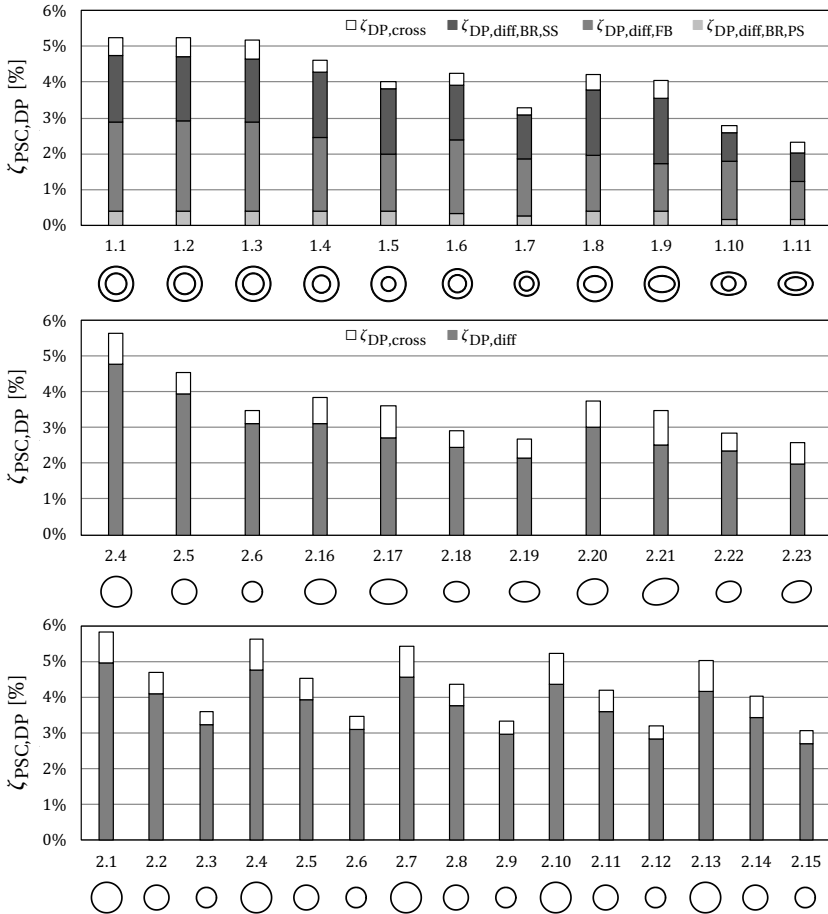


Figure 5.56 Composition of loss due to PSCs based on the correlation of DUNHAM AND PHILLIPSEN [31] at OP-2 (BEP)

deviations from the ideal flow (Subsec. 5.4.2). In contrast, a quite satisfying agreement of $\zeta_{PSC,CFD}/\zeta_{PSC,DP} \approx 1.16$ (average) is found with the correlation of DUNHAM AND PHILLIPSEN [31], whereby it is important to point out that in the derivation of loss coefficient $\zeta_{PSC,DP}$ the doubling of TRAUPEL’s theoretical attempt is neglected (Subsec. 5.4.3).

For the variation of radial PSC position over a wide span range a unique trend can be detected (Fig. 5.57, bottom). While the results for $\zeta_{PSC,CFD}/\zeta_{PSC,DP}$ show a relatively constant, slightly decreasing tendency around an average

Table 5.6 Deviation between CFD and analytical results, complementary to Fig. 5.57

	V1.1–1.11		V2.4–2.6 / 2.16–2.23		V2.1–2.15	
	$\zeta_{\text{CFD}}/\zeta_{\text{T}}$	$\zeta_{\text{CFD}}/\zeta_{\text{DP}}$	$\zeta_{\text{CFD}}/\zeta_{\text{T}}$	$\zeta_{\text{CFD}}/\zeta_{\text{DP}}$	$\zeta_{\text{CFD}}/\zeta_{\text{T}}$	$\zeta_{\text{CFD}}/\zeta_{\text{DP}}$
upper limit	1.97	1.40	2.05	1.25	2.04	1.31
average	1.62	1.17	1.74	1.14	1.41	1.07
lower limit	1.32	1.00	1.42	1.02	0.98	0.93
CFD model	<i>PSC-1</i>		<i>PSC-2</i>			

value of approximately 1.07 when relocating the PSC in CFD model *PSC-2* from the shroud region down to mid-span, the deviation between $\zeta_{\text{PSC,T}}$ and CFD significantly decreases and catches up at mid-span. This tendency is further examined below by means of Figs. 5.58 and 5.60.

Focus on Qualitative Comparison Following the brief overview on quantitative agreement between CFD and analytical results, Figs. 5.58 to 5.60 put the focus on a more qualitative comparison. As expected, the slopes of $\zeta_{\text{PSC,CFD}}$ partly differ from the ones of w/w_{V0} (Sec. 5.8). However, besides deviations resulting from inaccuracies due to compromises resting in the averaging approach (Subsec. 3.4.1 and 5.4.4) the general trend of w/w_{V0} is captured.

For the variation of **Radial PSC Position** the most significant trend of $\zeta_{\text{PSC,CFD}}/\zeta_{\text{PSC,T}}$ and $\zeta_{\text{PSC,CFD}}/\zeta_{\text{PSC,DP}}$ was already addressed above, based on results from CFD model *PSC-2* in Fig. 5.57 (bottom). This general trend is reproducible for all three investigated LW diameters. Related results can be found for the narrow variation of radial PSC position within CFD model *PSC-1* (see Fig. 5.57 (top), 'V1.1–V1.2–V1.3'). In addition to the bar diagrams in Fig. 5.57 the similar scenario can be observed in Figs. 5.58 and 5.60 and can be explained by the fact that TRAUPEL's formulation predicts a rise of the loss coefficient due to the shortening of PSC length l_{PSC} with decreasing radial position D_{PSC} . In contrast, CFD as well as the correlation results of DUNHAM AND PHILLIPSEN [31] show a reduction which corresponds to the decrease of blockage area as depicted in Figs. 5.24 and 5.25 (right).⁶¹ For mid-span position a good match between both correlation results and CFD exists. When further examining the curves of $\zeta_{\text{PSC,CFD}}$ and $\zeta_{\text{PSC,DP}}$ in Fig. 5.60 it is obvious that for the present LP blading DUNHAM AND PHILLIPSEN [31] under-predict the effectiveness of altering radial PSC position. This slight discrepancy might be temporarily enhanced by a simple correction of the

⁶¹The opposed tendency of $\zeta_{\text{PSC,T}}$ and $\zeta_{\text{PSC,CFD}}$ was already briefly addressed in Ref. [50].

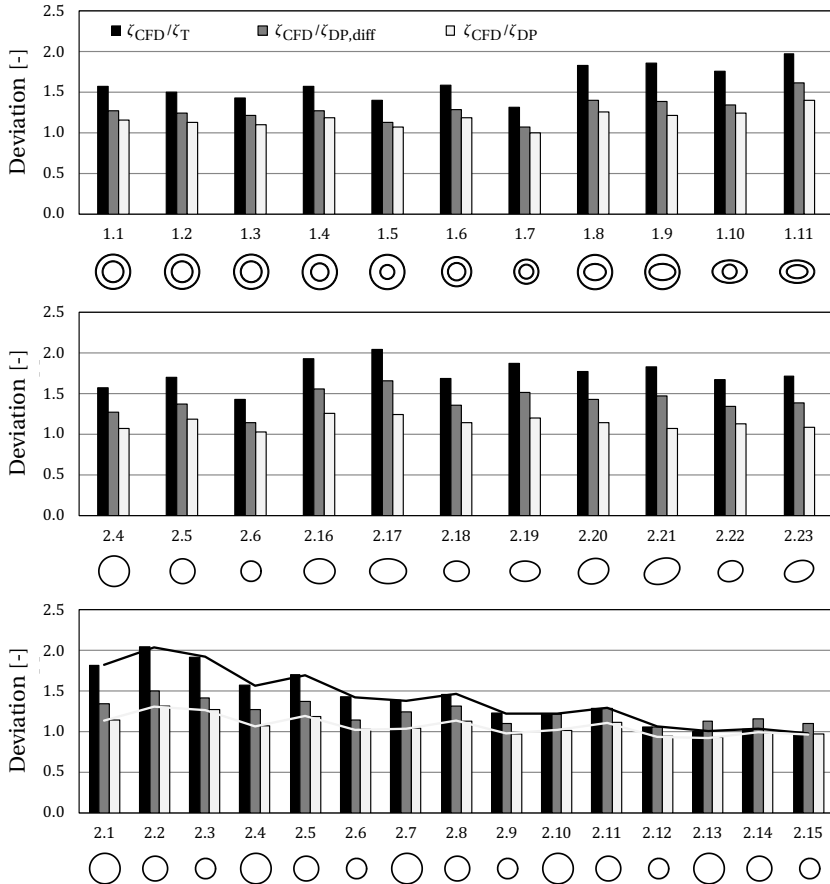


Figure 5.57 Deviation of loss coefficient ζ_{PSC} based on CFD results and on the correlations of TRAUPEL [123] and DUNHAM AND PHILLIPSEN [31] at OP-2 (BEP)

slope of curve $\zeta_{PSC,DP} = f(D_{PSC}/D_{PSC,ref})$ by a factor of three, while fixing the well-corresponding results at mid-span. Nevertheless, the good agreement at 50% span indicates that in particular the basic approach of DUNHAM AND PHILLIPSEN [31] is promising with respect to further refinement for the investigated type of LP blade (Fig. 1.5).

For the variation of **PSC Diameter** at reference span, Figs. 5.58 and 5.59 show deviations between CFD and correlation output for the slopes of modifications 'V1.1–V1.4–V1.5', 'V1.1–V1.6–V1.7' and 'V2.4–V2.5–V2.6'. For TRAUPEL's correlation the linear slope within these modifications is caused by the di-

rect proportionality between $\zeta_{PSC,T}$ and d_{PSC} , see Eq. (5.20). In real flows the PSC diameter (d_{FB} , d_{LW}) has an influence on both loss due to diffusion as well as loss due to cross flow. The latter is not captured by TRAUPEL's correlation. In DUNHAM AND PHILLIPSEN's approach (5.21) the term for loss due to cross flow (5.30) adds a slight deviation from the linear trend of loss due to diffusion (5.25),⁶² leading to a retarded decrease of $\zeta_{PSC,DP}$ for linearly decreasing PSC diameter, compare discussion on $\zeta_{PSC,DP,cross}$ above (Tab. 5.5 and Fig. 5.56, top/middle). However, according to the CFD results for OP-2, the reduction of the loss coefficient is inverse, meaning an over-proportional decrease for linearly decreasing PSC diameter. This trend of $\zeta_{PSC,CFD}$ is confirmed by w/w_{V0} and was clarified in Sec. 5.8. In contrast, for OP-3 it was found that this tendency is lost or even contrary (see Figs. 5.24, 5.27 and most significantly Fig. 5.26), which on the other hand correlates to the results in Ref. [125] (OP-3 \approx OP-[125], see Tab. 5.4). Thus, in the present case this OP-dependent trend can only be reproduced by $\zeta_{PSC,DP}$ for overload.

For the variation of **Cross-Sectional PSC Shape** a decreasing effectiveness with increasing aspect ratio of the ellipse can be seen in Figs. 5.58 and 5.59 for the results of $\zeta_{PSC,CFD}$, which was also reported in Sec. 5.8 based on the results of w/w_{V0} at OP-2 (compare to Figs. 5.24 and 5.27). Only modification 'V1.4–V1.8–V1.9' deviates from this general trend. Both correlations can reproduce the diminishing effectiveness with basically good agreement, whereby the bar diagrams in Fig. 5.57 show that the deviations increase within the individual variations 'V2.5–V2.16–V2.17' and 'V2.6–V2.18–V2.19'. The rise of $\zeta_{PSC,CFD}/\zeta_{PSC,T}$ and $\zeta_{PSC,CFD}/\zeta_{PSC,DP,diff}$ when changing the PSC cross section from circular to elliptical and further increasing the aspect ratio can be mainly reduced to the drag coefficient for an elliptical shape (Tabs. B.1 and B.3) which was evaluated with the empirical correlation (5.32) of HOERNER [47] and is obviously predicted too low. When adding the loss component $\zeta_{PSC,DP,cross}$ to $\zeta_{PSC,DP,diff}$, the rise of $\zeta_{PSC,CFD}/\zeta_{PSC,DP}$ is mitigated disproportionately. Based on the loss composition evaluated for DUNHAM AND PHILLIPSEN's correlation and discussed above (Fig. 5.56 and Tab. 5.5) it was already questioned if this increasing loss due to cross flow with increasing aspect ratio d_{PSC}/d_{PSC}^* is reasonable. Present results reveal that at least for this comparison it yields better agreement, quantitatively (Fig. 5.57) and qualitatively (Fig. 5.59). Similar conclusions were drawn in Ref. [125] for CFD model *PSC-1*.

This discussion can be extended by looking at the performance of *inclined* elliptical shapes in Fig. 5.59. CFD results show that $\zeta_{PSC,CFD}$ is reduced when turning the ellipse towards the flow direction, see also discussion in Sec. 5.8.

⁶²Compare trend of $\zeta_{PSC,DP}$ and $\zeta_{PSC,DP,diff}$ for diameter variation in Fig. 5.57 (top/middle).

However, the conventional evaluation of both correlations would lead to a contrary trend, namely a rise of the loss coefficient, which is due to the definition of the PSC blockage area in axial direction. 3D CFD results in Fig. 5.46 (V2.19) show that the flow basically follows the non-inclined elliptical shape and only slight premature separation is present. However, when comparing meridional velocity contours of inclined and non-inclined PSC configurations in Fig. 5.46 (V2.19 versus V2.23) it is evident that an evaluation of the blockage area in local flow direction will yield more reasonable results. This basic thought was adopted for the LW only, in order to demonstrate the effect of an inclined elliptical shape. Moreover, it follows the evaluation procedure and trend of free blade channel area in Fig. 5.27 (right). Taking the blockage area in local flow direction upstream of the elliptical PSC instead of considering the axial direction of the machine (for both inclined and non-inclined LWs) gives trends of $\zeta_{\text{PSC,DP}}$ and $\zeta_{\text{PSC,T}}$ which basically correspond to the CFD results, see Fig. 5.59. The gain of an inclined elliptical shape is, however, underestimated by both analytical approaches. With this correction, also the approach for mixing mass flow rates in the definition of $\zeta_{\text{PSC,DP,cross}}$ could be reconsidered and adjusted for elliptical (inclined) shapes. Accordingly, this topic could be further tracked in additional CFD studies on the formation of cross flow, preferably in a simplified cascade model, as it was developed e.g. in the bachelor thesis of MAIER [78].

Drag Coefficients of PSCs in LP Steam Turbine Blading Discussed correlations are based on ideal, uniform flow conditions and do not account for all the flow features induced by a PSC in LP steam turbine blading. Since the drag coefficient is the only parameter that fills the gap between the unknown real flow conditions and the analytical approach it is obvious that an adjustment of the correlation outcome by means of c_D can be meaningful.

For TRAUPEL's approach, the adjustment of loss due to PSCs with circular cross section placed at reference span needs to be in the order of $\zeta_{\text{PSC,CFD}}/\zeta_{\text{PSC,T}} \approx 1.5$ (averaged among V1.1–V1.7 and V2.4–V2.6), which equals the use of $c_D \approx 1.8$. DUNHAM AND PHILLIPSEN [31] pursue another way by introducing loss due to cross flow and applying a different approach for the reference velocity. With this sophisticated correlation, the correspondence to CFD results is very well and unscaled c_D -values are in a reasonable range ($\zeta_{\text{PSC,CFD}}/\zeta_{\text{PSC,DP}} \approx 1.1 \rightarrow c_D \approx 1.3$).⁶³

⁶³Besides these conclusions for BEP condition (OP-2), the closeness of agreement is also OP-dependent and gets worse at overload (OP-3). Information on this topic is appended in Sec. B.3.

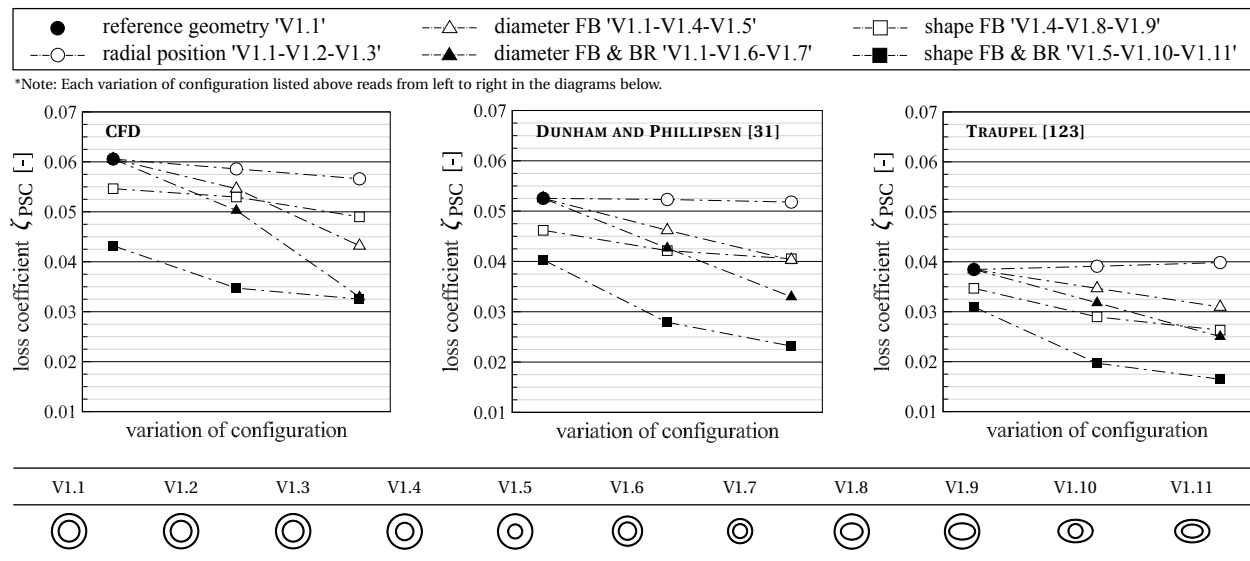


Figure 5.58 Loss coefficient ζ_{PSC} based on CFD results and on the correlations of TRAUPEL [123] and DUNHAM AND PHILLIPSEN [31] for PSC configurations with friction bolt (FB) and blade reinforcements (BR) according to Tab. B.1 (OP-2)

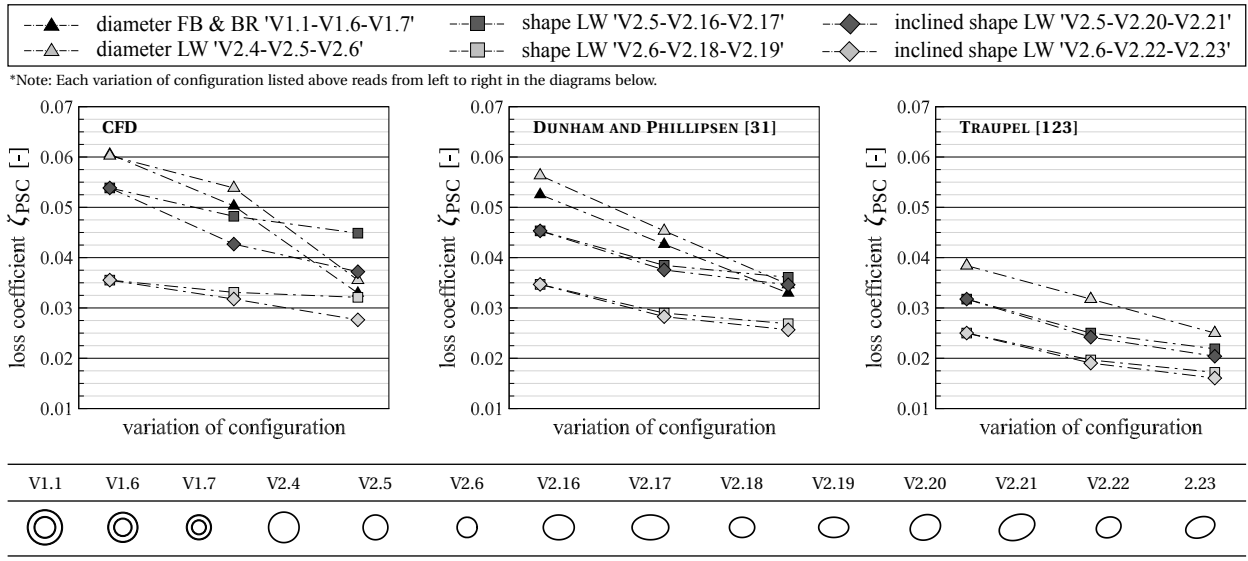


Figure 5.59 Loss coefficient ζ_{PSC} based on CFD results and on the correlations of TRAUPEL [123] and DUNHAM AND PHILLIPSEN [31] for PSC configurations with lacing wire (LW) according to Tabs. B.2 and B.3 (OP-2)

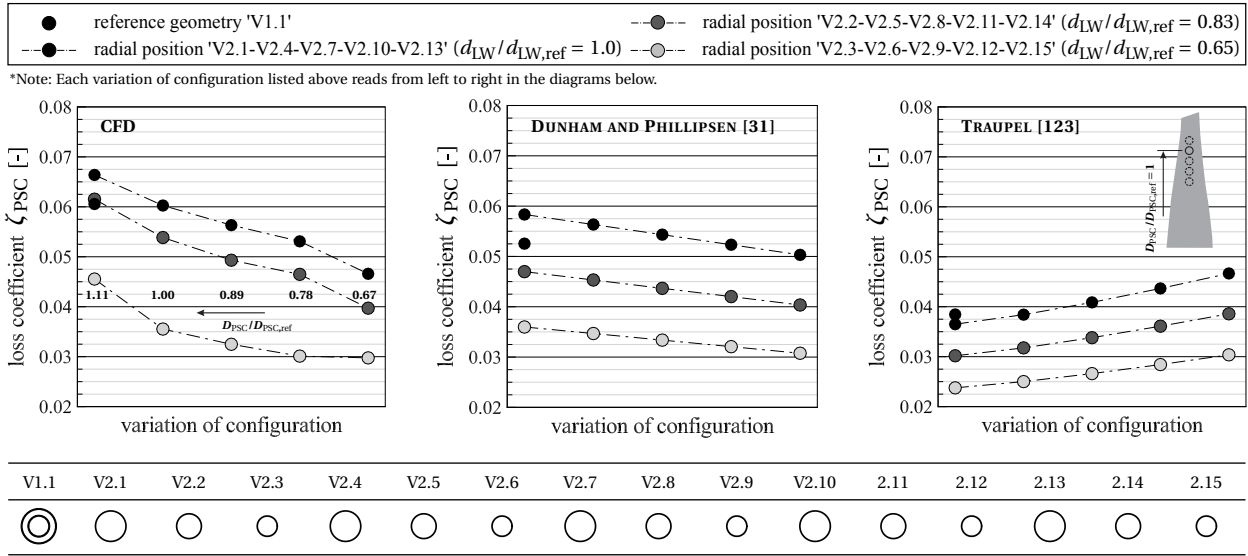


Figure 5.60 Loss coefficient ζ_{PSC} based on CFD results and on the correlations of TRAUPEL [123] and DUNHAM AND PHILLIPSEN [31] for PSC configurations with lacing wire (LW) according to Tabs. B.2 and B.3 – Variation of **radial PSC position** $D_{PSC}/D_{PSC,ref} = 1.11, 1, 0.89, 0.78$ and 0.67 at **three** PSC diameters $d_{LW}/d_{LW,ref} = 1.0, 0.83$ and 0.65 (OP-2)

5.10 Key Points on Loss due to PSCs

Two different PSC concepts were highlighted in the presented study, both popular in industrial steam turbine applications. One is a friction bolt (FB) mounted between blade reinforcements (BR) and the other one is a simple lacing wire (LW). Two different OPs were considered, one being at BEP condition (OP-2) and the other one at moderate overload (OP-3).

Performance Assessment of PSC Designs

3D CFD results of more than 40 PSC configurations were analyzed and assessed in terms of reduction in specific work output w/w_{V0} compared to a freestanding blade configuration, ranging from 1.3% to 3.6% for OP-2 and 1.5% to 4.9% for OP-3. The built up database provides thorough insights into the loss due to PSCs in LP steam turbine blading.

- 1) The vortex system induced by each PSC was used as indicator for the magnitude of loss and the corresponding total pressure contour downstream of the PSC showed good correlation with the evaluated performance. In this context it was shown that the flow features around the PSC are sensitive to the inflow condition and particularly OP-dependent.
- 2) For reference geometry with FB & BR mounted at 75% blade span, the reduced work is in the range of 3.6% for OP-2 and increases to 4.9% for OP-3. A reference LW with the same blockage area gives values of 3.6% (OP-2) and 3.9% (OP-3). The rather complex design of FB & BR suggests higher loss potential and was compared to the LW concept by means of three equivalent diameters. For OP-2 (BEP) the approach of using d_{eqv} has proven validity, based on the overall good agreement of work output. However, for OP-3 (moderate overload) the LW concept exceeds the FB & BR by up to 1% w/w_{V0} output.
- 3) A strong dependency of loss on the radial PSC position was found. The lost work output decreases by up to 1.5% from 75% to 50% span. Besides the variation of aerodynamic stage parameters along the radial PSC position, the linear change of PSC blockage area is obviously governing the loss. Generally, the potential for loss reduction within this PSC variation increases with the OP and d_{PSC} . Interestingly, the local torque reduction near the PSC is diminishing towards overload. However, this is compensated by less torque being recovered, mainly in the blade shroud area. A modification of axial PSC position was tested at reference span and can further reduce the loss significantly.

- 4) Based on the variation of radial PSC position, a significant OP-dependency in terms of loss magnitude was detected. While for higher PSC positions the work output decreases towards overload, a PSC located at lower span yields better performance. This *inversed loss tendency* is caused by a unique span-wise redistribution of mass flow rate and corresponding torque generation.
- 5) A modification of PSC diameter d_{PSC} at constant span was performed for different span positions and CFD results reveal an OP-related tendency. For OP-2 a non-linear increase of w/w_{V0} due to a linear PSC diameter reduction was detected. In contrast, for OP-3 this trend is linear. The varying impact of loss due to cross flow was found to be mainly responsible for the difference in work increase.
- 6) Besides the reduction of PSC blockage area, a change of FB and LW cross section from circular to streamlined (elliptical) can further reduce the losses. Inclining the ellipsis towards the flow direction yields additional benefit. Interestingly, with increasing working point the gain potential for an elliptical shape modification at small diameter is increasing but for larger diameter it is reduced. A teardrop-shaped PSC on the other hand performed slightly worse than its elliptic counterpart. This suggests that the shape of a streamlined PSC cross section in LP turbine blading should be chosen carefully, especially with respect to large inflow pitch angles. In contrast to FB and LW, an elliptical BR increases the losses.
- 7) Nowadays, there is the ambition to consider wetness in the design process of LP blading and aside from aerodynamic issues, also optimize the turbines towards decreasing wetness losses. Presented results show that it is recommended to include the PSCs within the numerical model, if nucleation and corresponding losses are of interest. For the PSC parameter study, however, it can be concluded that a separate consideration of wetness loss change among the investigated configurations with regard to the overall aerodynamic loss is not justified, since the variation of wetness loss is small.

Comparison of CFD Results to Analytical Loss Correlations

Following the performance assessment of PSC designs, enthalpy-based loss coefficients from 3D CFD results ($\zeta_{\text{PSC,CFD}}$) of selected PSC configurations out of the database were compared to the loss correlations of TRAUPEL [123] ($\zeta_{\text{PSC,T}}$) and DUNHAM AND PHILLIPSEN [31] ($\zeta_{\text{PSC,DP}}$), whereby it was focused on a best efficiency point (OP-2).

- 1) For PSCs located at reference span, TRAUPEL [123] underestimates the loss by a factor of 1.3 to 2.0. DUNHAM AND PHILLIPSEN [31] yield better agreement ranging between 1.0 and 1.4, which can be mainly attributed to the more realistic representation of the mean velocity, leading to a significant increase of predicted loss due to diffusion.
- 2) DUNHAM AND PHILLIPSEN's [31] correlation can be used to investigate stepped PSC geometries without the need for equivalent diameters. The evaluation of loss composition for reference PSC configuration with FB & BR shows that the FB (48.0%) and suction-sided BR (35.2%) are the main loss contributors. Besides these contributions that account for loss due to diffusion, the FB adds an additional 9.6% for loss due to cross flow. A reference LW with the same blockage area gives values of 84.4% (diffusion) and 15.6% (cross flow).
- 3) For cylindrical wires tested over a wide span and d_{PSC} range, a satisfying averaged agreement close to unity is found with the correlation of DUNHAM AND PHILLIPSEN [31]. In contrast, TRAUPEL's [123] approach shows a dominant trend with high deviations in upper span regions, significantly decreasing towards mid-span. Accordingly, both approaches perform well for mid-span but only $\zeta_{PSC,DP}$ can cope with a span-wise PSC variation.
- 4) Although the correlation of DUNHAM AND PHILLIPSEN [31] under-predicts the effectiveness of altering radial PSC position, the good agreement at 50% span indicates that this approach is promising with respect to further refinement for the investigated type of LP blade facing highly span-wise varying flow conditions. Considering altering OPs, a first verification shows that scaling the correlation outcome for reference span by the ratio of exit MACH numbers can roughly capture the loss increase from BEP to moderate overload.
- 5) For the variation of cross-sectional PSC shape a decreasing effectiveness with increasing aspect ratio of the ellipse was found. Both correlations can reproduce this effect with basically good agreement. However, compared to the CFD results, both attempts also overpredict the loss reduction due to elliptical shapes compared to cylindrical ones, which can be blamed on the deficiencies in predicting the drag coefficients for elliptical shapes by an empirical correlation of HOERNER [47]. An evaluation of inclined elliptical shapes revealed that the blockage area needs to be evaluated in local flow direction, in order to get acceptable correlation trends.

6 | Conclusion and Outlook

6.1 Conclusion

For the research on low-pressure (LP) industrial steam turbines (IST), the question on the *impact of part-span connectors (PSC) on aero-thermodynamics* has been raised. Object of investigation was a full-scale, three-stage LP IST featuring rotor blading coupled by lacing wire (LW) in the penultimate and friction bolts (FB) & blade reinforcements (BR) in the last stage.

Test rig measurements under real steam conditions and three-dimensional computational fluid dynamics (3D CFD) utilizing a non-equilibrium steam (NES) model revealed a strongly pronounced effect of the PSCs on aero-thermodynamics, whereby the flow-impact of FB & BR results in a considerably large reduction of last-stage efficiency by almost 4% at the best efficiency point (BEP). The comparison between CFD and experiment showed a generally good agreement at different operating points (OP) along the investigated speed line. Most notably, the total pressure losses due to wakes and vortices can be captured very well in magnitude and location. The applied CFD model was developed to investigate the impact of PSCs with engineering accuracy. As a conventional one-passage model it is suitable for an industrial design process. Based on the success of its experimental validation carried out, the model proved validity to capture the 3D flow field in LP steam turbine blading with PSC over a wide range of OPs. It is therefore sufficient for engineering practice and gives confidence for further numerical studies in this field.

3D CFD enabled deeper insights into the flow field and disclosed a modification of fundamental blade design parameters caused by the presence of the PSC within the flow channel. Major concerns are a change of expansion characteristic caused by the blocking of the steam flow as well as a span-wise redistribution of mass flow rate and altered torque generation. Apart from these predominantly aerodynamic effects, also a consideration of wetness loss suggests the PSCs to be included in a numerical 3D approach.

For a detailed consideration of PSC optimization issues and loss composition in the last stage blading (LSB), a one-stage CFD model with parameterized PSC geometry was developed, highlighting the PSC concepts of FB & BR and LW, both popular in industrial steam turbine applications. Based on a comparison of these concepts, the use of equivalent diameters for describing the complex FB & BR geometry is valid for BEP operating conditions. The PSC vortex system and related downstream total pressure drops proved to be suitable indicators for the magnitude of loss. The built up database provides thorough insights into the loss due to PSCs in LP steam turbine blading and leads to the conclusion that besides the facing flow condition, the PSC blockage area is gov-

erning the loss. The stage performance might be most significantly increased by moving the cylindrical PSC down to mid-span and further by lowering its diameter. The shape of a streamlined PSC cross section on the other hand can provide additional benefit but should be chosen carefully, especially with respect to large inflow pitch angles present in LSB with high annulus area ratio. Besides the PSC diameter, position and shape, the loss magnitude is further depending on the operating condition.

Within the early design process, blade designers often rely on analytical, drag-based PSC loss correlations like the one of TRAUPEL [123] or DUNHAM AND PHILLIPSEN [31], while accepting the commonly known deficiencies and unknown quantitative correspondence to reality. The present work gives insights into the loss composition. Premised on a comparison of coefficients from the present database of a typical LP IST blade at BEP condition it can be concluded that for cylindrical PSCs, both approaches perform well at mid-span with an agreement to CFD close to unity. However, only DUNHAM AND PHILLIPSEN [31] can cope with a radial PSC variation and keep up the good correspondence also at higher spans. The presented findings are promising with respect to further refinement for the investigated type of LSB facing highly varying flow conditions along the span, though care should be taken for defining appropriate drag coefficients (c_D) in LP steam turbine blading, especially for streamlined shapes. Regarding the choice of c_D , the presented study provides useful indications.

6.2 Outlook

The present work is a first comprehensive study, investigating the impact of PSCs on aero-thermodynamics in LP stages of typical industrial steam turbines by applying modern measurement and simulation techniques and considering analytical approaches. Following the conclusive statements above, further steps might be taken in successive studies.

The applied CFD model was validated for one basic PSC configuration over a wide operating range and a generally good agreement was found. In order to enhance the foundation for CFD-based loss approaches it is recommended to investigate further configurations in the test rig, particularly with different PSC diameters and varying span position. This might open the considered loss correlations to a wider field of application in steam and gas turbines and supersede the need for experiment-based calibration factors. In this context it is strongly suggested to simultaneously check the vibrational behaviour of each coupled blade system, combining research on aero-thermodynamics

with structural integrity. Based on the good agreement between simulated and measured vibrational characteristics of the reference geometry, discussed e.g. in a co-authored publication of DROZDOWSKI ET AL. [27], the implementability of modified PSC configurations is promising.

The loss correlation of DUNHAM AND PHILLIPSEN [31] has proven its applicability for PSCs in LP steam turbine blading but industrial design processes might have the need for further refinement. Particularly an OP-dependency could be incorporated. First approaches based on the exit MACH number are promising. Accordingly, the PSC study database could be extended by additional OPs. Another point is to reconsider the definition of loss due to cross flow when applied to elliptical PSC shapes. This topic could be further tracked in CFD studies on the formation of cross flow, preferably in a simplified linear cascade. Besides this, it has to be considered that all blade design parameters inherent to the loss correlations presented will influence the predicted magnitude of loss. A consideration with respect to variable LP rotor blade design was not part of the present thesis but is a potential task for future work.

The aforementioned linear cascade is suggested to be based on several profile sections of a typical IST reaction blade. A comparison between RANS, URANS and experimental data can contribute additional insights into the flow field in LP steam turbine blading with PSC and generally enhance the validation status by means of a simplified model. The choice of steam as working fluid is optionally, particularly with regard to the live steam capabilities available at ITSM. Another benefit from this experimental and numerical setup would be a comparison in terms of loss coefficients. As discussed in this work, especially the 3D URANS approach might improve the level of agreement, when considering the uncertainty in choosing appropriate c_D -values.

For deeper investigations on the asymmetric diffuser pressure field and the flow-impact of PSCs, it might be of academic interest to build up a 360 degree model of the last stage, the diffuser and the exhaust hood and apply transient CFD methods. In the light of today's affordable computing power, performing 3D URANS simulations for this type of flow problem is feasible but still highly challenging. In this context it has to be kept in mind that the associated effort does no longer allow using the analyses as part of an industrial design process.

Bibliography

- [1] ACCORNERO, A. AND MARETTO, L.: Field Measurements in LP Cylinder of a 320 MW Turbine, in: *Aerothermodynamics of Low Pressure Steam Turbines and Condensers*, ed. Moore, M. J.; Sieverding, C. H., VON KARMAN Institute Book, Chap. 6.2., pp. 185–197, Springer, 1987
- [2] ACCORNERO, A.; DORIA, G.; MARETTO, L. AND ZUNINO, E.: Flow in a 320 MW Low-Pressure Section: Theoretical and Experimental Evaluation, in: *Steam Turbines for Large Power Outputs*, VON KARMAN Institute for Fluid Dynamics – Lecture Series 1980-6, 1980
- [3] ADELMANN, T.: CFD-Studie zum aerodynamischen Einfluss von Koppелеlementen im Schaufelkanal einer dreistufigen ND-Industriedampfturbine, Student Thesis, Institute of Thermal Turbomachinery and Machinery Laboratory (ITSM), University of Stuttgart, 2013
- [4] AHMAD, M.: Experimental Assessment of Droplet Impact Erosion of Low-Pressure Steam Turbine Blades, PhD Thesis, Institute of Thermal Turbomachinery and Machinery Laboratory (ITSM), University of Stuttgart, 2009
- [5] AINLEY, D. G. AND MATHIESON, G. C. R.: A Method of Performance Estimation for Axial-Flow Turbines, Reports and Memoranda No. 2974, Aeronautical Research Council, Dec. 1951
- [6] ANSYS, Inc.: ANSYS CFX-Solver Theory Guide, Release 15.0, 2013
- [7] BAKHTAR, F.; YOUNG, J. B.; WHITE, A. J. AND SIMPSON, D. A.: Classical Nucleation Theory and its Application to Condensing Steam Flow Calculations, Proc. IMechE, Part C: J. Mech. Engrg. Sci., Vol. 219(12), pp. 1315–1333, 2005
- [8] BAUMANN, K.: Some Recent Developments in Large Steam Turbine Practice, J. Inst. Electr. Eng., Vol. 59(302), pp. 565–623, 1921
- [9] BEEVERS, A.; CONGIU, F.; PENGUE, F. AND MOKULYS, T.: An Analysis of the Merits of CFD for the Performance Prediction of a Low Pressure Steam Turbine Radial Diffuser, in: Proc. ASME Turbo Expo 2010: Power for Land, Sea, and Air, Glasgow, UK, June 14–18, 2010
- [10] BENIM, A. C.; PASQUALOTTO, E. AND S. H. SUH: Modelling Turbulent Flow Past a Circular Cylinder by RANS, URANS, LES and DES, Progress in Computational Fluid Dynamics, Vol. 8(5), pp. 299–307, 2008
- [11] BENIM, A. C.; CAGAN, M.; NAHAVANDI, A. AND PASQUALOTTO, E.: RANS Predictions of Turbulent Flow Past a Circular Cylinder Over the Critical Regime, in: Proc. 5th IASME / WSEAS International Conference on Fluid Mechanics and Aerodynamics, pp. 232–237, Athens, Greece, Aug. 25–27, 2007

- [12] BOSDAS, I.; MANSOUR M.; KALFAS, A. I.; ABHARI, R. S. AND SENOO, S.: Unsteady Wet Steam Flow Field Measurements in the Last Stage of Low Pressure Steam Turbine, *Trans. ASME, J. Eng. Gas Turb. Power*, Vol. 138(3), p. 032601, 2016
- [13] BRÄUNLING, W. J. G.: *Flugzeugtriebwerke: Grundlagen, Aero-Thermodynamik, ideale und reale Kreisprozesse, Thermische Turbomaschinen, Komponenten, Emissionen und Systeme*, 3. Aufl., Springer, 2009
- [14] BRÜGGEMANN, C.: *CFD-Studie zum aerodynamischen Einfluss der Geometrie von Koppелеlementen im Schaufelkanal einer ND-Industriedampfturbine*, Student Thesis, Institute of Thermal Turbomachinery and Machinery Laboratory (ITSM), University of Stuttgart, 2013
- [15] BURTON, Z.; INGRAM, G. AND HOGG, S.: A Novel Method of Coupling the Steam Turbine Exhaust Hood and the Last Stage Blades Using the Non-Linear Harmonic Method, ASME Paper No. GT2013-94184, in: *Proc. ASME Turbo Expo 2013: Turbine Technical Conference and Exposition*, San Antonio, Texas, USA, June 3–7, 2013
- [16] BURTON, Z.; INGRAM, G. L. AND HOGG, S.: A Literature Review of Low Pressure Steam Turbine Exhaust Hood and Diffuser Studies, *Trans. ASME, J. Eng. Gas Turb. Power*, Vol. 135(6), p. 062001, 2013
- [17] CAMPBELL, W.: The Protection of Steam Turbine Disc Wheels From Axial Vibrations, *Trans. ASME*, Vol. 46, pp. 31–60, 1924
- [18] CASEY, M. AND WINTERGERSTE, T. (eds.): *Best Practice Guidelines, ERCOFTAC Special Interest Group on “Quality and Trust in Industrial CFD”*, 2000
- [19] CHANDLER, K.; MELAS, M. AND JORGE, T.: A Study of Spontaneous Condensation in an LP Test Turbine, ASME Paper No. GT2015-42458, in: *Proc. ASME Turbo Expo 2015: Turbine Technical Conference and Exposition*, Montréal, Canada, June 15–19, 2015
- [20] CHIMA, R. V.: Computational Modeling of Vortex Generators for Turbomachinery, ASME Paper No. GT-2002-30677, in: *Proc. ASME Turbo Expo 2002: Power for Land, Sea, and Air*, Amsterdam, The Netherlands, June 3–6, 2002
- [21] CRAIG, H. R. M. AND COX, H. J. A.: Performance Estimation of Axial Flow Turbines, in: *Proc. Instn. Mech. Engrs.*, Vol. 185, pp. 407–424, 1970
- [22] CUMPSTY, N. A. AND HORLOCK, J. H.: Averaging Nonuniform Flow for a Purpose, *Trans. ASME, J. Turbomach.*, Vol. 128(1), pp. 120–129, 2006

- [23] DAHLMANN, P.: Strömungssimulation einer ND-Industriedampfturbine, Student Thesis, Institute of Thermal Turbomachinery and Machinery Laboratory (ITSM), University of Stuttgart, 2012
- [24] DENTON, J. D.: The Calculation of Three-Dimensional Viscous Flow Through Multistage Turbomachines, *Trans. ASME, J. Turbomach.*, Vol. 114(1), pp. 18–26, 1992
- [25] DENTON, J. D.: Loss Mechanisms in Turbomachines, *Trans. ASME, J. Turbomach.*, Vol. 115(4), pp. 621–656, 1993
- [26] DENTON, J. D. AND SINGH, U. K.: Time Marching Methods for Turbomachinery Flow Calculation, in: *Application of Numerical Methods to Flow Calculations in Turbomachines*, VON KARMAN Institute for Fluid Dynamics – Lecture Series 1979-07, 1979
- [27] DROZDOWSKI, R.; VÖLKER, L.; HÄFELE, M. AND VOGT, D. M.: Experimental and Numerical Investigation of the Nonlinear Vibrational Behavior of Steam Turbine Last Stage Blades with Friction Bolt Damping Elements, ASME Paper No. GT2015-42244, in: *Proc. ASME Turbo Expo 2015: Turbine Technical Conference and Exposition*, Montréal, Canada, June 15–19, 2015
- [28] DROZDOWSKI, R.; VÖLKER, L.; HÄFELE, M. AND VOGT, D. M.: Numerical and Experimental Analysis of LP Steam Turbine Blades Coupled with Lacing Wire, Paper No. ETC2015-105, in: *Proc. 11th Europ. Conf. on Turbomachinery, Fluid Dynamics and Thermodynamics*, Madrid, Spain, March 23–27, 2015
- [29] DROZDOWSKI, R.; VÖLKER, L.; HÄFELE, M. AND VOGT, D. M.: Numerical and Experimental Analysis of Low-Pressure Steam Turbine Blades Coupled with Lacing Wire, *Proc. IMechE, Part A: J. Power and Energy*, Vol. 230(3), pp. 332–342, 2016
- [30] DUNHAM, J. AND CAME, P. M.: Improvements to the Ainley-Mathieson Method of Turbine Performance Prediction, *Trans. ASME, J. Eng. Power*, Vol. 92, pp. 252–256, 1970
- [31] DUNHAM, J. AND PHILLIPSEN, B.: The Application of a Streamline Curvature Code to the Design of Turbochargers, IMechE Paper No. C602/030/2002, in: *Proc. 7th International Conference on Turbochargers and Turbocharging*, pp. 169–179, London, UK, May 14–15, 2002
- [32] DZUNG, L. S.: Mittelungsverfahren in der Theorie der Schaufelgitter, *Brown Boveri Mitteilungen*, Bd. 54(1), S. 37–44, 1967

- [33] DZUNG, L. S.: Konsistente Mittelwerte in der Theorie der Turbomaschinen für kompressible Medien, Brown Boveri Mitteilungen, Bd. 58(10), S. 485–492, 1971
- [34] EGLER, S.: Fehlerabschätzung der Sondenauswertung am Endstufenversuchsstand, Diploma Thesis, Institute of Thermal Turbomachinery and Machinery Laboratory (ITSM), University of Stuttgart, 2008
- [35] ESGAR, G. M. AND SANDERCOCK, D. M.: Some Observed Effects of Part-Span Dampers on Rotating Blade Row Performance Near Design Point, Tech. Rep. NASA TM-X-2696, NASA Lewis Research Center, 1973
- [36] ESTABROOK, J.E. AND LEGER, R.H.: Steam Turbines for Industrial Applications, Tech. Rep. GER-3706D, General Electric Power Systems, Marlborough, MA, 2000
- [37] EYB, G.: Experimentelle Untersuchung des Strömungsfeldes am Modell einer ND-Dampfturbinen-Endstufe, PhD Thesis, Institute of Thermal Turbomachinery and Machinery Laboratory (ITSM), University of Stuttgart, 1989
- [38] FU, X.: 3D-Strömungssimulation einer dreistufigen Niederdruck-Dampfturbine, Diploma Thesis, Institute of Thermal Turbomachinery and Machinery Laboratory (ITSM), University of Stuttgart, 2009
- [39] GERBER, A. G.: Inhomogeneous Multifluid Model for Prediction of Nonequilibrium Phase Transition and Droplet Dynamics, Trans. ASME, J. Fluids Eng., Vol. 130(3), pp. 1–11, 2008
- [40] GREITZER, E. M.; TAN, C. S. AND GRAF, M. B. (eds.): Internal Flow - Concepts and Applications, 1st edn., Cambridge University Press, 2004
- [41] GRÜBEL, M.; STARZMANN, J.; SCHATZ, M.; EBERLE, T.; VOGT, D. M. AND SIEVERDING, F.: Two-Phase Flow Modeling and Measurements in Low-Pressure Turbines – Part 1: Numerical Validation of Wet Steam Models and Turbine Modeling, Trans. ASME, J. Eng. Gas Turb. Power, Vol. 137(4), p. 042602, 2015
- [42] GYARMATHY, G.: Basis of a Theory for Wet Steam Turbine, PhD Thesis, Eidgenössische Technische Hochschule (ETH) Zürich, Translation into English, 1962
- [43] S. HAVAKECHIAN AND R. GREIM: Aerodynamic design of 50 per cent reaction steam turbines, Proc. Instn. Mech. Engrs., Vol. 213, Part C, 1999
- [44] HENEKA, A.: Strömungsmessungen an Niederdruck-Dampfturbinen, Forschung in der Kraftwerkstechnik 1977, pp. 61–66, 1977

- [45] HERMELER, J.; TRUCKENMUELLER, F. AND DECKERS, M.: New Generation of Titanium and Steel LP Turbine Blade-path, in: Proc. POWER-GEN Europe 2005, Milan, Italy, June 28–30, 2005
- [46] HODAPP, H.: Experimentelle und theoretische Untersuchungen zum Schwingungsverhalten von rundumgekoppelten und paketierte Beschaukelungen in Axialturbinen, PhD Thesis, Institute of Thermal Turbomachinery and Machinery Laboratory (ITSM), University of Stuttgart, 1991
- [47] HOERNER, S. F. (ed.): Fluid-Dynamic Drag, 2nd edn., Hoerner Fluid Dynamics, 1965
- [48] HORLOCK, J. H.: Losses and Efficiencies in Axial-Flow Turbines, Int. J. Mech. Science, Vol. 2(1), pp. 48–75, 1960
- [49] HÄFELE, M.; TRAXINGER, C.; GRÜBEL, M.; SCHATZ, M.; VOGT, D. M. AND DROZDOWSKI, R.: Experimental and Numerical Investigation of the Flow in a LP Industrial Steam Turbine with Part-Span Connectors, ASME Paper No. GT2015-42202, in: Proc. ASME Turbo Expo 2015: Turbine Technical Conference and Exposition, Montréal, Canada, June 15–19, 2015
- [50] HÄFELE, M.; TRAXINGER, C.; GRÜBEL, M.; SCHATZ, M.; VOGT, D. M. AND DROZDOWSKI, R.: Numerical and Experimental Study on Aerodynamic Optimization of Part-Span Connectors in the Last Stage of a Low-Pressure Industrial Steam Turbine, Proc. IMechE, Part A: J. Power and Energy, Vol. 229(5), pp. 465–476, 2015
- [51] HÄFELE, M.; TRAXINGER, C.; GRÜBEL, M.; SCHATZ, M.; VOGT, D. M. AND DROZDOWSKI, R.: Numerical and Experimental Study on Aerodynamic Optimization of Part-Span Connectors in the Last Stage of an LP Industrial Steam Turbine, Paper No. ETC2015-054, in: Proc. 11th Europ. Conf. on Turbomachinery, Fluid Dynamics and Thermodynamics, Madrid, Spain, March 23–27, 2015
- [52] HÄFELE, M.; TRAXINGER, C.; GRÜBEL, M.; SCHATZ, M.; VOGT, D. M. AND DROZDOWSKI, R.: Experimental and Numerical Investigation of the Flow in a Low-Pressure Industrial Steam Turbine with Part-Span Connectors, Trans. ASME, J. Eng. Gas Turb. Power, Vol. 138(7), p. 072604, 2016
- [53] HÄFELE, M.; VOGT, D. M. AND DROZDOWSKI, R.: Numerical Modelling of a Three Stage Low Pressure Industrial Steam Turbine with Part-Span Connectors, in: Proc. ANSYS Conference & 32. CADFEM Users' Meeting, Nürnberg, Germany, June 4–6, 2014

- [54] HÄFELE, M.; STARZMANN, J.; GRÜBEL, M.; SCHATZ, M.; VOGT, D. M.; DROZDOWSKI, R. AND VÖLKER, L.: Numerical Investigation of the Impact of Part-Span Connectors on Aero-Thermodynamics in a Low Pressure Industrial Steam Turbine, ASME Paper No. GT2014-25177, in: Proc. ASME Turbo Expo 2014: Turbine Technical Conference and Exposition, Düsseldorf, Germany, June 16–20, 2014
- [55] HÄFELE, M.: Wirkungsgradvergleich SK28-mk2/SK28-mk5, Tech. Rep. A-08-2009, Institute of Thermal Turbomachinery and Machinery Laboratory (ITSM), University of Stuttgart, 2009
- [56] IDEL'ČIK, I. E.: Handbook of Hydraulic Resistance, 1st edn., Israel Program for Scientific Translations, Jerusalem, 1966
- [57] INTERNATIONAL ENERGY AGENCY (IEA): Key World Energy Statistics, 2018
- [58] IPCC: Climate Change 2014: Synthesis Report. Contribution of Working Groups I, II and III to the Fifth Assessment Report of the Intergovernmental Panel on Climate Change [Core Writing Team, Pachauri, R.K. and Meyer, L.A. (eds.)]. IPCC, Geneva, Switzerland, 151 pp., 2014
- [59] ISO 5167-1:2003: Measurement of fluid flow by means of pressure differential devices inserted in circular cross-section conduits running full – Part 1: General principles and requirements, International Organization for Standardization, 2003
- [60] ISO 5167-2:2003: Measurement of fluid flow by means of pressure differential devices inserted in circular cross-section conduits running full – Part 2: Orifice plates, International Organization for Standardization, 2003
- [61] JAROSCH, J.: Beitrag zum Schwingungsverhalten gekoppelter Schaufelsysteme, PhD Thesis, Institute of Thermal Turbomachinery and Machinery Laboratory (ITSM), University of Stuttgart, 1983
- [62] KACKER, S. C. AND OKAPUU, U.: A Mean Line Prediction Method for Axial Flow Turbine Efficiency, Trans. ASME, J. Eng. Power, Vol. 104(1), pp. 111–119, 1982
- [63] KIRILLOV, I. I. AND KUZ'MIČEV, R. B.: Energieverluste durch Bindedrähte in einer Turbinenstufe (*Translation into German*), Élektričeskie stancii, Vol. 7, pp. 38–42, 1962
- [64] KIRILLOV, I. I. AND KUZ'MIČEV, R. B.: Power Losses in a Turbine Stage due to the Lashing Wires (*in Russian*), Élektričeskie stancii, Vol. 7, pp. 38–42, 1962

- [65] KOCH, C. C. AND SMITH, JR., L. H.: Loss Sources and Magnitudes in Axial-Flow Compressors, *Trans. ASME, J. Eng. Power*, pp. 411–424, 1976
- [66] KOCH, C. C.; BILWAKESH, K. R. AND DOYLE, V. L.: Evaluation of Range and Distortion Tolerance for High Mach Number Transonic Fan Stages, *Tech. Rep. NASA CR-72806*, NASA Lewis Research Center, 1971
- [67] KRAUS, M.: Literaturrecherche zum aerodynamischen Einfluss von Kopelementen im Schaufelkanal von Turbomaschinen, Student Thesis, Institute of Thermal Turbomachinery and Machinery Laboratory (ITSM), University of Stuttgart, 2013
- [68] LAKSHMINARAYANA, B.: *Fluid Dynamics and Heat Transfer of Turbomachinery*, John Wiley & Sons, 1996
- [69] LANGSTON, L. S.: Crossflows in a Turbine Cascade Passage, *Trans. ASME, J. Eng. Power*, Vol. 102, pp. 866–874, 1980
- [70] LAURIEN, E. AND OERTEL, JR., H.: *Numerische Strömungsmechanik*, 5. Aufl., Springer Vieweg, 2013
- [71] LEWIS, G. W. AND HAGER, R. D.: Effect of Damper on Overall and Blade-Element Performance of a Compressor Rotor Having a Tip Speed of 1151 Feet per Second and an Aspect Ratio of 3.6, *Tech. Rep. NASA TM-X-3041*, 1974
- [72] LEWIS, JR., G. W. AND URASEK, D. C.: Comparison of the Effect of Two Damper Sizes on the Performance of a Low-Solidity Axial-Flow Transonic Compressor Rotor, *Tech. Rep. NASA TM-X-2536*, NASA Lewis Research Center, 1972
- [73] LEYZEROVICH, A.: *Wet-Steam Turbines For Nuclear Power Plants*, PennWell, Tulsa, Oklahoma, 2005
- [74] LI, B. AND LI, J.: Numerical Investigations on the Aerodynamic Performance of Last Stage Bucket with Part-Span Connector, ASME Paper No. IMECE2014-38039, in: *Proc. ASME 2014 International Mechanical Engineering Congress & Exposition*, Montréal, Canada, Nov. 14–20, 2014
- [75] LI, L.; DU, C.; FAN, X. AND ZHONG, G.: Optimisation of a Low-Pressure Multistage Steam Turbine Towards Decreasing the Wetness Losses and Aerodynamic Losses, *Proc. IMechE, Part A: J. Power and Energy*, Vol. 230(4), pp. 345–353, 2016
- [76] MACHIDA, M.; YODA, H.; SAITO, E. AND NAMURA, K.: Development of Long Blades with Continuous Cover Blade Structure for Steam Turbines, *Hitachi Review*, Vol. 51(5), pp. 143–147, 2002

- [77] MAIER, R.: Wirkungsgraduntersuchungen am Endstufenversuchsstand bei variierten Betriebszuständen, in: Festschrift – 65. Geburtstag Prof. Dr.-Ing. Jakob Wachter, pp. 147–167, 1985
- [78] MAIER, S.: Erstellung eines Modells zur numerischen Modellierung der Zylinderumströmung im Schaufelkanal einer Turbomaschine, Bachelor Thesis, Institute of Thermal Turbomachinery and Machinery Laboratory (ITSM), University of Stuttgart, 2014
- [79] MENTER, F. R.: Zonal Two Equation k - ω Turbulence Models for Aerodynamic Flows, AIAA Paper 93-2906, 1993
- [80] MENTER, F. R.: Eddy Viscosity Transport Equations and their Relation to the k - ϵ Model, Tech. Rep. NASA Technical Memorandum 108854, NASA Ames Research Center, Moffett Field, California, 1994
- [81] MENTER, F. R.: Two-Equation Eddy-Viscosity Turbulence Models for Engineering Applications, AIAA J., Vol. 32(8), pp. 1598–1605, 1994
- [82] MISTRY, H.; SANTHANAKRISHNAN, M.; LIU, J.; STEIN, A.; DEY, S. AND SLEPSKI, J.: Aerodynamic Performance Assessment of Part-Span Connector of Last Stage Bucket of Low Pressure Steam Turbine, ASME Paper No. POWER2011-55265, in: Proc. ASME 2011 Power Conference, Denver, Colorado, USA, July 12–14, 2011
- [83] MURATA, Y.; SHIBUKAWA, N.; MURAKAMI, I.; KANEKO, J. AND OKUNO, K.: Development of 60Hz Titanium 48-Inch Last Stage Blade for Steam Turbine, ASME Paper No. POWER2011-55465, in: Proc. ASME 2011 Power Conference, Denver, Colorado, USA, July 12–14, 2011
- [84] MUSCH, C.; STÜER, H. AND HERMLE, G.: Optimization Strategy for a Coupled Design of the Last Stage and the Successive Diffuser in a Low Pressure Steam Turbine, Trans. ASME, J. Turbomach., Vol. 135(1), p. 011013, 2013
- [85] NAUMANN, H. G.: Steam Turbine Blade Design Options: How to Specify or Upgrade, in: Proc. 11th Turbomachinery Symposium, pp. 29–50, Houston, Texas, USA, 1982
- [86] NIEDERER, C.: Parametrisierung und numerische Modellierung einer gekoppelten ND-Endstufenlaufschaukel, Student Thesis, Institute of Thermal Turbomachinery and Machinery Laboratory (ITSM), University of Stuttgart, 2014
- [87] PANNING, L.: Auslegung von Reibelementen zur Schwingungsdämpfung von Turbinenschaufeln, PhD Thesis, Institute of Dynamics and Vibration Research, University of Hannover, 2005

- [88] PCA ENGINEERS LTD.: Streamline Curvature Analysis of Axial Flow Turbines - Program SC90T Version 11.1, Userguide, 2009
- [89] PETR, V. AND KOLOVRATNIK, M.: Wet Steam Energy Loss and Related Baumann Rule in Low Pressure Steam Turbines, Proc. IMechE, Part A: J. Power and Energy, Vol. 228(2), pp. 206–215, 2014
- [90] PFEIFFER, R.: Einfluß unterschiedlicher Paketierungen auf Schwingungsverhalten und Verbundfaktoren von Dampfturbinen-Beschaufelungen, PhD Thesis, Institute of Thermal Turbomachinery and Machinery Laboratory (ITSM), University of Stuttgart, 1985
- [91] PIANKO, M. AND WAZELT, F.: Propulsion and Energetics Panel Working Group 14 on Suitable Averaging Techniques in Non-Uniform Internal Flows, AGARD Advisory Report No. 182, Advisory Group for Aerospace Research and Development, 1983
- [92] PRASAD, A.: Calculation of the Mixed-Out State in Turbomachine Flows, Trans. ASME, J. Turbomach., Vol. 127(3), pp. 564–572, 2005
- [93] ROBERTS, W. B.; CROUSE, J. E. AND SANDERCOCK, D. M.: Off-Design Correlation for Losses due to Part-Span Damper on Transonic Rotors, Tech. Rep. NASA TP-1693, NASA Lewis Research Center, 1980
- [94] ROBERTS, W. B.: Correlation of Part-Span Damper Losses Through Transonic Rotors Operating Near Design Point, Tech. Rep. NASA TM-X-3542, NASA Lewis Research Center, 1977
- [95] ROBERTS, W. B.: Reduction of Shock Losses in Transonic Rotors by Internal Area Ruling for Part-Span Dampers, VON KARMAN Institute for Fluid Dynamics – Lecture Series 1999-02, 1999
- [96] RUBECHINI, F.; MARCONCINI, M.; ARNONE, A.; CECCHI, S. AND DACCA, F.: Some Aspects of CFD Modeling in the Analysis of a Low-Pressure Steam Turbine, ASME Paper No. GT2007-27235, in: Proc. ASME Turbo Expo 2007: Power for Land, Sea, and Air, Montréal, Canada, May 14–17, 2007
- [97] RUCKWIED, P.: Konstruktion einer geschlossenen Kalibrierstrecke zur Sondenkalibrierung, Student Thesis, Institute of Thermal Turbomachinery and Machinery Laboratory (ITSM), University of Stuttgart, 2005
- [98] RZHEZNIKOV, Y. B. AND TROSHCHENKOVA, L. N.: Losses due to Lacing in a Turbine Stage, Teploenergetika, Vol. 19(1), pp. 89–90, 1972
- [99] SCHATZ, M.; HÄFELE, M. AND MÜLLER, F.: Strömungs- und Schwingungsmesstechnik für Turbomaschinen, Lecture Notes, Institute of Thermal Turbomachinery and Machinery Laboratory (ITSM), University of Stuttgart, 2014

- [100] SCHATZ, M.; EBERLE, T.; GRÜBEL, M.; STARZMANN, J.; VOGT, D. M. AND SÜRKEN, N.: Two-Phase Flow Modeling and Measurements in Low-Pressure Turbines – Part 2: Turbine Wetness Measurement and Comparison to CFD-Predictions, *Trans. ASME, J. Eng. Gas Turb. Power*, Vol. 137(4), p. 042603, 2015
- [101] SCHLICHTING, H. AND GERSTEN, K.: *Grenzschicht-Theorie*, 10. Aufl., Springer, 2006
- [102] SENOO, S.; ONO, H.; SHIBATA, T.; NAKANO, S.; YAMASHITA, Y.; ASAI, K.; SAKAKIBARA, K.; YODA, H. AND KUDO, T.: Development of Titanium 3600rpm-50inch and 3000rpm-60inch Last Stage Blades for Steam Turbines, Paper No. IGTC2011-0249, in: *Proc. International Gas Turbine Congress 2011 (IGTC'11)*, Osaka, Japan, Nov. 13–18, 2011
- [103] SENOO, S.; ASAI, K.; KUROSAWA, A. AND LEE, G.: Titanium 50-inch and 60-inch Last-Stage Blades for Steam Turbines, *Hitachi Review*, Vol. 62(1), pp. 23–30, 2013
- [104] SHAPIRO, A. H.: *The Dynamics and Thermodynamics of Compressible Fluid Flow*, Wiley, 1953
- [105] SHIBUKAWA, N.; MURATA, Y.; HASHIDATE, T. AND KAWASAKI, S.: Development of Titanium 48-inch Last Stage Series for 3600rpm Steam Turbine, Paper No. IGTC2011-0211, in: *Proc. International Gas Turbine Congress 2011 (IGTC'11)*, Osaka, Japan, Nov. 13–18, 2011
- [106] SIEMENS: *Industrial Steam Turbines – The comprehensive product range from 2 to 250 megawatts*, Advertising Brochure, SIEMENS AG, 2013
- [107] SIGG, R.; HEINZ, CH.; CASEY, M. V. AND SÜRKEN, N.: Numerical and Experimental Investigation of a Low Pressure Steam Turbine during Windage, *Proc. IMechE, Part A: J. Power and Energy*, Vol. 223(6), pp. 697–708, 2009
- [108] SIGG, R.: *Numerische Untersuchung von Lastvariationen und Nässephänomenen an einer Niederdruck-Dampfturbine*, PhD Thesis, Institute of Thermal Turbomachinery and Machinery Laboratory (ITSM), University of Stuttgart, 2010
- [109] SIGLOCH, H.: *Technische Fluidmechanik*, 8. Aufl., Springer, 2012
- [110] SMITH, A.: The Influence of Moisture on the Efficiency of a One-Third Scale Model Low Pressure Steam Turbine, *Proc. Instn. Mech. Engrs.*, Vol. 180(15), pp. 39–49, 1965
- [111] SMITH, A.: Survey of Twisted Blading Development in Steam Turbines, *Proc. Instn. Mech. Engrs.*, Vol. 184(26), pp. 449–474, 1969

- [112] STARZMANN, J.: Numerische Untersuchung der Zweiphasenströmung und Analyse von Nässeverlusten in Niederdruckdampfmaschinen, PhD Thesis, Institute of Thermal Turbomachinery and Machinery Laboratory (ITSM), University of Stuttgart, 2014
- [113] STARZMANN, J. AND CASEY, M. V. AND SIEVERDING, F.: Non-Equilibrium Condensation Effects on the Flow Field and the Performance of a Low Pressure Steam Turbine, ASME Paper No. GT2010-22467, in: Proc. ASME Turbo Expo 2010: Power for Land, Sea, and Air, Glasgow, Scotland, UK, May 14–18, 2010
- [114] STARZMANN, J.; CASEY, M. V.; MAYER, J. F. AND SIEVERDING, F.: Wetness Loss Prediction for a Low Pressure Steam Turbine Using Computational Fluid Dynamics, Proc. IMechE, Part A: J. Power and Energy, Vol. 228(2), pp. 216–231, 2014
- [115] STEIN, P.; PFISTER, C.; SELL, M.; GALPIN, P. AND HANSEN, T.: Computational Fluid Dynamics Modeling of Low Pressure Steam Turbine Radial Diffuser Flow by Using a Novel Multiple Mixing Plane Based Coupling – Simulation and Validation, Trans. ASME, J. Eng. Gas Turb. Power, Vol. 138(4), p. 041604, 2016
- [116] SZWEDOWICZ, J.; SECALL-WIMMEL, T. AND DÜNCK-KERST, P.: Damping Performance of Axial Turbine Stages with Loosely Assembled Friction Bolts: The Nonlinear Dynamic Assessment, Trans. ASME, J. Eng. Gas Turb. Power, Vol. 130(3), p. 032505, 2008
- [117] SZWEDOWICZ, J.; SECALL-WIMMEL, TH.; DÜNCK-KERST, P.; SONNENSCHNEIN, A.; REGNERY, D. AND WESTFAHL, M.: Scaling Concept for Axial Turbine Stages with Loosely Assembled Friction Bolts: The Linear Dynamic Assessment, Trans. ASME, J. Eng. Gas Turb. Power, Vol. 130(3), p. 032504, 2008
- [118] SÜRKEN, N.: Dampfturbinentechnologie, Lecture Notes, Institute of Thermal Turbomachinery and Machinery Laboratory (ITSM), University of Stuttgart, 2014
- [119] TANAKA, Y.; YOKOTA, H.; OHYAMA, H.; NAKANO, T. AND KOENEKE, C. E.: Advanced Design of Mitsubishi Large Steam Turbines, in: Proc. POWERGEN Europe 2003, Düsseldorf, Germany, May 6–8, 2003
- [120] TRAUPEL, W.: Neue allgemeine Theorie der mehrstufigen axialen Turbinenmaschine, PhD Thesis, Eidgenössische Technische Hochschule (ETH) Zürich, 1942
- [121] TRAUPEL, W.: Thermische Turbinenmaschinen, Bd. 1: Thermodynamisch-strömungstechnische Berechnung, 1. Aufl., Springer, 1958

- [122] TRAUPEL, W.: Thermische Turbomaschinen, Bd. 1: Thermodynamisch-strömungstechnische Berechnung, 2. Aufl., Springer, 1966
- [123] TRAUPEL, W.: Thermische Turbomaschinen, Bd. 1: Thermodynamisch-strömungstechnische Berechnung, 3. Aufl., Springer, 1977
- [124] TRAUPEL, W.: Thermische Turbomaschinen, Bd. 2: Geänderte Betriebsbedingungen, Regelung, Mechanische Probleme, Temperaturprobleme, 3. Aufl., Springer, 1981
- [125] TRAXINGER, C.: Numerische Untersuchung des durch Koppелеlemente verursachten Verlustes in einer ND-Dampfturbinenstufe, Master Thesis, Institute of Thermal Turbomachinery and Machinery Laboratory (ITSM), University of Stuttgart, 2015
- [126] TROILO, M.: Streamline Curvature Method, in: Aerothermodynamics of Low Pressure Steam Turbines and Condensers, VON KARMAN Institute Book, Chap. 2.1., pp. 25–44, Springer, 1987
- [127] TRUCKENBRODT, E.: Fluidmechanik, Band 2: Elementare Strömungsvorgänge dichte veränderlicher Fluide sowie Potential- und Grenzschichtströmungen, 4. Aufl., Springer, 2008
- [128] UNFCCC: Historic Paris Agreement on Climate Change: 195 Nations Set Path to Keep Temperature Rise Well Below 2 Degrees Celsius, Article, <https://unfccc.int/news/finale-cop21>, 2015
- [129] VERSTRAETE, T.; PRINSIER, J.; DI SANTE, A.; DELLA GATTA, S. AND COSI, L.: Design Optimization of a Low Pressure Steam Turbine Radial Diffuser Using an Evolutionary Algorithm and 3D CFD, in: Proc. ASME Turbo Expo 2012: Turbine Technical Conference and Exposition, Copenhagen, Denmark, June 11–15, 2012
- [130] VGB POWER TECH: Facts and Figures - Electricity Generation, 2018
- [131] VOGT, D. M AND CASEY, M. V.: Grundlagen der thermischen Strömungsmaschinen, Lecture Notes, Institute of Thermal Turbomachinery and Machinery Laboratory (ITSM), University of Stuttgart, 2019
- [132] VÖLKER, L.: Neue Aspekte der aerodynamischen Gestaltung von Niederdruck-Endstufen-Beschaufelungen, PhD Thesis, Institute of Thermal Turbomachinery and Machinery Laboratory (ITSM), University of Stuttgart, 2006
- [133] WADIA, A. R. AND SZUCS, P. N.: Inner Workings of Shrouded and Unshrouded Transonic Fan Blades, Trans. ASME, J. Turbomach., Vol. 130(3), p. 031010, 2008

- [134] WAGNER, W. AND KRETZSCHMAR, H.-J.: International Steam Tables – Properties of Water and Steam based on the Industrial Formulation IAPWS-IF97, Springer, 2007
- [135] WILCOX, D. C.: Turbulence Modeling for CFD, 2nd edn., DCW Industries, Inc., La Cañada, California, 1994
- [136] WOLTER, I.: Experimentelle Untersuchung des Schwingungsverhaltens von Turbinen-Laufschaukeln unter realen Betriebsbedingungen mit und ohne Kopplung durch einen eingelegten Dämpferdraht, PhD Thesis, Institute of Thermal Turbomachinery and Machinery Laboratory (ITSM), University of Stuttgart, 1980
- [137] WU, Y. T.; FUNK, C. K.; HSU, P.; MOINE, J. L.; ZHOU, R.; SUBRAMANIAN, C. S.; CAMPBELL, C. X. AND MARRA, J. J.: Design Optimization of Turbo-Machinery Components with Independent FEA and CFD Tools in an Optimization Software Environment - A Mid-Span Shroud Ring Study Case, ASME Paper No. IMECE2011-62083, in: Proc. ASME 2011 International Mechanical Engineering Congress & Exposition, Denver, Colorado, USA, Nov. 11–17, 2011
- [138] YOUNG, J. B.: The Spontaneous Condensation of Steam in Supersonic Nozzles, Physicochemical Hydrodynamics, Vol. 3(1), pp. 57–82, 1982
- [139] YUCE, M. I. AND KAREEM, D. A.: A Numerical Analysis of Fluid Flow Around Circular and Square Cylinders, Journal American Water Works Association, Vol. 108(10), pp. E546–E554, 2016
- [140] ZDRAVKOVICH, M. M.: Flow Around Circular Cylinders, Vol. 1, Oxford University Press, 1997
- [141] ZDRAVKOVICH, M. M.: Flow Around Circular Cylinders, Vol. 2, Oxford University Press, 2003

A | CFD and Wet Steam Modelling

A.1 NAVIER-STOKES Equations

According to LAURIEN AND OERTEL, JR. [70], the NAVIER-STOKES Equations for compressible, three-dimensional flows can be formulated in vector notation as

$$\frac{\partial \vec{U}}{\partial t} + \sum_{m=1}^3 \frac{\partial \vec{F}_m}{\partial x_m} + \sum_{m=1}^3 \frac{\partial \vec{G}_m}{\partial x_m} = \vec{0}, \quad (\text{A.1})$$

whereby Eq. (A.1) does not include gravitational effects and considers a stationary, Cartesian coordinate system. Here, \vec{U} is the state or solution vector containing the conservative variables¹ and \vec{F}_m and \vec{G}_m are the vectors of convective and diffuse fluxes, respectively (spatial directions $m = 1,2,3$). Thus,

$$\vec{U} = \begin{bmatrix} \rho \\ \rho c_1 \\ \rho c_2 \\ \rho c_3 \\ \rho e_t \end{bmatrix}, \quad \vec{F}_m = \begin{bmatrix} \rho c_m \\ \rho c_m c_1 + \delta_{m1} p \\ \rho c_m c_2 + \delta_{m2} p \\ \rho c_m c_3 + \delta_{m3} p \\ \rho c_m h_t \end{bmatrix} \quad \text{and} \quad \vec{G}_m = \begin{bmatrix} 0 \\ -\tau_{m1} \\ -\tau_{m2} \\ -\tau_{m3} \\ -\sum_{l=1}^3 c_l \tau_{lm} + \dot{q}_m \end{bmatrix}, \quad (\text{A.2})$$

where the 1st component of vectors is the continuity equation, the 2nd to 4th components are the momentum equations in three spatial directions and the 5th component is the energy equation. Here, the total internal energy e_t and the total enthalpy h_t are calculated as

$$e_t = e + \frac{1}{2} \tilde{c}^2 \quad \text{with} \quad \tilde{c} = [c_1 \ c_2 \ c_3]^T \quad (\text{A.3})$$

and

$$h_t = e_t + \frac{p}{\rho} = e + \frac{1}{2} \tilde{c}^2 + \frac{p}{\rho} = h + \frac{1}{2} \tilde{c}^2. \quad (\text{A.4})$$

The heat flux densities are calculated according to FOURIER's law² of heat conduction

$$\dot{q}_m = -\lambda \frac{\partial T}{\partial x_m}, \quad (\text{A.5})$$

¹The conservation variables for mass, momentum and energy are noted in volume-specific form. This notation is commonly used in numerical fluid mechanics and has advantages when dealing with cell-oriented numerical schemes, where the volume is constant but the mass flow rate can vary, LAURIEN AND OERTEL, JR. [70]. Thus, mass-specific quantities are multiplied by ρ .

²Named after French mathematician and physicist Joseph FOURIER (1768–1830).

where λ is the thermal conductivity of the considered fluid. The friction-induced shear and normal stresses for NEWTONian fluids are determined as

$$\tau_{ij} = \mu \left(\frac{\partial c_i}{\partial x_j} + \frac{\partial c_j}{\partial x_i} \right) - \frac{2}{3} \mu \delta_{ij} \sum_{k=1}^3 \frac{\partial c_k}{\partial x_k} \quad (\text{A.6})$$

according to STOKES' law for frictional forces in viscous fluids, which couples the stresses τ_{ij} with the velocity field and is a generalization of NEWTON's elementary friction law, see e.g. SCHLICHTING AND GERSTEN [101]. In Eq. (A.6), μ is the dynamic viscosity of the fluid and δ_{ij} is the KRONECKER delta³, i.e. $\delta_{ij} = \{1 \text{ if } i = j; 0 \text{ if } i \neq j\}$.

A.2 Grid Independency Study

In order to figure out the sufficient resolution for grid-independent numerical results, grid studies are commonly carried out, comparing the impact of grid fineness on results of relevant flow and performance values. Such studies have been accomplished for all three CFD models introduced in Sec. 3.3, whereby results of CFD model *PSC-2* for operating point OP-2 are exemplary presented in the following. Among the models presented (Sec. 3.3), this model has the highest relevance for engineering practice, since it considers a simple lacing wire which is used since the early steam turbine developments, see e.g.

³Named after German mathematician Leopold KRONECKER (1823–1891).

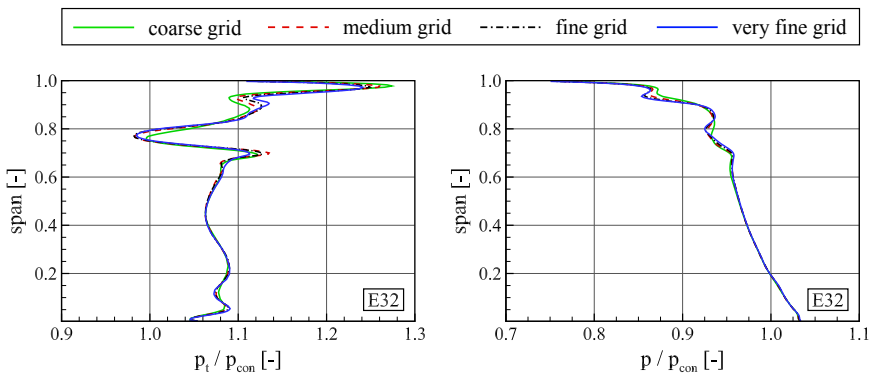


Figure A.1 Radial profiles of total and static pressure in evaluation plane E32 for CFD model *PSC-2* (Fig. 3.6 (right)) with *PSC* configuration V2.5 (Tab. B.3) at OP-2

Table A.1 Grid sizes, y^+ -values and CFD results of mass flow rate \dot{m} , specific work w and loss coefficient ζ_{PSC} , normalized to values obtained with the very fine (vf) grid, for CFD model *PSC-2* (Fig. 3.6, right) with PSC configuration V2.5 (Tab. B.3) at OP-2

grid	coarse	medium	fine	very fine
no. of elements ($\times 10^6$)	0.6	1.0	1.6	2.5
area-averaged y^+ -value	3.3	2.8	2.4	2.1
mass flow rate $\dot{m}/\dot{m}_{\text{vf}}$	1.00034	1.00019	1.00008	1
specific work w/w_{vf}	1.00190	1.00080	1.00025	1
loss coefficient $\zeta_{\text{PSC}}/\zeta_{\text{PSC,vf}}$	0.98828	0.99560	0.99907	1

TRAUPEL [121] or KIRILLOV AND KUZ'MIČEV [64], and is still very common in steam turbine applications nowadays, DROZDOWSKI ET AL. [29]. Furthermore, the majority of CFD calculations for the present thesis have been performed with this particular model, see Subsec. 3.3.2. Four levels of grid refinement were utilized. Table A.1 shows reference values for grid size and y^+ . The latter are area-averaged over blade and PSC surfaces of rotor R3.

Results of the grid study show small differences between the grids regarding radial profiles of circumferentially averaged flow values, compare the span-wise distributions of total and static pressure shown in Fig. A.1. The comparison of 1D values shown in Tab. A.1 focuses on quantities relevant for the performance assessment of PSC designs and the comparison of CFD results to analytical loss correlations, see Secs. 5.8 and 5.9, respectively. The work output of the one-stage configuration (*PSC-2*) differs approximately in 0.11% between the coarse and the medium grid, 0.05% between the medium and the fine grid and 0.03% between the fine and the very fine grid. Slightly larger deviations are found when considering the enthalpy loss coefficient according to Eq. (5.15). Here, ζ_{PSC} differs approximately in 0.74% between the coarse and the medium grid, 0.35% between the medium and the fine grid and 0.09% between the fine and the very fine grid. Based on these observations the medium grid size would be sufficient, if only averaged data would be of interest. However, to leave a margin for detailed investigations of the flow field in the turbine, all results presented in this thesis were obtained with a grid size and mesh quality comparable to the fine grid.

A.3 The Condensation Model

The non-equilibrium steam model used for this investigation accounts for wet steam effects, as discussed in Sec. 3.2. The condensation model is described below, compare to Ref. [54]. To model the droplet formation, the classical homogeneous nucleation rate

$$J = \frac{q_c}{1 + \varepsilon} \sqrt{\frac{2\sigma}{\pi m_m^3}} \frac{\varrho_g^2}{\varrho_l} \exp\left(-\frac{4\pi\sigma}{3k_B T_g} r_{\text{crit}}^2\right) \quad (\text{A.7})$$

is used. Here, ε is the non-isothermal correction according to KANTROWITZ, see BAKHTAR ET AL. [7].

$$\varepsilon = 2 \frac{\kappa - 1}{\kappa + 1} \frac{L}{R T_g} \left(\frac{L}{R T_g} - \frac{1}{2} \right) \quad (\text{A.8})$$

In Eqs. (A.7) and (A.8), κ is the ratio of specific heat capacities c_p and c_v , R is the specific gas constant of water, k_B is the BOLTZMANN constant⁴, σ is the surface tension, q_c is the condensation coefficient (generally taken as 1), m_m is the mass of a single water molecule and r_{crit} is the critical radius. More detailed information about the nucleation model is given by BAKHTAR ET AL. [7]. The growth of droplet radius r is modelled according to YOUNG [138].

$$\frac{dr}{dt} = \frac{\lambda_g}{\varrho_l L r} \frac{\Delta T \left(1 - \frac{r_{\text{crit}}}{r}\right)}{1 + 3.78(1 - \nu) \frac{\text{Kn}}{\text{Pr}}} \quad (\text{A.9})$$

Here, λ_g is the thermal conductivity of vapour, Kn is the KNUDSEN number according to GYARMATHY [42] and Pr is the PRANDTL number.⁵ The ν correction of YOUNG [138] can be used to calibrate the model to experimental data. In Eq. (A.10), T_s is the saturation temperature and α is set to 9.

$$\nu = \frac{R T_s}{L} \left(\alpha - 0.5 - \frac{2 - q_c}{2 q_c} \left(\frac{\kappa + 1}{2\kappa} \right) \left(\frac{c_p T_s}{L} \right) \right) \quad (\text{A.10})$$

⁴Named after Austrian physicist and philosopher Ludwig Eduard BOLTZMANN (1844–1906).

⁵Named after German physicist Ludwig PRANDTL (1875–1953), who contributed significant findings to the basic understanding of fluid mechanics and developed the boundary layer theory, see e.g. TRUCKENBRODT [127] or SCHLICHTING AND GERSTEN [101].

A.4 MOLLIER h, s -diagram

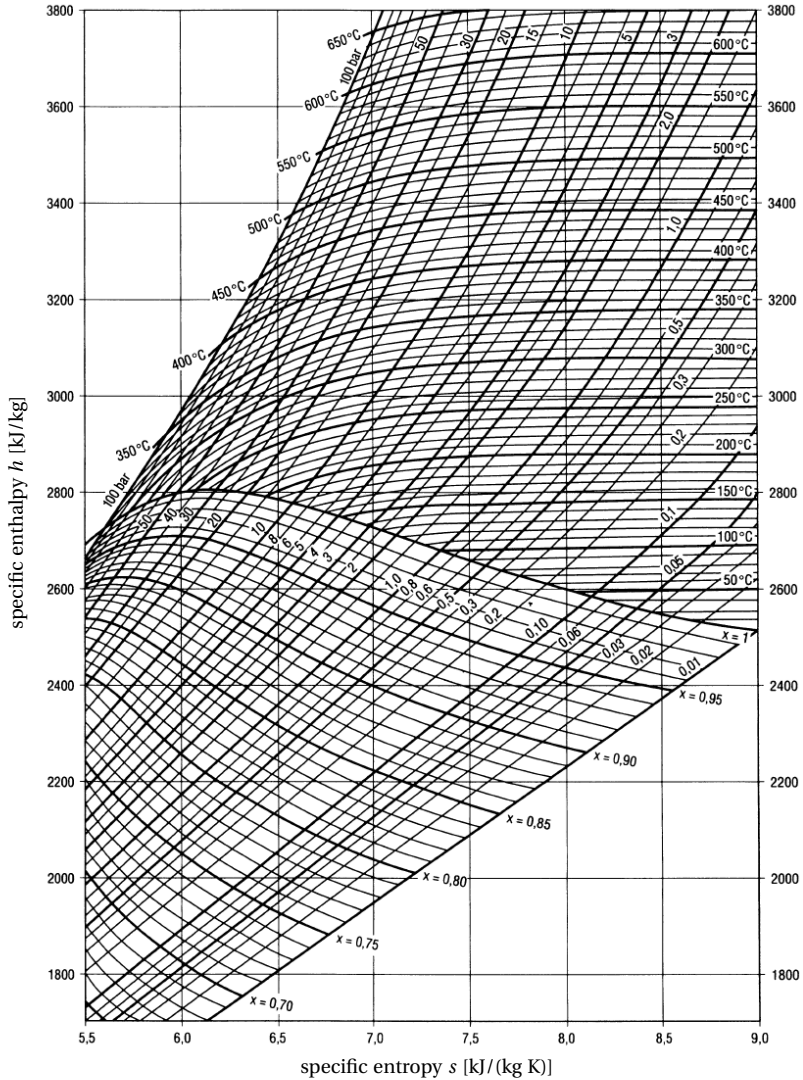


Figure A.2 MOLLIER h, s -diagram^a [109]

^aNamed after German physicist Richard MOLLIER (1863–1935).

B | PSC Parameter Study

B.1 PSC Parameters and Cross Sections

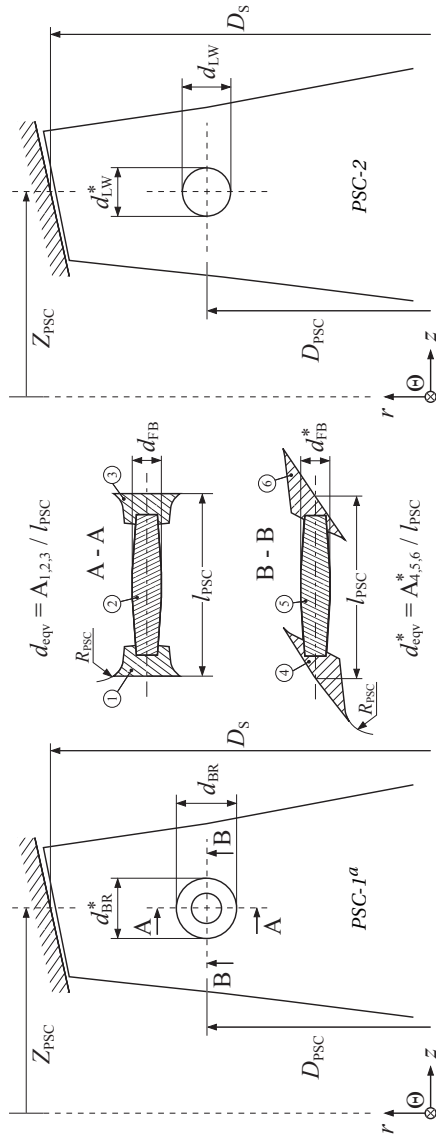


Figure B.1 Sketch of investigated LP blade (rotor R3) with parameters of PSC-1 (left/middle) and PSC-2 (right)

^aSketch and parameters of PSC-1 according to HÄFELE ET AL. [50].

Table B.1 Parameters and cross sections of PSC-1 according to Fig. B.1 (left/middle) and HÄFELE ET AL. [50]

V	1.1	1.2	1.3	1.4	1.5	1.6	1.7	1.8	1.9	1.10	1.11
cross section ^a											
$d_{\text{FB}}/d_{\text{FB,ref}}$	1	1	1	0.83	0.67	0.83	0.67	0.83	0.83	0.67	0.67
$d_{\text{BR}}/d_{\text{BR,ref}}$	1	1	1	1	1	0.83	0.67	1	1	0.67	0.67
$d_{\text{FB}}/d_{\text{LW,ref}}$	0.83	0.83	0.83	0.69	0.55	0.69	0.55	0.69	0.69	0.55	0.55
$d_{\text{eqv}}/d_{\text{LW,ref}}$	1	1	1	0.90	0.81	0.83	0.65	0.90	0.90	0.66	0.66
$D_{\text{PSC}}/D_{\text{PSC,ref}}$	1 ^b	0.99	0.98	1	1	1	1	1	1	1	1
$d_{\text{FB}}^*/d_{\text{FB}}$	1	1	1	1	1	1	1	1.25	1.5	1	1.5
$d_{\text{BR}}^*/d_{\text{BR}}$	1	1	1	1	1	1	1	1	1	1.5	1.5
$d_{\text{eqv}}^*/d_{\text{eqv}}$	1	1	1	1	1	1	1	1.13	1.25	1.22	1.48
$l_{\text{PSC}}/l_{\text{PSC,ref}}$	1	0.99	0.97	1	1	1	1	1	1	1	1
$c_{\text{D}}(\text{FB \& BR})^c$	1.2	1.2	1.2	1.2	1.2	1.2	1.2	1.0	0.91	0.93	0.78
$c_{\text{D}}(\text{FB})^d$	1.2	1.2	1.2	1.2	1.2	1.2	1.2	0.92	0.77	1.2	0.77
$c_{\text{D}}(\text{BR,PS})^e$	1.2	1.2	1.2	1.2	1.2	1.2	1.2	1.2	1.2	0.81	0.81
$c_{\text{D}}(\text{BR,SS})^f$	1.2	1.2	1.2	1.2	1.2	1.2	1.2	1.2	1.2	0.76	0.76

^aOrientation of PSC cross sections according to coordinate system in Fig. B.1.

^bReference geometry V1.1 \rightarrow PSC at 75% blade span.

^cV1.8 to V1.11 according to Eq. (5.32) of HOERNER [47] with d_{eqv}^* and d_{eqv} , see Fig. B.1.

^dV1.8, V1.9 and V1.11 according to Eq. (5.32) of HOERNER [47] with d_{FB}^* and d_{FB} , see Fig. B.1.

^eV1.10 and V1.11 according to Eq. (5.32) of HOERNER [47] with $d_{\text{BR,PS}}^*$ and $d_{\text{BR,PS}}$, see Fig. B.1.

^fV1.10 and V1.11 according to Eq. (5.32) of HOERNER [47] with $d_{\text{BR,SS}}^*$ and $d_{\text{BR,SS}}$, see Fig. B.1.

Table B.2 Parameters and cross sections of PSC-2 for span-wise variation at $Z_{\text{PSC,ref}}$ according to Fig. B.1 (right)

V	2.1	2.2	2.3	2.7	2.8	2.9	2.10	2.11	2.12	2.13	2.14	2.15
cross section												
$d_{\text{LW}}/d_{\text{LW,ref}}$	1	0.83	0.65	1	0.83	0.65	1	0.83	0.65	1	0.83	0.65
$D_{\text{PSC}}/D_{\text{PSC,ref}}$	1.11	1.11	1.11	0.89	0.89	0.89	0.78	0.78	0.78	0.67	0.67	0.67
$d_{\text{LW}}^*/d_{\text{LW}}$	1	1	1	1	1	1	1	1	1	1	1	1
$l_{\text{PSC}}/l_{\text{PSC,ref}}$	1.05	1.05	1.05	0.95	0.95	0.95	0.90	0.90	0.90	0.85	0.85	0.85
c_{D}	1.2	1.2	1.2	1.2	1.2	1.2	1.2	1.2	1.2	1.2	1.2	1.2

Table B.3 Parameters and cross sections of PSC-2 for variation at reference position $D_{\text{PSC,ref}}$, $Z_{\text{PSC,ref}}$ (Fig. B.1 (right))

V	2.4	2.5	2.6	2.16	2.17	2.18	2.19	2.20	2.21	2.22	2.23
cross section ^a											
$d_{\text{LW}}/d_{\text{LW,ref}}$	1	0.83	0.65	0.83	0.83	0.65	0.65	0.85	0.89	0.67	0.70
$D_{\text{PSC}}/D_{\text{PSC,ref}}$	1	1	1	1	1	1	1	1	1	1	1
$d_{\text{LW}}^*/d_{\text{LW}}$	1	1	1	1.25	1.5	1.25	1.5	1.19	1.35	1.19	1.35
$l_{\text{PSC}}/l_{\text{PSC,ref}}$	1	1	1	1	1	1	1	1	1	1	1
c_{D}^b	1.2	1.2	1.2	0.91	0.77	0.91	0.77	0.91	0.77	0.91	0.77

^aOrientation of PSC cross sections according to coordinate system in Fig. B.1.

^bV2.16 to V2.23 according to Eq. (5.32) of HOERNER [47] with d_{LW}^* and d_{LW} , see Fig. B.1. Note that for evaluating the drag coefficients of V2.20 to V2.23, d_{LW}^* and d_{LW} of configurations V2.16 to V2.19 were used.

Table B.4 Parameters and cross sections of PSC-2 for variation of axial PSC position, zigzag configurations (δ_{zigzag} is defined in Fig. 1.10) and streamlined (teardrop) PSCs

V	2.24	2.25	2.26	2.27	2.28	2.29	V2.30	V2.31
cross section ^a	○	○	○	○	○	○	◐	◑
$d_{\text{LW}}/d_{\text{LW,ref}}$	0.83	0.83	0.65	0.65	0.65	0.65	0.83	0.65
$D_{\text{PSC}}/D_{\text{PSC,ref}}$	1	1	1	1	1	1	1	1
$d_{\text{LW}}^*/d_{\text{LW}}$	1	1	1	1	1	1	1.5	1.5
$l_{\text{PSC}}/l_{\text{PSC,ref}}$	1	1.01	1	1.01	0.85	0.75	1	1
$\Delta Z_{\text{PSC}}/C_{z,\text{PSC}}$	-0.13	0.13	-0.13	0.13	-	-	-	-
δ_{zigzag} [°]	-	-	-	-	7.5	15	-	-

^aOrientation of PSC cross sections according to coordinate system in Fig. B.1, except configurations V2.28 and V2.29.

B.2 Supplementary CFD Results

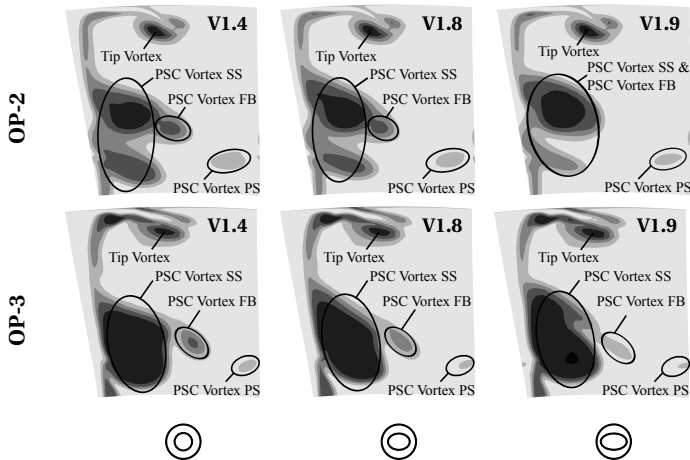


Figure B.2 Total pressure contour on axial plane (67.5% to 100% span) 1.3 d_{BR}^* downstream of PSC, scaled from plane-wise $p_{t,\text{max}}$ (light gray) to $p_{t,\text{min}}$ (dark gray/black) at the respective OP

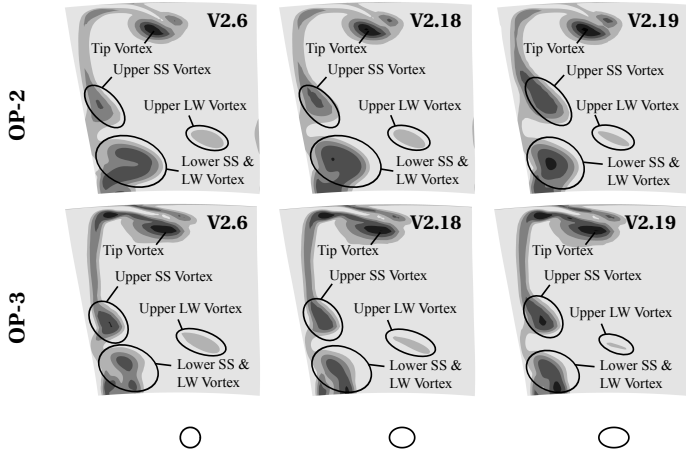


Figure B.3 Total pressure contour on axial plane (67.5% to 100% span) $1.3 d_{BR}^*$ downstream of PSC, scaled from plane-wise $p_{t,max}$ (light) to $p_{t,min}$ (dark) at the respective OP

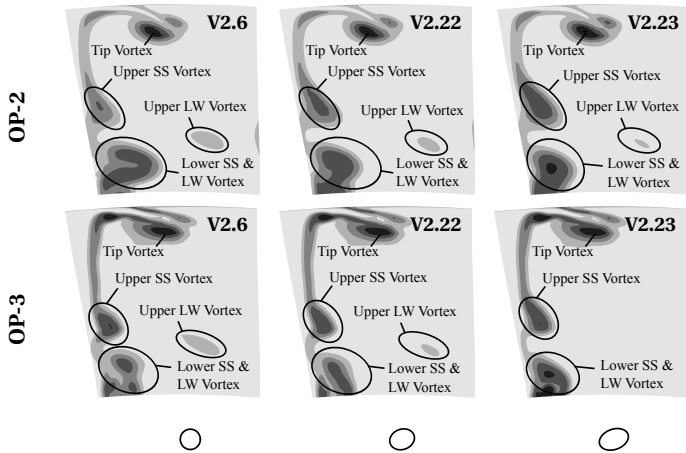


Figure B.4 Total pressure contour on axial plane (67.5% to 100% span) $1.3 d_{BR}^*$ downstream of PSC, scaled from plane-wise $p_{t,max}$ (light) to $p_{t,min}$ (dark) at the respective OP

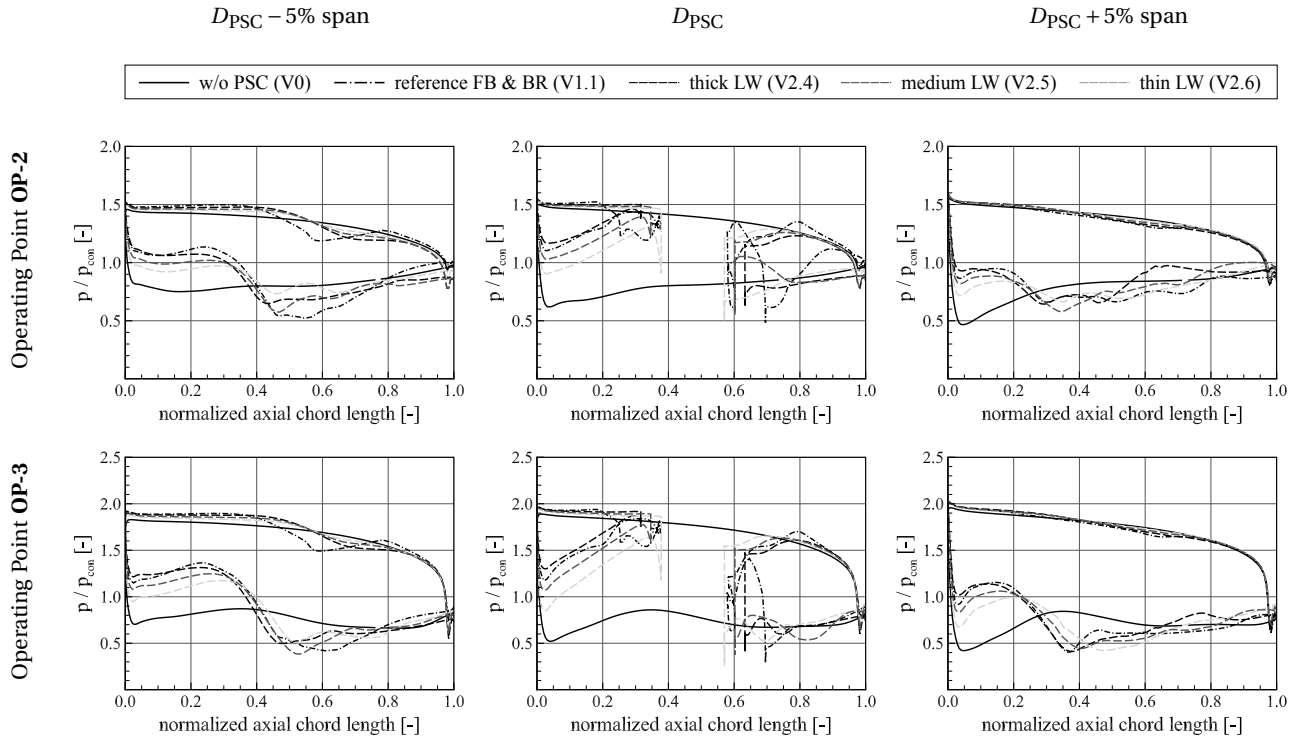


Figure B.5 Comparison of CFD predicted chord-wise blade loading at the radial PSC position (D_{PSC}) and 5% blade span below and above the PSC at **OP-2** and **OP-3** for variation of PSC diameter according to Tabs. B.1 and B.3

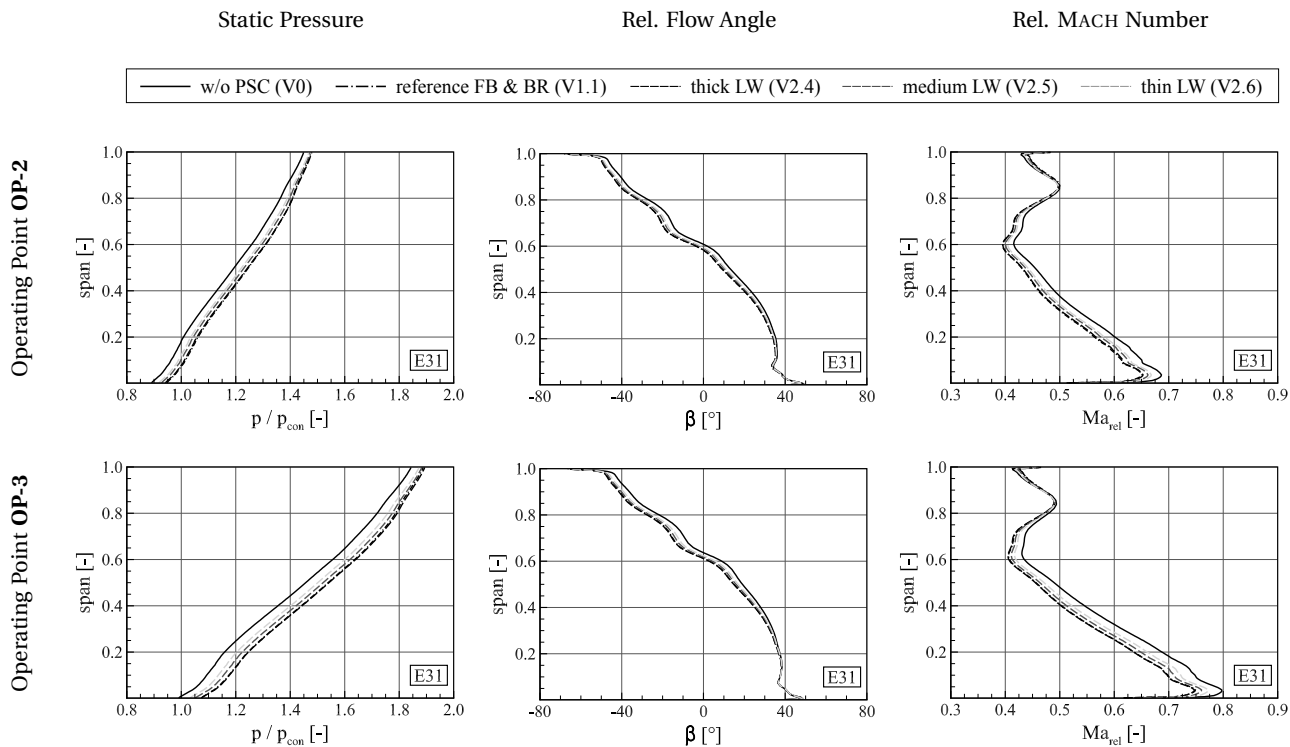


Figure B.6 Comparison of CFD predicted radial profiles of static pressure, relative flow angle and relative MACH number in evaluation plane E31 (see Fig. 3.5) at OP-2 and OP-3 for variation of PSC diameter according to Tabs. B.1 and B.3

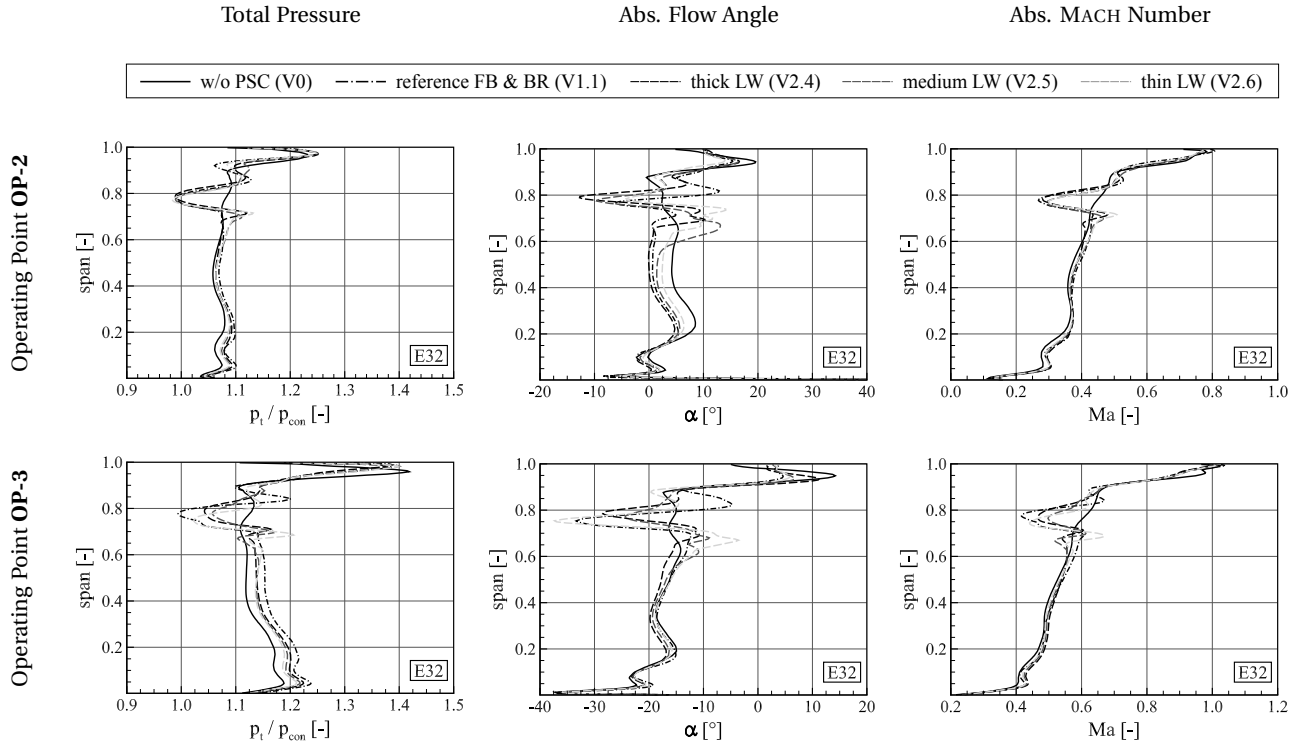


Figure B.7 Comparison of CFD predicted radial profiles of total pressure, absolute flow angle and absolute MACH number in evaluation plane E32 (see Fig. 3.5) at OP-2 and OP-3 for variation of PSC diameter according to Tabs. B.1 and B.3

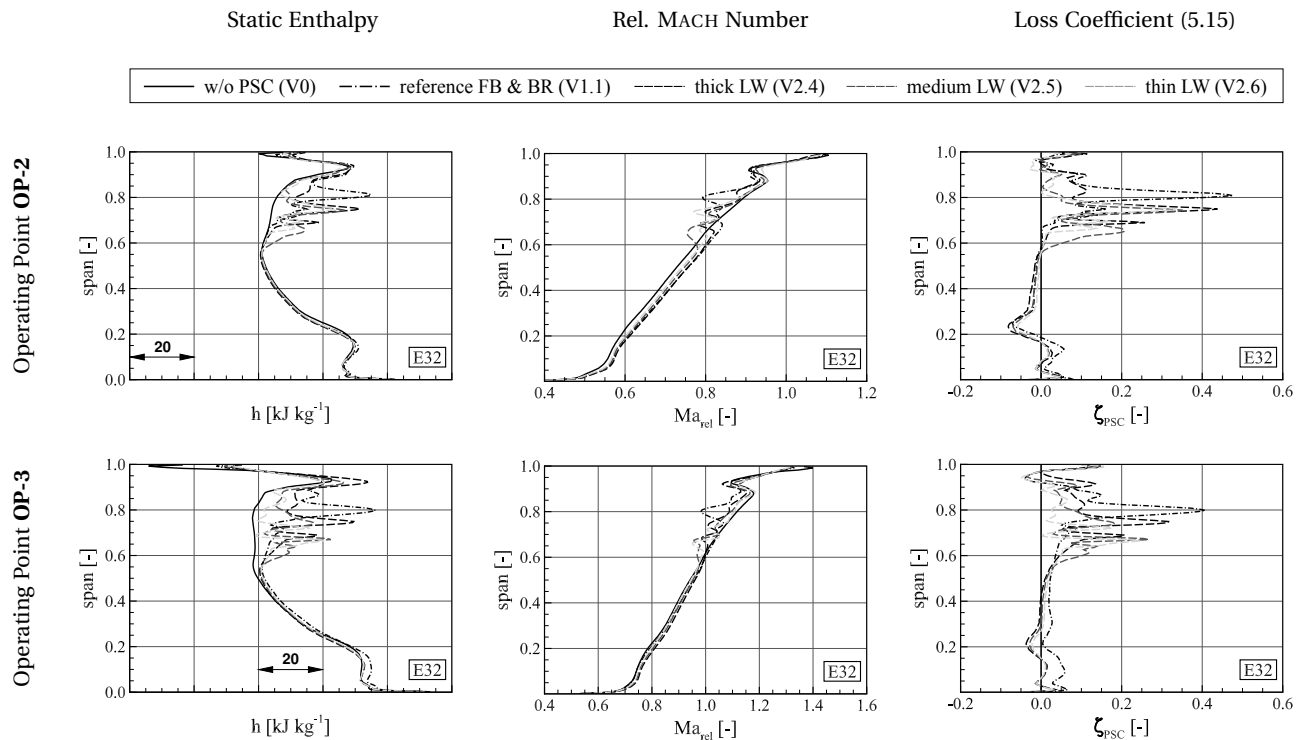


Figure B.8 Comparison of CFD predicted radial profiles of static enthalpy, relative MACH number and loss coefficient in evaluation plane E32 (see Fig. 3.5) at OP-2 and OP-3 for variation of PSC diameter according to Tabs. B.1 and B.3

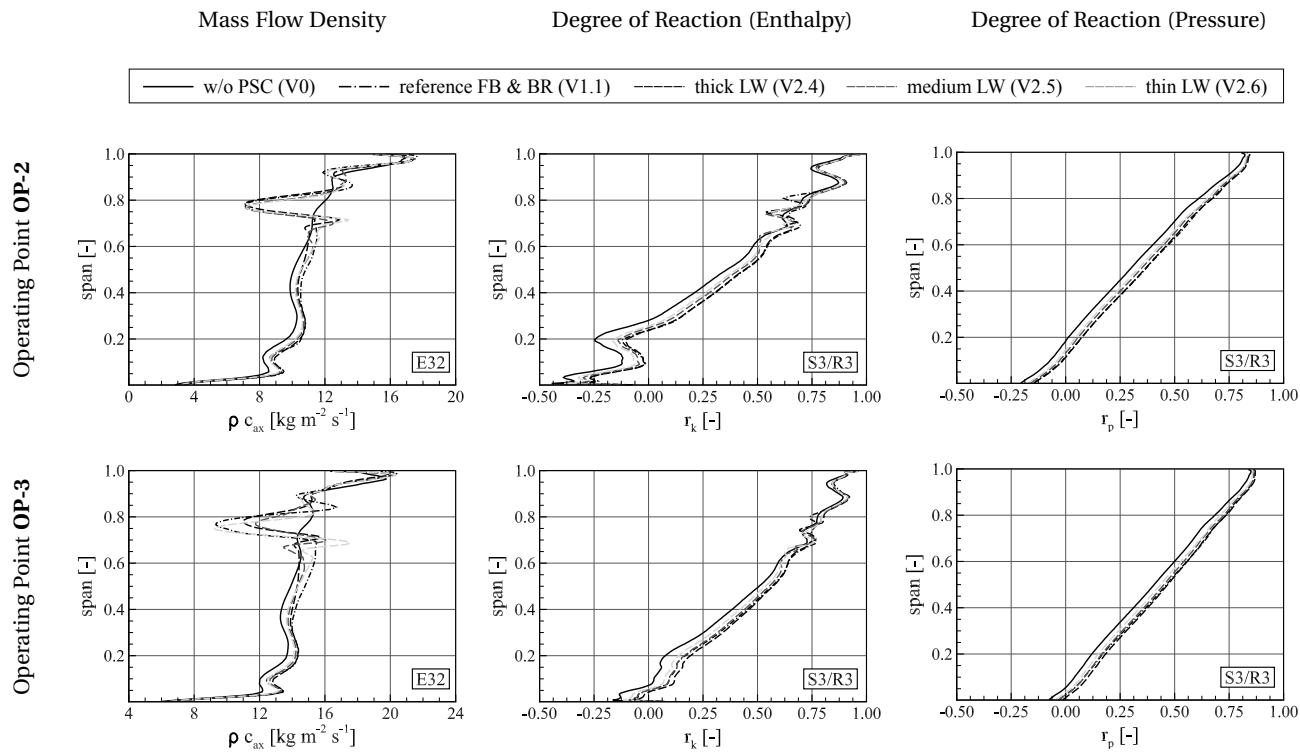


Figure B.9 Comparison of CFD predicted radial profiles of mass flow density in evaluation plane **E32** (see Fig. 3.5) and enthalpy-based and pressure-based degree of reaction at **OP-2** and **OP-3** for variation of PSC diameter according to Tabs. B.1 and B.3

B.3 Remarks on OPs and Loss Correlations

Besides the conclusions drawn in Subsec. 5.9.2 based on an OP at BEP condition (OP-2), it has to be considered that the closeness of agreement is also OP-dependent and gets worse at moderate overload (OP-3). For PSCs located at upper span, the under-prediction of loss is severe, see Fig. B.10. In contrast, due to the OP-dependent *inversed loss tendency* discussed on Page 141, both correlations over-predict the loss at lower span region (Fig. B.10, bottom). DUNHAM AND PHILLIPSEN [31] report that in their experience the drag

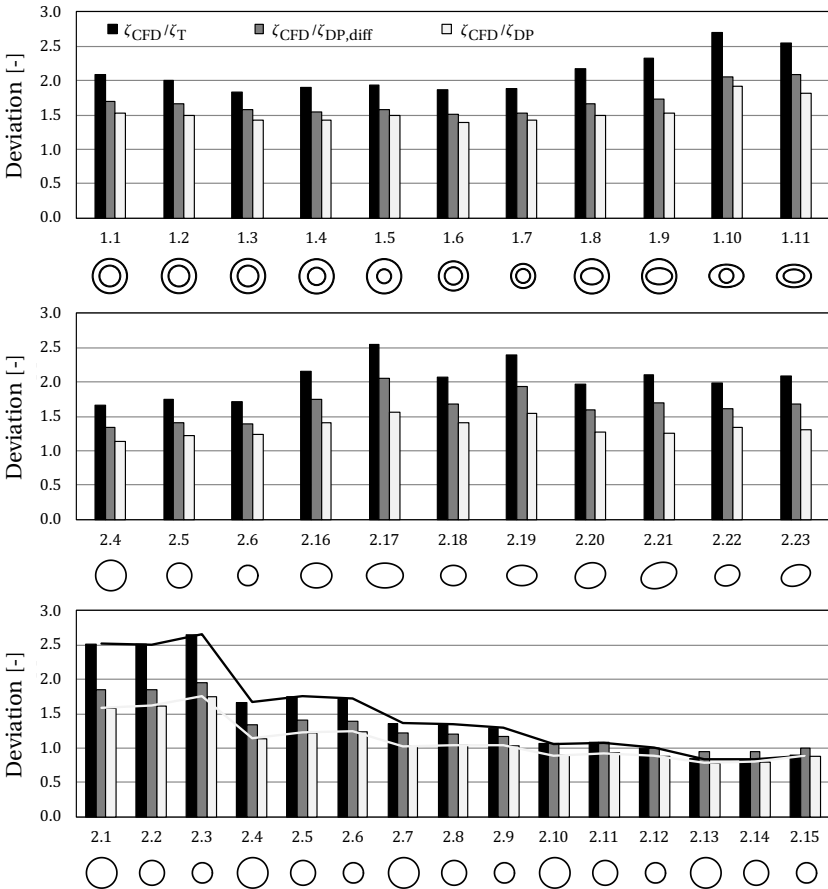


Figure B.10 Deviation of loss coefficient ζ_{PSC} based on CFD results and on the correlations of TRAUPEL [123] and DUNHAM AND PHILLIPSEN [31] at OP-3 (overload)

coefficient needed to be a function of the MACH number in order to get acceptable conformity with experimental data. This basic dependency is also reported by ZDRAVKOVICH [140] and was discussed in Sec. 5.3.1 by means of Fig. 5.7 for ideal compressible flow around circular cylinders. Scaling the results of drag loss for circular PSCs at reference span (V1.1–V1.7 and V2.4–V2.6) by the ratio of exit MACH numbers (Tab. 5.4) yields an improved correspondence, being of the same magnitude than for OP-2 ($\zeta_{\text{PSC,CFD}}/\zeta_{\text{PSC,T}} \approx 1.5$, $\zeta_{\text{PSC,CFD}}/\zeta_{\text{PSC,DP}} \approx 1.1$), compare to Subsec. 5.9.2.

C | Steam Cycle and Test Facility at ITSM

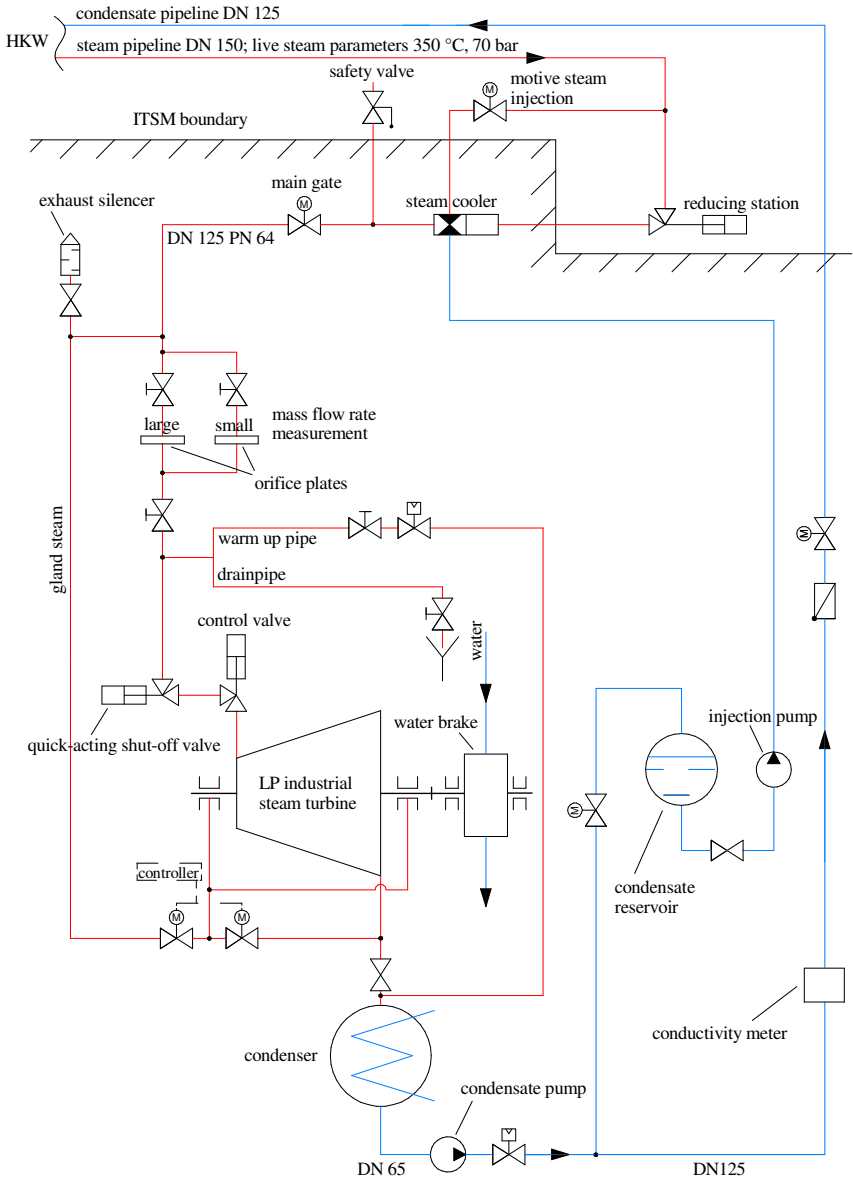


Figure C.1 Steam cycle and industrial steam turbine test facility at ITSM

Lebenslauf

Persönliche Daten

Name: Markus Häfele
Geburtsdatum: 16. November 1979
Geburtsort: Lima/Peru
Familienstand: verheiratet
Staatsangehörigkeit: deutsch

Ausbildung

1987 – 1991 Johann-Georg-Fischer-Schule Süßen
1991 – 2000 Rechberg-Gymnasium Donzdorf (Abitur)
2000 – 2001 Zivildienst, Sozialstation Wilhelmshilfe e.V.
2001 – 2008 Studium des Allgemeinen Maschinenwesens,
Universität Stuttgart (Dipl.-Ing.)
2007 – 2008 Diplomarbeit bei Voith Siemens Hydro
Power Generation, Inc., York, PA, USA

Berufstätigkeit

2008 – 2015 Wissenschaftlicher Mitarbeiter,
Institut für Thermische Strömungsmaschinen und
Maschinenlaboratorium (ITSM), Universität Stuttgart,
Prof. M. Casey, D. Phil und Prof. Tekn. Dr. D. Vogt
2016 – heute Entwicklungsingenieur für Wasserturbinen,
Wasserkraft Volk AG, Gutach im Breisgau

